The Interspike-Interval Statistics of Non-Renewal Neuron Models

D I S S E R T A T I O N

zur Erlangung des akademischen Grades

doctor rerum naturalium
(Dr. Rer. Nat.)
im Fach Physik

eingereicht an der
Mathematisch-Naturwissenschaftlichen Fakultät I
Humboldt-Universität zu Berlin

von
Dipl. Phys. Tilo Schwalger

Präsident der Humboldt-Universität zu Berlin:
Prof. Dr. Jan-Hendrik Olbertz

Dekan der Mathematisch-Naturwissenschaftlichen Fakultät I:
Prof. Stefan Hecht, PhD

Gutachter:
1. Prof. Dr. Benjamin Lindner (HU Berlin)
2. Prof. Dr. Lutz Schimansky-Geier (HU Berlin)
3. Prof. Fabrizio Gabbiani, PhD (BCM Houston, USA)

Tag der mündlichen Prüfung: 1. März 2013

Abstract

The spontaneous activity of a neuron as well as its response to constant stimuli is often characterized by irregular and irreproducible spike trains. This variability is due to various sources of neuronal noise. Many statistical features of these spike trains such as the variability of interspike intervals (ISIs) and spike counts have been theoretically understood by means of reduced stochastic neuron models that are amenable to a mathematical analysis. Most of these models belong to the class of *renewal models*, in which the ISIs within a spike train are statistically independent. Because of this convenient mathematical property, renewal models have proven very successful in explaining the first-order ISI statistics. However, numerous experimental studies have reported correlations between ISIs – a higher-order statistics that cannot be described by a renewal model. The present thesis deals with the theoretical analysis of *non-renewal models*. In particular, two scenarios are investigated more closely: neurons in the presence of colored noise representing temporally correlated inputs and neurons exhibiting spike-frequency adaptation in the presence of different sources of noise. Using extended integrate-and-fire neuron models, approximation techniques are put forward to analytically calculate the stationary ISI statistics in the sub- and suprathreshold spiking regime. The analysis focuses on the serial correlation coefficient (SCC).

The perfect integrate-and-fire (PIF) model, which is the canonical model for suprathreshold periodic firing, serves as the basis for further extensions that render the model non-renewal. In the first part, the PIF model is driven by colored noise in the form of a multi-dimensional Ornstein-Uhlenbeck process, which represents a broad class of possible colored noise processes. For this case, general formulas for the coefficient of variation, the SCC, the ISI density and the Fano factor are derived. For the special case of exponentially-correlated noise, it is shown that colored noise with a large correlation time can lead to strongly peaked ISI densities with a large skewness and kurtosis. As another special case, a superposition of harmonic noise and exponentially-correlated noise is considered. With such colored noise, complex serial correlation structures that have been observed in electro-sensory neurons of paddlefish can be explained theoretically.

In the second part, a white-noise driven PIF model is extended by a *deterministic adaptation* current that realizes an inhibitory feedback. An expression for the SCC is derived for weak noise, which is valid for arbitrary feedback strengths and adaptation time constants. The theory reproduces short-range, negative serial correlations, which have been frequently reported for neurons with spike-frequency adaptation. It also reveals an optimal ratio of time scales for which adjacent ISIs are most strongly anti-correlated. Furthermore, two dynamical regimes are identified, where the SCC is either negative at all lags or alternates in sign. By applying weak-noise approximation techniques, the stationary Fokker-Planck equation corresponding to the two-dimensional Langevin equation can be solved, which results in explicit expressions for the membrane potential distribution and the distribution of the adaptation variable upon firing. Finally, it is shown how the ISI density, the linear response function and the power spectrum can be computed for slow adaptation currents and arbitrary noise strength. The theory explicitly reveals the inverse Gaussian statistics of ISIs, the high-pass filter property of adaptation and the reduction of the power spectrum at low frequencies due to negative serial correlations.

In the third part, the effect of a *stochastic adaptation* current is studied. This situation arises when the adaptation current is mediated by a finite population of "adaptation channels" (channel noise). By using the diffusion approximation it is shown that slow adaptation channels introduce an intrinsic source of colored noise. The station-

ary dynamics can be further approximated by a PIF model without adaptation but a rescaled colored noise – a case that has been analyzed in the first part of the thesis. As a consequence, the serial correlations are positive if the dominating noise emerges from the slow adaptation current, which is in marked contrast to the negative correlations observed for a deterministic adaptation current and fast sources of noise. The colored noise also shapes the ISI densities towards a density that is more peaked than an inverse Gaussian ISI density. This suggests an indirect method to determine the time scales of the noise which underlies the response variability solely on the basis of the ISI statistics. In particular, negative SCCs and inverse Gaussian ISI densities hint at fast noise sources, whereas positive SCCs and peaked ISI densities indicate the presence of slow noise. Applying this method to in vivo spiking data of locust auditory receptor cells reveals strong evidence for two distinct sources of noise, slow adaptation channel noise and fast channel noise.

In the fourth part, the subthreshold, excitable regime is addressed. It is assumed that the neuron keeps a memory through an internal variable with a finite number of discrete states. Firing events are generated by a state-dependent escape rate, whereas the dynamics of the internal variable is given by a Markovian jump process. For this model a general kinetic scheme is constructed that keeps track of the number of spikes at a given time. The spike count statistics is used to derive the general structure of the SCC. The theoretical results are first applied to a leaky integrate-and-fire model that is driven by a dichotomous colored noise. As a result, the spike train switches randomly between two renewal processes. The serial correlations are positive and become maximized at an optimal ratio of the two firing rates. Furthermore, an improved non-Markovian theory is developed that also captures more regular spiking states with a small coefficient of variation including the supra-threshold regime. Finally, it is shown by simple models with self-inhibitory feedback how the general Markovian theory can be employed to study negative serial correlations in excitable neuron models with discrete adaptation states.

This thesis presents a number of analytical approaches for analyzing non-renewal models and provides explicit formulas for higher-order spiking statistics. These results are useful for a general theory of non-renewal models, for gaining further insights into functional aspects of non-renewal spiking and for the interpretation of spike train data. The results also shed light on possible sources of noise in sensory neurons.

Zusammenfassung

Die spontane Aktivität von Neuronen sowie deren Antwort auf zeitlich konstante Reize ist oftmals gekennzeichnet durch irreguläre und nicht-reproduzierbare Abfolgen von elektrischen Pulsen (Spikes). Diese Variabilität von Pulszügen wird durch verschiedene Rauschquellen verursacht. Viele statistische Eigenschaften von Pulszügen wie etwa die Statistik der Interspike-Intervalle (ISIs) können durch reduzierte stochastische Neuronenmodelle theoretisch verstanden werden. Die meisten dieser Modelle gehören zur Klasse der Erneuerungsmodelle, in welchen die ISIs statistisch unabhängig voneinander sind. Aufgrund dieser für die mathematische Analyse vorteilhaften Eigenschaft haben sich Erneurungsmodelle als sehr erfolgreich erwiesen, die Statistiken erster Ordnung wie die ISI Varianz und die ISI Verteilung zu berechnen und zu erklären. Etliche experimentelle Studien haben jedoch gezeigt, dass Statistiken höherer Ordnung, wie das Vorhandensein von Korrelationen zwischen ISIs, nicht vereinbar sind mit einem Erneuerungsmodell. Die vorliegende Doktorarbeit beschäftigt sich mit der theoretischen Untersuchung von *Nicht-Erneuerungsmodellen*. Insbesondere werden zwei Szenarien eingehender studiert: Neuronen unter dem Einfluss von farbigem Rauschens, welches zeitlich korrelierte Eingangsströme repräsentiert und Neuronen mit Feuerraten-Adaption unter dem Einfluss von verschiedenen Arten von Rauschen. Einfache Erweiterungen von "Integrate-and-fire"-Modellen sowie die Verwendung von Näherungsmethoden erlauben es, die ISI-Statistik sowohl für das unter- als auch für das überschwellige Feuer-Regime analytisch zu berechnen. Ein besonderer Schwerpunkt liegt hier auf der Berechnung des seriellen Korrelationskoeffizienten (SCC).

Im überschwelligen Feuer-Regime dient das sogenannte "perfect integrate-and-fire"-Modell (PIF-Modell) als Grundlage für Erweiterungen, die das PIF-Modell in ein Nicht-Erneuerungsmodell überführen. Im ersten Teil wird ein PIF-Modell betrachtet, das durch farbiges Rauschen in Form eines mehrdimensionalen Ornstein-Uhlenbeck-Prozesses getrieben wird. Solch ein Prozess realisiert eine große Modell-Klasse von farbigen Rauschprozessen. Für diesen recht allgemeinen Fall werden analytische Formeln für den Koeffizienten der Variation, den SCC, die ISI-Dichte und den Fano-Faktor hergeleitet. Für den speziellen Fall von exponentiell-korreliertem Rauschen wird gezeigt, dass lange Korrelationszeiten zu ausgeprägteren Maxima in der ISI-Dichte führen. In einem weiteren Spezialfall wird eine Überlagerung von exponentiell-korreliertem Rauschen und harmonischem Rauschen betrachtet. Mit diesem Modell können komplexe Korrelationsstrukturen, die in elektro-sensorischen Neuronen des Löffelstörs beobachtet werden, theoretisch erklärt werden.

Im zweiten Teil wird ein durch weißes Rauschen getriebenes PIF-Modell durch einen deterministischen Adaptionsstrom erweitert, der einen negativen Rückkopplungsmechanismus darstellt. Für dieses Modell, kann eine Formel für den seriellen Korrelationskoeffizienten gefunden werden, die für beliebige Rückkopplungsstärken und Adaptionszeitkonstanten gültig ist. Diese Theorie reproduziert die negativen Korrelationen, die häufig bei Neuronen mit Feuerraten-Adaption gemessen wurden, und offenbart ein optimales Zeitskalenverhältnis, für welches die Anti-Korrelationen maximal sind. Weiterhin kann die zweidimensionale Fokker-Planck-Gleichung, die dem Modell entspricht, für den stationären Fall gelöst werden, falls das Rauschen schwach ist. Aus dieser Lösung kann die Verteilung der Adaptionsvariablen direkt nach dem Feuern sowie die Membranpotentialverteilung abgeleitet werden. Schließlich wird aufgezeigt, wie die ISI-Dichte, die lineare Antwortfunktion und das Leistungsspektrum für den Fall von langsamer Adaption berechnet werden kann. Die Theorie zeigt die inverse Gauss-Statistik für die ISIs, die typische Hochpass-Eigenschaft von Adaption sowie die Reduzierung des Leistungsspektrums bei tiefen Fre-

quenzen aufgrund negativer serieller Korrelationen.

Im dritten Teil wird der Effekt eines stochastischen Adaptionsstroms untersucht. Diese Situation tritt auf, wenn der Adaptionsstrom aus einer endlichen Anzahl von "Adaptionskanälen" resultiert (Kanalrauschen). Unter Benutzung der Diffusionsnäherung wird gezeigt, dass langsame Adaptionskanäle eine intrinsische Quelle für farbiges Rauschen darstellen. Weiterhin kann die stationäre Dynamik des Modells durch ein PIF-Modell mit farbigem Rauschen anstelle eines Adaptionsstroms genähert werden. Genau dieser Fall wurde im ersten Teil theoretisch untersucht. Infolgedessen sind die Korrelationen positiv, wenn langsames Adaptionskanalrauschen dominiert, wohingegen die Korrelationen negativ sind, wenn schnelle Fluktuationen dominieren. Das farbige Rauschen des Adaptionsstroms beeinflusst auch die Gestalt der ISI-Dichte, die ein ausgeprägteres Maximum besitzt als eine entsprechende inverse Gauss-Verteilung. Das legt eine indirekte Methode nahe, mit der die Zeitskalen des dominierenden Rauschens allein aus der Statistik der Interspike-Intervalle abgeschätzt werden können. Insbesondere, weisen negative Korrelationen und inverse Gauss-Dichten für die ISIs auf schnelles Rauschen hin, wohingegen positive Korrelationen und ein ausgeprägtes Maximum in den ISI-Dichten auf die Anwesenheit von langsamem Rauschen hindeutet. Die Anwendung dieser Idee auf Pulszüge auditorischer Rezeptorzellen von Heuschrecken erlaubt in der Tat Rückschlüsse auf das zugrundeliegende Rauschen. Insbesondere scheint für diese Zellen langsames Rauschen zur Variabilität der Spikes beizutragen.

Der vierte Teil wendet sich dem unterschwelligen, anregbaren Feuer-Regime zu. Es wird zusätzlich angenommen, dass das Feuern von einer versteckten Variablen abhängt, die eine endliche Anzahl diskreter Zustände annehmen kann. Spikes werden durch eine zustandsabhängige Feuerrate generiert, und die versteckte Variable wird als diskreter Markov-Prozess modelliert. Für dieses Modell wird ein allgemeines Markov-Schema vorgeschlagen, welches auch die Pulszahlen explizit als Zustände des Systems einbezieht. Die Statistik der Pulszahlen kann dann genutzt werden, um die allgemeine Struktur des seriellen Korrelationskoeffizienten abzuleiten. Diese Markov-Theorie wird zuerst auf ein "leaky integrate-and-fire"-Modell angewendet, welches durch dichotomes farbiges Rauschen getrieben wird. Die seriellen Korrelationen sind in diesem Fall positiv und werden maximal bei einer endlichen Amplitude des dichotomen Rauschens. Eine alternative Nicht-Markov-Theorie liefert bessere Übereinstimmungen im Fall von regulläreren Pulszügen. Schließlich wird ein einfaches Modell mit negativer Rückkopplung betrachtet, welches Modellen mit Adaptionsströmen ähnelt. Die Markov-Theorie kann negative Korrelationen in diesen Modellen erklären.

Diese Doktorarbeit entwickelt eine Reihe analytischer Methoden zur Untersuchung von Nicht-Erneuerungsprozessen und beinhaltet eine Vielzahl analytischer Formeln für die Feuerstatistik höherer Ordnung. Diese Resultate sind hilfreich für die Entwicklung einer allgemeinen Theorie von Nicht-Erneuerungsmodellen, für das Verstehen funktionaler Aspekte von Nicht-Erneuerungsmodellen sowie für die Interpretation von Spike-Daten einzelner Neuronen.

Contents

Chapter 1.

Introduction

This thesis is concerned with the on-going activity of single neurons. Neurons, also known as nerve cells, are fascinating types of cells that are able to communicate with other cells by means of short electrical pulses called spikes or action potentials. The spikes are thought to be the biophysical basis of information processing and information transmission in the nervous system. For instance, all information that we receive from our environment, e.g. if we see an object or hear a sound, is encoded by sensory neurons into sequences of spikes, called spike trains, which carry the information about the light or sound stimulus. These spikes are sent to the brain, where they are further processed by other neurons. Thus, we may think of spike trains as being the language of neurons. The nervous system contains a gigantic number of neurons, which are highly interconnected via small junctions called synapses. For example, the human brain houses about 100 billion neurons, each of which receives spikes from thousands of other neurons and responds with an incessant sequence of spikes. Our brain is never quiet but sustains an inconceivably complex spiking activity – even if sensory stimuli are absent. It is a fundamental paradigm in neuroscience that our mental functions such as perceptions, thoughts, feelings, the control of what we say and how we move are ultimately encoded in the complex patterns of spikes in the brain [Kandel et al., 2000] (although the neural code is not yet known).

To understand how the brain computes with spikes, neurons are often regarded as the basic computational units of a large network. Therefore, it is crucial to first understand the properties of single neurons. It turns out, however, that these units are themselves highly complex systems. In fact, nerve cells are extended, macroscopic structures that typically consist of three main parts, dendrites, soma and axon (a schematic sketch is shown in Fig. 1.1). A neuron is confined by a cell membrane with intricate electrical properties: small proteins called ion pumps maintain concentration gradients of different ions between inside and outside the cell and establish an electrical potential difference across the membrane. This causes a permanent flow of ions through thousands of *ion channels* – tiny pores embedded in the cell membrane. Each channel is a macromolecule that is subject to collisions by molecules of the surrounding fluid. These permanent kicks make a channel open and close in an irregular and unpredictable fashion, which leads to fluctuations of the total membrane current. Moreover, the current through the membrane is not simply proportional to the membrane potential but it can change in a disproportionately large ("non-linear") manner: in particular, if the membrane potential is excited above a certain threshold, a strong positive feedback mechanism is initiated that generates the famous action potential [Hodgkin and Huxley, 1952]. From the spike initiation zone called axon-hillock, the electrical impulse travels along the axon, a long nerve fiber that projects

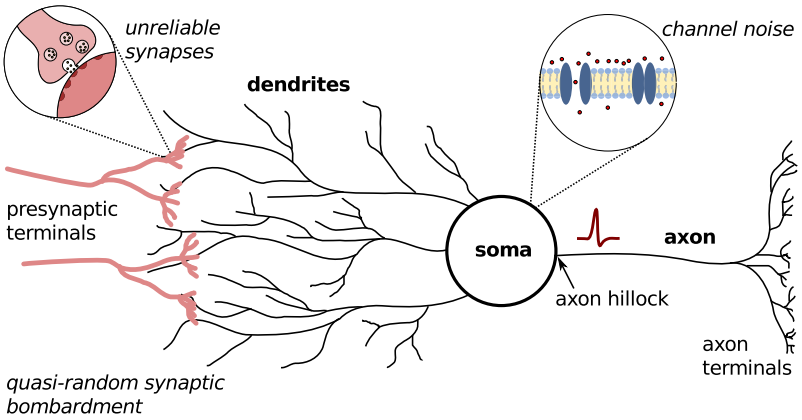

Figure 1.1.: Schematic sketch of a neuron and major sources of noise. The dendrites collect synaptic input currents from presynaptic neurons or, in the case of a sensory neuron, transduction currents from mechano-sensory receptors. These currents are processed by the non-linear kinetics of voltage-gated ion channels in the cell membrane of the soma (cell body) and the axon hillock (spike initiation zone) leading to a sequence of stereotypical action potentials. These "spikes" propagate along the axon and are delivered to postsynaptic neurons via synapses in the axonal terminals. The spike generation is influence by various sources of noise. The primary noise sources are *channel noise* and synaptic noise. The latter can be subdivided into the *quasi-random background activity* of a large number of weakly-correlated presynaptic neurons and the amplitude fluctuations of single synaptic events due to an *unreliable synaptic transmission process*.

to target neurons (Fig. 1.1). Other feedback processes which occur on longer time scales allow the neuron to adapt to a wide range of stimulus intensities. Non-linear processes with fluctuations and feedback on multiple time scales as described above are known to produce highly complex behavior. Note that the picture becomes even more involved if the spatial dependence of the membrane potential is taken into account. For certain neurons, this might even require to consider subcellular structures like parts of the dendritic tree as separate computational units [Häusser and Mel, 2003, Herz et al., 2006, Larkum et al., 2009].

What can theoretical physics contribute to the understanding of single neurons? First of all, physics is the mathematical description of nature and is thus also concerned with complex systems like the neuron. In the last decades, a great multitude of complex systems – as diverse as lasers, chemical reactions, biological systems, ecological systems or the weather – have been explored using mathematical methods. Especially concepts from nonlinear dynamics and statistical physics have proven useful to describe various complex phenomena. In many cases, the idea is to reduce a high-dimensional system to the dynamics of only a few (stochastic) variables that describe qualitative aspects of the full system. Often, the dynamics is formulated in terms of non-linear, stochastic processes, where the stochasticity ("noise") subsumes the fast degrees of freedom that are not explicitly accounted for. A central tenet is to find the simplest description of the system that still retains a given set of features (as e.g. certain experimental facts). Such *minimal models* are attractive for several reasons. Firstly, a minimal model points out the most relevant parameters of a complex system and hence leads to an appreciable understanding. Secondly, due to their simplicity, these models are generic in the sense that the qualitative behavior is robust with respect to details of the full system. Thirdly, minimal

models may permit a mathematical analysis, especially the derivation of *analytical formulas* for quantities that can be measured in experiments or simulations. An analytical formula is a (simple) functional relationship between such a quantity and the parameters of the model, i.e. it summarizes the dependencies on all external and internal parameters in a single mathematical expression. This substantially facilitates the discovery and formulation of interesting and experimentally testable hypotheses. Moreover, analytical calculations often involve approximations (often inspired by methods from theoretical physics) that require a good intuition and thus understanding of the system.

Minimal models of neurons have a long tradition in theoretical neuroscience [Lapicque, 1907, FitzHugh, 1961, Gerstein and Mandelbrot, 1964, Stein, 1965, Holden, 1976, Izhikevich, 2005]. Most models are formulated by dynamical systems that realize generic behavior like excitability or oscillations. Setting up a minimal model can be considerably facilitated by the fact that the computationally relevant information of a neuron is only carried by the spike times. The reason for this is that spikes have a stereotypical shape that does not convey any information. As a consequence, it is not necessary to model the complicated feedback process of an action potential explicitly. As shown in Sec. 1.1.2, this allows to build a minimal spiking neuron model with only a single variable, the membrane potential, and a so-called fire-and-reset rule. This simplified description belongs to the famous class of *integrate-and-fire models*. It has been shown that these simple models are able to predict the spike times of real neurons remarkably well [Badel et al., 2008, Gerstner and Naud, 2009, Mensi et al., 2011].

As mentioned above, the reduction of the complex neural dynamics might demand a stochastic description. Modeling the membrane potential as a stochastic process entails that the firing of action potentials is also stochastic. Indeed, experimental recordings, especially *in vivo*, have shown that spike patterns are often highly irregular and irreproducable, which is consistent with a stochastic description (see Sec. 1.1). Consequently, spike patterns must be quantified by statistical measures. Of particular interest is the statistics of the intervals between subsequent spikes, the so-called *interspike intervals*. Can we understand the interspike interval statistics of a real neuron? And what does the statistics tell us about the underlying stochastic dynamics of the neuron or its input? It has been one of the great successes of theoretical neuroscience to explain the variability and typical distributions of interspike intervals by simple, stochastic integrate-and-fire models [Gerstein and Mandelbrot, 1964, Stein, 1965, Ricciardi and Sacerdote, 1979, Tuckwell, 1989, Burkitt, 2006a]. In these models, the membrane potential is driven by so-called white noise, either in the form of Poissonian shot noise or Gaussian white noise. Here, the qualifier "white" means that the noise has equal power at all frequencies. It can be concluded that, in many cases, noise is an essential ingredient of a minimal neuron model. The most important sources of neural noise are discussed in Sec. 1.1 and are summarized in Fig. 1.1.

Most of the standard neuron models, including the classical Hodgkin-Huxley model, do not retain a noticeable memory of their dynamics that extends over two or more interspike intervals (ISIs). As a consequence, most neuron models generate spike trains with (approximately) independent interspike intervals. A spike generating model with such a property is called a *renewal model*. The term "renewal" means that the state of the spike generator is "renewed" after each spike which leaves no memory of previous ISIs. This class of spike trains is widely employed to model neural spiking. Renewal models are

theoretically well understood and convenient for the mathematical analysis [Cox, 1962, Gerstner and Kistler, 2002]. The reason for this is that the statistics of a renewal model is completely determined by the distribution of interspike intervals. In integrate-and-fire neuron models with white noise, the ISI density amounts to the famous first-passage-time problem, which has a long history in the theory of stochastic processes [Schrödinger, 1915, Pontryagin et al., 1933]. Once an analytical formula for the ISI density has been obtained for a given renewal model, further important characteristics of the spike train such as the power spectrum, the auto-correlation function, and the spike-count distribution can be computed analytically [Cox and Lewis, 1966, van Vreeswijk, 2010].

Although mathematically convenient, renewal models cannot describe correlations between ISIs. Such correlations have been, however, frequently observed in real spike trains both in peripheral and central neurons as well as across many species [for a review see Farkhooi et al., 2009, Avila-Akerberg and Chacron, 2011]. It has been demonstrated for certain sensory neurons that the sequential arrangement of ISIs matters: Compared to corresponding renewal ISI sequences, in which all correlations have been eliminated by a shuffling of ISIs, the original ISI sequences proved to be more capable of detecting weak signals [Ratnam and Nelson, 2000, Chacron et al., 2001, Engel et al., 2009] and were more suitable for information processing due to a reduced noise power at low frequencies [Chacron et al., 2004a, 2005a]. Information carried by the sequential order of ISIs is completely ignored by a renewal model.

In order to account for correlations in the sequence of ISIs, *non-renewal models* have been proposed that keep a memory of previous ISIs. Moreover, simple extensions of the standard renewal models such as the inclusion of synaptic dynamics, adaptation mechanisms or the presence of temporally-structured input currents introduces correlations between ISIs and thus renders the model non-renewal. In contrast to renewal models, however, the theory of non-renewal neuron models is still poorly developed. In particular, a theory for ISI correlation has been put forward only for a few special cases [Middleton et al., 2003, Lindner, 2004a, Lindner et al., 2005a]. The most likely reason is that these models are difficult to analyze because of their inherently non-Markovian character [Verechtchaguina et al., 2006]. Over the last decade, researchers have started to explore the correlation structure of non-renewal models using numerical simulations [Wang, 1998, Chacron et al., 2000, Liu and Wang, 2001, Chacron et al., 2003, Muller et al., 2007, Benda et al., 2010]. These studies have linked short-range negative correlations, which are characteristic for adapting neurons, to self-inhibitory feedback mechanisms such as adaptation currents or dynamic thresholds. However, the emergence of negative correlations in adapting neuron models has resisted a theoretical analysis. It is one of the main goals of the present thesis to derive analytical formulas for the ISI correlations. Such formulas may help to understand under which conditions negative correlations can be expected and how they depend on the system's parameters.

Non-renewal behavior is also expected when a neuron receives an external signal with a temporal structure. In the simplest case, the signal can be modeled by a Gaussian random process with an exponentially decaying correlation function. Often a random input signal with temporal correlations is referred to as colored "noise", a term that I will also frequently employ regardless of whether the input is meaningless noise or a meaningful signal (or a mixture of both). The case of an exponential correlation function has been theoretically studied by Middleton et al. [2003], Lindner [2004a]. The authors found that the

ISI correlations were positive and decayed exponentially at a rate that corresponds to the decay rate of the input correlations. Thus, the ISI correlation structure of the neural output strongly resembled the input correlation structure. This suggests, that non-renewal statistics such as the ISI correlation coefficient might be the most significant statistics to infer the (possibly unknown) correlation structure of the input. To investigate this hypothesis, it is important to know how a general input stimulus with a non-exponential correlation function translates into ISI correlations.

Organization of the thesis

In the remainder of this chapter I will review important concepts that are needed for the present study. This includes the introduction of stochastic integrate-and-fire models (Sec. 1.1), the theory of stationary point processes (Sec. 1.2) as well as models with colored noise and spike-frequency adaptation (Sec. 1.3). In **Chap. 2**, I generalize the theory of Lindner [2004a] to arbitrary Gaussian stimuli, in order to study the effect of colored noise with a general correlation structure. Specifically, I derive the ISI statistics for a perfect integrate-and-fire (PIF) model (the canonical model for a tonically firing neuron) that is driven by a weak Gaussian stimulus with an arbitrary correlation function. The general relations between input and output statistics show that both ISI density and serial correlations are affected by colored noise. In particular, it will be shown theoretically that exponentially-correlated colored noise shapes the ISI density towards a more skewed and peaked distribution. As another application, the ISI statistics of a model for electrosensory afferents of paddlefish [Engel et al., 2009] is calculated, which exhibits complex spike pattern [Neiman and Russell, 2004, 2005].

In **Chap. 3**, I consider a white-noise driven PIF model with an adaptation current that is triggered by its own spikes. This model is similar in spirit to previous integrate-and-fire-type models with a spike-triggered adaptation mechanism [Liu and Wang, 2001, Chacron et al., 2003, Benda et al., 2010]. In particular, it shows spike-frequency adaptation to step stimuli and exhibits negative ISI correlations. Despite the apparent simplicity of previous models it turned out to be rather difficult to obtain explicit expressions for the ISI correlation coefficient. In contrast, the *adapting PIF model* can be treated analytically because the steady-state of the noiseless dynamics, which constitutes a limit cycle, can be calculated explicitly. Using linearization techniques I will derive the weak-noise limit of the ISI correlation coefficient. Furthermore, based on weak noise approximations, the stationary Fokker-Planck equation can be solved resulting in explicit expressions for the distribution of the adaptation current upon firing and the membrane potential distribution. The presented approach does neither rely on a weak feedback assumption [Urdapilleta, 2011] nor does it assume a slow adaptation dynamics that averages the feedback [Wang, 1998, La Camera et al., 2004]. It only assumes that the noise is weak. This allows us to explore the whole dynamical range including fast and strong adaptation. The chapter is concluded by an analysis of the effect of a slow adaptation current on the dynamical response function and the power spectrum. In summary, Chap. 3 provides an extensive theoretical analysis of an adapting neuron model in the presence of white noise.

The analysis of Chap. 2 and 3 provides theoretical insights into how colored noise and adaptation affect the ISI statistics. An intriguing idea is whether these insights can be used to address the inverse problem: given experimentally measured ISI density and

ISI correlations, what does it tell us about the underlying stochastic spike generator? I will show in **Chap. 4**, how the theory together with experimental and simulation studies can be used to make strong hypotheses about the primary sources of noise that cause ISI variability in auditory receptor neurons of locust. For these cells, the spiking response to pure tone stimuli have been recorded *in vivo* at different sound intensities by K. Fisch [Fisch, 2011]. These cells exhibit pronounced spike-frequency adaptation and ISI variability. We hypothesize that the variability is caused by channel noise from different ion channel populations including not only channel populations with fast channel kinetics, but also a population that mediates a slow adaptation current. I will show by mathematical analysis that slow adaptation channel noise acts as a source of colored noise and that an adapting PIF model with adaptation channel noise can be approximately mapped to a non-adapting PIF model driven by colored noise. To this approximation, the theoretical results of Chap. 2 can be applied. As a result, ISI variability caused by fast channel noise is characterized by an inverse Gaussian ISI density and negative ISI correlations (as shown in Chap. 3), whereas slow adaptation channel noise leads to more skewed and peaked ISI densities and positive ISI correlations. On the basis of this theoretical finding, the experimental ISI statistics and a simulation study of channel noise suggest that both fast channel noise and slow adaptation channel noise contribute to the ISI variability in locust auditory receptor cells [Fisch, 2011].

The analysis of Chap. 2–4 applies quite generally to neurons that operate in the so-called supra-threshold regime, in which the mean currents are sufficient to drive the membrane potential periodically above the firing threshold ("mean-driven regime"). For weak noise and constant input, these neurons fire almost periodically (also called repetitive or tonic spiking), which can be described by the dynamics along a limit cycle. For such a limit-cycle dynamics the canonical model is indeed the perfect integrate-and-fire model, which was the basis of Chap. 2–4. However, many neurons, e.g. in the cortex, fire in a different, so-called sub-threshold regime, in which the mean currents alone are not sufficient to reach the threshold, but current fluctuations are necessary to raise the membrane potential above the threshold. **Chap. 5** is concerned with non-renewal spiking models that operate in this sub-threshold regime (also called excitable or fluctuation-driven regime). Unfortunately, the weak-noise approximation techniques used to calculate the ISI statistics in the supra-threshold cannot be carried over to the sub-threshold regime. In fact, even for the weakest noise the spiking dynamics is not a small perturbation of the deterministic limit, in which by definition of the sub-threshold regime no spikes occur at all. Instead, the noise-induced spiking is modeled by "escape" rates that depend on a hidden variable such as an adaptation current or a temporally correlated signal. As a further simplification, it is assumed that the hidden variable is defined on a discrete state space. In this framework, I derive the ISI correlation coefficient for a general Markovian dynamics of the hidden variable. The theory is then applied to the two standard situations: firstly, a neuron that is driven by colored noise (in the form of a dichotomous Markov process), and secondly, a neuron with self-inhibitory feedback.

The more involved calculations are presented in the appendix separately for each chapter. I hope that in this way the main ideas are laid out in a more accessible way.

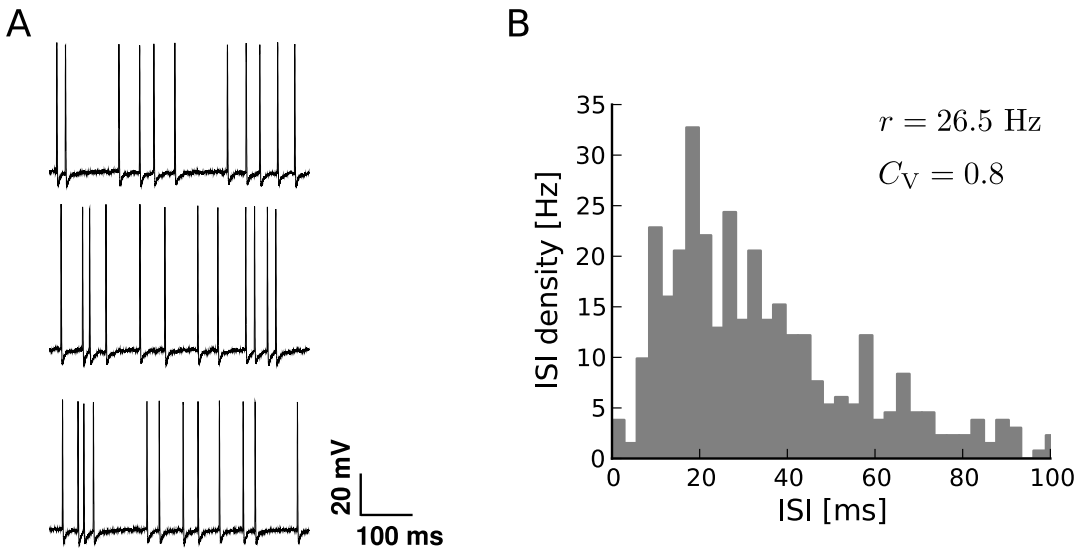

Figure 1.2.: Neural response variability. **A** Three responses of an auditory receptor cell to the same pure tone stimulus of 6 kHz frequency and 38 dB sound pressure level recorded intracellularly from the axon. The variability is evident in the spike timings and the interspike intervals. Figure adopted from Fisch [2011]. **B** The corresponding histogram of interspike intervals over 100 trials shows a broad distribution. Values for the firing rate r and the coefficient of variation C_V, a measure of variability (see Sec. 1.2.1), are given in the panel. The value $C_V = 0.8$ indicates a rather large variability, which is almost as large as for a Poisson process ($C_{V,Poisson} = 1$). The fluctuations of the histogram are due to the limited statistics of ISIs ($N_{ISI} = 464$). ISI data have been provided by K. Fisch.

1.1. Neural noise and simple stochastic models

Neurons exhibit a high response variability to repeated presentations of one and the same stimulus [van Steveninck et al., 1997, Shadlen and Newsome, 1998, Kreiman et al., 2000, Ronacher et al., 2004], in particular if stimuli do not vary in time [Mainen and Sejnowski, 1995, Schaette et al., 2005]. Figure 1.2A shows an example of such response variability in an auditory receptor cell of a grasshopper Fisch [2011]: applying the same pure tone acoustic stimulus, the receptor cell responds with a variable number of spikes as well as variable spike timings across different trials. In each single trial the occurrence of spikes is highly irregular, which becomes particularly apparent in the broad distribution of interspike intervals (Fig. 1.2B). In addition to the neural response variability, many neurons fire spontaneously even in the absence of a sensory stimulus [Gerstein and Mandelbrot, 1964, Brenner et al., 2002]. These two examples are clear manifestations of the fact that the firing of action potentials *in vivo* is a genuine stochastic process.

The stochasticity of neural spiking is due to several sources of noise at different levels of the neural pathway [Faisal et al., 2008]. Figure 1.1 illustrates the most important sources of neural noise. At the microscopic level, thermal noise caused by molecular agitation gives rise to fluctuations in the potential difference across the resistive membrane. This inevitable source of noise, also called Johnson-Nyquist noise, is small compared to other sources of noise. However, thermal noise has important consequences for the functioning of ion channels: the spontaneous changes of the conformational states (e.g. open or closed states) of these macromolecules are essentially driven by thermal noise due to permanent collisions with molecules in the surrounding medium. This random opening

and closing of ion channels in turn causes fluctuations of ionic currents that result from a finite population of channels. These fluctuations are termed *channel noise* and are probably the major source of noise that is intrinsic to the cell [Lecar and Nossal, 1971, White et al., 2000, Jacobson et al., 2005]. Ion channel noise will be discussed in more detail below (Sec. 1.1.1) and is the dominant source of noise in certain primary sensory neurons. A simple model of a primary receptor cell in the auditory system of locust in the presence of different types of channel noise will be analyzed in Chap. 4. In contrast, in central neurons of the cerebral cortex the by far largest amount of noise is synaptic noise [Destexhe and Paré, 1999]. This noise originates from the *synaptic bombardment* of the neuron by a myriad of other neurons that make synaptic contact onto it. Presynaptic spikes, which arrive at synapses in an irregular succession, cause small postsynaptic currents that add to a synaptic current that drives the membrane potential. Due to the enormous number of weakly correlated inputs, the synaptic current appears to be quasi-random, irrespective of whether the input is random background activity or a highly complex deterministic process that could constitute the signal. In either case, synaptic noise also includes truly stochastic elements that arise from molecular events at the synapses (e.g. probabilistic transmitter release). This results in *amplitude fluctuations of post-synaptic currents* [Bekkers et al., 1990, Zucker and Regehr, 2002, Rosenbaum et al., 2012], hence synapses must be regarded as unreliable devices.

The spontaneous neural activity as well as the response of neurons to stimuli cannot be understood without taking into account these fluctuations [Knight, 1972b]. Moreover, noise can have a positive influence on neural function, e.g. by stochastic resonance [Wiesenfeld et al., 1994, Gammaitoni et al., 1998, Anishchenko et al., 1999], gain modulation [Chance et al., 2002], decorrelation of spiking activity [Knight, 1972a], enhancement of signal detection [Engel et al., 2009], or fast transmission of noise coded signals [Lindner and Schimansky-Geier, 2001, Silberberg et al., 2004].

1.1.1. The Langevin equation: application to channel noise

The most important concept for analyzing the effect of noise on the ISI statistics are stochastic differential equations. In physicists' parlance these equations are often called Langevin equations named after Paul Langevin, who used a stochastic differential equation to describe the motion of Brownian particles. Similar equations can also be derived for neural noise. The main assumption behind these derivations is the existence of a small time scale Δt which is small enough to allow a time discretization of the neural dynamics of size Δt (i.e. on the time scale Δt the dynamics evolves approximately linear in time) and large enough to accommodate a large number of stochastic events. According to the central limit theorem, the summed effect of a large number of independent stochastic events can be described by a *single* Gaussian random variable, which dictates the change of the dynamics on the time interval Δt. Taking Δt as macroscopically infinitesimal the discrete time description attains the form of a differential equation that contains a stochastic term. This so-called "Langevin equation" is an approximate description with two important advantages: it allows very efficient simulations of the dynamics and it is mathematically much more tractable than a detailed Markov model of the neural dynamics. In a different context, this approach has been applied to a population of chemically reacting particles by Gillespie [2000]. A practically analogous situation arises for a

population of ion channels in the membrane of a neuron, and it is rather straightforward to derive a "chemical Langevin equation" for ion channels. Below I will briefly outline such a derivation using the example of channel noise in order to illustrate the emergence of a Langevin equation and to provide the tools that are needed in Chap. 4. Because the Langevin equation describes diffusion processes, this approach is also called *diffusion approximation*. This approximation has been applied by many authors to study the effect of channels on the neural dynamics [see e.g. Lecar and Nossal, 1971, Fox and Lu, 1994, Chow and White, 1996, Fox, 1997, Ochab-Marcinek et al., 2009]. A general review of channel noise in neurons is given in [White et al., 2000].

Channel noise

Let us consider a population of N independent ion channels. The simplest model of an ion channel is a Markovian two-state model that can reside in an open (conducting) or in a closed (non-conducting) state. Let $\alpha(V)$ be the transition rate from the closed to the open state and let $\beta(V)$ be the transition rate from the open to the closed state. The transition rates may depend on the membrane potential V, which is an important feature of many ion channels. Hence, we have the reaction scheme

$$\text{closed} \underset{\beta(V)}{\overset{\alpha(V)}{\rightleftharpoons}} \text{open} \tag{1.1}$$

for each channel. Let furthermore n_{op} and n_{cl} denote the number of open and closed channels, respectively. It is sufficient to discuss the dynamics of n_{op} in the following because $n_{\text{cl}} = N - n_{\text{op}}$. The number of open channels n_{op} is a random variable due to the random activity of the single channels. What is the stochastic time evolution $n_{\text{op}}(t)$? To answer this question, we need to know how n_{op} changes from time t to time $t + \Delta t$, where Δt is a small time span. This change $\Delta n(t) = n_{\text{op}}(t + \Delta t) - n_{\text{op}}(t)$ is given by the difference of the number of opening transitions and the number of closing transitions during the time interval Δt. Because V can change over time, the time interval should be small enough to ensure that the rates $\alpha(V)$ and $\beta(V)$ do not vary strongly on this time scale. If we further choose Δt such that $\alpha(V)\Delta t \ll 1$, each of the closed channels has the small probability $\alpha(V)\Delta t$ to open during Δt and the probability of several openings of a single channel is negligibly small. For the population of the $N - n_{\text{op}}(t)$ closed channels, the number of opening transitions in the interval Δt follows a Poisson distribution with mean and variance equal to $(N - n_{\text{op}}(t))\alpha(V)\Delta t$. Similarly, if $\beta(V)\Delta t \ll 1$, the number of closing transitions has mean and variance $n_{\text{op}}(t)\beta(V)\Delta t$. In total, the expected change of the number of open channels is thus $\langle \Delta n(t) \rangle = (N - n_{\text{op}}(t))\alpha(V)\Delta t - n_{\text{op}}(t)\beta(V)\Delta t$ and the variance of this change is $\langle \Delta n(t)^2 \rangle = (N - n_{\text{op}}(t))\alpha(V)\Delta t + n_{\text{op}}(t)\beta(V)\Delta t$ because the number of opening and closing transitions is independent. The distribution of the number of transitions in Δt is approximately Gaussian if the mean number of transitions is sufficiently large. That means that the change of the number of open channels is determined by its mean and variance. Thus, we have the representation

$$\Delta n(t) = \langle \Delta n(t) \rangle + \sqrt{\langle \Delta n(t)^2 \rangle}\mathcal{N}_t, \tag{1.2}$$

where $\mathcal{N}_t$ is a sequence of Gaussian random numbers with $\langle \mathcal{N}_t \rangle = 0$ and $\langle \mathcal{N}_t \mathcal{N}_{t'} \rangle = \delta_{t,t'}$. In other words, at each time step $\mathcal{N}_t$ is independently drawn from a Gaussian distribution with zero mean and unit variance.

It is useful to consider the relative change of $n_{\mathrm{op}}(t)$ by introducing the fraction of open channels $W(t) = n_{\mathrm{op}}(t)/N$. Dividing Eq. (1.2) by $N\Delta t$ and using the expressions for $\langle \Delta n(t) \rangle$ and $\langle \Delta n(t)^2 \rangle$ yields

$$\frac{W(t+\Delta t) - W(t)}{\Delta t} = (1 - W(t))\alpha(V) - W(t)\beta(V) + \sqrt{\frac{(1 - W(t))\alpha(V) + W(t)\beta(V)}{N\Delta t}}\mathcal{N}_t. \tag{1.3}$$

On a time scale much larger than Δt this equation can be regarded as a differential equation; in this coarse-grained view Δt is often referred to as macroscopically infinitesimal. This means that Eq. (1.3) can be formally written as

$$\dot{W} = (1 - W)\alpha(V) - W\beta(V) + \sqrt{\frac{(1 - W)\alpha(V) + W\beta(V)}{N}}\xi(t), \tag{1.4}$$

where $\xi(t) = \mathcal{N}_t/\sqrt{\Delta t}$ is a so-called Gaussian white noise process with the properties

$$\langle \xi(t) \rangle = 0, \qquad \langle \xi(t)\xi(t') \rangle = \delta(t - t'). \tag{1.5}$$

Equation (1.4) is called a Langevin equation. In the limit $\Delta t \to 0$, $\xi(t)$ rapidly varies between plus infinity and minus infinity. For this reason, the Langevin equation (1.4) is somewhat formal and should be interpreted in the discretized form Eq. (1.3)[1]. Nevertheless, stochastic differential equations of the form Eq. (1.4) are extremely useful in applications and theory and will play a central role in this thesis. One reason is its intuitive representation as a continuous, deterministic dynamical system which is driven by a highly fluctuating noise "force". For instance, for infinitely many channels, $N \to \infty$, the noise term vanishes and the fraction of open channels $W(t)$ follows a smooth deterministic trajectory. For finite N, however, this smooth trajectory is perturbed by fluctuations arising from the non-vanishing noise term in Eq. (1.4) resulting in a ragged motion of $W(t)$. These fluctuations of the fraction of open channels, which are caused by a finite number of ion channels, are called *channel noise*. An illustration of channel noise for a model of an adaptation current, which will be used in Chap. 4, is shown in Fig. 1.3.

As can be seen from the noise term in Eq. (1.4), a smaller population of ion channels results in a larger channel noise (cf. also Fig. 1.3A and B). However, the amount of fluctuations also depends on the open probability itself. To estimate this dependence, it is convenient to rewrite Eq. (1.4) in a slightly different form:

$$\tau_w(V)\dot{W} = -W + w_\infty(V) + \sqrt{2\tau_w(V)\sigma_w^2(V, W)}\xi(t) \tag{1.6}$$

with the time constant and the steady-state open probability

$$\tau_w(V) = \frac{1}{\alpha(V) + \beta(V)}, \qquad w_\infty(V) = \frac{\alpha(V)}{\alpha(V) + \beta(V)} \tag{1.7}$$

[1] Eq. (1.3) corresponds to the Ito interpretation of the Langevin equation (1.4), in which the prefactor of $\xi(t)$ is evaluated at the beginning of the time interval.

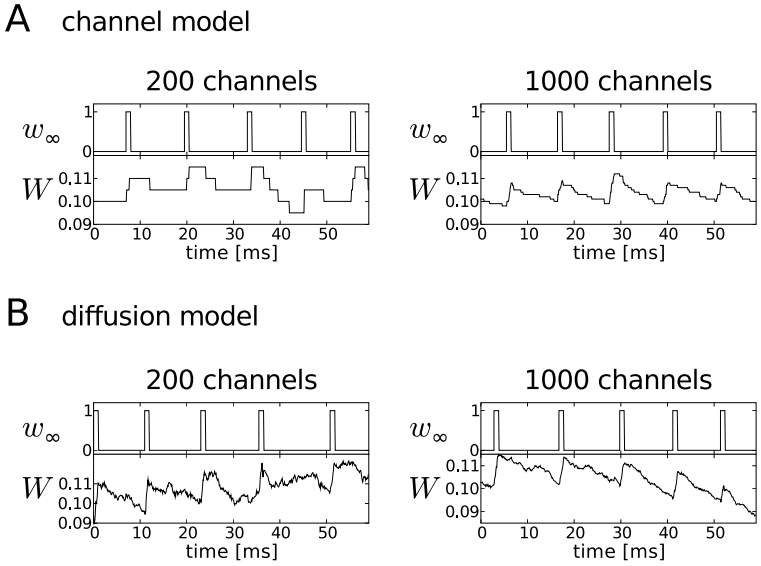

Figure 1.3.: Channel noise in the fraction of open ion channels W and diffusion approximation. Trajectories of W are depicted for populations of 200 (left) and 1000 (right) two-state channels that mediate an adaptation current (see Chap. 4). **A** Simulation of the full channel model with opening rates $\alpha = w_\infty/\tau_w$ and closing rates $\beta = (1 - w_\infty)/\tau_w$, where w_∞ is shown vs. time in the top panels. **B** Trajectories of the diffusion model, Eq. (1.6), for which the diffusion approximation of the corresponding channel model has been applied. For $N = 1000$ the fluctuations of W for both models are small and resemble each other. Note that $w_\infty(t)$ is different for the channel model and the diffusion model because w_∞ depends on W through a feedback mechanism (cf. Chap. 4). Parameter values: $\tau_w = 100$ ms.

and the strength of channel noise

$$\sigma_w^2(V, W) = \frac{1}{2N} \left[(1 - W) w_\infty(V) + W(1 - w_\infty(V)) \right]. \tag{1.8}$$

In the deterministic limit $N \to \infty$, the fraction of open channels obeys $\tau_w(V)\dot{W} = -W + w_\infty(V)$. Thus, if V changes only slowly, the fraction of open channels adiabatically adjusts to the steady-state open probability $w_\infty(V)$. In this case, the noise strength becomes roughly $\sigma_w^2(V, w_\infty(V)) = [1 - w_\infty(V)]w_\infty(V)/N$. This relation clearly illustrates the fact that the fluctuations vanish if the steady-state open probability is zero or one. In these cases, all channels are closed or open, respectively. In particular, there is no variability in the number of open channels. On the other hand, for an intermediate open probability there is variability, which becomes maximal when the open probability is $\frac{1}{2}$.

How does channel noise enter into the neural dynamics? For simplicity, let me assume that the neuron can be described by a single compartment with a single membrane potential V. The insulating membrane can be regarded as a capacitor that separates ionic charges located on the inside and outside of the membrane. Furthermore, the ion channels and ion pumps give rise to membrane conductances that are connected in parallel to the capacitor. In such an electrical circuit the change of voltage must be balanced by all currents that flow across the membrane. Accounting for membrane and synaptic currents as well as, in an experimental setup, an injected current the current balance equation

reads

$$C_\mathrm{m}\dot{V} = -\sum_k^{N_\mathrm{m}} I_k - I_\mathrm{syn} + I_\mathrm{ext}, \tag{1.9}$$

where C_m is the membrane capacitance, I_k are membrane currents corresponding to N_m different types of ion channels (outward currents are defined positive), I_syn is the total synaptic current and I_ext denotes an externally injected current. The capacitance C_m and the membrane currents I_k carried by the conductances are proportional to the area A of the membrane. To remove this dependence on A, the specific membrane capacitance $c_\mathrm{m} = C_\mathrm{m}/A$ and the currents per unit area $i_k = I_k/A$ are introduced. Furthermore, the currents i_k can be related to the membrane potential through $i_k = g_k(V - E_k)$ (Ohm's law). Here, E_k is the so-called reversal potential and g_k is the conductance per unit area that are associated with the current of type k. Using these definitions, Eq. (1.9) can be rewritten as

$$c_\mathrm{m}\dot{V} = -\sum_k^{N_\mathrm{m}} g_k(V - E_k) - \frac{I_\mathrm{syn} - I_\mathrm{ext}}{A}. \tag{1.10}$$

Channel noise associated with ion channels of type k enters this dynamics through the conductance g_k. In fact, g_k is proportional to the number of open channels $n_{\mathrm{op},k}$ and the conductance of a single channel $\hat{g}_k$ and is inversely proportional to the membrane area. Hence, it holds $g_k = \frac{\hat{g}_k n_{\mathrm{op},k}}{A} = \frac{\hat{g}_k N_k}{A} W_k$, where N_k and W_k are the total number of channels and the fraction of open channels of type k, respectively. If the ion channels of type k can be modeled by two-state processes with transition rates α_k and β_k and if the diffusion approximation is applicable, $W_k(t)$ obeys the Langevin equation (1.4). In such a model it is possible to vary the number of channels N_k and to study the effect of channel noise. To this end, it is desirable that the variation is performed in such a way that only the size of fluctuations is changed, but not the deterministic part of the current. This requires that the maximal conductance $\bar{g}_k = \hat{g}_k N_k/A$ remains constant. For instance, channel noise can be increased by decreasing the membrane area A while keeping a constant channel density N_k/A.

1.1.2. Stochastic integrate-and-fire neuron models

Equation (1.10) is capable of producing highly nonlinear dynamics that can generate action potentials, because the membrane conductances g_k are itself active dynamical variables that may depend on other quantities such as the membrane potential or the intracellular calcium concentration. Such neuron models are called *conductance-based*. For instance, the sodium conductance is activated when V is sufficiently depolarized causing sodium ions to rush into the cell, which in turn leads to a further depolarization and an even larger sodium conductance. This positive feedback process constitutes the rapid upstroke of an action potential. The neuron is repolarized by the delayed activation of potassium channels that allow potassium ions to flow out of the cell and by the additional inactivation of sodium channels. The potassium outflux even causes a hyperpolarization following the spike, where the membrane potential is below the resting potential. The whole trajectory of such an action potential has a stereotypical shape that is the same for all spikes (Fig. 1.4A). This suggests a simplification of a conductance-based model: instead of modeling the complicated, non-linear action potential, one may employ a model that generates only the spike times but not the action potentials them-

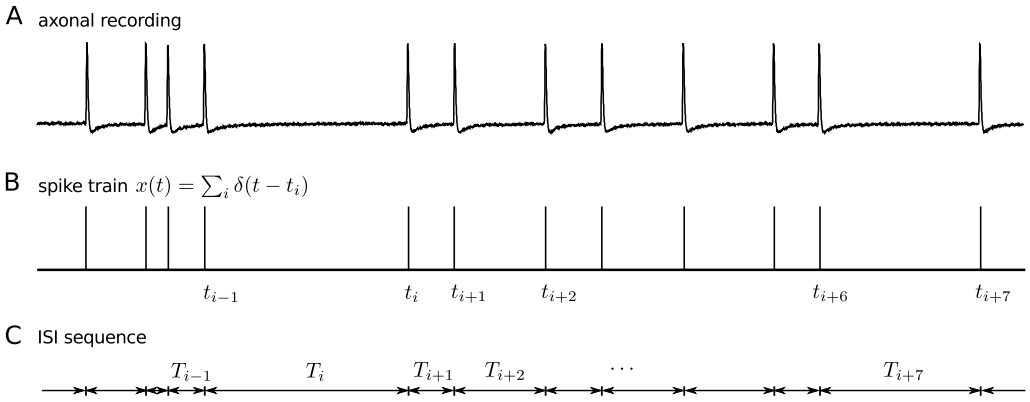

Figure 1.4.: Spike train and sequence of interspike intervals. A Intracellular recording from the axon of an auditory receptor cell of locust (adopted from [Fisch, 2011]). The recording shows action potentials with a stereotypical shape. **B** This spike train can be approximated by a sequence of delta-functions centered at the spike times. **C** The intervals between subsequent spikes form a sequence $\{\dots, T_i, T_{i+1}, T_{i+2}, \dots\}$, the interspike interval (ISI) sequence. The statistical properties of this sequence, especially correlations within the sequence, is the main topic of the present study.

selves. In *integrate-and-fire neuron models* the spike times are defined as the events where the membrane potential reaches a firing threshold V_{th}. In contrast to conductance-based models, the dynamics of the membrane potential is only modeled below the threshold (subthreshold dynamics). Thus, the suprathreshold part of the action potential is not described explicitly, whereas the hyperpolarization part is modeled by an explicit reset of V to some reset potential $V_{\text{r}} < V_{\text{th}}$.

The leaky integrate-and-fire model

A further simplification is achieved by assuming that below threshold the membrane conductances are "passive", i.e. that the channel kinetics (e.g. given by the rates α and β in the two-state model) is approximately independent of V or any other dynamical variable. Under this assumption, the membrane conductances can be split into a constant mean conductance $\langle g_k \rangle$ and channel noise δg_k: $g_k = \langle g_k \rangle + \delta g_k$. Similarly, the total synaptic current can be expressed in the form $I_{\text{syn}} = \sum_k^{N_{\text{s}}} g_{\text{s},k} A (V - E_{\text{s},k})$, where the N_{s} different synaptic conductances (per membrane area) can be represented as $g_{\text{s},k} = \langle g_{\text{s},k} \rangle + \delta g_{\text{s},k}$. Here, $\delta g_{s,k}$ are fluctuations due to presynaptic shot noise. For large channel populations and massive synaptic input, we can apply the diffusion approximation, according to which δg_k and $\delta g_{s,k}$ are Gaussian processes. For convenience, the membrane and synaptic currents can be combined into one sum comprising $N_{\text{m}} + N_{\text{s}}$ conductances g_k. Then, Eq. (1.10) yields the passive subthreshold dynamics,

$$c_{\text{m}} \dot{V} = -g_0 (V - E_0) - \sum_{k=1}^{N_{\text{m}}+N_{\text{s}}} \delta g_k (V - E_k) + \frac{I_{\text{ext}}}{A}, \tag{1.11}$$

where $g_0 = \sum_{k=1}^{N_{\text{m}}+N_{\text{s}}} \langle g_k \rangle$ is an effective conductance and $E_0 = \sum_{k=1}^{N_{\text{m}}+N_{\text{s}}} \langle g_k \rangle E_k / g_0$ is the resting potential.

Equation (1.11) contains nonlinear terms, because the noises δg_k are multiplied by the

voltage-dependent factor $(V - E_k)$ (multiplicative noise). In an approximation, known as the effective-time-constant approximation [Burkitt, 2001, Steinmetz et al., 2000, Richardson and Gerstner, 2005], this nonlinearity is removed by setting $\delta g_k V \approx \delta g_k E_0$, which is valid if $|V - E_0| \ll |E_0 - E_k|$. Dividing Eq. (1.11) by g_0, we obtain

$$\tau_\mathrm{m} \dot{V} = -V + \mu + \eta(t), \tag{1.12}$$

where $\tau_\mathrm{m} = c_\mathrm{m}/g_0$ is the *membrane time constant*, $\mu = E_0 + I_\mathrm{ext}/(g_0 A)$ is the *base "current"* (in units of voltage) and $\eta(t)$ is a Gaussian noise process with zero mean and correlation function

$$\langle \eta(t)\eta(t') \rangle = \sum_{k=1}^{N_\mathrm{m}+N_\mathrm{s}} \left(\frac{E_0 - E_k}{g_0} \right)^2 \langle \delta g_k(t) \delta g_k(t') \rangle. \tag{1.13}$$

The neuron model is completed by a fire-and-reset rule that states that if the membrane potential reaches the threshold V_th at time t, a spike is registered at that time and the membrane potential is reset to $V_\mathrm{r} < V_\mathrm{th}$. In formulae,

$$\text{if } V(t-) = V_\mathrm{th} \text{: } V(t+) \to V_\mathrm{r}, \qquad \{t_i\}_{i \in \mathbb{N}} = \{ t \in \mathbb{R} | V(t-) = V_\mathrm{th} \}, \tag{1.14}$$

where $\{t_i\}_{i\in\mathbb{N}}$ denotes the set of spike times. The subthreshold dynamics, Eq. (1.12), together with the fire-and-reset rule, Eq. (1.14), defines the famous *leaky integrate-and-fire model* driven by Gaussian noise.

The ordered sequence of spike times $\{t_i\}$ with $t_i < t_j$ for $i < j$ is the actual output of the model. Mathematically, such a sequence is a realization of a so-called point process because the spike times can be thought of as random points on the time axis. An equivalent description of the output is given by the stochastic process $x(t) = \sum_i \delta(t - t_i)$. This process will be referred to as the spike train associated with the set $\{t_i\}$ because it exhibits sharp δ-pulses centered at the spike times and is zero otherwise. Figure 1.4B shows an example of a delta-spike train associated with the spike times that have been extracted from an experimental spike train recording.

Ornstein-Uhlenbeck process and white-noise limit. Often the Gaussian noise $\eta(t)$ is not derived from an underlying biophysical model as it was done in Eq. (1.13), but is rather postulated on a phenomenological basis or in a feasible form that allows a mathematical analysis. One popular noise model is the Ornstein-Uhlenbeck process defined by the Langevin equation

$$\tau \dot{\eta} = -\eta + \sqrt{2D}\xi(t), \tag{1.15}$$

where $\xi(t)$ is Gaussian white noise as defined in Sec. 1.1.1 and D is the noise intensity of $\eta(t)$. The stationary process exhibits an exponential correlation function

$$C_\eta(t) = \langle \eta(t')\eta(t'+t) \rangle = \frac{D}{\tau} \exp\left(-\frac{|t|}{\tau} \right). \tag{1.16}$$

Thus, the time constant τ is the correlation time of the noise and $\sigma_\eta^2 = D/\tau$ is its variance. An equivalent description of the statistical properties of the Gaussian process $\eta(t)$ can be formulated in terms of the power spectral density, or simply called power spectrum,

which is defined as the Fourier transform of the correlation function,

$$S_\eta(\omega) = \int_{-\infty}^{\infty} \mathrm{d}t\, C_\eta(t) e^{i\omega t}. \tag{1.17}$$

For the Ornstein-Uhlenbeck process, the exponential correlation function gives rise to the Lorentzian spectrum $S_\eta(\omega) = 2D/(1+\tau^2\omega^2)$. In the limit $\tau \to 0$, the power spectrum is equal to $2D$ at all frequencies. A noise process with such a flat power spectrum is called white noise. The correlation function, being the inverse Fourier transform of the power spectrum, becomes delta-correlated in this limit, which is consistent with our previous definition Eq. (1.5).

Gaussian white noise is one of the simplest models to study the effect of fluctuations on the firing statistics. In particular, using the notation $\xi(t)$ for a Gaussian process with correlation function $\langle \xi(t)\xi(t')\rangle = \delta(t-t')$, and setting $\eta(t) = \sqrt{2D}\xi(t)$, the leaky integrate-and-fire (LIF) model driven by white Gaussian noise reads

$$\tau_\mathrm{m}\dot{V} = -V + \mu + \sqrt{2D}\xi(t), \qquad \text{if } V = V_\mathrm{th}\text{: } V \to V_\mathrm{r}. \tag{1.18}$$

This model has a long history in theoretical neuroscience [Capocelli and Ricciardi, 1971, Ricciardi, 1977, Tuckwell, 1989]. It allows to study basic statistical properties of stationary spike trains as well as signal transmission properties of neurons in a noisy environment [Brunel and Hakim, 1999, Lindner and Schimansky-Geier, 2001, Lindner et al., 2002, Burkitt, 2006a,b].

The mean-driven and fluctuation-driven firing regime

Depending on the parameter μ the LIF model can operate in a mean-driven firing regime or a fluctuation-driven firing regime (Fig. 1.5): For $\mu > V_\mathrm{th}$, the mean driving current μ is strong enough to generate spikes already in the deterministic model, i.e. for $D = 0$. In this so-called *suprathreshold regime* (also called *mean-driven*, *oscillatory* or *tonically firing regime*) the deterministic dynamics generates a periodic spike pattern with interspike intervals (ISIs) equal to $T = \tau_\mathrm{m} \ln[\mu/(\mu - V_\mathrm{th})]$. In the presence of noise, the spike train is not strictly periodic anymore (Fig. 1.5A) because the ISIs become random variables. This is reflected in a finite distribution of ISIs (Fig. 1.5C). Nevertheless, if the noise is weak the spike train is still rather regular. The regularity of a stationary spike train can be quantified by the coefficient of variation (CV) defined as the ratio of standard deviation to mean of the ISIs. For a periodic spike train with unique ISI the CV is equal to zero, whereas for a completely random spike train (a so-called Poisson process) the CV is equal to unity. In the mean-driven regime with low noise, the CV is significantly smaller than one. This regime will be considered in Chap. 2 – 4.

In contrast, the LIF model with $\mu < V_\mathrm{th}$ is a prototypical model for the *fluctuation-driven regime* (Fig. 1.5B). In this case, the deterministic model remains below the threshold and hence does not generate spikes. However, in the presence of noise the firing threshold can be reached due to fluctuations of the membrane potential. This regime is also called *excitable* or *subthreshold regime* [Lindner et al., 2004]. Figure 1.5D shows that the ISIs in this regime are approximately exponentially distributed except for small ISIs that are improbable due to neural refractoriness. The CV of an exponential distribution is equal to one

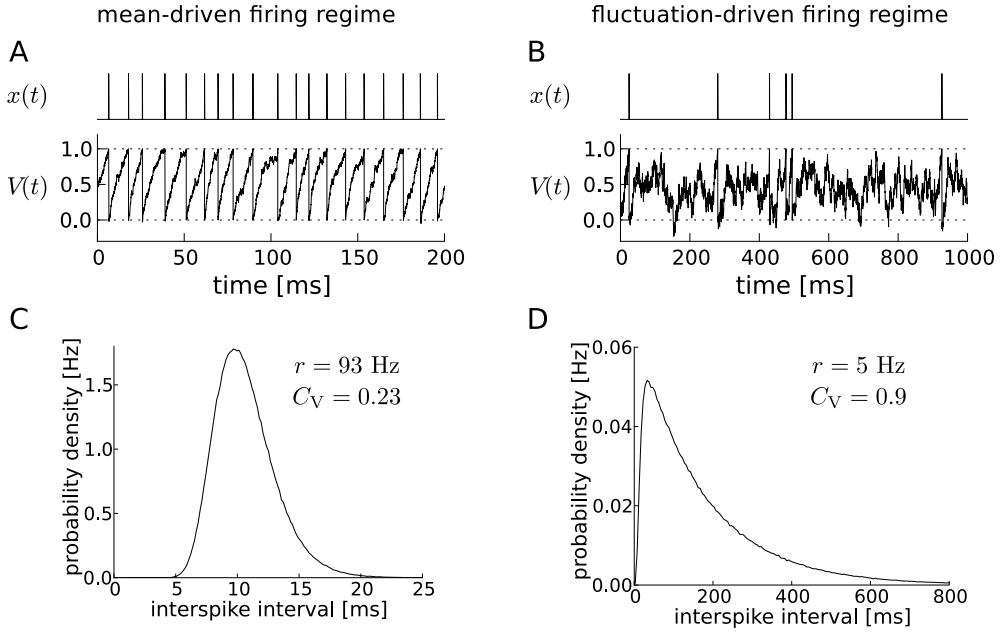

Figure 1.5.: The mean-driven and the fluctuation-driven regime of the LIF model. A Trajectory $V(t)$ and spike train $x(t)$ of the LIF model driven by white Gaussian noise, Eq. (1.18), for $\mu = 1.5\ V_{\mathrm{th}}$ (suprathreshold or mean-driven regime) and $D = 0.02\ V_{\mathrm{th}}^2$ms. The corresponding ISI density (**C**) possesses a coefficient of variation (CV) much smaller than unity. **B** Trajectory $V(t)$ and spike train $x(t)$ for $\mu = 0.5\ V_{\mathrm{th}}$ (subthreshold or fluctuation-driven regime) and $D = 0.05\ V_{\mathrm{th}}^2$ms. The corresponding ISI density (**D**) is close to an exponential distribution with a CV close to unity. Parameter values in both cases: $\tau_{\mathrm{m}} = 10$ ms, $V_{\mathrm{th}} = 1$.

and corresponds to a Poisson process, for which all spikes are independent. Such highly irregular spiking with a nearly exponential ISI density and CVs close to one are typical for cortical neurons *in vivo* [Softky and Koch, 1993]. This suggests that these neurons operate in the fluctuation-driven regime, most probably caused by balanced excitatory and inhibitory synaptic input. The analysis of non-renewal models that exhibit fluctuation-driven spiking will be analyzed in Chap. 5.

It should be mentioned that the assumption of a passive membrane in the whole subthreshold region can be relaxed and a more realistic subthreshold voltage dynamics can be modeled by non-linear integrate-and-fire models of the form

$$\tau_{\mathrm{m}}\dot{V} = f(V) + \mu + \sqrt{2D}\xi(t), \qquad \text{if } V = V_{\mathrm{th}}\text{: } V \to 0. \tag{1.19}$$

This model exhibits the desirable property that it is still one-dimensional, but is capable to capture realistic spike-initiation dynamics by properly choosing the function $f(V)$. In particular, the exponential voltage-dependence $f(V) = -V + \Delta_T \exp\left(\frac{V-V_{\mathrm{th}}}{\Delta_T}\right)$ has proven to be an accurate description of the subthreshold dynamics of real neurons [Fourcaud-Trocmé et al., 2003, Badel et al., 2008]. This is due to the fact that close to the threshold the activation curve of the fast sodium conductance depends approximately exponentially on the voltage. This example shows beautifully that a simple extension of the LIF model can account for more realistic features like the non-linear, multidimensional dynamics of fast conductances and voltage. Yet, the nonlinear integrate-and-fire model

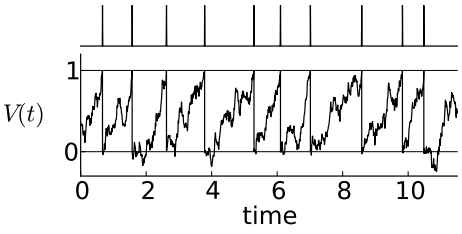

Figure 1.6.: The perfect integrate-and-fire model driven by white Gaussian noise. A typical realization $V(t)$ for $\mu = 1$, $D = 0.125$ and $V_{\rm th} = 1$ (time in units of the mean interspike interval). The generated spike train is indicated on the top.

also has important limitations, one of which is related to the fact that a one-dimensional neuron model driven by white noise cannot reproduce non-renewal spiking statistics. Because $V(t)$ is a Markov process, any memory is erased upon spiking by the fire-and-reset rule. Thus, all white-noise driven one-variable spiking models including the LIF model belong to the class of renewal models.

Slow conductances or other slow processes, as e.g. adaptation processes, can keep a memory beyond the last spike and hence induce ISI correlations. To model such non-renewal behavior at least a second variable must be coupled to the voltage dynamics. In the spirit of the above example, I will analyze in this thesis simple extensions of basic integrate-and-fire models that generate non-renewal spike trains. Investigations of such minimal models may lead to an understanding of basic principles underlying non-renewal spiking statistics. Certainly, the extension to multivariate models comes at a price: for the sake of analytical tractability, the subthreshold dynamics will be linear in its variables. Of particular importance will be various extensions of the perfect integrate-and-fire model, a model in which the driving currents do not depend on the membrane potential at all.

1.1.3. The workhorse – the perfect integrate-and-fire model

We saw that the noiseless LIF model makes a transition from a quiescent state without spikes (subthreshold regime, $\mu < V_{\rm th}$) to a state of periodic spiking (suprathreshold regime, $\mu > V_{\rm th}$). Hence, the noiseless LIF model exhibits a bifurcation at $\mu = V_{\rm th}$. In the presence of noise, this bifurcation corresponds to a transition from the fluctuation-driven to the mean-driven firing regime. If the mean current μ is increased even further, the neuron will be driven so strongly that it fires like a pacemaker. In this tonically firing regime, far beyond the bifurcation, the tonic part of the driving dominates any voltage-dependence of the driving current. In the LIF model, Eq. (1.12), this means that for $\mu \gg V_{\rm th}$ the leak term $-V$ can be neglected against the base current μ. Thus, the subthreshold dynamics becomes $\dot{V} = \mu/\tau_{\rm m} + \eta/\tau_{\rm m}$. Upon renormalization of the base current and the noise by the membrane time constant, we obtain

$$\dot{V} = \mu + \eta(t), \qquad \text{if } V = V_{\rm th}\colon V \to V_{\rm r}. \tag{1.20}$$

Here, $\eta(t)$ denotes again a zero-mean Gaussian noise. This model is called the perfect integrate-and-fire model, or in short PIF model because it perfectly integrates its inputs. A typical trajectory of the model and the associated spike train is shown in Fig. 1.6. Despite its simplicity, this model has been extremely successful in explaining the firing statistics of single neurons. In their milestone paper, Gerstein and Mandelbrot [1964] showed that the ISI distribution of certain neurons can be simply explained by a PIF

model that is driven by white noise, i.e.

$$\dot{V} = \mu + \sqrt{2D}\xi(t), \qquad \text{if } V = V_{\text{th}}\text{: } V \to V_{\text{r}}. \tag{1.21}$$

Specifically, let $P_{\text{WN}}(T)\Delta T$ be the probability that a given interspike interval T_i of the white-noise driven PIF model falls between T and $T + \Delta T$. The ISI density $P_{\text{WN}}(T)$ is equivalent to the first-passage-time density of a Brownian particle with drift towards an absorbing barrier. A classical result due to Schrödinger [1915] states that this density is given by

$$P_{\text{WN}}(T) = \frac{V_{\text{th}}}{\sqrt{4\pi DT^3}} \exp\left[-\frac{(\mu T - V_{\text{th}})^2}{4DT}\right], \tag{1.22}$$

This probability density is known as the inverse Gaussian probability density. A typical example of this distribution is shown in Fig. 1.7A(i).

The PIF model driven by white Gaussian noise is a renewal model and represents one of the rare cases, for which the ISI density can be calculated exactly. This exactly solvable case will serve as an important reference statistics, to which corresponding non-renewal models will be compared. There is a deeper reason to this: in the suprathreshold regime with constant input and sufficiently weak noise, any spiking neuron model behaves like a PIF model because this model is the most basic description for the dynamics on a limit cycle. In fact, the PIF model has the form of a phase oscillator for a phase $V(t)V_{\text{th}}$ with constant phase velocity μ/V_{th}. On the other hand, the phase dynamics of any limit cycle oscillator can be mapped to a phase oscillator with constant velocity by a proper variable transformation. In this sense, the PIF model can be regarded as the canonical model for supra-threshold periodic firing and an inverse Gaussian ISI density can be expected for sufficiently weak noise. A further reason, why the PIF model will serve as the workhorse in a major part of this thesis (Chap. 2– 4), is that it allows non-trivial extensions that are still analytically tractable (albeit only by means of approximations and under certain assumption).

1.2. Renewal vs. non-renewal spike trains

The spikes generated by a stochastic neuron model like the LIF or PIF model can be regarded as random points on the time axis (Fig. 1.4B). Therefore, the ordered sequence of spike times t_i with

$$-\infty < \cdots < t_0 < t_1 < t_2 < \cdots < \infty \tag{1.23}$$

is also called a point process. As already mentioned, this point process can be associated with a δ-spike train defined on the set of spike times,

$$x(t) = \sum_i \delta(t - t_i). \tag{1.24}$$

In what follows, we are particularly interested in the statistical description of stationary point processes. These are processes for which $x(t)$ is a stationary stochastic process, i.e. its statistics does not depend on absolute time. One can think of a stationary spike train as being generated by a spiking neuron model that has been initiated at time $t = -\infty$ and that is homogeneous in time (i.e. all model parameters are constant). Because

stationary point processes play a crucial role in the present thesis, I will briefly outline the most important concepts and useful relations of the statistics of point processes in the following.

What kind of statistics should we look at in order to characterize a spike train? In general, the statistics of a point process can be described in terms of distribution functions or generating functionals, much in the same way as for ordinary stochastic processes [Stratonovich, 1967, van Kampen, 1992]. However, there are certain kinds of statistics that are of particular significance for the analysis of single neuron spike data:

1. the statistics of the sequence of interspike intervals
2. the statistics of the nth-order intervals, i.e. statistics of the sum of n subsequent ISIs
3. the second order statistics of the spike train $x(t)$ (auto-correlation, power spectrum)
4. the statistics of the number of spikes in a time window $(0, t)$.

1.2.1. Interspike interval statistics

Because the main focus of this thesis is on the statistics of interspike intervals (ISIs), I will elaborate on this kind of statistics, which is concerned with the times between two subsequent spikes

$$T_i = t_i - t_{i-1} \tag{1.25}$$

(Fig. 1.4C). The ISIs T_i form a stochastic sequence $\{T_i\} : \ldots, T_0, T_1, T_2, \ldots$, which can be interpreted as a stochastic process with discrete time: the index i is simply regarded as a discrete time argument[2]. As for stochastic processes, it is often useful to consider an ensemble of sequences instead of a single sequence $\{T_i\}$. Then, the statistics of the ISI sequence is completely determined by the hierarchy of distribution functions defined by

$$p_i^{(1)}(T) = \langle \delta(T - T_i) \rangle, \tag{1.26}$$

$$p_{ij}^{(2)}(T^{(1)}, T^{(2)}) = \langle \delta(T^{(1)} - T_i)\delta(T^{(2)} - T_j) \rangle, \tag{1.27}$$

$$p_{ijk}^{(3)}(T^{(1)}, T^{(2)}, T^{(3)}) = \langle \delta(T^{(1)} - T_i)\delta(T^{(2)} - T_j)\delta(T^{(3)} - T_k) \rangle, \tag{1.28}$$

$$\ldots\ldots\ldots,$$

where $\langle \cdot \rangle$ denotes the ensemble average.

ISI density and joint density

For a stationary spike train, the ensemble of ISI sequences is also stationary. As a consequence, the first-order distribution function, Eq. (1.26), does not depend on the index i. In this case, $p_i^{(1)}(T)$ is equal to the ISI density

$$P(T) = \lim_{\Delta t \to 0} \frac{\text{Prob}\{T < T_i < T + \Delta t\}}{\Delta t}. \tag{1.29}$$

[2] A stochastic process $\{X_i\}$ with discrete time $i \in \mathbb{Z}$ will be referred to as a *stochastic sequence* to emphasize the difference to a stochastic process with continuous time. The bracket notation is used to distinguish the sequence $\{X_i\}$ from the particular random variable X_i at "time" i. A well-known example of a stochastic sequence would be a Markov chain.

A typical example of an ISI density is shown in Fig. 1.7A(i). It is an important characteristics of the spiking statistics and can be estimated from an experimental spike train recording by computing a normalized histogram of the ISIs (see Fig. 1.2B). A broad distribution of ISIs reflects a high irregularity of the spike train.

The second-order distribution function, Eq. (1.27), of a stationary ISI sequence only depends on the difference $|i - j|$ of the indices. Of particular interest is the joint density of adjacent ISIs, $p^{(2)}_{i,i+1}(T^{(1)}, T^{(2)})$, which is equal to

$$P(T^{(1)}, T^{(2)}) = \lim_{\Delta t \to 0} \frac{\text{Prob}\{T^{(1)} < T_i < T^{(1)} + \Delta t \wedge T^{(2)} < T_{i+1} < T^{(2)} + \Delta t\}}{\Delta t^2}. \qquad (1.30)$$

Examples of joint densities are shown in Fig. 1.7A,B(iii).

An important class of point processes are *renewal processes* [see e.g. Cox, 1962, Cox and Lewis, 1966, Cox and Isham, 1980]. These processes have the property that all T_i in the sequence $\{T_i\}$ are statistically independent. This means that the distribution functions factorize into the first-order distribution function:

$$p^{(n)}_{i_1 \cdots i_n}(T^{(1)}, \ldots, T^{(n)}) = p^{(1)}_{i_1}(T^{(1)}) \cdots p^{(1)}_{i_n}(T^{(n)}), \quad n \geq 2 \qquad \text{(renewal process)}. \quad (1.31)$$

In particular, the joint density of adjacent ISIs factorizes into the single ISI densities,

$$P(T^{(1)}, T^{(2)}) = P(T^{(1)})P(T^{(2)}), \qquad \text{(renewal process)}. \qquad (1.32)$$

Figure 1.7A(iv) illustrates this equality for a white-noise driven PIF model, which generates a renewal spike train.

For a general, non-renewal process, the distribution functions of the ISI sequence do not factorize. The statistical dependence of adjacent ISIs can be measured by the deviation of the joint density $P(T^{(1)}, T^{(2)})$ from the product of the single ISI densities $P(T^{(1)})P(T^{(2)})$ that would be expected for a renewal process with the same first-order statistics. Hence, we define the "correlation map"

$$\delta P(T^{(1)}, T^{(2)}) = P(T^{(1)}, T^{(2)}) - P(T^{(1)})P(T^{(2)}), \qquad (1.33)$$

that shows which combinations (T_i, T_{i+1}) are more or less likely than expected for a renewal process. Clearly, for a renewal process $\delta P(T^{(1)}, T^{(2)}) = 0$, which is illustrated for a PIF model driven by white noise in Fig. 1.7A(iv). In contrast, a non-vanishing correlation map is shown in Fig. 1.7B(iv) for a PIF model that is driven by colored noise. This reveals that colored noise induces correlations between ISIs and hence renders the model non-renewal.

Moments of the first-order ISI statistics

Having considered various distribution functions for the ISI sequence, we now turn to the moments and cumulants of the ISIs. For a stationary ISI sequence, the first-order ISI statistics of T_i, which is given by the ISI density $P(T)$, does not depend on the index i. Thus, the k-th moment will be simply denoted by $\langle T^k \rangle$ in what follows. It is useful to

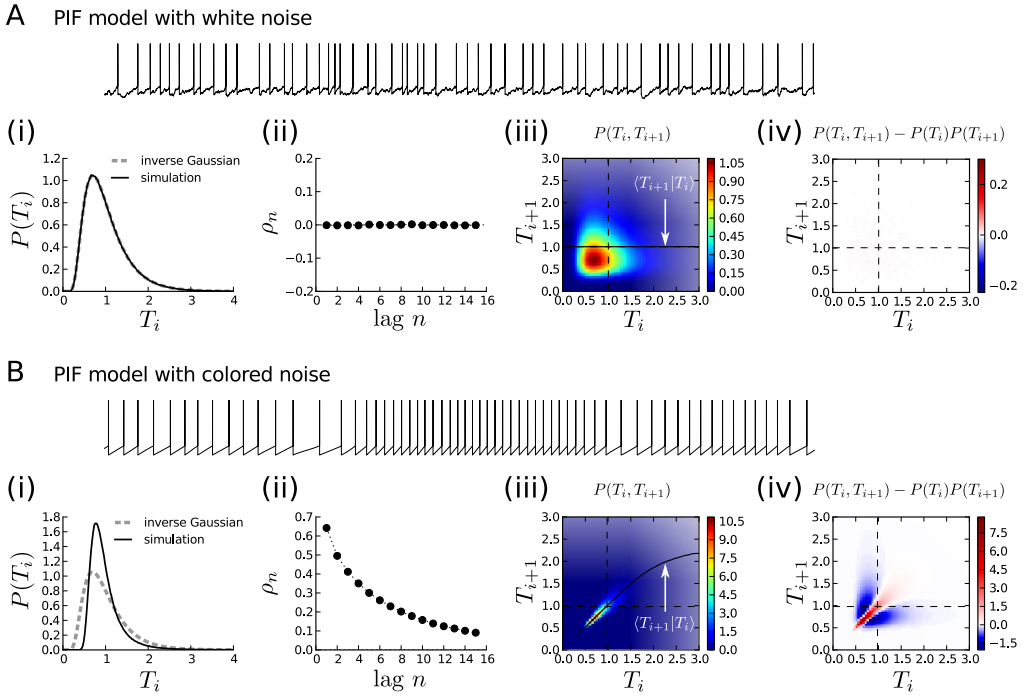

Figure 1.7.: Emergence of non-renewal spiking statistics due to colored noise. Comparison of two PIF models driven by **A** uncorrelated "white" noise ($D = 0.125$) and **B** exponentially correlated "colored" noise ($\sigma_\eta^2 = 0.13$, $\tau_c = 10$). In both cases, the mean ISI is $\langle T_i \rangle = 1$ and the coefficient of variation is $C_V = 0.5$. The first model generates a *renewal* spike train (top), the statistics of which is completely determined by the inverse Gaussian ISI density $P(T_i)$ **(i)**. This renewal property is revealed by a serial correlation coefficient ρ_n that is zero at all lags **(ii)**, and a joint density $P(T_i, T_{i+1})$ **(iii)** that factors into the single ISI densities due to statistical independence, hence the difference $\delta P(T_i, T_{i+1}) = P(T_i, T_{i+1}) - P(T_i)P(T_{i+1})$ vanishes **(iv)**. The conditional mean of T_{i+1} given T_i, $\langle T_{i+1}|T_i\rangle$, is shown as a function of T_i by the black solid line in **(iii)**. The SCC ρ_1 can be interpreted as the slope of this function at $T_i = \langle T_i \rangle$, which indeed vanishes for the renewal spike train in **A**. In contrast, in the case of colored noise (**B**) the ISI density is more peaked than an inverse Gaussian with the same CV **(i)**. Furthermore, the serial correlations are positive **(ii)**, which is reflected in the positive slope of the conditional mean ISI **(iii)**. Also, the function δP **(iv)** reveals an excess of short-short and long-long pairs (T_i, T_{i+1}) (red region) as compared to the shuffled ISI sequence. The positive correlations are due to the slow modulation of the firing rate by the slow colored noise, which is clearly visible in the spike trace.

introduce the Laplace transform

$$\bar{P}(s) = \int_0^\infty \mathrm{d}T\, e^{-sT} P(T), \tag{1.34}$$

from which the k-th ISI moment can be generated by the formula

$$\langle T^k \rangle = (-1)^k \left. \frac{\mathrm{d}^k \bar{P}}{\mathrm{d}s^k} \right|_{s=0}. \tag{1.35}$$

Hence, $\bar{P}(s)$ will be called ISI moment generating function. Furthermore, it is convenient to introduce the ISI cumulants defined by

$$\kappa_k = (-1)^k \left. \frac{\mathrm{d}^k \ln \bar{P}}{\mathrm{d}s^k} \right|_{s=0}. \tag{1.36}$$

The first four cumulants are related to the ISI moments by [see e.g. van Kampen, 1992]

$$\kappa_1 = \langle T \rangle, \tag{1.37}$$
$$\kappa_2 = \langle T^2 \rangle - \langle T \rangle^2 = \langle \Delta T^2 \rangle, \tag{1.38}$$
$$\kappa_3 = \langle T^3 \rangle - 3\langle T \rangle \langle T^2 \rangle + 2\langle T \rangle^3 = \langle \Delta T^3 \rangle, \tag{1.39}$$
$$\kappa_4 = \langle T^4 \rangle - 3\langle T^2 \rangle^2 - 4\langle T \rangle \langle T^3 \rangle + 12\langle T \rangle^2 \langle T^2 \rangle - 6\langle T \rangle^4 = \langle \Delta T^4 \rangle - 3\langle \Delta T^2 \rangle, \tag{1.40}$$

where $\Delta T = T - \langle T \rangle$.

The cumulants can be used to characterize the shape of the ISI density. An important measure that quantifies the variability of ISIs is the *coefficient of variation* (CV) defined as the ratio

$$C_\mathrm{V} = \frac{\sqrt{\langle \Delta T^2 \rangle}}{\langle T \rangle} = \frac{\sqrt{\kappa_2}}{\kappa_1}. \tag{1.41}$$

A CV equal to zero indicates a perfectly regular, i.e. periodic, spike train, whereas a CV equal to 1 indicates a highly irregular spike train. For instance, the Poisson process, for which spikes occur completely independently, exhibits a CV equal to 1. Furthermore, the asymmetry of the ISI density can be quantified by the skewness defined as

$$\gamma_\mathrm{s} = \frac{\kappa_3}{\kappa_2^{3/2}}. \tag{1.42}$$

The skewness of ISI densities is typically positive, indicating that the right tail is longer than the left tail of the distribution and that the bulk of the ISIs as quantified by the median is smaller than the mean ISI. If the skewness is close to zero the left and right tails are balanced and the median is close to the mean ISI. Finally, the ISI density can be characterized by the excess kurtosis defined by

$$\gamma_\mathrm{e} = \frac{\kappa_4}{\kappa_2^2}. \tag{1.43}$$

Roughly speaking, the excess kurtosis (or in short kurtosis) indicates how much of the variability is due to events that strongly deviate from the mean value. For instance, a unimodal ISI density with a heavier tail compared to another ISI density with the same CV,

tends to exhibit a larger kurtosis. This is typically accompanied by a more pronounced peak close to the mean value to balance the heavy tail.

Second-order ISI statistics: the serial correlation coefficient

While renewal processes are completely defined by the first-order ISI statistics given by the ISI density $P(T)$ (cf. Eq. (1.31)), non-renewal processes can also be characterized by higher-order ISI statistics. In particular, the distribution function $p_{ij}^{(2)}(T_i, T_j)$ can be used to form the second-order moment

$$\langle T_i T_{i+n} \rangle = \iint \mathrm{d}T_i \mathrm{d}T_{i+n}\, T_i T_{i+n} p_{i,i+n}^{(2)}(T_i, T_{i+n}). \tag{1.44}$$

Note that this quantity does not depend on the index i due to stationarity. Subtracting the squared mean ISI yields the covariance between two ISIs that are lagged by an integer $n \geq 1$:

$$\mathrm{cov}(T_i, T_{i+n}) = \langle T_i T_{i+n} \rangle - \langle T \rangle^2 = \langle (T_i - \langle T \rangle)(T_{i+n} - \langle T \rangle) \rangle. \tag{1.45}$$

An important statistics, which quantifies the correlations among ISIs is the serial correlation coefficient (SCC) [Cox and Lewis, 1966]. It is define as the covariance between T_i and T_{i+n} normalized by the ISI variance:

$$\rho_n = \frac{\langle T_i T_{i+n} \rangle - \langle T \rangle^2}{\langle T^2 \rangle - \langle T \rangle^2}. \tag{1.46}$$

This quantity can be regarded as the normalized auto-correlation function of the stochastic sequence $\{T_i\}$. It is one of the most important measures to characterize the non-renewal properties of a spike train because it reveals the correlation structure as a function of the distance between ISIs. In fact, it is the main goal of this thesis to derive analytical expressions for the SCC for various non-renewal neuron models.

Clearly, for a renewal process, all correlations between ISIs vanish except for the trivial self-correlation at lag $n = 0$, hence $\rho_n = \delta_{n,0}$. In contrast, for a general non-renewal process the SCC at a given lag can attain values between -1 (completely anti-correlated) and $+1$ (completely correlated). In particular, it has been argued by Wang [1998] that the SCC for adjacent ISIs, ρ_1, can be interpreted as the slope at $T_i = \langle T \rangle$ of the conditional mean ISI $\langle T_{i+1} | T_i \rangle$ plotted as a function of T_i (Fig. 1.7A,B(iii), black line). More precisely, let $\alpha(T_i) = \langle T_{i+1} | T_i \rangle$ be the conditional mean ISI given that the preceding ISI was equal to T_i. Then, the SCC at lag 1 is approximately given by $\rho_1 \approx \alpha'(\langle T \rangle)$.[3]

Figure 1.7A(ii) and (iii) illustrate the vanishing correlations of a PIF model driven by white noise as it is expected for a renewal model. On the other hand, a PIF model driven by slow exponentially-correlated noise shows clear positive serial correlations that decay with increasing lag (Fig. 1.7B(ii)). This is confirmed by the positive slope of the con-

[3] In fact, assuming $\alpha(\langle T \rangle) \approx \langle T \rangle$, a Taylor expansion about $T_i = \langle T \rangle$ yields $\alpha(T_i) \approx \langle T \rangle + \alpha'(\langle T \rangle)(T_i - \langle T \rangle)$. The cross-correlation can now be written as

$$\begin{aligned} \langle T_i T_{i+1} \rangle &= \iint \mathrm{d}T_i \mathrm{d}T_{i+1}\, T_i T_{i+1} P(T_i, T_{i+1}) = \int \mathrm{d}T_i\, T_i P(T_i) \int \mathrm{d}T_{i+1}\, T_{i+1} P(T_i | T_{i+1}) \\ &= \int \mathrm{d}T_i\, T_i P(T_i) \alpha(T_i) \approx \langle T \rangle^2 + \alpha'(\langle T \rangle)(\langle T^2 \rangle - \langle T \rangle^2). \end{aligned}$$

Inserting this expression into the definition of ρ_1 yields $\rho_1 \approx \alpha'(\langle T \rangle)$.

ditional mean ISI $\langle T_{i+1}|T_i\rangle$ (Fig. 1.7B(iii)). The correlation map in Fig. 1.7B(iv) reveals that the positive correlations arise from an excess of short-short and long-long ISI pairs, which are clearly visible in the spike train of Fig. 1.7B. Here, the correlation structure originates from a slow modulation of the firing rate caused by the slow noise. Another common correlation pattern are negative short-range correlations. Figure 1.14A shows the ISI statistics of a white noise driven PIF model with an additional adaptation current. In this case, the SCC is strongly negative at lag one and negligibly small at higher lags. The conditional mean ISI is larger if the previous ISI was smaller and vice versa, which confirms the negative SCC at lag one. The correlation map reveals that the negative correlations are indeed caused by an excess of short-long and long-short pairs and a lack of short-short and long-long pairs. This pattern is also apparent from a trace of the spike train. It is one major goal of this thesis to explain these negative correlations theoretically.

Sequential average vs. ensemble average

The statistics of the ISIs has been defined on the basis of ensemble averages with respect to a stationary ensemble of ISI sequences $\{T_i\}$. The advantage of this approach is that the ISI statistics can be treated analogously to the standard statistics (e.g. moments and correlation function) of a stationary stochastic process, albeit in discrete time. However, for the analysis of experimental as well as simulation data the ensemble averages are rather impractical. Furthermore, for the theoretical analysis of a non-renewal model, stationarity imposes non-trivial conditions on the state of the model upon firing, which are crucial for proper ensemble averages. I will briefly dwell on these subtle issues because they are essential for the theory of non-renewal models.

Assume that we want to compute the stationary ISI statistics, say the second moment $\langle T^2\rangle$, of some non-renewal neuron model. How can we do this using stochastic simulations of the model? A naïve implementation of the ensemble average would be: initiate the model at time $t = 0$, label the first ISI with the index $i_0 = 1$, simulate the system until the ith ISI occurs, compute T_i^2 and repeat the procedure over many trials. As a result, an estimate of the ensemble average $\langle T_i^2\rangle$ is obtained, which converges to the stationary value $\langle T^2\rangle$ if the index i is chosen sufficiently large. Obviously, this implementation is inefficient because in each trial one has to simulate the transient dynamics until the system has equilibrated. There are two much more efficient ways that avoid simulating the transients. The first method is to simulate a single long ISI sequence and to compute the sequential average along the sequence:

$$\langle f_1(T_i)\rangle = \frac{1}{N}\sum_{i=1}^{N} f_1(T_i), \qquad \langle f_2(T_i, T_{i+n})\rangle = \frac{1}{N-n}\sum_{i=1}^{N-n} f_2(T_i, T_{i+n}), \qquad \dots \tag{1.47}$$

where N is the length of the sequence (ideally, $N \to \infty$) and f_1 and f_2 are some one- and two-point functions of the random variables T_i. For large N the initial transient becomes insignificant. This method relies on the fact that for a stationary, ergodic process the ensemble average is equal to the temporal average. The second method is to prepare the model at time $t = 0$ in a state that corresponds to the stationary ensemble conditioned on those realizations that experienced a spike at time $t = 0$. This ensemble will be referred to as the *conditional ensemble*. Specifically, this requires to determine the distribution of the internal state conditioned on a firing event, which corresponds to the distribution

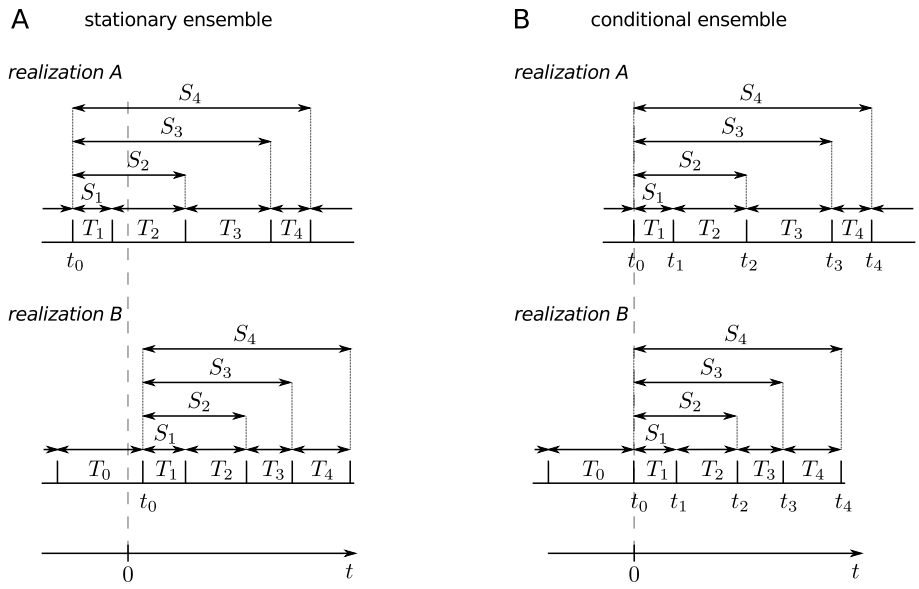

Figure 1.8.: Illustration of the nth-order intervals in different ensembles. **A** Two representative spike train realizations ("A" and "B") of a stationary ensemble, for which the ensemble statistics is homogeneous in time. The position of the stationary ISI sequences $\{T_i\}$ and the n-th-order intervals S_n is completely random with respect to the absolute time t, as indicated by the random position of the spike time t_0. **B** Shifting each realization in time such that $t_0 = 0$ (alignment) leads to the stationary ensemble conditioned on a spike at time $t = 0$ ("conditional ensemble"). Here, S_n coincides with the n-th spike time.

of states of a long trajectory sampled at the spike times. Then, the ISI statistics can be computed for $i = 1$ by averaging over many trials. In each trial the system is initialized randomly according to the distribution upon firing. The obvious problem is that in most cases this distribution is not exactly known.

The sequential average is preferable in simulations because the long trajectory naturally samples the state space upon firing, making the complicated preparation of the initial state superfluous. On the other hand, the sequential average is often infeasible for analytical calculations of the ISI statistics. In this case, it is most natural to describe the dynamics of the whole ensemble by an evolution equation for the probability distribution instead of tracking a single trajectory. For stochastic neuron models that constitute a (possibly multi-dimensional) Markov process, the evolution of the probability distribution can be described by a Fokker-Planck equation (cf. Chap. 2 and 3) or a master equation (cf. Chap. 5). These equations require the initial distribution at time $t = 0$. In the conditional ensemble (spike at $t = 0$) the initial distribution is given by the distribution of the state upon firing. Finding analytical expressions for this distribution or approximations thereof will be a recurrent theme in this thesis. Having determined the initial conditions that correspond to the conditional ensemble, the further strategy is to relate the dynamics of the probability distribution to the ISI density, which then enables ensemble averaging. This often amounts to solving a first-passage-time problem with respect to the firing threshold.

1.2.2. The statistics of the n-th-order intervals

From the ISI sequence $\{T_i\}$ one can form a new random variable, termed the n-th-order interval, by summing up n subsequent ISIs, where $n = 1, 2, \ldots$ is an integer. The first-order statistics of these sums can be used to calculate the second-order statistics of the ISI sequence. Specifically, let me define the n-th order intervals S_n as the sum

$$S_n = T_1 + \cdots + T_n = t_n - t_0, \qquad n \geq 1 \tag{1.48}$$

(see Fig. 1.8A). Note that using this notion, the statistics of the single ISI can also be called first-order interval statistics. In the stationary ensemble, the spike time t_0 is a random variable, especially it is different in each realization. For the calculation of the n-th-order interval statistics the conditional ensemble ("spike at $t = 0$") is advantageous, because with respect to this ensemble the statistics of the n-th spike time after $t = 0$ is equivalent to the n-th-order interval statistics. We can construct the conditional ensemble from the stationary one by shifting the time axis in each realization such that the origin coincides with t_0, i.e. $t_0 = 0$ (Fig. 1.8B). It follows that in the conditional ensemble the n-th-order interval is equal to the n-th spike time:

$$S_n = t_n. \tag{1.49}$$

Thus, the n-th-order interval will be denoted by t_n in what follows.

Using the rules for the addition of (correlated) stochastic variable the mean and variance of t_n are obtained as $\langle t_n \rangle = n\langle T \rangle$ and

$$\langle \Delta t_n^2 \rangle = n\langle \Delta T^2 \rangle \left[1 + 2 \sum_{k=1}^{n-1} \left(1 - \frac{k}{n} \right) \rho_k \right], \tag{1.50}$$

where ρ_k is the serial correlation coefficient (SCC) [see e.g. Cox and Lewis, 1966]. Equation (1.50) can be inverted to yield a formula for the SCC [Lindner, 2004a, Schwalger, 2006]:

$$\rho_n = \frac{\langle \Delta t_{n+1}^2 \rangle - 2\langle \Delta t_n^2 \rangle + \langle \Delta t_{n-1}^2 \rangle}{2\langle \Delta T_1^2 \rangle} \tag{1.51}$$

Here, the condition $\langle \Delta t_0^2 \rangle = \langle \Delta t_{-1}^2 \rangle = 0$ is imposed. The relation (1.51) will be utilized in Chap. 2 for the calculation of the SCC by means of the n-th-order interval statistics.

Analogously to the ISI moments, the n-th-order moments can be obtained from the moment generating function $\bar{P}_n(s)$ defined as the Laplace transformation of the n-th-order interval density $P_n(t) = \langle \delta(t - t_n) \rangle$ (cf. Eq. (1.34), (1.35)). This approach will be analyzed in detail in Chap. 2, where I will derive a perturbation expansion of the n-th-order moment generating function. For non-renewal processes, the analytical calculation of $\bar{P}_n(s)$ is generally a hard theoretical problem. In marked contrast, for renewal processes the computation of the moment generating function is simple. In fact, the Laplace transform of the distribution of the sum of independent ISIs reduces to the product of the Laplace transforms of the ISI densities:

$$\bar{P}_n(s) = [\bar{P}(s)]^n. \tag{1.52}$$

This simple relation is the basis of renewal theory [Cox, 1962]. Its mathematical conve-

nience may be one reason why renewal models are so popular in theoretical neuroscience.

1.2.3. Firing rate, correlation function and power spectrum of the spike train

Let us now turn to the first- and second-order statistics of the spike train $x(t) = \sum_i \delta(t - t_i)$. The ensemble average of $x(t)$ yields the firing rate

$$\langle x(t) \rangle = r(t) = \lim_{\Delta t \to 0} \frac{\text{Prob}\{\text{spike in } (t, t + \Delta t)\}}{\Delta t}, \tag{1.53}$$

i.e. the probability per unit time for the occurrence of a spike at time t. In fact, $\langle \delta(t - t_i) \rangle$ can be regarded as the probability density for the i-th spike time to occur at time t; therefore the sum over all spike times must be the probability density that some spike, no matter which one, occurs at time t, which proves that $\langle x(t) \rangle = r(t)$. For a stationary spike train, the ensemble average must be equal to a constant firing rate, which will be denoted by r_0.

The correlation function of a stationary spike train $C(\tau) = \langle x(t)x(t + \tau) \rangle - r_0^2$ can be calculated in a similar way [4] resulting in

$$C(\tau) = r_0 \delta(\tau) + r_0(m(\tau) - r_0) \tag{1.54}$$

[see also Cox and Lewis, 1966, Gabbiani and Koch, 1989]. Here, the conditional firing rate given a spike at time $t = 0$,

$$m(\tau) = \lim_{\Delta t \to 0} \frac{\text{Prob}\{\text{spike in } (\tau, \tau + \Delta t) \,|\, \text{spike at } t = 0\}}{\Delta t}, \tag{1.55}$$

has been introduced. Put differently, $m(\tau)$ is the firing rate with respect to the conditional ensemble. In addition to that, this conditional firing rate can also be interpreted as the sum of the probability densities that at time τ the first, the second, and so on, spike occurred. For $\tau \geq 0$, the conditional firing rate is thus equivalent to the sum of the n-th-order interval densities, and by symmetry

$$m(\tau) = \sum_{n=1}^{\infty} P_n(|\tau|). \tag{1.56}$$

This relation links the second-order spike train statistics with the n-th-order interval statistics.

It is often more instructive to consider the second-order properties of the spike train in the frequency domain. This is expressed by the power spectrum defined as the Fourier

[4] To see this, recall that the expression $\langle \delta(t - t_i)\delta(t + \tau - t_j) \rangle$ can be regarded as the joint probability density that the i-th spike occurs at time t and the j-th spike occurs at time $t + \tau$. Thus, one can write

$$\begin{aligned}
\langle x(t)x(t + \tau) \rangle &= \sum_{i,j} \langle \delta(t - t_i)\delta(t + \tau - t_j) \rangle = \sum_i \langle \delta(t - t_i)\delta(t + \tau - t_i) \rangle + \sum_{i \neq j} \langle \delta(t - t_i)\delta(t + \tau - t_j) \rangle \\
&= r_0 \delta(\tau) + \frac{\text{Prob}\{\text{spike in } (t, t + \Delta t) \;\&\; \text{spike in } (t + \tau, t + \tau + \Delta t)\}}{\Delta t^2} \\
&= r_0 \delta(\tau) + \frac{\text{Prob}\{\text{spike in } (\tau, \tau + \Delta t) \,|\, \text{spike in } (0, \Delta t)\,\}}{\Delta t} \cdot \frac{\text{Prob}\{\text{spike in } (0, \Delta t)\}}{\Delta t}.
\end{aligned}$$

transform of the correlation function. Applying the Fourier transform to Eq. (1.54) and using the Laplace transform of Eq. (1.56) the spike train power spectrum reads [cf. also Cox and Lewis, 1966]

$$S_x(\omega) = r_0 \left\{ 1 + \sum_{n=1}^{\infty} [\bar{P}_n(i\omega) + \bar{P}_n^*(-i\omega)] \right\} - 2\pi r_0^2 \delta(\omega), \tag{1.57}$$

where $\bar{P}_n^*(s)$ denotes the complex conjugate of the moment generating function $\bar{P}_n(s)$. For renewal processes, the identity (1.52) can be used in Eq. (1.57), which turns the infinite sums into geometric series. This results in the simple formula [see e.g. Stratonovich, 1967]

$$S_x(\omega) = r_0 \frac{1 - |\tilde{P}(\omega)|^2}{|1 - \tilde{P}(\omega)|^2}, \tag{1.58}$$

where $\tilde{P}(\omega) = \bar{P}^*(-i\omega)$ is the one-sided Fourier transform of the ISI density. For a non-renewal process, however, the calculation of the power spectrum is much more difficult. Even if we were able to find expressions for the n-th-order moment generating functions $\bar{P}_n(s)$ (one example is provided in Chap. 2), it would be infeasible in most cases to evaluate the infinite sums in Eq. (1.57). To still find approximations of the power spectrum in the case of a neuron model with feedback (adaptation), I will pursue in Chap. 3.4.3 another approach that was proposed by Lindner et al. [2005b]. This approach starts with the following (equivalent) definition of the power spectrum [see e.g. Stratonovich, 1967]

$$\langle \tilde{x}(\omega) \tilde{x}^*(\omega') \rangle = 2\pi S_x(\omega) \delta(\omega - \omega'), \tag{1.59}$$

where $\tilde{x}(\omega) = \int \mathrm{d}t\, x(t) e^{i\omega t}$ is the Fourier transform of the stochastic process $x(t)$. Using a linear response ansatz for $\tilde{x}(\omega)$ it is indeed possible to determine the non-renewal effect of weak feedback on the power spectrum.

1.2.4. The count statistics

The count statistics is concerned with the statistics of the stochastic process

$$N(t) = \int_0^t \mathrm{d}t'\, x(t'). \tag{1.60}$$

$N(t)$ is called the counting process because it is equal to the number of spikes in the interval $(0, t)$. Averaging Eq. (1.60) yields the mean spike count $\langle N(t) \rangle = r_0 t$. This entails that the stationary firing rate equals the inverse mean ISI because for $t \to \infty$

$$r_0 = \frac{\langle N(t) \rangle}{t} \simeq \frac{N(t)}{t} \simeq \frac{N(t)}{t_{N(t)}} = \frac{1}{\frac{1}{N(t)} \sum_{i=1}^{N(t)} T_i} \simeq \frac{1}{\langle T \rangle}. \tag{1.61}$$

Thus, we conclude that $\langle N(t) \rangle = t / \langle T \rangle$. What is the variance of the spike count? On the one hand, it can be shown by using the definition (1.60) that $\langle \Delta N(t)^2 \rangle = 2t \int_0^\infty \mathrm{d}\tau C(\tau)(1 - \tau/t)$ [Cox and Lewis, 1966, Cox and Isham, 1980], which for large t is asymptotic to $tS_x(0)$. This reveals that for finite $S_x(0)$ the variance grows linearly in time, i.e. the spike count is a diffusion process on large time scales. On the other hand, the spike count vari-

ance can be related asymptotically to the variance of the n-th-order interval as follows: for large times, t can be approximated by a multiple of the ISI, i.e. $t \simeq n\langle T\rangle$ for some integer n. Let us now consider the n-th-order interval t_n, which is spread about its mean $\langle t_n\rangle = n\langle T\rangle$. Asymptotically, the variability of $N(t)$ is completely due to the variability of t_n, which allows us to assume the deterministic relationship

$$N(t) \simeq N(t_n) + \frac{1}{\langle T\rangle}(t - t_n) = n + \frac{t - t_n}{\langle T\rangle}. \tag{1.62}$$

From this we find the mean $\langle N(t)\rangle = t/\langle T\rangle$ and the variance $\langle \Delta N(t)^2\rangle = \langle \Delta t_n^2\rangle/\langle T\rangle^2$. The n-th-order variance is given by Eq. (1.50) which for large n becomes $\langle \Delta t_n^2\rangle = n\langle \Delta T^2\rangle \times [1 + 2\sum_{k=1}^{\infty}\rho_k]$. It is convenient to normalize the spike count variance by the mean spike count which has a finite asymptotic value if the spike count grows diffusively. This quantity is called *Fano factor* and is defined by

$$F(t) = \frac{\langle \Delta N(t)^2\rangle}{\langle N(t)\rangle}. \tag{1.63}$$

It is a frequently-used measure that characterizes the variability of a spike train on a time scale t. Using the asymptotic results for the mean and variance of $N(t)$ we obtain

$$\lim_{t\to\infty} F(t) = \frac{S_x(0)}{r_0} = C_{\mathrm{V}}^2\left[1 + 2\sum_{k=1}^{\infty}\rho_k\right]. \tag{1.64}$$

This important relation shows how ISI correlations affect the long-term count variability and the spike-train power spectrum at zero frequency. In particular, for a renewal model, for which the correlations vanish, Eq. (1.64) leads to $F(\infty) = C_{\mathrm{V}}^2$ and $S_x(0) = r_0 C_{\mathrm{V}}^2$. The Fano factor will be inspected for a neuron driven by colored noise in Chap. 2.1.5. Furthermore, for an adapting neuron driven by white noise I will show in Chap. 3 how negative serial correlations reduce the power of the spike train at low frequencies ("noise shaping"), an effect that has been investigated for a simpler model in Chacron et al. [2004a], Lindner et al. [2005a].

Finally, the count statistics offers a further method to compute higher-order ISI statistics. Such a method will be put forward in Chap. 5. It is based on the following non-trivial relationships between the count and interval statistics derived by McFadden [1962]:

$$\langle T^2\rangle = 2\langle T\rangle\int_0^{\infty} \mathrm{d}t\, p(0,t), \qquad \langle T_i T_{i+n}\rangle = \langle T\rangle\int_0^{\infty} \mathrm{d}t\, p(n,t). \tag{1.65}$$

Here, $p(n,t) = \mathrm{Prob}\{N(t) = n\}$ is the distribution of the spike count for a time window t in the stationary ensemble.

1.2.5. Example: PIF model with white noise and inverse Gaussian statistics

Because the PIF model will be the starting point for further extensions, which are then compared to the basic white-noise driven renewal case, let me briefly state the stationary spiking statistics for the basic case. A detailed analysis of the PIF model for white vs. exponentially-correlated colored noise, as well as analytical results for the latter case can

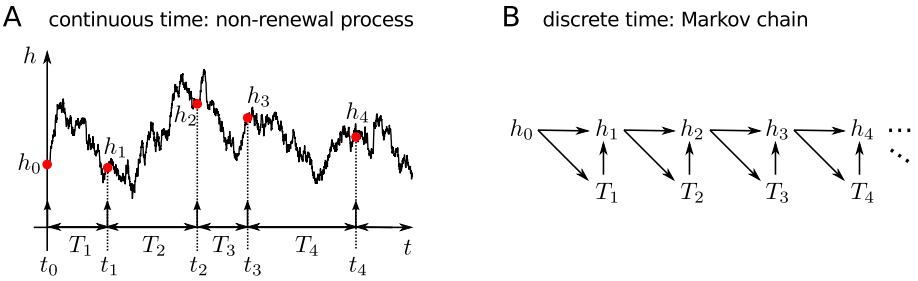

Figure 1.9.: Non-renewal models with an underlying Markov process can be reduced to a Markov chain. A The ISI sequence $\{T_1, T_2, T_3, \dots\}$ is a non-Markovian process because spiking is subject to a hidden Markov process $h(t)$ (solid line). Thus, the spike train is non-renewal (a so-called Markov-renewal process). **B** In contrast, the sequence of values of the hidden variable sampled at the spike times, $h_i \equiv h(t_i)$, is Markovian (Markov chain). The sequence of tuples (h_i, T_i) also forms a Markov chain. The arrows indicate causal dependencies.

.

be found in [Lindner, 2004a].

A typical trajectory of the model for white or colored noise is depicted in Fig. 1.7. It is a nice feature of the PIF model that the mean ISI and thus the firing rate do not depend on the noise, in particular, it holds

$$\langle T \rangle \equiv \frac{1}{r} = \frac{V_{\text{th}}}{\mu}. \tag{1.66}$$

This is due to the fact that for large times the spike count can be replaced by the freely diffusing trajectory $V(t)/V_{\text{th}}$ that starts at $V(0) = 0$ but is not reset upon threshold crossings. The mean of the free process is $\langle V(t) \rangle / V_{\text{th}} = \mu t / V_{\text{th}}$, hence the firing rate is μ / V_{th}. For the white noise case, the coefficient of variation (CV) reads [see e.g. Tuckwell, 1988]

$$C_{\text{V}} = \sqrt{\frac{2D}{V_{\text{th}}\mu}}. \tag{1.67}$$

The ISI density is given by the inverse Gaussian density [Schrödinger, 1915, Gerstein and Mandelbrot, 1964] which can be parametrized by the mean ISI and the CV:

$$P_{\text{WN}}(T) = \sqrt{\frac{\langle T \rangle}{2\pi C_{\text{V}}^2 T^3}} \exp\left[-\frac{(T - \langle T \rangle)^2}{2C_{\text{V}}^2 \langle T \rangle T} \right]. \tag{1.68}$$

Furthermore, the skewness and kurtosis of the inverse Gaussian are given by

$$\gamma_{\text{s}} = 3C_{\text{V}} \tag{1.69}$$

and

$$\gamma_{\text{e}} = 15C_{\text{V}}^2. \tag{1.70}$$

1.2.6. Non-renewal models subject to a hidden Markov process

The non-renewal models considered in this thesis retain a memory due to an underlying ("hidden") Markov process $h(t)$. This process may be a one-dimensional (Chap. 3)

or multidimensional process (Chap. 2) and it may be discrete (Chap. 5) or continuous. For instance, in the above example of a colored noise driven PIF model, Eq. (1.20), the Ornstein-Uhlenbeck process $\eta(t)$ plays the role of the hidden Markov process $h(t)$. On the other hand, in models with adaptation (see below) $h(t)$ assumes the role of an adaptation current. It is insightful to sample the hidden Markov process at the moments of spiking, which yields the sequence $\{h_i \equiv h(t_i)\}$ (Fig. 1.9A). In the case of an adaptation current, $h(t)$ has discontinuities at the spike times. To avoid ambiguity, we agree upon the rule that h_i will always be evaluated immediately after the spike, i.e. $h_i = h(t_i+)$. Now, although the ISI sequence $\{T_i\}$ is non-Markovian, the sequence $\{h_i\}$ is Markovian. In fact, in our models the tuple (h_i, T_i) only depends on h_{i-1} (Fig. 1.9B):

$$P(h_i, T_i|h_{i-1}, T_{i-1}; h_{i-2}, T_{i-2}; \dots) = P(h_i, T_i|h_{i-1}). \tag{1.71}$$

Processes with this property are also known as *Markov-renewal processes*, which are an obvious generalization of renewal processes [Cox and Miller, 1965]. Integrating the last equation with respect to T_i yields the Markov property of the sequence $\{h_i\}$:

$$P(h_i|h_{i-1}, T_{i-1}; h_{i-2}, T_{i-2}; \dots) = p_{\mathrm{tr}}(h_i|h_{i-1}), \tag{1.72}$$

where $p_{\mathrm{tr}}(h_i|h_{i-1})$ is the *transition probability distribution* of the Markov chain. Similarly, integrating over h_i shows that the statistics of the interspike interval T_i is completely determined by the knowledge of h_{i-1}:

$$P(T_i|h_{i-1}, T_{i-1}; h_{i-2}, T_{i-2}; \dots) = P(T_i|h_{i-1}), \tag{1.73}$$

where $P(T_i|h_{i-1})$ defines the *conditional ISI statistics*. The probability density $P_i(h)$ of the variable h_i fulfills the Chapman-Kolmogorov equation in the form

$$P_i(h) = \int \mathrm{d}h'\, p_{\mathrm{tr}}(h|h') P_{i-1}(h'). \tag{1.74}$$

The equilibrium distribution of h_i that is iteratively attained in the limit $i \to \infty$ is called the *upon firing distribution* and will be denoted by $P_{\mathrm{f}}(h)$ (cf. Sec. 1.2.1).

In general, the ISI statistics of the non-renewal models with a hidden Markov process, can be explicitly expressed in terms of the transition probability distribution $p_{\mathrm{tr}}(h_i|h_{i-1})$, the upon firing distribution $P_{\mathrm{f}}(h)$ and the conditional ISI statistics. For instance, the ISI density and its moments are obtained by averaging the conditional statistics with respect to $P_{\mathrm{f}}(h)$:

$$P(T_i) = \int \mathrm{d}h_{i-1}\, P(T_i|h_{i-1}) P_{\mathrm{f}}(h_{i-1}), \qquad \langle T^n \rangle = \int \mathrm{d}h\, \langle T^n|h\rangle P_{\mathrm{f}}(h), \tag{1.75}$$

where $\langle T^n|h\rangle$ denotes the conditional average of T_i^n given the initial value $h_{i-1} = h$. Similarly, the cross moments of two ISIs with lag $n \geq 1$, which enter the serial correlation coefficient, can be written as

$$\langle T_1 T_{n+1}\rangle = \int \mathrm{d}h_0\, P_{\mathrm{f}}(h_0) \int \left(\prod_{k=1}^{n} \mathrm{d}h_k p_{\mathrm{tr}}(h_k|h_{k-1}) \right) \langle T_{n+1}|h_n\rangle \langle T_1|h_0, h_1\rangle. \tag{1.76}$$

Eq. (1.75) and (1.76) illustrate the importance of the transition probability density and

especially the upon firing distribution for the ISI statistics of non-renewal models.

1.2.7. Experimental evidence for non-renewal spiking

Non-renewal spiking has been frequently observed throughout the nervous system and across different species [for a review, see Farkhooi et al., 2009, Avila-Akerberg and Chacron, 2011]. Typical examples of non-renewal statistics that have been measured in experiments are presented in Fig. 1.10. In particular, three types of correlations have been repeatedly encountered. Firstly, a negative SCC at lag 1 and small correlations at higher lags seem to be a typical pattern for many neurons both from primary sensory systems [Ratnam and Nelson, 2000, Chacron et al., 2000] (Fig. 1.10A) and from the cortex [Nawrot et al., 2007, Engel et al., 2008] (Fig. 1.10B,C). This means that a short ISI is more likely followed by a long ISI and vice versa. This is clearly visible in Fig. 1.10A(i), which depicts a voltage trace of an electroreceptor afferent cell of a weakly electric fish [Chacron et al., 2005a]. A common strategy to assess the effect of correlations between ISIs on various statistical quantities is to shuffle the sequence of ISIs. This operation eliminates all correlations (Fig. 1.10A(ii)), but preserves the first-order ISI statistics: in fact, the distribution of ISIs is invariant with respect to shuffling. Relating to this, a renewal model that possesses the same first-order ISI statistics as a given non-renewal model will be referred to as "the corresponding renewal model" in what follows. Figure 1.10A(iii) shows that the spike train has reduced power at low frequencies as compared to the corresponding renewal spike train. This effect is known as "noise shaping" and can be roughly explained by Eq. (1.64). According to this equation the zero-frequency limit of the power spectrum is reduced if the sum $\sum_k^\infty \rho_k$ is negative, which is obviously the case for the data in Fig. 1.10A.

Secondly, *positive* correlations have also been reported: In Lowen and Teich [1992], the positive correlations were weak but long-range, which rendered the Fano factor a more convenient measure to study non-renewal properties than the SCC itself (Fig. 1.10D). In this example, the Fano factor was significantly larger than unity for large observation times t, i.e. the long-term variability was much larger than that of a Poisson process. Moreover, the Fano factor increased with t like a power law over at least two orders of magnitude without saturating at large t. This has lead to the interpretation that spike trains may exhibit fractal structures. In contrast, the shuffled ISI spike train did not show such a large spike count variability on long time scales. In virtue of Eq. (1.64), it can be concluded that the sum of the SCCs, $\sum_{k=1}^\infty \rho_k$, is large and positive, if not infinite. In the latter case, which corresponds to a truly non-saturating Fano factor, the divergence of the sum indicates that the serial correlations decay slowly and non-geometrically.

Thirdly, more complex oscillating patterns of the SCC have been observed in experiments on the electrosensory system of paddlefish [Neiman and Russell, 2001, Bahar et al., 2001, Neiman and Russell, 2004]. Figure 1.10D presents two examples of such patterns of an afferent neuron that innervates epithelial hair cells of an electroreceptor. It has been shown by Neiman and Russell [2005] that these patterns can be well explained by an oscillatory neuron (the afferent neuron) that is driven by another oscillator that resides in the epithelial tissue. The frequency of the epithelial oscillator and the intrinsic firing frequency of the afferent neuron are clearly visible in the spike train power spectrum. The correlation pattern is essentially determined by the ratio of these two frequencies and

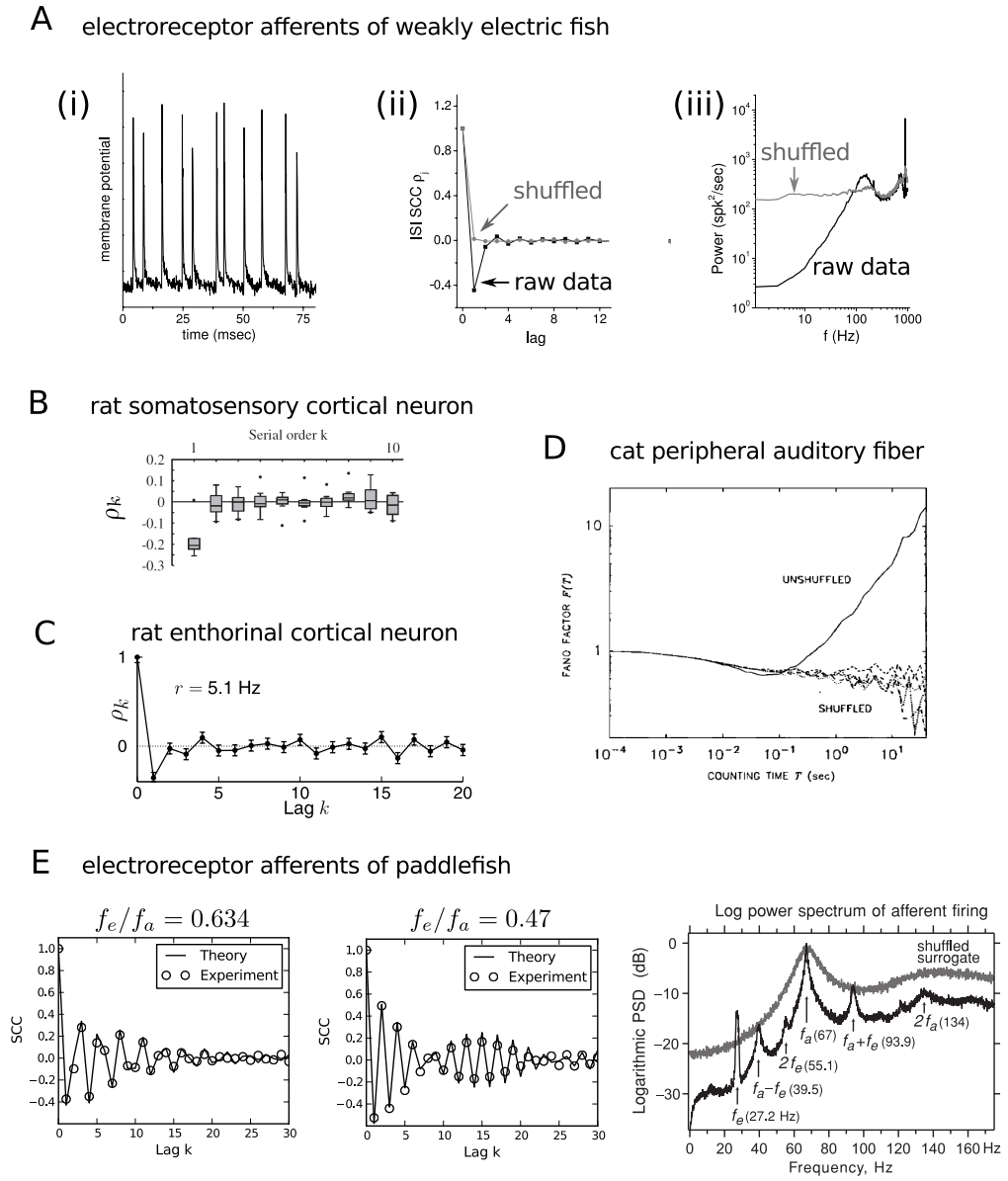

Figure 1.10.: Non-renewal spiking in various neural systems. Spike train recordings often show non-renewal statistics, especially correlations between ISIs. **A** Spike patterns of P-unit electroreceptor afferents **(i)** reveal anti-correlations between adjacent ISIs (long-short combinations). The serial correlation coefficient is indeed negative at lag 1 and vanishes at higher lags **(ii)**. A shuffling of the ISI sequence removes the serial correlations, but keeps the same first-order ISI statistics. Compared to this renewal spike train the unshuffled spike train exhibits reduced power at low frequencies as predicted by Eq. (1.64). Figures taken from Chacron et al. [2005a]. **B,C** Similar correlation patterns with *short-range negative correlations* can be found in central, cortical neurons (**B** from Nawrot et al. [2007], **C** from Engel et al. [2008]). **D** The Fano factor of an auditory fiber of a cat reveals a large long-term variability of the spike count that strongly increases with the observation time. This has been ascribed to long-range correlations in the spike train. According to the general relation (1.64) the large value of the Fano factor implicitly shows the dominance of long-range *positive ISI correlations*, which have been indeed observed in these fibers (from Lowen and Teich [1992]). **E** Complex long-range correlation patterns are found in primary electrosensory afferents of paddlefish. These cells are driven by stochastic oscillations generated by epithelial hair cells. The frequency of the epithelial oscillation and the eigenfrequency of the afferent neuron are reflected by peaks in the spike train power spectrum and their frequency ratio crucially shapes the correlation structure. Also note that a shuffling of ISIs strongly changes the power spectrum. A theoretical expression for the SCC (cf. Chap. 2.4) has been fitted to the data in Bauermeister [2012]. Right figure modified from Neiman and Russell [2004].

by the coherence of the driving oscillator. In Chap. 2.4, I will derive analytical formulas for the ISI statistics including the SCC using a model studied by Engel et al. [2009]. The theoretical results can be well fitted to the data (Fig. 1.10D, see also [Bauermeister, 2012]), which may be used to infer unknown parameters like the quality factor of the epithelial oscillator.

Besides examples from neuroscience, non-renewal behavior has been observed in many other systems that generate sequences of discrete events. For instance, it has been recently demonstrated that a laser with optical feedback exhibits intrinsic correlations of intervals between power dropouts [Schwalger et al., 2012]. Additionally, strong positive serial correlation can be induced by modulating the intensity of the lasers pump current. In geophysics, memory in the sequence of earth quake recurrence times with positive correlations have been reported in [Livina et al., 2005].

1.3. Sources of non-renewal spiking

Non-renewal spiking is expected in any more involved spiking neuron model that includes e.g. sources of colored noise (e.g. synaptically filtered shot noise or temporally structured inputs), slow subthreshold-activated currents (possibly leading to subthreshold resonance), negative feedback either of self-inhibitory nature or through recurrent, inhibitory network connections, mechanisms leading to bursting or effects due to the spatial extension of neurons. In some of these cases, ISI correlations have been theoretically predicted [e.g. Liu and Wang, 2001, Middleton et al., 2003, Lindner, 2004a, Engel et al., 2008, 2009]. Among the potential mechanisms of non-renewal spiking, particularly important sources of ISI correlations are temporally structured external inputs and self-inhibitory feedback such as spike-triggered adaptation mechanisms. It should be mentioned that ISI correlations frequently arise in two other cases that will not be dealt with in this thesis. Firstly, on a population level negative correlations emerge when renewal spike trains are superimposed. The superposition of spike trains and the emergence of correlations has been theoretically investigated by Lindner [2006], Deger et al. [2012]. Secondly, ISI correlations also arise in any non-stationary setup [Perkel et al., 1967], which may be due to time-dependent inputs or transients. In the following, however, I will exclusively consider the case of a stationary ISI sequence, i.e. I will assume that ensemble averages can always be performed with respect to an underlying stationary ensemble or a stationary set of experimental trials.

1.3.1. Colored noise

It has been theoretically shown for simple neuron models that noise with temporal correlations (so-called "colored noise" as opposed to temporally uncorrelated white noise) often leads to positive ISI correlations [Middleton et al., 2003, Lindner, 2004a, Schwalger and Schimansky-Geier, 2008]. Figure 1.7B illustrates the strong effect of a slow Ornstein-Uhlenbeck process on the ISI statistics. Colored noise can arise due to different mechanisms. One source of temporal correlations is the filtering of presynaptic input through the dynamics of the postsynaptic conductances. The time constants of this filter, which are ultimately set by the kinetics of ion channels and other molecular processes of the synaptic receptor, are diverse and depend on the type of synapse. The simplest model

for synaptic filtering is a first-order low-pass filter that corresponds to an instantaneous conductance change followed by an exponential decay with a synaptic time constant τ_s. Typical synaptic time constants are of the order of 1 ms for fast excitatory (AMPA) receptors and 5 ms for inhibitory synaptic receptors, but can also become rather large (up to $\tau_s \sim 100$ ms) for excitatory NMDA receptors. For exponential synapses, the total conductance caused by many presynaptic events can be approximated by an Ornstein-Uhlenbeck process with a correlation time equal to the synaptic time constant (similar as in Sec. 1.1.2). Importantly, the effect of colored noise on ISI correlations depends on the relative size of the correlation time compared to the mean ISI: serial correlations are expected only if input correlations extend at least one ISI.

Apart from synaptic filtering at the postsynaptic side of the synapse, let me mention two other reasons why synaptic input is in general a colored noise process. Firstly, on the presynaptic side, an effect called short-term synaptic plasticity can be modelled as amplitude modulations of the presynaptic spike trains on a time scale of the order of 100 ms Lindner et al. [2009]. It has been shown that the modulated spike trains exhibit non-flat power spectra even if the presynaptic spike times form a Poisson process [Merkel and Lindner, 2010]. Second, spike trains of neurons are usually not Poissonian and the superposition of many independent spike trains is thus not Poissonian either [Lindner, 2006]. As a consequence, the total input from a large presynaptic population is non-Poissonian, and hence colored, even before the synaptic dynamics.

Colored noise can also be employed as a model of a stimulus because natural stimuli are characterized by long-range temporal correlations. However, unlike purely deterministic stimuli colored noise has a finite correlation time like many natural stimuli. Sometimes temporally-structured inputs are indeed noise rather than a stimulus: in the electro-sensory system of paddlefish, primary sensory afferents are perpetually driven by stimulus-unrelated, stochastic oscillations, i.e. a colored noise with a pronounced peak in the power spectrum [Neiman and Russell, 2005]. It has been suggested by theoretical analysis that in this system the presence of stochastic oscillations may be beneficial for the detection of weak signals [Engel et al., 2009]. In all previous examples, the origin of the colored noise can be regarded as external to the cell. It will be shown in Chap. 4, however, that intrinsic noise associated with slow ionic channels, yields a source of colored noise that is intrinsic to the cell.

1.3.2. Spike-triggered adaptation mechanisms

The second important mechanism that generates correlated ISIs are self-inhibitory feedback mechanisms. The intrinsic negative feedback is triggered by the output spikes and leads to a wide-spread phenomenon called spike-frequency adaptation. The latter refers to the following experimental observation that has been found in many types of neurons: in response to a current step of an injected current the neuron initially fires at a high firing rate, which then slowly decays to some lower firing rate called the adapted state. A typical example is shown in Fig. 1.11. Intuitively speaking, the neuron emphasizes fast changes in the stimulus whereas it decreases the firing rate if the stimulus does not exhibit any further changes. Eventually, the neuron reaches a stationary state (adapted state), where all transients have declined. This stationary spiking state and its statistical analysis is one of the main topics of this thesis. Although spike-frequency adaptation be-

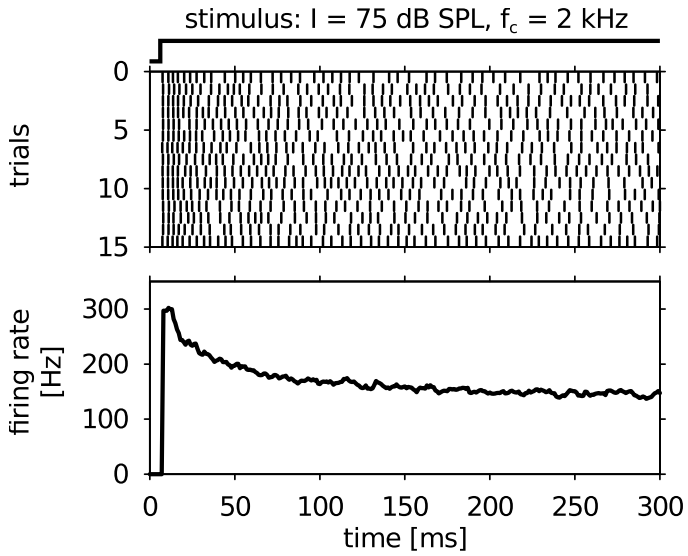

Figure 1.11.: Spike frequency adaptation Response of an auditory receptor neuron in the locust to a pure tone sound stimulus that is switched-on as indicated in the top panel (SPL – sound pressure level, f_c – stimulus frequency). The neuron responds first vigorously but adapts to the constant stimulus by a decay of the firing rate. The middle panel shows the spike time for 15 representative trials, the bottom panel depicts the firing rate obtained from an ensemble average of 70 trials. Figure modified from [Fisch, 2011].

comes most evident in the transient dynamics, it is also reflected in the stationary state. In fact, as pointed out by several studies [Geisler and Goldberg, 1966, Wang, 1998, Ratnam and Nelson, 2000, Chacron et al., 2000, Liu and Wang, 2001, Chacron et al., 2001], spike-triggered adaptation mechanisms reveal themselves in the occurrence of *short-range, negative serial correlations*, similar to those observed in experiments (cf. Fig. 1.10A-C).

Short-range, negative serial correlations can be phenomenologically captured in generalized integrate-and-fire models via introduction of a slow inhibitory feedback variable, either acting as a dynamic threshold or as an inhibitory conductance or current [Geisler and Goldberg, 1966, Chacron et al., 2000, Liu and Wang, 2001, Muller et al., 2007, Nesse et al., 2010, Benda et al., 2010] (Fig. 1.12, 1.14A). The link between adaptation and negative serial correlations has been established only on the basis of numerical simulations. A theoretical description of serial correlations in these models, however, has not been achieved so far. In Chap. 3 and 4, I will derive explicit expression for the SCC which reveal the conditions under which negative correlations appear. Surprisingly, it turns out that the correlations are negative only if an adapting neuron model is driven by fast fluctuations, in marked contrast to slow fluctuations that lead to positive serial correlations (Fig. 1.14B). In fact, a closer look at previous modeling studies that reported negative serial correlations reveals that fast fluctuations have been considered, either in the form of Poissonian shot noise or (nearly) white gaussian noise. However, as will be shown in Chap. 4, slow fluctuations can easily arise if the slow adaptation mechanism is noisy.

Among the potential mechanisms that have been suggested to cause spike frequency adaptation, we consider in this thesis the important class of spike-triggered adaptation currents [Benda and Herz, 2003]. Different ionic currents have been suggested to underlie adaptation, prominent examples are the M-type current [Brown and Adams, 1980, Madison and Nicoll, 1984], the AHP current [Madison and Nicoll, 1984] and the slow

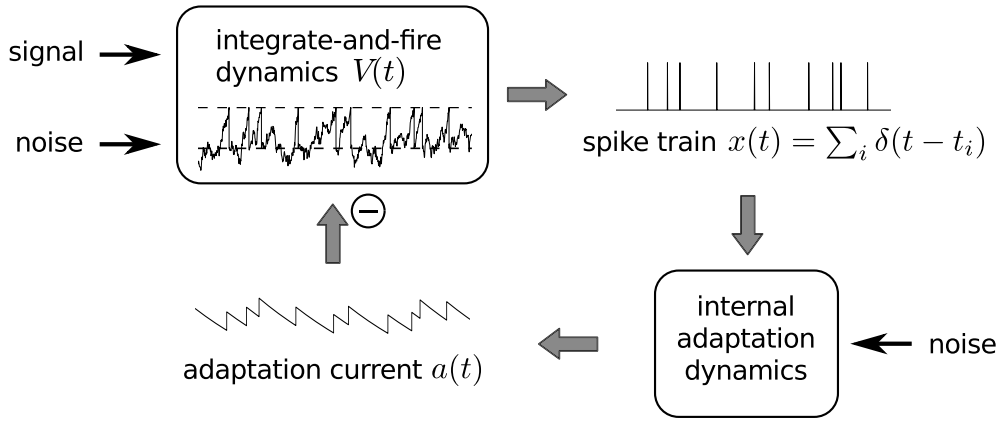

Figure 1.12.: Negative feedback loop of a neuron with spike-triggered adaptation. The membrane potential dynamics is affected by external input currents ("signal"), noise and an inhibitory adaptation current $a(t)$. The latter is driven by the output spike train $x(t)$, which in turn is generated by the membrane potential dynamics. Noise can also enter on the level of the intrinsic adaptation dynamics causing a stochastic adaptation current (in this example, a deterministic adaptation current is shown).

recovery from inactivation of the fast sodium current [Fleidervish et al., 1996]. The M-type current[5] is mediated by KCNQ channels [Wang et al., 1998], which are slow non-inactivating voltage-gated potassium channels with a high threshold, i.e channels are mainly activated during spikes. The time scale of activation and deactivation is on the order of several tens of milliseconds. The M-type current slowly builds up in response to elevated spiking activity, which, as a potassium current, inhibits the neuron on a longer time scale and hence leads to adaptation. Spike-frequency adaptation is often related to the so-called afterhyperpolarization (AHP) current that causes a marked hyperpolarization following a current-induced burst of spikes [Madison and Nicoll, 1984]. The AHP current is a calcium-dependent potassium current. The intracellular calcium increases during spikes through the activation of voltage-dependent calcium channels and slowly decreases due to buffering, diffusion and calcium pumps [Benda and Herz, 2003]. Elevated spiking activity thus accumulates intracellular calcium on a longer time scale leading to adaptation through the inhibitory effect of the potassium current.

There has been much speculation about the role of spike frequency adaptation. In general, it is believed that adaptation enables a high sensitivity (gain) of a sensory system over a wide range of stimulus intensities [Koshland et al., 1982, Wark et al., 2007, Keener and Sneyd, 2008]. For instance, during the day the human retina can adapt to different levels of background light varying over more than 8 orders of magnitude [Hood and Finkelstein, 1986] due to numerous adaptation processes. Further roles that have been suggested for single neurons include forward masking (a strong stimulus can suppress subsequent stimuli) [Sobel and Tank, 1994, Wang, 1998, Liu and Wang, 2001], highpass-filtering of behaviorally relevant signals [Glantz and Schroeter, 2004, Benda et al., 2005, Benda and Hennig, 2008], selective response to looming stimuli (reacting to an object approaching on a collision course) [Gabbiani and Krapp, 2006, Peron and Gabbiani, 2009a,b], reducing low-frequency noise and increasing information transfer of slow stimuli ("noise shaping" due to negative serial correlations, see Sec. 1.2.7) [Chacron et al.,

[5]The name "M" derives from the toxin muscarine, which suppresses the M current.

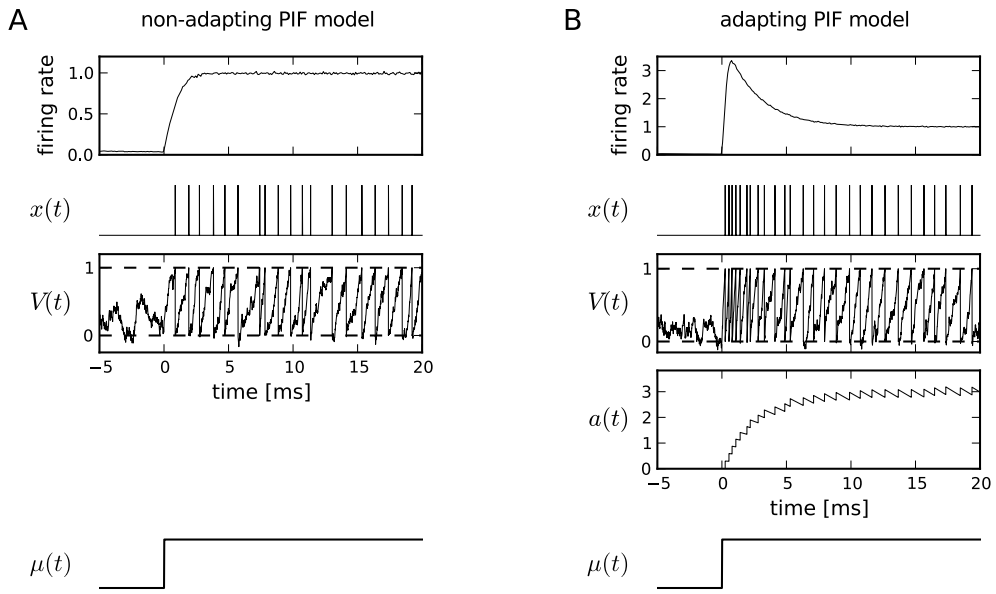

Figure 1.13.: Response of a PIF model to a step current in the absence (A) and presence (B) of an adaptation current. At time $t = 0$ the base current $\mu(t)$ is increased from $\mu_1 = 0$ to some finite value $\mu_2 > 0$ (bottom trace). A single realization in response to this current step is shown in the middle panels: **A** In the PIF model *without* adaptation current, Eq. (1.21), ($D = 0.5$, $\mu_2 = 10$) there is only one variable, the membrane potential $V(t)$, which generates the spike train $x(t)$. **B** A single realization of the PIF model *with* adaptation current, Eq. (1.77) ($\tilde{\Delta} = 3$, $\tau_a = 10$, $D = 0.5$, $\mu_2 = 40$, $D_a = 0$). The additional adaptation variable $a(t)$ shows the typical jump-and-decay dynamics of an adaptation current like the M current. The response averaged over many realizations of $x(t)$ yields the instantaneous firing rate $r(t)$. The adapting PIF model shows the typical transient response of spike-frequency adaptation, whereas the PIF model without adaptation current exhibits no adaptation.

2004b, Lindner et al., 2005a], enhancement of synchronization [Ermentrout et al., 2001, Ladenbauer et al., 2012] and control of network oscillations [van Vreeswijk and Hansel, 2001, Fuhrmann et al., 2002].

A simple model with adaptation

One-dimensional integrate-and-fire models do not feature spike-frequency adaptation, which is illustrated using the example of a PIF model in Fig. 1.13A. However, adaptation can be realized in integrate-and-fire models by including a second variable that mimics a spike-triggered adaptation current [Treves, 1993, Stemmler et al., 1995, Liu and Wang, 2001, Dayan and Abbott, 2005, Brette and Gerstner, 2005] or a dynamic threshold [Geisler and Goldberg, 1966, Chacron et al., 2000, 2003][6]. For instance, the PIF model, Eq. (1.21), can be equipped with an "adaptation current" $a(t)$, which typically reads

$$\dot{V} = \mu - a + \sqrt{2D}\xi(t) \tag{1.77a}$$

$$\tau_a \dot{a} = -a + \sqrt{2D_a}\xi_a(t). \tag{1.77b}$$

[6]For a comparison of models with an adaptation current versus models with a dynamic threshold see [Benda et al., 2010]

The dynamics is complemented by the rule

$$\text{if } V = V_{\text{th}}\text{:} \quad V \to V_{\text{r}} \quad \text{and} \quad a \to a + \Delta. \tag{1.78}$$

In other words, the adaptation current increases by a fixed amount Δ upon each spike and relaxes with a time constant τ_{a} in between spikes. Figure 1.13B reveals that this model shows indeed spike-frequency adaptation. Thus, in the following this model will be referred to as the *adapting PIF model*.

In Eq. (1.77), a white noise term $\xi_a(t)$ with intensity D_a has been included into the adaptation dynamics in order to account for a possible source of noise that is associated with the adaptation mechanism. In Chap. 3, we analyze the commonly considered case of a *deterministic adaptation current*, i.e. the noise term $\xi_a(t)$ is omitted ($D_a = 0$). In this case, negative serial correlations can be observed (Fig. 1.14A). Note the prevalence of short-long-short ISI sequences in the spike train, which cause anti-correlations. In contrast, the limit case, where the stochasticity is solely due to a *stochastic adaptation current*, i.e. where the noise intensity D is set to zero, is depicted in Fig. 1.14B. In this case, a peaked ISI density and positive serial correlations are observed, which resemble the previously discussed case of a colored-noise driven PIF model. I will show in Chap. 4 that channel noise associated with slow adaptation currents acts indeed as a source of colored noise.

1.4. Aim of the study

The thesis aims at a mathematical analysis of the stationary firing statistics of integrate-and-fire models that are driven by colored noise or are subject to an adaptation current. Both cases are important examples of non-renewal models, the theory of which is far less developed than for renewal integrate-and-fire models. Thus, a major goal of the present study is to contribute to the theory of non-renewal neuron models. To this end, I want to present various analytical approaches and approximation techniques, reveal common concepts and provide analytical expressions for measurable quantities like the serial correlation coefficient. Furthermore, I want to demonstrate that the ISI statistics can differ greatly between different non-renewal models. These models often leave a characteristic signature in the ISI statistics. Here, analytical expressions help to understand the mechanisms that lead to certain distinct statistical properties. It will be shown that such insights can be utilized to infer unknown physiological properties from experimentally measured spike trains. Specifically, a method will be proposed that allows to draw conclusions about the time scale of the noise that causes spike response variability on the basis of the ISI statistics. This method shall be applied to an auditory receptor neuron of a grasshopper to hypothesize the dominating source of spiking variability.

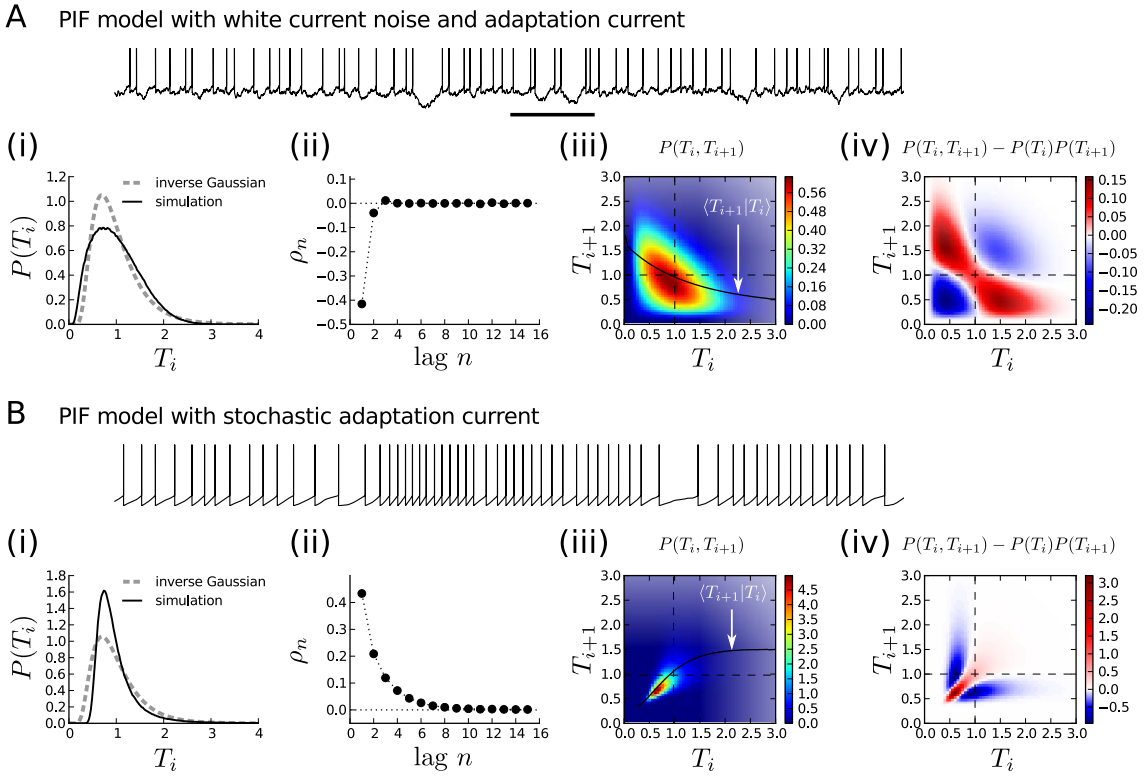

Figure 1.14.: Non-renewal spiking statistics due to an adaptation current. **A** PIF model with a fast deterministic adaptation current ($\Delta = 2$, $\tau_a = 2$, $D_a = 0$) and white current noise ($D = 0.356$). The ISI density is less peaked than an inverse Gaussian with the same mean and CV **(i)**. It possesses pronounced negative serial correlations at lag 1 **(ii)**, which is reflected in the negative slope of the conditional mean ISI **(iii)** and in the function δP **(iv)**: δP reveals a shortage of short-short and long-long pairs (T_i, T_{i+1}) (blue regions) and an excess of *short-long* and *long-short* pairs (red regions) as compared to the shuffled ISI sequence. This implies that subsequent ISIs are anti-correlated. The lack of short-short ISI pairs and the alternating pattern *short-long-short-long* is clearly visible in the spike trace (underlined by the black bar). **B** PIF model with a stochastic adaptation current ($\Delta = 0.4$, $\tau_a = 10$, $D_a = 9$) in the absence of fast fluctuations ($D = 0$). The ISI statistics is similar to that of a colored noise driven PIF model (cf. Fig. 1.7B): the ISI density is more peaked than the corresponding inverse Gaussian **(i)** and the serial correlations are positive **(ii),(iii)** due to an excess of short-short ISI pairs **(iv)**. In both cases **A** and **B**, the mean ISI and the CV were the same ($\langle T_i \rangle = 1$, $C_V = 0.5$).

Chapter 2.

The perfect integrate-and-fire model driven by colored noise

One of the simplest situations in which a spiking neuron model exhibits non-renewal firing statistics arises if the model is driven by an external input (stimulus or noise) as illustrated in Fig. 2.1. Of course, by the very nature of nerve cells as input-output devices, this situation should be relevant to virtually any neuron. External inputs usually possess temporal correlations unless the input is purely white noise, which is, however, a mathematical abstraction rather than physical reality. If the temporal correlations of the input extend over one or more interspike intervals, successive intervals become correlated. Such extended temporal correlations can arise for many reasons: For instance, natural stimuli are often broadband including components that are slower than the neurons spiking dynamics. Furthermore, presynaptic input, although often close to Poisson shot noise for cortical neurons in vivo (no correlations), is filtered by the synaptic dynamics. As a result, the input current is then endowed with temporal correlations, which have correlation times corresponding to the synaptic dynamics.

One may wonder whether the correlation structure of the stimulus or the noise can be preserved in the correlation structure of the neuronal output. More general, one might ask what is the statistics of the output spike train for a given input statistics. This question is crucial for understanding the spontaneous activity of neurons. To answer this question, I will focus on the statistics of the interspike interval (ISI) sequence generated by the stationary spiking activity of a model neuron. In particular, this concerns the probability density of ISIs, the associated coefficient of variation (CV), the skewness and the kurtosis, as well as the serial correlation coefficient (SCC) of the ISI sequence.

From another point of view, one could also ask the inverse question: Given the statistics of the neuronal output, what is the underlying statistics of the neuronal input? This question will be central in chapter 4 where the source of spiking variability of an auditory receptor neuron *in vivo* is inferred solely on the basis of the ISI statistics. In general, the inverse question is a complicated and unresolved problem because it requires a detailed characterization of the input-output relation of a highly nonlinear complex system. In particular, it is not clear whether this relation is unique. To solve the inverse problem, analytical formulas for the input-output relationship of simple model neurons can be of great benefit.

To characterize the relation between input and output statistics analytically, a perfect integrate-and-fire (PIF) model is considered in this chapter. This model is a minimal model of a strongly driven neuron, and has been already introduced as a working model in Sec. 1.1.3. Furthermore, the stimulus is assumed to be a Gaussian process with zero

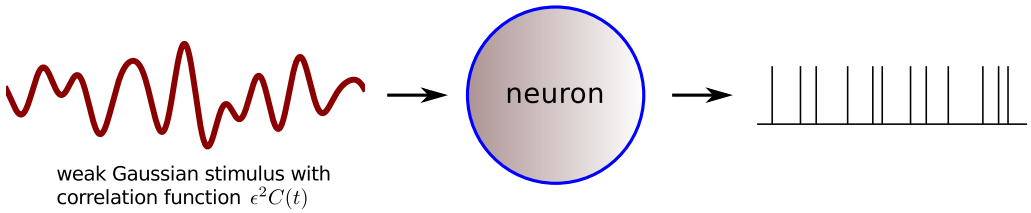

Figure 2.1.: Basic setup of this chapter. A perfect integrate-and-fire neuron model is driven by weak colored noise with correlation function $C(t)$ representing temporally-structured neural input. What is the statistics of the output spike train?

mean, which is completely determined by its correlation function (or equivalently its power spectrum). If the stimulus is not delta-correlated or white, the stimulus will be simply called *colored noise* in the following, irrespective of the actual origin of the input (signal or noise). An example of a colored noise statistics and the associated ISI statistics is shown in Fig. 2.2. The mathematical problem can be stated as follows: Given an arbitrary correlation function (or spectrum) of the colored noise, what is the ISI density, its CV, skewness and kurtosis and what are the serial correlations among ISIs? This question has been addressed in the literature for the special case of exponentially correlated noise (Ornstein-Uhlenbeck process) by Middleton et al. [2003], Lindner [2004a].

Here, I will generalize the theory of Lindner [2004a] to inputs modeled by an arbitrary multi-dimensional Ornstein-Uhlenbeck process (OUP). A projection of such an OUP onto some arbitrary direction can create a great manifold of Gaussian processes with a variety of power spectra. For instance, stochastic oscillations that have a pronounced peak in the power spectrum can be modeled already by a bivariate OUP, so-called harmonic noise [Schimansky-Geier and Zülicke, 1990]. For the rather broad class of input processes that can be modeled by a multivariate OUP, I will show in this chapter how the input correlation structure is transmitted into the statistics of the interspike intervals. One of the main results will be simple relations that connect the input correlation function with the statistics of the nth-order intervals (variance, skewness, probability density).

This chapter is organized as follows: First, the general theory for a PIF model driven by a d-dimensional OUP is presented. The calculation of the cumulants of the nth-order intervals involves the solution of the corresponding Fokker-Planck equation. This solution will be carried out using perturbation theory with respect to weak noise. The calculation of the leading order will be explained in Sec. 2.1.2 to illustrate the general idea of the applied method. The more technical computations of higher orders are presented separately in the appendix A.1. The result are general formulas for the nth-order variance and skewness as well as the serial correlation coefficient (Sec. 2.1.3). In addition to that, I will also put forward general formulas for the nth-order interval density, Sec. 2.1.4 and A.4, and the Fano factor for large time windows, Sec. 2.1.5. In Sec. 2.3 a PIF model driven by a superposition of independent, multivariate OUPs will be investigated.

As a special case, I will re-examine the one-dimensional OUP (Sec. 2.2), for which the analytical results of Lindner [2004a] are an excellent test case of the general theory. Moreover, this model allows to analyze the effect of the noise correlation time on the shape of the ISI density. The insights of this analysis will play an important role in Chap. 4. As a second special case, I investigate a PIF model that is driven by a superposition of independent noises in Sec. 2.3. Finally, I study the special case of a driving that consists of

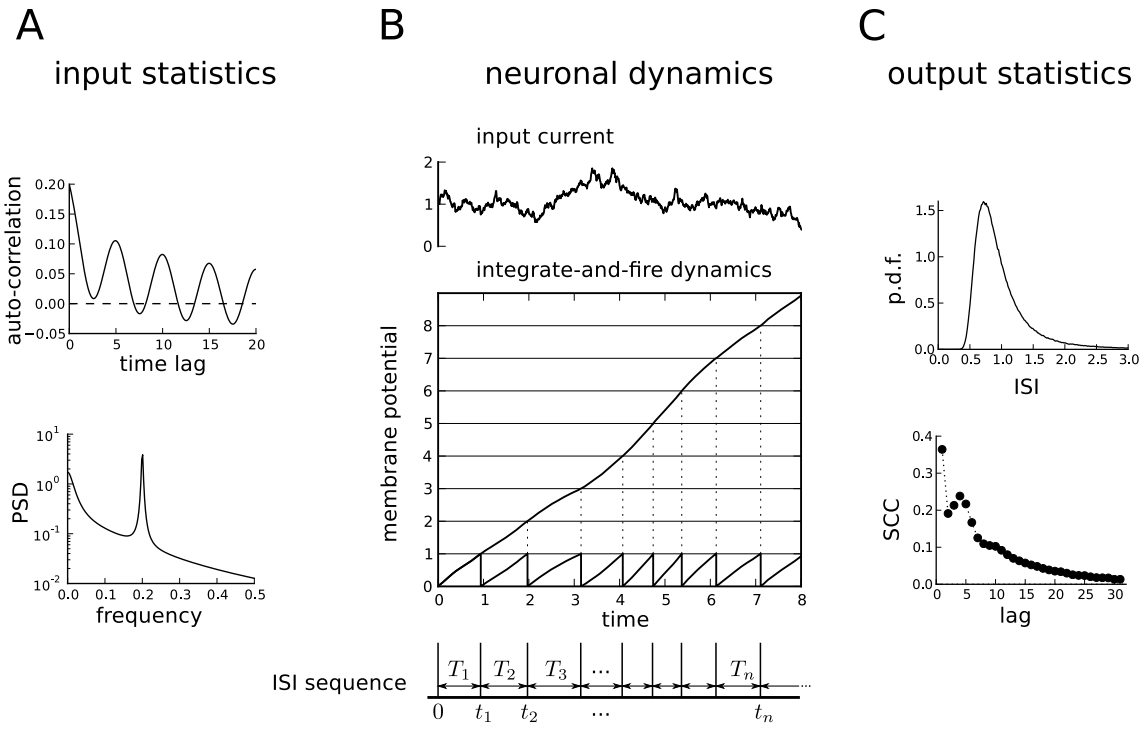

Figure 2.2.: Example of an input-output relationship. The stationary activity of a PIF neuron can be characterized by linking the statistics of the driving current ("input") with the PIF neuron's spiking statistics ("output"). **A** The input current is modeled by a Gaussian process with a given mean and auto-correlation function (or, equivalently a given power spectral density, PSD). **B** In the PIF model the input current is integrated until the membrane potential V hits the threshold $V_{\text{th}} = 1$, whereupon V is reset to zero. The n-th spike time is equivalent to the first time, when the trajectory crosses the threshold at $V = n$, in a setup where V is *not* reset. **C** The output statistics can be characterized by the ISI density and the serial correlation coefficients. The latter are related to the statistics of the n-th spike time (n-th-order interval) by Eq. (1.51). In the particular example, the input current was modeled as a superposition of two Ornstein-Uhlenbeck processes ($\tau_c = 1$ and $\tau_c = 10$) and harmonic noise (damped natural frequency $\Omega/(2\pi) = 0.2$, quality factor $Q = 50$) (for details, see Sec. 2.2 and 2.4).

harmonic noise and a one-dimensional OUP (Sec. 2.4). This model has been proposed as a simple model for electro-sensory afferents of paddlefish [Engel et al., 2009]. Due to the oscillatory nature of harmonic noise, the ISI patterns will be rather different compared to the case of a one-dimensional OUP.

2.1. General theory for the n-th order interval statistics

In general, the PIF model driven by a colored noise $\eta(t)$ may be written in the following form

$$\dot{V} = \mu + \epsilon\eta(t), \tag{2.1}$$

where V denotes the membrane potential, μ is a constant base current and ϵ is a small parameter that scales the noise intensity of $\eta(t)$. The colored noise is assumed to arise from a d-dimensional Ornstein-Uhlenbeck process $\mathbf{Y}(t)$ as the projection onto some projection vector $\mathbf{b}$: $\eta(t) = \mathbf{b} \cdot \mathbf{Y}(t)$. The Ornstein-Uhlenbeck process is defined by the Langevin

system

$$\dot{\mathbf{Y}} = \mathrm{A}\mathbf{Y} + \mathrm{B}\boldsymbol{\xi}(t), \tag{2.2}$$

where A and B are constant matrices that satisfy the following conditions: It is assumed that the deterministic dynamics

$$\dot{\mathbf{Y}} = \mathrm{A}\mathbf{Y} \tag{2.3}$$

has a stable equilibrium point at $\mathbf{Y} = 0$. This means that all eigenvalues of the so-called drift matrix A have negative real parts. Furthermore, the matrix B must be semi-definite, i.e. for any vector $\mathbf{a} \in \mathbb{R}^d$ it holds $\mathbf{a}^{\mathrm{T}}\mathrm{B}\mathbf{a} \geq 0$ (the operation $\mathbf{a}^{\mathrm{T}}$ denotes the transpose of $\mathbf{a}$). Finally, $\boldsymbol{\xi}(t) = (\xi_1(t), \ldots, \xi_d(t))^{\mathrm{T}}$ is a noise vector with components that satisfy $\langle \xi_i(t)\xi_j(t')\rangle = \delta_{i,j}\delta(t-t')$.

The model is augmented with a fire and reset rule: whenever $V = V_{\mathrm{th}}$ a spike is registered and the membrane potential is reset to $V = 0$. For the following calculations it is convenient to pass to a non-dimensional model by measuring voltage in units of V_{th} and time in units of the mean ISI V_{th}/μ. This corresponds to a transformation to the new quantities

$$X = \frac{V}{V_{\mathrm{th}}}, \qquad \hat{t} = \frac{\mu}{V_{\mathrm{th}}}t, \qquad \hat{\mathbf{b}} = \frac{\mathbf{b}}{\mu} \qquad \hat{\mathrm{A}} = \frac{V_{\mathrm{th}}}{\mu}\mathrm{A}, \qquad \hat{\mathrm{B}} = \sqrt{\frac{V_{\mathrm{th}}}{\mu}}\mathrm{B}. \tag{2.4}$$

This results in the non-dimensionalized Langevin equation

$$\dot{X} = 1 + \epsilon\mathbf{b}\mathbf{Y}, \tag{2.5a}$$

$$\dot{\mathbf{Y}} = \mathrm{A}\mathbf{Y} + \mathrm{B}\boldsymbol{\xi}(t), \tag{2.5b}$$

where the hats on top of the non-dimensional quantities have been omitted for notational simplicity. In this model the firing threshold has been transformed to unity. Hence, a spike is triggered if $X(t) = 1$, whereupon X is reset to zero. Throughout the following sections, the non-dimensional model Eq. (2.5) will be considered.

The statistics of the multivariate Ornstein-Uhlenbeck process $\mathbf{Y}(t)$ are well known, [see e.g. Risken, 1984]. In particular, the stationary auto-correlation function of the input noise $\eta(t) = \mathbf{b} \cdot \mathbf{Y}(t)$ is given by[1]

$$C(t) \equiv \langle \eta(t')\eta(t'+t)\rangle = \mathbf{b}^{\mathrm{T}} e^{t\mathrm{A}}\sigma\mathbf{b}. \tag{2.7}$$

Here, σ is the covariance matrix of the stationary Ornstein-Uhlenbeck process, which has the elements

$$\sigma_{ij} = \langle Y_i Y_j\rangle, \tag{2.8}$$

and $e^{t\mathrm{A}}$ denotes the matrix exponential defined by the series representation $e^{t\mathrm{A}} = \sum_{k=0}^{\infty} \frac{1}{k!}(t\mathrm{A})^k$.

[1] This relation can be obtained from the formal solution of Eq. (2.5b), which for $t > 0$ is [Risken, 1984]

$$\mathbf{Y}(t'+t) = e^{t\mathrm{A}}\mathbf{Y}(t') + \int_{t'}^{t'+t} \mathrm{d}t''\, e^{(t'+t-t'')\mathrm{A}}\mathrm{B}\boldsymbol{\xi}(t''). \tag{2.6}$$

Then in the ensemble averaged product $\langle \mathbf{Y}(t')\mathbf{Y}^{\mathrm{T}}(t'+t)\rangle$ the noise term vanishes and leaves $\langle \mathbf{Y}(t')\mathbf{Y}^{\mathrm{T}}(t'+t)\rangle = \sigma e^{t\mathrm{A}^{\mathrm{T}}}$.

The covariance matrix is connected to the drift matrix A and the diffusion matrix

$$\beta = \frac{1}{2}\mathrm{B}^{\mathrm{T}}\mathrm{B} \tag{2.9}$$

by the well-known relation [see e.g. Risken, 1984, van Kampen, 1992].

$$\mathrm{A}\sigma + \sigma\mathrm{A}^{\mathrm{T}} = -2\beta. \tag{2.10}$$

This relation represents a system of linear algebraic equations for the elements of the covariance matrix σ_{ij}.

The nth-order intervals are first-passage times. For the computation of the ISI statistics it is convenient to adopt the conditional ensemble, in which all realizations have a spike at the origin $t = 0$ (cf. Sec. 1.2.2 and Fig. 2.3). This corresponds to the initial condition $X(0) = 0$, which is the value of the trajectories immediately after the reset. In the conditional ensemble, the initial values $\mathbf{Y}(0)$ are distributed according to the noise-upon-firing density $P_{\mathrm{f}}(\mathbf{Y})$. This function is the stationary probability density associated with the sequence $\mathbf{Y}_i \equiv \mathbf{Y}(t_i)$ ($\mathbf{Y}(t)$ sampled at the spike times t_i). Let the index $i = 0$ be assigned to the spike at the origin, i.e. $t_0 = 0$. Then the spike time t_1 is equal to the first ISI T_1. Furthermore, in the conditional ensemble the probability density of t_1 and the ISI density (associated with a long ISI sequence) are equal. More generally, the n-th spike time t_n coincides with the first n-th order interval, i.e. the sum of the first n successive ISIs,

$$t_n = T_1 + \cdots + T_n. \tag{2.11}$$

In addition to that, the nth-order interval density (i.e. the p.d.f. of all sums of n successive ISIs of a long ISI sequence) equals the probability density of t_n:

$$P_n(t) = \langle \delta(t - t_n) \rangle. \tag{2.12}$$

The first ISI $T_1 = t_1$ is clearly the time when the trajectory reaches the threshold for the first time: $X(t_1) = 1$ and $X(t) < 1$ for $0 < t < t_1$. Thus, the calculation of the statistics of T_1 is a first-passage time (FPT) problem. In the PIF model, it turns out that higher-order interval statistics can be formulated as a FPT problem as well. To illustrate this point, it is useful to visualize the trajectory as the position of a particle that starts at $X(0) = 0$ and slides down an incline with stochastic velocity $\dot{X}(t) = 1 + \epsilon\mathbf{b} \cdot \mathbf{Y}(t)$ (Fig. 2.3A, upper panel). A passage of the threshold at $X = 1$ entails an instantaneous reset to $X = 0$, which closes one cycle or ISI. The nth-order interval t_n amounts to the duration of n subsequent cycles. In total the particle has to pass the net distance n because in each cycle the particle must pass from $X = 0$ to $X = 1$ (note that the whole path will be longer because the particle can also go backwards). The duration t_n can be precisely replicated in another scenario, where the particle is not reset but is allowed to slide down the incline beyond $X = 1$ (Fig. 2.3A, lower panel). Now, the time the particle needs to reach the point $X = n$ for the first time is exactly the same as before because the velocity $\dot{X}(t)$ is independent of the position X and is unaffected by the reset. Thus, the nth-order interval t_n is equal to the first-passage time of the particle on an extended incline with respect to the n-fold threshold $X = n$. As a consequence, the nth-order interval density is simply given by

the FPT density of a particle with a boundary at $X = n$ instead of a boundary at $X = 1$ [Lindner, 2004a].

2.1.1. Fokker-Planck equation

An alternative way to formulate the PIF model is based on its ensemble dynamics. In particular, consider an ensemble of trajectories that are generated by the Langevin dynamics Eq. (2.5). This ensemble can be described by the probability density $p(x, \mathbf{y}, t) = \langle \delta(X(t) - x)\delta(\mathbf{Y}(t) - \mathbf{y})\rangle$ to find a particular trajectory in the state $X(t) = x$ and $\mathbf{Y}(t) = y$ at time t. For the linear system, Eq. (2.5), $p(x, \mathbf{y}, t)$ obeys the Fokker-Planck equation (FPE)

$$\frac{\partial p}{\partial t} = -(1 + \epsilon \sum_{i=1}^{d} b_i y_i)\frac{\partial p}{\partial x} - \sum_{i,j=1}^{d} A_{ij}\frac{\partial}{\partial y_i}(y_j p) + \sum_{i,j=1}^{d} \beta_{ij}\frac{\partial^2 p}{\partial y_i \partial y_j}, \tag{2.13}$$

[see e.g. van Kampen, 1992]. This equation has the form of a continuity equation

$$\partial_t p + \partial_x J_x + \sum_{i=1}^{d} \frac{\partial J_i}{\partial y_i} = 0, \tag{2.14}$$

where the components of the probability current density $\mathbf{J} = (J_x, J_1, \ldots, J_d)^{\mathrm{T}}$ are identified as

$$J_x(x, \mathbf{y}, t) = (1 + \epsilon \mathbf{b} \cdot \mathbf{y})\, p(x, \mathbf{y}, t), \tag{2.15}$$

$$J_i(x, \mathbf{y}, t) = \sum_{j=1}^{d} \left(A_{ij} y_j - \beta_{ij}\frac{\partial}{\partial y_j} \right) p(x, \mathbf{y}, t), \qquad i = 1, \ldots, d. \tag{2.16}$$

In general, the probability density and current is defined on the whole $d + 1$-dimensional space. In many cases, however, the domain of solution will be restricted to the half-space of the form

$$\mathcal{V}_n = \left\{ (x, \mathbf{y}) \in \mathbb{R}^{d+1} \,\middle|\, x < n \right\} \tag{2.17}$$

for some integer n. These half-spaces are bordered by the respective hyperplanes

$$\Theta_n = \left\{ (x, \mathbf{y}) \in \mathbb{R}^{d+1} \,\middle|\, x = n \right\}. \tag{2.18}$$

In the following, these hyperplanes play the role of the nth-order threshold and the reset for $n \geq 1$ and $n = 0$, respectively.

Boundary conditions

The boundary conditions for the FPE depend on the specific question one is interested in. The main issues here are the position of the threshold, and hence the domain of solution, and whether trajectories are reinserted at the reset upon threshold crossings or not. In any case, the probability density and the probability current must vanish at infinitely distant boundaries (relative to the origin). These so-called natural boundary conditions can be written as

$$\lim_{x \to \pm\infty} p(x, \mathbf{y}, t) = 0 \tag{2.19}$$

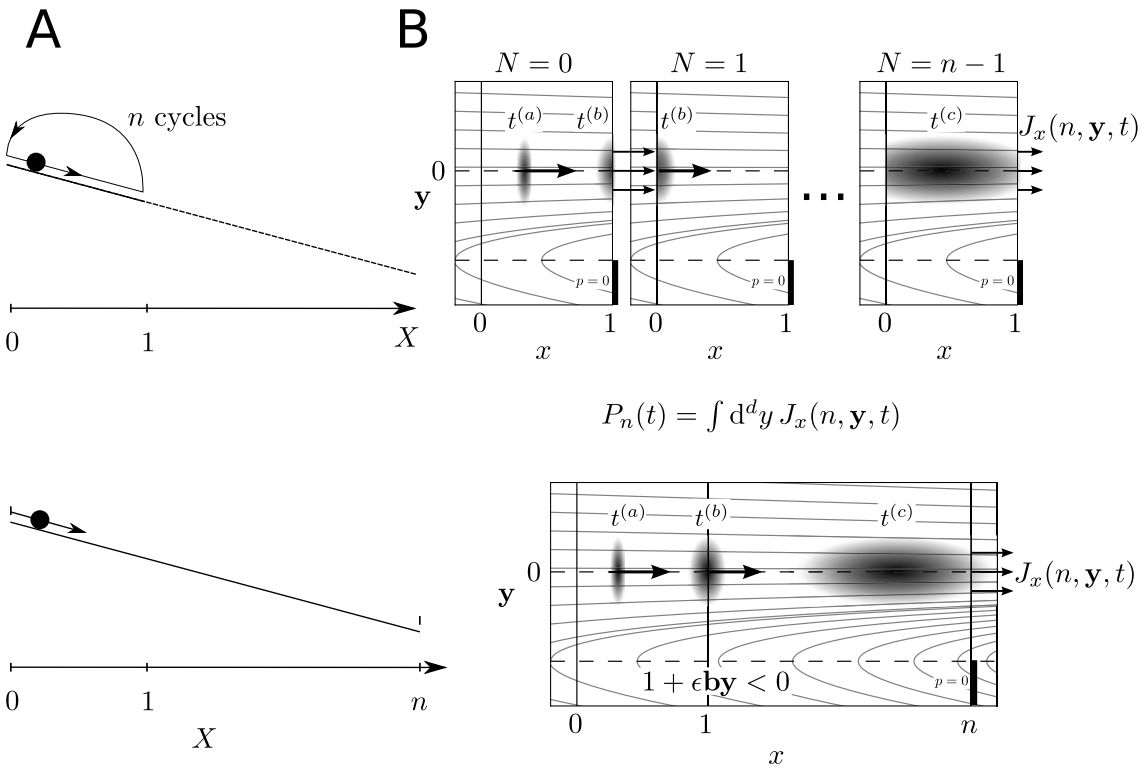

Figure 2.3.: Illustration of the nth-order interval statistics. **A** The PIF model can be interpreted as a particle sliding down an incline with instantaneous reset if $X = 1$. The nth-order interval t_n equals the duration of n cycles (upper panel). Equivalently, t_n is given by the passage from 0 to n without reset (lower panel). **B** The upper panel shows n copies of the phase space to count the number of spikes $N(t)$. The components of the vector $\mathbf{y}$ have been projected onto one coordinate for illustration purpose. The probability density $p(x, \mathbf{y}, t)$ is sketched for three different times $t^{(a)} < t^{(b)} < t^{(c)}$. At time $t^{(a)}$ no spike occurred with high probability (N=0), at time $t^{(b)}$ part of the trajectories have crossed the threshold at $x = 1$ and have been reinserted at $x = 0$, but with incremented spike count $N = 1$. At time $t^{(c)}$ most trajectories are about to cross the threshold for the n-th time. The integrated probability current in x direction at the threshold yields the probability density of t_n. The lower panel shows the extended phase space with a threshold at $x = n$. The hyperplane defined by $1 + \epsilon \mathbf{by} = 0$ is indicated by the lower dashed line. Below this line trajectories move backwards. Since trajectories are not allowed to cross the threshold with negative velocity, the probability density $p(x, \mathbf{y}, t)$ must be zero at the threshold $x = n$ as indicated by the thick black line.

and

$$\lim_{y_i \to \pm\infty} p(x, \mathbf{y}, t) = 0, \qquad \lim_{y_i \to \pm\infty} \frac{\partial}{\partial y_j} p(x, \mathbf{y}, t) = 0, \qquad i, j = 1, \ldots, d. \tag{2.20}$$

In order to obtain the nth-order interval statistics in the Fokker-Planck formalism, one generally needs to keep track of the spike count by an additional variable N as shown in Fig. 2.3B (upper panel). However, in the case of a PIF model, this rather complicated procedure is not necessary, because the nth-order interval is equivalent to the first passage time with respect to the boundary Θ_n (Fig. 2.3B, lower panel). A common approach to treat FPT problems in the ensemble picture, is to prevent trajectories from re-entering the domain $\mathcal{V}_n$ once they have crossed the boundary Θ_n for the first time. In particular, trajectories are not reinserted at the reset. In this way, the probability density integrated over the whole domain $\mathcal{V}_n$ declines and yields the probability that a trajectory has not yet reached the threshold. This so-called "survival probability" can then be related to the FPT density (see below). To prevent trajectories from recrossing the threshold, the probability current across the boundary Θ_n is required to be non-negative. Since this current is given by $J_x(n, \mathbf{y}, t) = (1 + \epsilon \mathbf{b} \cdot \mathbf{y}) p(x, \mathbf{y}, t)$, non-negativity implies the additional boundary condition

$$p(n, \mathbf{y}, t) = 0 \qquad \forall \mathbf{y} : 1 + \epsilon \mathbf{b} \cdot \mathbf{y} < 0 \tag{2.21}$$

(see also Brunel and Sergi [1998] for a similar situation). There are several ways to think of this condition, one of which is to take trajectories that approach the threshold from "above", i.e. with a negative velocity $\dot{X}(t) \equiv 1 + \epsilon \mathbf{b} \cdot \mathbf{Y} < 0$, out of the ensemble[2]. As a consequence, trajectories cannot be found right below the threshold with a negative velocity – this fact is expressed by the condition (2.21).

The boundary condition Eq. (2.21) renders the FPE hard to solve analytically, especially because it is inconveniently imposed on the half-hyperplane $1 + \epsilon \mathbf{b} \cdot \mathbf{y} < 0$. Fortunately, for sufficiently weak noise, i.e. for $\epsilon \ll 1$, the boundary condition is approximately satisfied by itself because the probability of $1 + \epsilon \mathbf{b} \cdot \mathbf{Y}$ being negative is vanishingly small (Fig. 2.3B). In the following, it will be therefore assumed that the variance of the colored noise is much smaller than unity, i.e.

$$\epsilon^2 \mathbf{b}^{\mathrm{T}} \sigma \mathbf{b} \ll 1. \tag{2.22}$$

Under this assumption, the boundary condition Eq. (2.21) that prevents recrossings can be safely ignored. This assumption is in line with the weak-noise perturbation ansatz used in this chapter, and hence, the boundary condition (2.21) will be disregarded in the following.

Initial conditions

As pointed out above, the natural ensemble for computing the interval statistics is the conditional ensemble. This ensemble is defined by the initial conditions of the trajectories: $X(0) = 0$ ("spike at $t = 0$") and $\mathbf{Y}(0)$ is randomly drawn from the noise-upon-firing

[2] This procedure causes a jump of the probability density and the probability current at the boundary from zero (below threshold) to some finite value (above threshold) for $1 + \epsilon \mathbf{b} \cdot \mathbf{y} < 0$ (thick line in Fig. 2.3B).

density $P_\mathrm{f}(\mathbf{Y})$. This implies the following initial probability density:

$$p(x, \mathbf{y}, 0) = \delta(x) P_\mathrm{f}(\mathbf{y}). \tag{2.23}$$

The noise-upon-firing density is the stationary probability density of the sequence $\{\mathbf{Y}_i = \mathbf{Y}(t_i)\}$:

$$P_\mathrm{f}(\mathbf{y}) = \lim_{k\to\infty} \langle \delta(\mathbf{Y}_k - \mathbf{y}) \rangle. \tag{2.24}$$

To determine $P_\mathrm{f}(\mathbf{y})$ let us for the moment return to the original model with threshold at $x = 1$ and *with* reset to $x = 0$. This corresponds to an absorbing boundary at $x = 1$ and a reinsertion of the out-flowing probability at the reset potential, such that the total probability in $\mathcal{V}_1$ is conserved. Following Lindner [2004a], this probability density can be related to the stationary probability density $p_s(x, \mathbf{y})$ of this model. In fact, consider the stationary probability current in x direction, $J_x^{(s)}(x, \mathbf{y}) = (1 + \epsilon \mathbf{b}\cdot\mathbf{y})\, p_s(x, \mathbf{y})$. The outflux of probability through the surface element $d\mathbf{S}(\mathbf{y})$ at the point $\mathbf{y}$ on the boundary Θ_1, is equal to $J_x^{(s)}(1, \mathbf{y})\mathrm{d}y_1 \cdots \mathrm{d}y_d$. In other words, $J_x^{(s)}(1, \mathbf{y})\mathrm{d}y_1 \cdots \mathrm{d}y_d$ is the fraction of trajectories that exit the domain $\mathcal{V}_1$ through the surface element $d\mathbf{S}(\mathbf{y})$ per unit time. This fraction must be proportional to the stationary probability density of $\mathbf{Y}$ upon firing:

$$P_\mathrm{f}(\mathbf{y}) \propto J_x^{(s)}(1, \mathbf{y}) = (1 + \epsilon \mathbf{b}\cdot\mathbf{y})\, p_s(1, \mathbf{y}). \tag{2.25}$$

Note that the factor of proportionality can be determined by a proper normalization of $P_\mathrm{f}(\mathbf{y})$.

The remaining problem consists in determining the stationary density $p_s(x, \mathbf{y})$. Strictly speaking, $p_s(x, \mathbf{y})$ is the stationary solution of the FPE (2.13) in the domain $\mathcal{V}_1$ with boundary conditions, Eq. (2.19), (2.20) and

$$p_s(0^+, \mathbf{y}) - p_s(0^-, \mathbf{y}) = p_s(1, \mathbf{y}) \tag{2.26}$$

$$p_s(1, \mathbf{y}) = 0 \qquad \forall \mathbf{y} : 1 + \epsilon \mathbf{b}\cdot\mathbf{y} < 0. \tag{2.27}$$

The first condition, Eq. (2.26), results from the reset of trajectories, which corresponds to a reinsertion of the probability current $J_x^{(s)}(1, \mathbf{y})$ at the reset Θ_0. This causes a jump of the probability current at $x = 0$: $J_x^{(s)}(0^+, \mathbf{y}) - J_x^{(s)}(0^-, \mathbf{y}) = J_x^{(s)}(1, \mathbf{y})$, which leads to the condition Eq. (2.26). The second condition, Eq. (2.27), is essentially the boundary condition (2.21) with $n = 1$, which prevents an influx of probability from above the threshold.

The exact stationary solution that satisfies the boundary conditions (2.26) and (2.27) is hard to obtain analytically. However, under the weak-noise assumption Eq. (2.22) the boundary conditions can be simplified as follows. In the case of weak noise, it is unlikely that $X(t)$ enters the region $x < 0$. As a necessary condition for this to occur, $\mathbf{Y}(t)$ would have to suffer a fluctuation to the region of negative velocities, $1 + \epsilon \mathbf{b}\cdot\mathbf{Y} < 0$ (Fig. 2.3B). However, such a fluctuation is rare by assumption (Eq. (2.22)). Thus, the probability density is practically restricted to the domain $0 \le x \le 1$, i.e. it is negligible outside this region. In addition to that, $p_s(0, \mathbf{y}) \approx 0$ for $1 + \epsilon \mathbf{b}\cdot\mathbf{y} < 0$. As a consequence, the boundary conditions (2.26) and (2.27) can be approximated by the periodic boundary condition $p_s(0, \mathbf{y}) = p_s(1, \mathbf{y})$. The stationary solution of the FPE (2.13) on the domain $0 \le x \le 1$ with periodic boundary condition is simple: It can be easily verified that the stationary probability density of $\mathbf{Y}$, $p_s(\mathbf{y})$, is a stationary solution of the FPE, for which the

periodic boundary condition in x is clearly satisfied. Furthermore, it is normalized with respect to the domain $0 \leq x \leq 1$, $\mathbf{y} \in \mathbf{R}^d$. The stationary density of $\mathbf{Y}$ is a multivariate Gaussian with covariance matrix σ, hence

$$p_s(x, \mathbf{y}) = p_s(\mathbf{y}) = \frac{1}{\sqrt{(2\pi)^d |\sigma|}} \exp\left(-\frac{1}{2}\mathbf{y}^{\mathrm{T}}\sigma^{-1}\mathbf{y}\right). \tag{2.28}$$

Finally, using Eq. (2.23) and (2.25) results in the initial condition

$$p(x, \mathbf{y}, 0) = \delta(x)\,(1 + \epsilon \mathbf{b}\cdot\mathbf{y})\,p_s(\mathbf{y}). \tag{2.29}$$

The n-th order interval density

Following Lindner [2004a], the nth-order interval density or, equivalently, the FPT density with respect to the boundary Θ_n can be obtained from the solution $p(x, \mathbf{y}, t)$ of the FPE with the natural boundary conditions (2.19),(2.20) and the initial condition (2.29). In fact, since trajectories are unlikely to re-enter the half-space $\mathcal{V}_n$, the probability that a given trajectory has not yet reached the threshold at time t is given by the so-called survivor function

$$S_n(t) = \int \mathrm{d}^d y \int_{-\infty}^{n} \mathrm{d}x\, p(x, \mathbf{y}, t). \tag{2.30}$$

The first-passage time density is then determined by the temporal change of the survivor function, $P_n(t) = -S_n'(t)$, or

$$P_n(t) = -\frac{\mathrm{d}}{\mathrm{d}t}\int \mathrm{d}^d y \int_{-\infty}^{n} \mathrm{d}x\, p(x, \mathbf{y}, t) = -\int \mathrm{d}^d y \int_{-\infty}^{n} \mathrm{d}x\, \partial_t p(x, \mathbf{y}, t). \tag{2.31}$$

Using the continuity equation (2.14) and taking into account that the currents vanish at infinity yields

$$P_n(t) = \int \mathrm{d}^d y\, J_x(n, \mathbf{y}, t) = \int \mathrm{d}^d y\,(1 + \epsilon \mathbf{b}^{\mathrm{T}}\mathbf{y}) p(n, \mathbf{y}, t). \tag{2.32}$$

2.1.2. The moment generating function of the n-th order interspike intervals

In the following, perturbation theory is used to calculate the moments of the n-th order intervals. A perturbation theory based on the probability density $P_n(t)$ is, however, singular, i.e. $P_n(t)$ cannot be expanded in powers of the small parameter ϵ. In fact, for $\epsilon = 0$, all trajectories have the initial conditions $x = 0$ and $\mathbf{y} = 0$, so that there is a sharp time of crossing the threshold at $x = n$. Specifically, $P_n(t) = \delta(t - n)$, i.e. the n-th order interval density exhibits a delta-singularity. This singularity is not removed by taking into account corrections due to a finite $\epsilon > 0$. However, a perturbation expansion of the Laplace transform

$$\bar{P}_n(s) = \int_0^\infty \mathrm{d}t\, e^{-st} P_n(t) \tag{2.33}$$

is not singular. For instance, for $\epsilon = 0$ the Laplace transform of the delta-shaped probability density becomes $\bar{P}_n^{(0)}(s) = \exp(-sn)$, which is a regular function. Therefore, in

order to find the corrections due to noise, $\bar{P}_n(s)$ is sought in the form

$$\bar{P}_n(s) = \bar{P}_n^{(0)}(s) + \epsilon \bar{P}_n^{(1)}(s) + \epsilon^2 \bar{P}_n^{(2)}(s) + \cdots . \tag{2.34}$$

If the noise is weak, it is sufficient to compute only the first few terms of this power series in ϵ.

Once an approximation for $\bar{P}_n(s)$ has been obtained, approximate expressions for the moments and cumulants of the n-th order intervals T_n can be derived in a straightforward manner. Indeed, the Laplace transform of the n-th order interval density can be interpreted as a moment generating function, in the sense that the k-th moment of T_n is given by

$$\langle T_n^k \rangle = (-1)^k \left. \frac{\mathrm{d}^k \bar{P}_n}{\mathrm{d}s^k} \right|_{s=0} . \tag{2.35}$$

Similarly, the logarithm of $\bar{P}_n(s)$ can be seen as the cumulant generating function because the k-th cumulant of T_n can be calculated by the formula [e.g. van Kampen, 1992]

$$\kappa_{k,n} = (-1)^k \left. \frac{\mathrm{d}^k \ln \bar{P}_n}{\mathrm{d}s^k} \right|_{s=0} . \tag{2.36}$$

In terms of the cumulants, the coefficient of variation and the serial correlation coefficient can be written as

$$C_V = \sqrt{\kappa_{2,1}} \tag{2.37}$$

and

$$\rho_n = \frac{\kappa_{2,n+1} - 2\kappa_{2,n} + \kappa_{2,n-1}}{2\kappa_{2,1}}, \tag{2.38}$$

respectively.

The moment generating function $\bar{P}_n(s)$ can be obtained from the solution of the Fokker-Planck equation $p(x, \mathbf{y}, t)$ via Eq. (2.32) and (2.33). However, it is not necessary to compute the probability density $p(x, \mathbf{y}, t)$ explicitly. Rather it is sufficient to calculate the transformed function

$$\varphi(x, \mathbf{k}, s) = \int_0^\infty \mathrm{d}t \, e^{-st} \int \mathrm{d}^d y \, e^{i\mathbf{k}\cdot\mathbf{y}} p(x, \mathbf{y}, t), \tag{2.39}$$

where $\mathbf{k}$ is a d-dimensional vector with elements k_i, $i = 1, \ldots, d$. Comparing this function with Eq. (2.32) and Eq. (2.33), the Laplace transform of the n-th order interval density can be generated from $\varphi(x, \mathbf{k}, s)$ as follows:

$$\bar{P}_n(s) = \left[\varphi - i\epsilon \mathbf{b} \cdot \nabla_{\mathbf{k}} \varphi \right]_{\mathbf{k}=0, x=n} . \tag{2.40}$$

Here, $\nabla_{\mathbf{k}} \varphi$ denotes the gradient of φ with respect to $\mathbf{k}$, i.e $\nabla_{\mathbf{k}} \varphi$ is a vector with elements $\partial_i \varphi \equiv \partial \varphi / \partial k_i$. On the other hand, φ satisfies the transformed equation

$$\begin{aligned} \partial_x \varphi - \mathbf{k}^{\mathrm{T}} \mathrm{A} \nabla_{\mathbf{k}} \varphi = &- \left(s + \mathbf{k}^{\mathrm{T}} \beta \mathbf{k} \right) \varphi + \delta(x) \exp\left(-\frac{\mathbf{k}^{\mathrm{T}} \sigma \mathbf{k}}{2} \right) \\ &+ i\epsilon \mathbf{b}^{\mathrm{T}} \left(\partial_x \nabla_{\mathbf{k}} \varphi + \delta(x) \sigma \mathbf{k} \exp\left(-\frac{\mathbf{k}^{\mathrm{T}} \sigma \mathbf{k}}{2} \right) \right), \end{aligned} \tag{2.41}$$

which results from a Fourier and Laplace transform of the Fokker-Planck equation[3].

Weak-noise expansion. Eq. (2.41) is a second-order partial differential equation, which is still difficult to solve because it contains the mixed derivative $\partial_x \nabla_{\mathbf{k}} \varphi$. In contrast to the Fokker-Planck equation (2.13), however, the zeroth-order solution of Eq. (2.41) (i.e. for $\epsilon = 0$) is not singular, but exhibits a finite jump at $x = 0$ (due to the delta function on the right hand side of Eq. (2.41)). Thus, I make the perturbation ansatz

$$\varphi = \varphi^{(0)} + \epsilon \varphi^{(1)} + \epsilon^2 \varphi^{(2)} + \cdots . \tag{2.42}$$

Substituting this ansatz into Eq. (2.41) and collecting like powers of ϵ results in the first-order partial differential equation

$$\partial_x \varphi^{(m)} - \mathbf{k}^{\mathrm{T}} \mathrm{A} \nabla_{\mathbf{k}} \varphi^{(m)} = -\left(s + \mathbf{k}^{\mathrm{T}} \beta \mathbf{k}\right) \varphi^{(m)} + I_m \tag{2.43}$$

with the inhomogeneities

$$I_0 = \delta(x) \exp\left(-\frac{\mathbf{k}^{\mathrm{T}} \sigma \mathbf{k}}{2}\right) \tag{2.44}$$

$$I_1 = i\mathbf{b}^{\mathrm{T}} \partial_x \nabla_{\mathbf{k}} \varphi^{(0)} + i\delta(x) \mathbf{b}^{\mathrm{T}} \sigma \mathbf{k} \exp\left(-\frac{\mathbf{k}^{\mathrm{T}} \sigma \mathbf{k}}{2}\right) \tag{2.45}$$

$$I_m = i\mathbf{b}^{\mathrm{T}} \partial_x \nabla_{\mathbf{k}} \varphi^{(m-1)}, \qquad m \geq 2. \tag{2.46}$$

Similarly, the coefficients $\bar{P}_n^{(m)}(s)$ of the moment generating function, Eq. (2.34), can be obtained by inserting the perturbation series into Eq. (2.40). This yields the relation

$$\bar{P}_n^{(m)}(s) = \left[\varphi^{(m)} - i\mathbf{b} \cdot \nabla_{\mathbf{k}} \varphi^{(m-1)}\right]_{\mathbf{k}=0, x=n} \tag{2.47}$$

for $m \geq 1$. In addition to that, the zeroth-order term is given by $\bar{P}_n^{(0)}(s) = \varphi^{(0)}(n, 0, s)$.

To solve Eq. (2.43) the method of characteristics is used. To this end, the variables x and $\mathbf{k}$ as well as the functions $\varphi^{(m)}$ are parametrized by a parameter τ and d initial constants c_i, $i = 1, \ldots, d$. The total derivative of $\varphi^{(m)}$ with respect to τ is $\mathrm{d}\varphi^{(m)}/\mathrm{d}\tau = \frac{\mathrm{d}x}{\mathrm{d}\tau} \partial_x \varphi^{(m)} + \sum_j \frac{\mathrm{d}k_j}{\mathrm{d}\tau} \partial_j \varphi^{(m)}$. Comparison with Eq. (2.43) reveals that a parametrization of the

[3] In fact, equation (2.41) can be derived by applying the transformation operator

$$\mathcal{F}: \qquad \mathcal{F}g(\mathbf{y}, t) = \int_0^\infty \mathrm{d}t\, e^{-st} \int \mathrm{d}^d y\, e^{i\mathbf{k}\cdot\mathbf{y}} g(\mathbf{y}, t),$$

to both sides of Eq. (2.13). The transformation of the time derivative $\partial_t p$ involves the Fourier transform of the initial probability density: $\mathcal{F}\partial_t p = s\varphi - \int \mathrm{d}^d y\, e^{i\mathbf{k}\cdot\mathbf{y}} p(x, \mathbf{y}, 0)$. Transforming Eq. (2.29) yields for the last term

$$\int \mathrm{d}^d y\, e^{i\mathbf{k}\cdot\mathbf{y}} p(x, \mathbf{y}, 0) = \delta(x) \exp\left(-\frac{\mathbf{k}^{\mathrm{T}} \sigma \mathbf{k}}{2}\right) \left(1 + i\epsilon \mathbf{b}^{\mathrm{T}} \sigma \mathbf{k}\right).$$

Using the relations $\mathcal{F}\{\mathbf{y}p\} = -i\nabla_{\mathbf{k}} \varphi$, $\mathcal{F}\{\frac{\partial}{\partial y_i}(y_j p)\} = -k_i \partial_j \varphi$ and $\mathcal{F}\{\partial^2 p / \partial y_i \partial y_j\} = -k_i k_j \varphi$ leads to Eq. (2.41).

solution can be obtained from the so-called characteristic equations

$$\frac{\mathrm{d}x}{\mathrm{d}\tau} = 1, \tag{2.48}$$

$$\frac{\mathrm{d}\mathbf{k}}{\mathrm{d}\tau} = -A^{\mathrm{T}}\mathbf{k}, \tag{2.49}$$

$$\frac{\mathrm{d}\varphi^{(m)}}{\mathrm{d}\tau} = -\left(s + \mathbf{k}^{\mathrm{T}}\beta\mathbf{k}\right)\varphi^{(m)} + I_m. \tag{2.50}$$

The first two equations can be easily integrated resulting in

$$x = \tau, \qquad \mathbf{k} = e^{-\tau A^{\mathrm{T}}}\mathbf{c}. \tag{2.51}$$

Here, A^{T} denotes the transpose of the matrix A and $e^{-\tau A^{\mathrm{T}}} = \left(e^{-\tau A}\right)^{\mathrm{T}}$ is the transpose of the matrix exponential $e^{-\tau A}$.

The further calculations are facilitated by making the ansatz

$$\varphi^{(m)}(\tau, \mathbf{c}) = \exp\left(-s\tau - \frac{1}{2}\mathbf{k}^{\mathrm{T}}\sigma\mathbf{k}\right)\psi^{(m)}(\tau, \mathbf{c}). \tag{2.52}$$

Substituting this ansatz into Eq. (2.50) yields the expression

$$\frac{\mathrm{d}\psi^{(m)}}{\mathrm{d}\tau} = -\left(\mathbf{k}^{\mathrm{T}}\beta\mathbf{k} - \frac{1}{2}\frac{\mathrm{d}}{\mathrm{d}\tau}(\mathbf{k}^{\mathrm{T}}\sigma\mathbf{k})\right)\psi^{(m)} + \hat{I}_m \tag{2.53}$$

where $\hat{I}_n = I_n \exp\left(s\tau + \frac{1}{2}\mathbf{k}^{\mathrm{T}}\sigma\mathbf{k}\right)$. These inhomogeneities can be expressed in terms of the lower-order functions $\psi^{(n-1)}$ as follows:

$$\hat{I}_0 = \delta(\tau), \tag{2.54}$$

$$\hat{I}_1 = i\mathbf{b}^{\mathrm{T}}\left[\partial_x\nabla_{\mathbf{k}}\psi^{(0)} - \sigma\mathbf{k}\partial_x\psi^{(0)} - s\left(\nabla_{\mathbf{k}}\psi^{(0)} - \sigma\mathbf{k}\psi^{(0)}\right) + \delta(\tau)\sigma\mathbf{k}\right] \tag{2.55}$$

$$\hat{I}_m = i\mathbf{b}^{\mathrm{T}}\left[\partial_x\nabla_{\mathbf{k}}\psi^{(m-1)} - \sigma\mathbf{k}\partial_x\psi^{(m-1)} - s\left(\nabla_{\mathbf{k}}\psi^{(m-1)} - \sigma\mathbf{k}\psi^{(m-1)}\right)\right], \quad m \geq 2. \tag{2.56}$$

Here, $\mathbf{k}$ has to be understood as $\mathbf{k}(\tau, \mathbf{c}) = e^{-\tau\mathrm{A}^{\mathrm{T}}}\mathbf{c}$ so that the inhomogeneities $\hat{I}_n$ are functions of τ and $\mathbf{c}$. The above ansatz simplifies equation (2.53) considerably because the prefactor in front of $\psi^{(m)}$ actually vanishes. In fact, using Eq. (2.49) the derivative contained in this prefactor can be carried out explicitly, yielding

$$\frac{\mathrm{d}}{\mathrm{d}\tau}(\mathbf{k}^{\mathrm{T}}\sigma\mathbf{k}) = \dot{\mathbf{k}}^{\mathrm{T}}\sigma\mathbf{k} + \mathbf{k}^{\mathrm{T}}\sigma\dot{\mathbf{k}} = -(\mathbf{k}^{\mathrm{T}}\mathrm{A}\sigma\mathbf{k} + \mathbf{k}^{\mathrm{T}}\sigma\mathrm{A}^{\mathrm{T}}\mathbf{k}) = -\mathbf{k}^{\mathrm{T}}(\mathrm{A}\sigma + \sigma\mathrm{A}^{\mathrm{T}})\mathbf{k} = 2\mathbf{k}^{\mathrm{T}}\beta\mathbf{k}. \tag{2.57}$$

In the last step, the relation (2.10) has been used. This results indeed in a cancellation of the first term of the right-hand-side of Eq. (2.53). As a result, $\psi^{(m)}$ can be easily integrated:

$$\psi^{(m)}(\tau, \mathbf{c}) = \int_{-\infty}^{\tau} \mathrm{d}\tau'\, \hat{I}_m(\tau', \mathbf{c}). \tag{2.58}$$

For $m = 0$, this formula yields

$$\psi^{(0)}(\tau, \mathbf{c}) = \theta(\tau), \tag{2.59}$$

where $\theta(\tau)$ denotes the Heaviside step function. For $m = 1$, the function $\hat{I}_1$ involves the derivatives of $\psi^{(0)}(\tau, \mathbf{c})$ with respect to x and $\mathbf{k}$. Because $\psi^{(0)} = \theta(\tau) = \theta(x)$ does not depend on $\mathbf{k}$, the derivatives are $\partial_x \psi^{(0)} = \delta(x)$ and $\nabla_{\mathbf{k}} \psi^{(0)} = 0$. Inserting these expressions into Eq. (2.55) results in

$$\psi^{(1)}(\tau, \mathbf{c}) = i\theta(\tau) s \int_0^\tau \mathrm{d}\tau_1 \, \mathbf{b}^{\mathrm{T}} \sigma e^{-\tau_1 \mathrm{A}^{\mathrm{T}}} \mathbf{c}. \tag{2.60}$$

In particular, setting $\mathbf{c} = 0$ reveals that the first-order correction $\psi^{(1)}$ and thus $\varphi^{(1)}$ vanishes for $\mathbf{k} = 0$ (recall that $\mathbf{k} = 0$ is equivalent to $\mathbf{c} = 0$). Furthermore, as shown in the appendix A.1, the gradient of $\psi^{(1)}$ with respect to $\mathbf{k}$ can be computed using the chain rule. The resulting expression is

$$(\nabla_{\mathbf{k}} \psi^{(1)})^{\mathrm{T}} = i\theta(t) s \int_0^\tau \mathrm{d}\tau_1 \, \mathbf{b}^{\mathrm{T}} \sigma e^{\tau_1 \mathrm{A}^{\mathrm{T}}}. \tag{2.61}$$

Moment generating function With these results it is already possible to calculate the moment generating function $\bar{P}_n(s)$ including the first correction due to noise. In fact, using Eq. (2.47) and (2.52), the perturbation terms $\bar{P}_n^{(m)}(s)$ can be computed directly from the functions $\psi^{(m)}(\tau, \mathbf{c})$:

$$\bar{P}_n^{(0)}(s) = e^{-sn} \, \psi^{(0)}\Big|_{\mathbf{c}=0, \tau=n} = e^{-sn} \tag{2.62}$$

and for $m \geq 1$

$$\bar{P}_n^{(m)}(s) = e^{-sn} \left[\psi^{(m)}(\tau, \mathbf{c}) - i\mathbf{b}^{\mathrm{T}} \nabla_{\mathbf{k}} \psi^{(m-1)}(\tau, \mathbf{c}) \right]_{\mathbf{c}=0, \tau=n}, \tag{2.63}$$

$$= -ise^{-sn} \int_0^n \mathrm{d}\tau_m \, \mathbf{b}^{\mathrm{T}} \nabla_{\mathbf{k}} \psi^{(m-1)}(\tau_m, \mathbf{c})\Big|_{\mathbf{c}=0}. \tag{2.64}$$

Because the gradient $\nabla_{\mathbf{k}} \psi^{(0)}$ vanishes for $\mathbf{c} = 0$, the first order perturbation term is

$$\bar{P}_n^{(1)}(s) = 0 \tag{2.65}$$

The first non-vanishing term is $\epsilon^2 \bar{P}_n^{(2)}(s)$, which can be obtained by using the expression for $\nabla_{\mathbf{k}} \psi^{(1)}$. Thus, together with the zeroth-order term the moment generating function reads

$$\bar{P}_n(s) = e^{-sn} \left(1 + \epsilon^2 s^2 \int_0^n \mathrm{d}\tau_2 \int_0^{\tau_2} \mathrm{d}\tau_1 \, C(\tau_1) + \mathcal{O}(\epsilon^4) \right), \tag{2.66}$$

where $C(t)$ is the correlation function of the noise as defined in Eq. (2.7).

Cumulants of the nth-order intervals The function $\bar{P}_n(s)$ can now be used to generate the cumulants of the nth-order intervals up to order ϵ^2 by means of Eq. (2.36). Evaluating the function $\bar{P}_n(s)$ at $s = 0$ recovers the correct normalization of the probability density $P_n(t)$: $\bar{P}_n(0) = \int_0^\infty \mathrm{d}t \, P_n(t) = 1$. Furthermore, taking the derivative with respect to s and setting $s = 0$ yields the first cumulant with a minus sign. This leads to the expected result $\langle t_n \rangle = n$ for the mean nth-order interval. In particular, for $n = 1$ one finds the mean ISI as $\langle T_i \rangle = 1$, as it should be. The second cumulant or variance of the n-th order interval

reads in leading order

$$\boxed{\kappa_{2,n} \equiv \mathrm{var}(t_n) = 2\epsilon^2 \int_0^n \mathrm{d}\tau_2 \int_0^{\tau_2} \mathrm{d}\tau_1\, C(\tau_1).} \tag{2.67}$$

This important formula will be extensively used in the following applications (Secs. 2.2 and 2.4). It relates the correlation function of the noise $C(t) = \mathbf{b}^{\mathrm{T}} \sigma e^{t\mathrm{A}^{\mathrm{T}}} \mathbf{b}$ with the variance of the nth-order interval, from which the leading order of the CV and the SCC can be calculated. Note that Eq. (2.67) has the same form as the variance of Brownian particle with bias if n and t_n are interpreted as time and position, respectively[4].

It can be seen from Eq. (2.66) that higher-order cumulants $\kappa_{m,n}$ of the nth-order intervals ($m \geq 3$) vanish up to order ϵ^2. To compute the leading order of the third cumulant $\kappa_{3,n}$ terms of order ϵ^4 in the perturbation expansion have to be taken into account. A detailed derivation of the next perturbation terms is presented in the appendix A.1. As a result, the leading-order can be expressed as a three-fold integral over the correlation function:

$$\kappa_{3,n} = 12\epsilon^4 \int_0^n \mathrm{d}\tau_3 \int_0^{\tau_3} \mathrm{d}\tau_2 \int_0^{\tau_2} \mathrm{d}\tau_1 \big[C(\tau_3-\tau_1)C(\tau_2) + C(\tau_1)C(\tau_3) + C(\tau_1)C(\tau_3-\tau_2)\big] + \mathcal{O}(\epsilon^6) \tag{2.68}$$

Note that unlike the variance, higher-order cumulants are in general non-linear functionals of the correlation function $C(t)$. As a consequence, the contributions of independent noises to the third cumulant do not simply add up linearly, as it is the case of the variance.

2.1.3. Coefficient of variation and serial correlation coefficient

If A is invertible, the integrals in Eq. (2.67) are simple and the n-th order variance can be written explicitly in terms of the drift matrix A and the covariance matrix σ:

$$\mathrm{var}(t_n) = 2\epsilon^2 \left(\mathbf{b}^{\mathrm{T}} \sigma \left(A^{\mathrm{T}}\right)^{-2} \left[e^{n\mathrm{A}^{\mathrm{T}}} - nA^{\mathrm{T}} - \mathbb{I}_d \right] \mathbf{b} \right). \tag{2.69}$$

In particular, for $n = 1$ we obtain the squared coefficient of variation of the ISIs:

$$C_{\mathrm{V}}^2 = 2\epsilon^2 \mathbf{b}^{\mathrm{T}} \sigma \left(A^{\mathrm{T}}\right)^{-2} \left[e^{\mathrm{A}^{\mathrm{T}}} - A^{\mathrm{T}} - \mathbb{I}_d \right] \mathbf{b}. \tag{2.70}$$

In practice, however, it is more convenient to compute the correlation function of the noise and use the integral formula (2.67).

The zeroth-order approximation of the SCC can be computed from the n-th order vari-

[4] Eq. (2.67) is closely related to the Kubo relation, according to which the effective diffusion coefficient $D_{\mathrm{eff}} = \frac{1}{2}\frac{\mathrm{d}}{\mathrm{d}t}\mathrm{var}(X(t))\Big|_{t\to\infty}$ of a Brownian particle is given by $D_{\mathrm{eff}} = \int_0^\infty \mathrm{d}\tau \, \left[\langle \dot{X}(t)\dot{X}(t+\tau)\rangle - \langle \dot{X}(t)\rangle^2\right]$. Indeed, if n is regarded as continuous time t and S_n is interpreted as the position $X(t)$, then differentiating Eq. (2.67) with respect to n yields for $n \to \infty$ on the one hand: $D_{\mathrm{eff}} = \epsilon^2 \int_0^\infty \mathrm{d}\tau\, C(\tau)$. On the other hand, the correlation function of the noise $\eta(t) = \mathbf{b} \cdot Y(t)$ is $C(\tau) = \epsilon^{-2}\left[\langle \dot{X}(t)\dot{X}(t+\tau)\rangle - \langle \dot{X}(t)\rangle^2\right]$, which recovers the Kubo relation.

ances by formula (1.51). Dividing the result by the squared CV, Eq. (2.70), yields

$$\rho_n = \frac{\mathbf{b}^{\mathrm{T}}\sigma\left(A^{\mathrm{T}}\right)^{-2}\left(\mathbb{I}_d - e^{\mathrm{A}^{\mathrm{T}}}\right)^2 e^{(n-1)\mathrm{A}^{\mathrm{T}}}\mathbf{b}}{2\mathbf{b}^{\mathrm{T}}\sigma\left(\mathrm{A}^{\mathrm{T}}\right)^{-2}\left[e^{\mathrm{A}^{\mathrm{T}}} - \mathrm{A}^{\mathrm{T}} - \mathbb{I}_d\right]\mathbf{b}}. \tag{2.71}$$

Thus, the SCC is essentially a superposition of exponential functions that decay for increasing lags n. The decay rates of the exponentials are given by the eigenvalues of the drift matrix A. Since these eigenvalues are negative by assumption, the SCC indeed vanishes in the limit $n \to \infty$, as it is required for any proper correlation function.

An important quantity is the sum of the SCCs over all lags, because according to Eq. (1.64) it characterizes the long-term variability of the spike count as expressed by the Fano factor. In fact, the Fano factor for infinitely large time windows, $F_\infty = \lim_{t\to\infty} F(t)$, is given by $F_\infty = C_{\mathrm{V}}^2\left(1 + 2\sum_{n=1}^{\infty}\rho_n\right)$, [see e.g. Cox and Lewis, 1966]. For the infinite sum of ρ_n, the formula $\sum_{n=1}^{\infty} e^{(n-1)\mathrm{A}^{\mathrm{T}}} = \left(\mathbb{I}_d - e^{\mathrm{A}^{\mathrm{T}}}\right)^{-1}$ for a geometric series can be used. Applying this to Eq. (2.71) leads to

$$\sum_{n=1}^{\infty}\rho_n = \frac{\mathbf{b}^{\mathrm{T}}\sigma\left(A^{\mathrm{T}}\right)^{-2}\left(\mathbb{I}_d - e^{\mathrm{A}^{\mathrm{T}}}\right)\mathbf{b}}{2\mathbf{b}^{\mathrm{T}}\sigma\left(\mathrm{A}^{\mathrm{T}}\right)^{-2}\left[e^{\mathrm{A}^{\mathrm{T}}} - \mathrm{A}^{\mathrm{T}} - \mathbb{I}_d\right]\mathbf{b}}. \tag{2.72}$$

Using the expression for the squared CV, Eq. (2.70), yields the long-time limit of the Fano factor:

$$F_\infty = -2\epsilon^2\mathbf{b}^{\mathrm{T}}\sigma\left(\mathrm{A}^{\mathrm{T}}\right)^{-1}\mathbf{b}. \tag{2.73}$$

2.1.4. The n-th order interval density

In the PIF neuron driven by white Gaussian noise, the ISIs are distributed according to the inverse Gaussian probability density, Eq. (1.68). What is the shape of the ISI density for a colored noise driving? This probability density function can be calculated analytically without resorting to perturbation theory. The only requirement is that the weak noise condition (2.22) is satisfied, so that boundary effects for negative "velocities" $\dot{X}$ can again be neglected. As shown in the appendix, Sec. A.2, this strategy results in the nth-order interval density

$$P_n(t) = \frac{1}{2\sqrt{4\pi\epsilon^2\gamma_1^3(t)}}\exp\left[-\frac{(t-n)^2}{4\epsilon^2\gamma_1(t)}\right]\left\{\frac{\left[(n-t)\gamma_2(t) + 2\gamma_1(t)\right]^2}{2\gamma_1(t)} - \epsilon^2\left[\gamma_2^2(t) - 2\gamma_1(t)C(t)\right]\right\}, \tag{2.74}$$

where

$$\gamma_1(t) = \int_0^t \mathrm{d}t'' \int_0^{t''} \mathrm{d}t'\, C(t') = \mathbf{b}^{\mathrm{T}}\sigma\left(A^{\mathrm{T}}\right)^{-2}\left[e^{t\mathrm{A}^{\mathrm{T}}} - tA^{\mathrm{T}} - \mathbb{I}_d\right]\mathbf{b}. \tag{2.75}$$

$$\gamma_2(t) = \int_0^t \mathrm{d}t' C(t') = \mathbf{b}^{\mathrm{T}}\sigma\mathrm{A}^{-1}\left(e^{t\mathrm{A}^{\mathrm{T}}} - \mathbb{I}_d\right)\mathbf{b}. \tag{2.76}$$

Expression (2.74) is exactly the same as that found by Lindner [2004a] for the case of a one-dimensional OUP. The only difference is a generalization of the functions $\gamma_1(t)$ and $\gamma_2(t)$ to arbitrary multivariate OUPs.

2.1.5. Long-time asymptotics of the Fano factor

The Fano factor is defined as the variance-to-mean ratio

$$F(t) = \frac{\langle \Delta N(t)^2 \rangle}{\langle N(t) \rangle}, \tag{2.77}$$

where $N(t)$ is the spike count of the stationary point process in the time window $[0, t]$. For the asymptotic behavior in the limit $t \to \infty$, the spike count can be replaced by the freely evolving Brownian motion on an incline $X(t)$ that starts at $X(0) = 0$, i.e. $X(t)$ is not reset upon threshold crossings. Although strictly speaking the initial value of X is uniformly distributed in the interval $[0, 1)$, the sharp initial condition $X(0) = 0$ is justified, because at large times the exact initial value becomes irrelevant. Thus, for large times it holds approximately

$$F(t) \approx \frac{\mathrm{var}(X(t))}{\langle X(t) \rangle}, \qquad t \gg 1. \tag{2.78}$$

Mean and variance of $X(t)$ can be computed from the characteristic function $\Theta(\omega, t) = \langle e^{i\omega X(t)} \rangle$ by

$$\langle X(t) \rangle = -i \frac{\mathrm{d}\Theta}{\mathrm{d}\omega}\bigg|_{\omega=0}, \qquad \mathrm{var}(X(t)) = -\frac{\mathrm{d}^2 \log \Theta}{\mathrm{d}\omega^2}\bigg|_{\omega=0}. \tag{2.79}$$

As shown in the appendix A.2, the characteristic function of $X(t)$ reads

$$\Theta(\omega, t) = \left[1 + i\epsilon^2 \omega \gamma_2(t)\right] \exp\left(i\omega t - \epsilon^2 \omega^2 \gamma_1(t)\right). \tag{2.80}$$

From this expression, mean and variance are generated as $\langle X(t) \rangle = t + \mathcal{O}(\epsilon^2)$ and $\mathrm{var}(X(t)) = 2\epsilon^2 \gamma_1(t) + \mathcal{O}(\epsilon^4)$, which results in the following expression for Fano factor:

$$F(t) = \frac{2\epsilon^2}{t} \int_0^t \mathrm{d}t_2 \int_0^{t_2} \mathrm{d}t_1 \, C(t_1) = 2\epsilon^2 \mathbf{b}^{\mathrm{T}} \sigma \left(\frac{(A^{\mathrm{T}})^{-2} \left[e^{tA^{\mathrm{T}}} - tA^{\mathrm{T}} - \mathbb{I}_d \right]}{t} \right) \mathbf{b}, \qquad t \gg 1. \tag{2.81}$$

In the long-time limit, the Fano factor saturates at

$$\lim_{t \to \infty} F(t) = -2\epsilon^2 \mathbf{b}^{\mathrm{T}} \sigma (\mathrm{A}^{\mathrm{T}})^{-1} \mathbf{b}. \tag{2.82}$$

This coincides precisely with the result found in Eq. (2.73).

2.2. The PIF model driven by exponentially correlated noise

In the following sections I will discuss particular examples in order to demonstrate how the general theory can be applied to specific models. In the simplest case, the PIF neuron is driven by only a single one-dimensional Ornstein-Uhlenbeck process. This case has been studied by Lindner [2004a], who derived several analytical expressions for the ISI statistics. Thus, the one-dimensional OUP can be used as a special case, for which the general theory can be tested. In addition to that, the known results are extended to higher-order cumulants of the ISIs such as the skewness and kurtosis. These measures

turn out to be useful to characterize the ISI distribution of a colored-noise driven PIF neuron as compared to the inverse Gaussian ISI statistics of a white-noise driven PIF neuron. In particular, the results of this section will be used extensively in Chap. 4, in order to access the dominating source of noise in an adapting sensory neuron.

In the case of a one-dimensional OUP, the dynamics of the subthreshold membrane potential $V(t')$ can be written in the form

$$\frac{\mathrm{d}V}{\mathrm{d}t'} = \mu + \eta \tag{2.83a}$$

$$\tau_c \frac{\mathrm{d}\eta}{\mathrm{d}t'} = -\eta + \sqrt{2D}\xi(t'), \tag{2.83b}$$

where μ is the base current, τ_c is the correlation time of the OUP $\eta(t')$ and D is the noise intensity. The firing threshold is at V_{th}: whenever V hits the threshold a spike is fired and V is reset to $V = 0$. First, the model can be transformed into a non-dimensional form by measuring time and voltage in units of V_{th}/μ and V_{th}, respectively. The dynamics for the corresponding non-dimensional variables $X = V/V_{\mathrm{th}}$, $\hat{\eta} = \eta/\mu$ in non-dimensional time $t = \mu t'/V_{\mathrm{th}}$ becomes

$$\dot{X} = 1 + \hat{\eta} \tag{2.84a}$$

$$\hat{\tau}\dot{\hat{\eta}} = -\hat{\eta} + \sqrt{2\hat{D}}\xi(t). \tag{2.84b}$$

The parameters of the model are the rescaled correlation time and noise intensity,

$$\hat{\tau} = \frac{\mu}{V_{\mathrm{th}}}\tau_c, \qquad \hat{D} = \frac{D}{\mu V_{\mathrm{th}}}, \tag{2.85}$$

respectively. In this scaling, the firing threshold is unity. As a final step, the non-dimensionalized model, Eq. (2.84), can be put into the general form Eq. (2.5), by rescaling the OUP $\hat{\eta}(t)$ by its standard deviation $\sqrt{\hat{D}/\hat{\tau}}$. The rescaled OUP, $Y = \sqrt{\frac{\hat{\tau}}{\hat{D}}}\hat{\eta}$, has unit variance. In terms of the rescaled variables, the PIF model can be finally written as

$$\dot{X} = 1 + \epsilon Y \tag{2.86}$$

$$\dot{Y} = -\frac{1}{\hat{\tau}}Y + \sqrt{\frac{2}{\hat{\tau}}}\xi(t) \tag{2.87}$$

with the weak-noise parameter

$$\epsilon = \sqrt{\frac{\hat{D}}{\hat{\tau}}} = \sqrt{\frac{D}{\tau_c \mu^2}}. \tag{2.88}$$

Comparing equation (2.86) with the general d-dimensional model, Eq. (2.5), one obtains the corresponding 1×1 "matrices" $\mathrm{A} = [-1/\hat{\tau}]$ and $\mathrm{B} = \left[\sqrt{2/\hat{\tau}}\right]$. This implies $\beta = 1/\hat{\tau}$ and, according to Eq. (2.10), $\sigma = 1$. The matrix exponentials become ordinary exponential functions. Finally, the one-dimensional projection "vector" $\mathbf{b}$ is equal to unity. Hence, the correlation function $C(t) \equiv \mathbf{b}^{\mathrm{T}}\sigma e^{t\mathrm{A}^{\mathrm{T}}}\mathbf{b}$ has the expected exponential

form

$$C(t) = \exp\left(-\frac{t}{\hat{\tau}}\right). \tag{2.89}$$

With the expression for the correlation function, the ISI density is immediately given by Eq. (2.74) with $n = 1$:

$$P(t) = \frac{1}{2\sqrt{4\pi\epsilon^2\gamma_1^3(t)}} \exp\left[-\frac{(t-1)^2}{4\epsilon^2\gamma_1(t)}\right] \left\{\frac{\left[(1-t)\gamma_2(t) + 2\gamma_1(t)\right]^2}{2\gamma_1(t)} - \epsilon^2\left[\gamma_2^2(t) - 2\gamma_1(t)C(t)\right]\right\},$$
$$\gamma_1(t) = \hat{\tau}^2\left(\frac{t}{\hat{\tau}} + e^{-t/\hat{\tau}} - 1\right), \qquad \gamma_2(t) = \hat{\tau}\left(1 - e^{-t/\hat{\tau}}\right). \tag{2.90}$$

This coincides precisely with the result of Lindner [2004a].

In the following, I am going to address the question of how a non-vanishing correlation time of the noise effects the statistics of interspike intervals. Furthermore, it is desirable to answer the inverse question: Given the statistics of interspike intervals (e.g. from an experimental recording), can we conclude about the color of the noise? This question will arise in Chap. 4, where the time scale of channel noise in an auditory receptor neuron will be inferred.

The limit of vanishing correlation time corresponds to a PIF neuron that is driven by Gaussian white noise. In this case, the ISIs are distributed according to the inverse Gaussian density,

$$P_{\mathrm{WN}}(t) = \frac{1}{\sqrt{4\pi\hat{D}t^3}} \exp\left[-\frac{(t-1)^2}{4\hat{D}t}\right]. \tag{2.91}$$

At fixed mean ISI, $\langle T\rangle = 1$, this probability density is uniquely determined by its coefficient of variation $C_{\mathrm{V}} = \sqrt{2\hat{D}}$. To access the influence of a finite correlation time in the case of colored noise, let us fix the CV while the correlation time $\hat{\tau}$ is varied. For a correlation time much smaller than the mean ISI ($0 < \hat{\tau} \ll 1$), the ISI density is still close to the inverse Gaussian density with the same mean and CV (Fig. 2.4). Note, the good agreement between simulation and the analytical approximation even for $\epsilon^2 = 1.3$. As shown below, this approximation converges indeed to the exact ISI density, the inverse Gaussian, in the white-noise limit. In contrast, for correlation times that are much larger than the mean ISI, the ISI density is much more peaked compared to the inverse Gaussian with equal mean and CV. Moreover, the ISI density exhibits a heavy tail that decays much slower than the exponential tail of the inverse Gaussian, Fig. (2.4)B.

The rescaled skewness and kurtosis To quantify the peaked shape and the heavy tail of the ISI density for large correlation times in comparison with an inverse Gaussian density with the same mean and CV, higher-order statistics beyond the variance are needed. To this end, consider the skewness and kurtosis of the ISIs, which can be computed from the third and fourth ISI cumulants by Eq. (1.42) and (1.43). For an inverse Gaussian the skewness is proportional to the CV and the kurtosis scales like the squared CV (cf. Eqs. (1.69) and (1.70)). This suggests to introduce rescaled versions of the skewness and the kurtosis that enable a direct comparison with the inverse Gaussian statistics as fol-

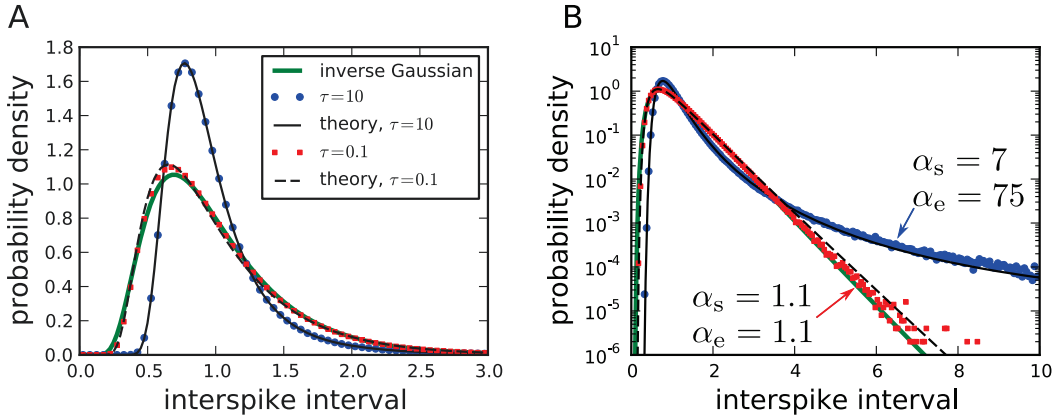

Figure 2.4.: ISI densities of a PIF neuron driven by a one-dimensional OUP. In all cases, the ISI densities have the same mean and variance ($C_V = 0.5$). **A** For a small correlation time, $\hat{\tau} = 0.1$ ($\hat{D} = 0.13$), the ISI density (red squares: simulation, dashed line: theory) is close to an inverse Gaussian density with the same CV (green solid line) corresponding to $\hat{\tau} = 0$. For larger correlation time ($\hat{\tau} = 10$, $\hat{D} = 1.33$), the ISI density is more peaked (simulation: blue circles, theory: black solid line). **B** Same as **A** but logarithmic y-axis, which reveals the exponential tail for small correlation time and the slow decay for large correlation time. The values of the skewness α_s and the kurtosis α_e as defined in Eq. (2.92) and (2.93) are indicated in the figure. For $\hat{\tau} = 0.1$ these values are close to unity which corresponds to an inverse Gaussian statistics, whereas for $\hat{\tau} = 10$ the skewness and kurtosis are much larger than for an inverse Gaussian.

lows:

$$\alpha_s = \frac{\gamma_s}{3C_V} = \frac{\kappa_1\kappa_3}{3\kappa_2^2} \tag{2.92}$$

and

$$\alpha_e = \frac{\gamma_e}{15C_V^2} = \frac{\kappa_1^2\kappa_4}{15\kappa_2^3}. \tag{2.93}$$

By defining the rescaled skewness and kurtosis in this manner, we obtain measures that are identical to unity for an inverse Gaussian ISI density. For larger (smaller) values, the ISI density is respectively more (less) skewed and more (less) peaked compared to an inverse Gaussian density. Table 2.1 presents the values of α_s and α_e for different ISI densities that are popular for modeling spike trains.

distribution	$P(t)$	$\langle T \rangle$	C_V	α_s	α_e
gamma	$\frac{\alpha(\alpha t)^{\alpha-1}}{\Gamma(\alpha)} e^{-\alpha t}$	1	$\alpha^{-1/2}$	$\frac{2}{3}$	$\frac{2}{5}$
inverse Gaussian	$\frac{1}{\sqrt{4\pi\hat{D}t^3}} \exp\left[-\frac{(t-1)^2}{4\hat{D}t}\right]$	1	$\sqrt{2\hat{D}}$	1	1
log-normal	$\frac{1}{t\sqrt{2\pi\sigma^2}} \exp\left[-\frac{\left(\ln(t)+\frac{\sigma^2}{2}\right)^2}{2\sigma^2}\right]$	1	$\sqrt{e^{\sigma^2}-1}$	$\frac{e^{\sigma^2}+2}{3}$	$\frac{e^{3\sigma^2}+3e^{2\sigma^2}+6e^{\sigma^2}+6}{15}$

Table 2.1.: Skewness α_s and kurtosis α_e for some common ISI probability densities. For the gamma distribution, the values of α_s and α_e are always smaller than unity, whereas for the log-normal distribution they are always larger than unity. Note that time is measured in units of the mean ISI.

The cumulants of the n-th order intervals can be readily obtained from the general

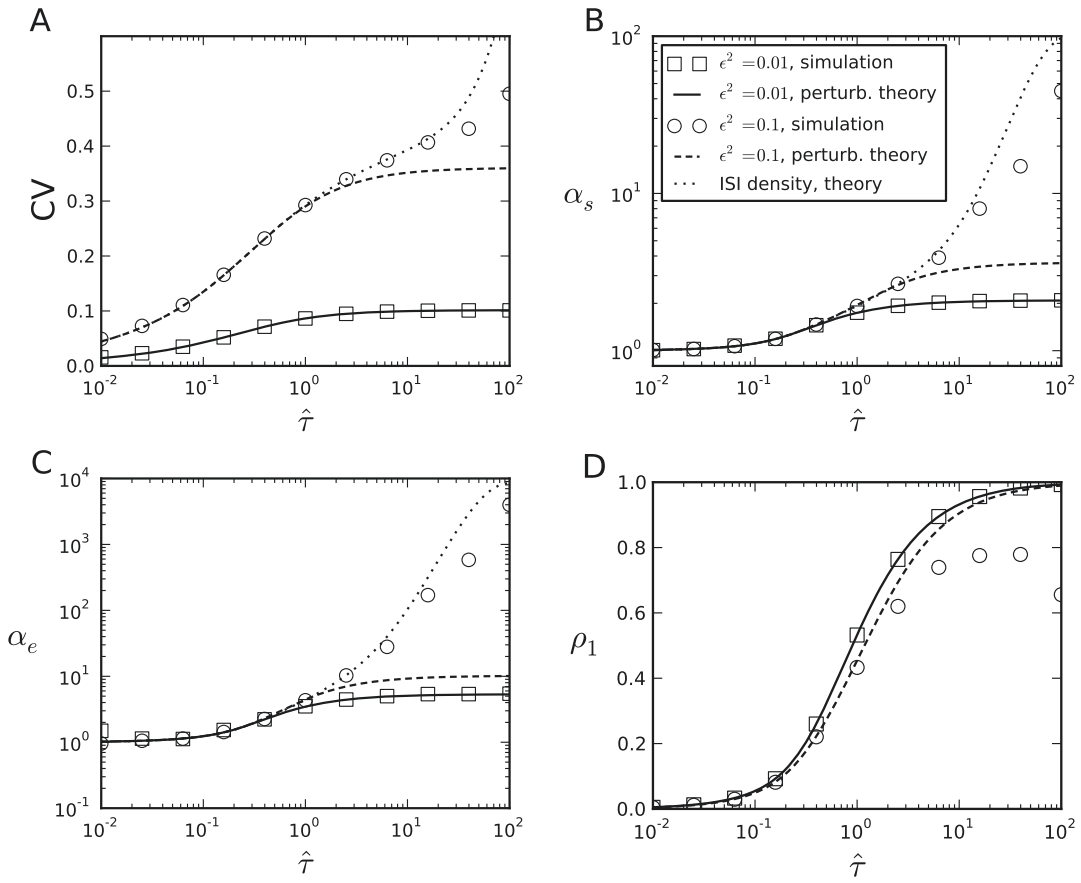

Figure 2.5.: ISI statistics of a PIF neuron driven by a one-dimensional OUP – dependence on the correlation time. The coefficient of variation **A**, the rescaled skewness α_s **B**, the rescaled kurtosis α_e **C** and the serial correlation coefficient at lag 1 **D** are depicted for $\epsilon^2 = 0.01$ (squares,solid line) and $\epsilon^2 = 0.1$ (circles, dashed and dotted line). The symbols represent simulation results, the solid and dashed lines show the result of the perturbation theory (Eq. (A.43) and Eq. (A.44) for α_s and α_e, respectively). The dotted lines show semi-analytical results obtained from a numerical integration of the ISI density, Eq. (2.74).

perturbation formulas in Sec. 2.1 and A:

$$\langle S_n \rangle = n, \tag{2.94}$$

$$\mathrm{var}(S_n) = 2\hat{\tau}^2 \left(\epsilon^2 K_{2,1} + \epsilon^4 K_{2,2} + \mathcal{O}(\epsilon^6) \right) \tag{2.95}$$

with

$$K_{2,1} = e^{-\frac{n}{\hat{\tau}}} + \frac{n}{\hat{\tau}} - 1 \tag{2.96a}$$

$$K_{2,2} = \frac{n}{\hat{\tau}} e^{-\frac{n}{\hat{\tau}}} + \left(1 - e^{-\frac{n}{\hat{\tau}}}\right)\left(1 - 2e^{-\frac{n}{\hat{\tau}}}\right). \tag{2.96b}$$

The case $n = 1$, recovers the squared coefficient of variation of the ISIs up to fourth order in ϵ that has been found in Lindner [2004a],

$$C_V^2 = \frac{2}{\theta}\left[\epsilon^2\left(1 - \frac{1 - e^{-\theta}}{\theta}\right) + \epsilon^4\left(e^{-\theta} + \frac{(1 - e^{-\theta})(1 - 2e^{-\theta})}{\theta}\right)\right], \tag{2.97}$$

where $\theta = 1/\hat{\tau}$. The CV increases monotonously with increasing $\hat{\tau}$ (Fig. 2.5A), which is consistent with similar findings in other studies [Schwalger and Schimansky-Geier, 2008]. Furthermore, the approximation based on perturbation theory captures the CV obtained from simulations rather well if the noise is sufficiently weak and the correlation time is not too large. The deviations found at large $\hat{\tau}$, seem to be mainly due to neglecting higher orders in the perturbation series rather than neglecting the reflecting boundary (see also the discussion below regarding the skewness).

The third and fourth cumulant as well as analytical formulas for the rescaled skewness (up to second-order) and kurtosis (up to first-order perturbation theory) are given in the appendix, Eq. (A.42). For the following discussion, however, let me consider only the leading-order term of the weak-noise expansion given by

$$\alpha_{\mathrm{s}}^{(0)} = \theta \frac{1 - e^{-\theta}}{\theta - 1 + e^{-\theta}} \tag{2.98}$$

and

$$\alpha_{\mathrm{e}}^{(0)} = \theta^2 \frac{7e^{-2\theta} + 2(\theta - 6)e^{-\theta} + 5}{5\left(\theta - 1 + e^{-\theta}\right)^2}. \tag{2.99}$$

Using these relations, it can be shown that in leading order, $\alpha_{\mathrm{s}} > 1$ and $\alpha_{\mathrm{e}} > 1$ and that both quantities converge to unity in the limit $\hat{\tau} \to 0$. For $\hat{\tau}$ much larger than the mean ISI, the leading orders saturate at $\alpha_{\mathrm{s}}^{(0)} = 2$ and $\alpha_{\mathrm{e}}^{(0)} = 24/5$. Thus, a finite correlation time of the Ornstein-Uhlenbeck noise results indeed in an ISI density that is more skewed and peaked than an inverse Gaussian density. This is also confirmed by simulations (Fig. 2.5B,C). For weak-noise, $\epsilon^2 = 0.01$, the perturbation theory agrees perfectly with simulations in a broad range of correlation times. For moderate noise, $\epsilon^2 = 0.1$, the theory saturates for large $\hat{\tau}$, while the rescaled skewness and kurtosis increase strongly. To test whether this deviation is due to neglecting higher-order terms in the perturbation series or due to boundary effects, the rescaled skewness and kurtosis were also computed numerically from the ISI density Eq. (2.74). The expression for the ISI density is exact to all orders in ϵ, provided that the effect of the reflecting boundary can be neglected. Put differently, the results obtained from computing the cumulants of the ISI density may be regarded as the full (i.e. infinite) perturbation series (if this series converges). Possible remaining deviations of this semi-analytic theory can then only be ascribed to boundary effects. Fig. 2.5A–C shows that the deviations at intermediate correlation times are indeed removed by the semi-analytic theory indicating that the deviations of the perturbation results are due to neglecting higher orders. At large $\hat{\tau}$, however, there is still a mismatch between simulations and semi-analytic theory. A closer inspection of this regime reveals that the approximation of the ISI density, Eq. (2.74), possesses negative parts (data not shown), which is in contradiction to the positivity of probability densities. Since in our approach the ISI density is approximated by the total probability flux across the threshold at time t, the negative values show that the number of trajectories crossing the threshold in the time interval $(t, t + \mathrm{d}t)$ from above is larger than the number of trajectories crossing the threshold from below; as a consequence the net flux is negative.

Finally, the SCC at lag n can be obtained from the nth-order variance, Eq. (2.94), by

means of the relation (1.51). As a result, I obtain

$$\rho_n = \frac{4\epsilon^2}{C_V^2\theta^2} e^{-n\theta} \left[\sinh^2\left(\frac{\theta}{2}\right) + \epsilon^2 \left(2e^{-n\theta}\sinh^2(\theta) + (n\theta - 3)\sinh^2\left(\frac{\theta}{2}\right) - \frac{\theta}{2}\sinh(\theta) \right) \right], \tag{2.100}$$

which is identical to the result of Lindner [2004a]. In leading order of ϵ the SCC decays exponentially with a decay "time" $\hat{\tau}$. In other words, the correlation structure of the input (exponential auto-correlation function with decay time $\hat{\tau}$) is conserved in the serial correlation structure of the ISIs. The exponential decay with respect to the lag has been extensively discussed elsewhere (Middleton et al. [2003], Lindner [2004a]).

The white-noise limit In many situations, input fluctuations of neurons are only shortly correlated in time. This concerns, for instance, synaptic background activity that is filtered through fast synapses, channel noise associated with fast ionic currents (e.g. sodium current) and thermal noise. In all these cases, the correlation time of the noise is much smaller than the typical interspike interval. A common approach to simplify the analysis of neuron models with rapid fluctuations is to approximate these fluctuations by white noise. In our model, this approximation would correspond to letting the correlation time of the Ornstein-Uhlenbeck process go to zero while keeping a constant noise intensity: $\hat{\tau} \to 0$, $\hat{D} = D/(V_{\text{th}}\mu) = \text{const.}$. The following problem arises with this limit: the variance $\epsilon^2 = \hat{D}/\hat{\tau}$ diverges, which clearly violates the assumption $\epsilon \ll 1$ of the theory. In particular, it is not clear to what extend the above formulas for the ISI statistics are valid for a PIF neuron driven by white-noise.

In contrast to the strict white-noise limit, one can assume a small, but non-vanishing correlation time $0 < \hat{\tau} \ll 1$. Then, the validity condition $\epsilon \ll 1$ can still be satisfied if the noise intensity is sufficiently small. Specifically, this requires $\hat{D} \ll \hat{\tau}$ and combining the conditions of small correlation time and small noise variance yields the range

$$\hat{D} \ll \hat{\tau} \ll 1. \tag{2.101}$$

The asymptotic behavior of the CV for $\hat{\tau} \ll 1$ can be obtained from Eq. (2.97). The resulting expression is

$$C_V \simeq \sqrt{2\hat{D}}, \qquad \hat{\tau} \ll 1, \tag{2.102}$$

which is the exact white noise limit even if $\hat{D}$ is not small. A similar phenomenon can be observed for the asymptotic behavior of the SCC, which is

$$\rho_n \simeq \frac{\hat{\tau}}{2}\delta_{n,1}, \qquad \hat{\tau} \ll 1. \tag{2.103}$$

In the limit $\hat{\tau} \to 0$ the SCC vanishes as expected for a PIF model driven by white noise. This is again correct even if $\hat{D}$ is not much smaller than $\hat{\tau}$; in fact, the expression (2.103) does not even depend on the noise intensity $\hat{D}$. For the ISI density, however, the formal limit

$$P_1(t) = \frac{1}{2}\left(\frac{(t+1)^2}{2t} - \hat{D} \right) P_{\text{WN}}(t), \qquad \hat{\tau} \to 0 \tag{2.104}$$

only reduces to the inverse Gaussian, Eq. (2.91), if the correct limit $\hat{\tau} \to 0$, $\hat{D} \ll \hat{\tau}$ (Eq. (2.101)) is performed. In this case, $P_{\text{WN}}(t)$ is strongly peaked about $\langle T \rangle = 1$. The

prefactor of $P_{\mathrm{WN}}(t)$ in Eq. (2.104), however, reduces to 1, if t is approximated by $\langle T \rangle = 1$, which recovers indeed the inverse Gaussian.

2.3. Superposition of independent Ornstein-Uhlenbeck processes

In many cases, fluctuations of the driving currents exhibit multiple time scales. For instance, neurons typically receive synaptic input through different populations of synapses, e.g. slow inhibitory synapses and fast excitatory synapses. Furthermore, channel noise might arise from both fast (e.g. sodium) channels and slow channels (e.g. adaptation channels). The simplest model that could account for noise with multiple time scales would be a superposition of *independent* noise processes with different time scales. How are the different inputs reflected in the output statistics and are they coded independently?

To answer these questions, suppose that the colored noise driving is a superposition of M independent Ornstein-Uhlenbeck processes $\mathbf{Y}_m(t)$, where $m = 1, \ldots, M$ and $0 < M \leq d$. Let d_m be the dimension of the process $\mathbf{Y}_m$, such that $d_1 + \cdots + d_M = d$. Each process is characterized by a $d_m \times d_m$ drift matrix A_m and a $d_m \times d_m$ matrix B_m. Then, the dynamical equation for the membrane potential may be written as

$$\dot{X} = 1 + \epsilon \left(\mathbf{b}_1^{\mathrm{T}} \mathbf{Y}_1 + \cdots + \mathbf{b}_M^{\mathrm{T}} \mathbf{Y}_M \right) \tag{2.105a}$$

$$\dot{\mathbf{Y}}_m = \mathrm{A}_m \mathbf{Y}_m + \mathrm{B}_m \boldsymbol{\xi}_m(t), \qquad m = 1, \ldots, M \tag{2.105b}$$

where the symbols $\mathbf{b}_m$ denote d_m-dimensional projection vectors. This scenario is a special case of the general model analyzed in the previous section. In fact, the system (2.105) can be represented in the general form (2.5) by introducing the stacked vectors $\mathbf{Y} = (\mathbf{Y}_1^{\mathrm{T}}, \ldots, \mathbf{Y}_M^{\mathrm{T}})^{\mathrm{T}}$ and $\mathbf{b} = (\mathbf{b}_1^{\mathrm{T}}, \ldots, \mathbf{b}_M^{\mathrm{T}})^{\mathrm{T}}$. Then, the total drift and noise strength matrices have the following block diagonal shape

$$\mathrm{A} = \begin{pmatrix} \mathrm{A}_1 & 0 & \cdots & 0 \\ 0 & \mathrm{A}_2 & \cdots & 0 \\ \vdots & \vdots & \ddots & \cdots \\ 0 & 0 & \cdots & \mathrm{A}_m \end{pmatrix}, \qquad \mathrm{B} = \begin{pmatrix} \mathrm{B}_1 & 0 & \cdots & 0 \\ 0 & \mathrm{B}_2 & \cdots & 0 \\ \vdots & \vdots & \ddots & \cdots \\ 0 & 0 & \cdots & \mathrm{B}_m \end{pmatrix}. \tag{2.106}$$

As a nice consequence, the matrix exponential $e^{t\mathrm{A}^{\mathrm{T}}}$ and the covariance matrix σ also have the same block diagonal shape. This also holds for the matrix product $\sigma e^{t\mathrm{A}^{\mathrm{T}}}$. Thus, the correlation function $C(t) = \mathbf{b}^{\mathrm{T}} \sigma e^{t\mathrm{A}^{\mathrm{T}}} \mathbf{b}$ decomposes into the sum of the individual correlation functions $C_m(t) = \mathbf{b}_m^{\mathrm{T}} \sigma e^{t\mathrm{A}_m^{\mathrm{T}}} \mathbf{b}_m$:

$$C(t) = C_1(t) + \cdots + C_M(t). \tag{2.107}$$

Note that this relation is exact to all orders of ϵ. Since the nth-order variance is in leading order of ϵ a linear functional of $C(t)$ (cf. Eq. (2.67)), the nth-order variance also decomposes into the sum of the individual nth-order variances. More precisely, let $\mathrm{var}(t_{n,m})$ denote the n-th order variance of a PIF model with drift $1 + \epsilon \mathbf{b}_m \cdot \mathbf{Y}_m$ for a specific inte-

ger m. Then, the nth-order variance resulting from the superposition of M independent Ornstein-Uhlenbeck processes is

$$\mathrm{var}(t_n) = \mathrm{var}(t_{n,1}) + \cdots + \mathrm{var}(t_{n,M}) + \mathcal{O}(\epsilon^4). \tag{2.108}$$

The additivity property also carries over to the covariance $\mathrm{cov}(T_i, T_{i+n})$ of the ISIs because according to Eq. (1.51) the covariance $\rho_n\langle\Delta T_i^2\rangle$ is linear in the nth-order variances. Hence,

$$\mathrm{cov}(T_i, T_{i+n}) = \sum_{m=1}^{M} \mathrm{cov}(T_{i,m}, T_{i+n,m}) + \mathcal{O}(\epsilon^4), \tag{2.109}$$

where $T_{i,m}$ denotes the ith ISI of a PIF model that is solely driven by the mth OUP. Similarly, the large-time Fano factor is the sum of the individual Fano factors,

$$F(t) = \sum_{m=1}^{M} F_m(t), \qquad t \gg 1, \tag{2.110}$$

because of the linearity of Eq. (2.81).

The additivity does not, however, apply to the serial correlation coefficients ρ_n because they are build as the ratio of covariance and variance. This ratio clearly cannot be decomposed into the sum of the individual SCCs. Moreover, Eq. (A.21) reveals that higher-order corrections of the n-th order variance are non-linear functionals of $C(t)$. Thus, the additivity property only holds for sufficiently weak noise.

2.3.1. The PIF model driven by multiple exponentially correlated noises

As a special case, let us consider a superposition of independent *one-dimensional* OUPs, i.e. $M = d$. In this case, the noises are exponentially correlated with correlation times $\hat{\tau}_i$, $i = 1, \ldots, d$. Furthermore, the drift matrix becomes strictly diagonal with the inverse correlation times on its diagonal: $\mathrm{A} = \mathrm{diag}(\hat{\tau}_1^{-1}, \ldots, \hat{\tau}_d^{-1})$. Similarly, the covariance matrix is diagonal with elements $\sigma_{ij} = \delta_{ij}$ (unit variances of the OUPs). Hence, the Langevin equation (2.105) can be written as

$$\dot{X} = 1 + \epsilon\,(b_1 Y_1 + \cdots + b_d Y_d) \tag{2.111a}$$

$$\dot{Y}_i = -\frac{1}{\hat{\tau}_i} Y_i + \sqrt{\frac{2}{\hat{\tau}_i}}\xi_i(t), \qquad i = 1, \ldots, d \tag{2.111b}$$

As illustrated in Fig. 2.6A, the input correlation function is comprised of exponentials:

$$C(t) = b_1^2 e^{-1/\hat{\tau}_1} + \cdots + b_d^2 e^{-1/\hat{\tau}_d}. \tag{2.112}$$

Correspondingly, the input power spectrum is a superposition of Lorentzians, $S(f) = S_1(f) + \cdots + S_d(f)$ with $S_i(f) = 2\hat{\tau}_i b_i^2 / \left[1 + (2\pi f \hat{\tau}_i)^2\right]$.

The diagonal form of the drift and covariance matrix simplifies the analytical results considerably because the matrix exponential can be computed easily. In particular, this

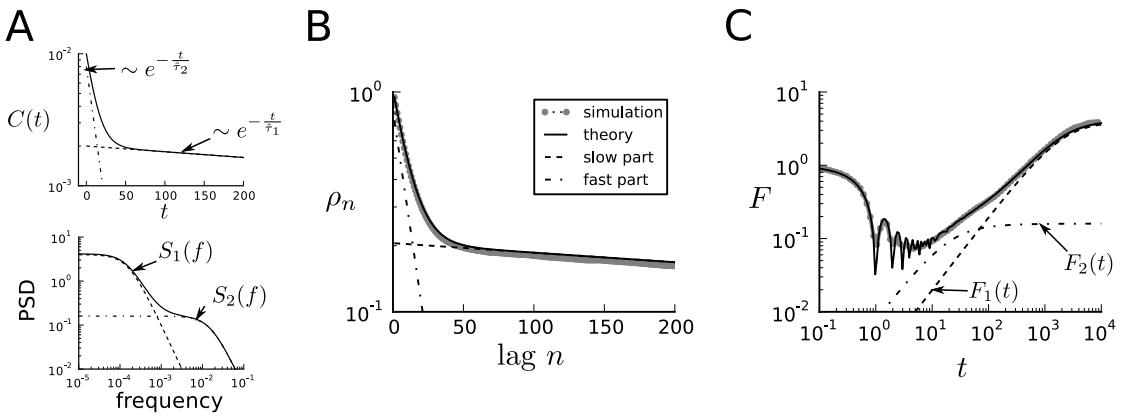

Figure 2.6.: PIF model driven by two exponentially correlated noises with different time scales. Input taken as a superposition of two one-dimensional Ornstein-Uhlenbeck processes with correlation times $\hat{\tau}_1 = 1000$ (slow part) and $\hat{\tau}_2 = 10$ (fast part). **A** The time scales are reflected in the input correlation function and power spectrum, which constitute a sum of the individual functions. Are these time scales also visible in the output statistics? **B** The serial correlation coefficient ρ_n (simulation: gray line, theory: black solid line) reveals two well-separated decays that correspond to correlation length $\hat{\tau}_1$ and $\hat{\tau}_2$, respectively. The two terms in the sum, Eq. (2.113), are drawn individually by dashed and dashed-dotted lines as indicated in the legend. **C** Fano factor as a function of the observation time t (simulations: gray line; theory, Eq. (2.116), black solid line). the individual terms of the large-time Fano factor formula, Eq. (2.114), are drawn by dashed and dashed-dotted lines as in **B**. The superposition of these terms yields a small shoulder between $t = \hat{\tau}_2$ and $t = \hat{\tau}_1$ in the large-time behavior. Parameter values: $\epsilon^2 = 0.01$, $b_1^2 = 0.2$, $b_2^2 = 0.8$

leads to an explicit expression for the SCC:

$$\rho_n = \frac{\sum_{i=1}^{d} b_i^2 \hat{\tau}_i^2 \left(1 - e^{-1/\hat{\tau}_i}\right)^2 \exp\left(-\frac{n-1}{\hat{\tau}_i}\right)}{2\sum_{i=1}^{d} b_i^2 \hat{\tau}_i^2 \left(e^{-1/\hat{\tau}_i} + \frac{1}{\hat{\tau}_i} - 1\right)} + \mathcal{O}(\epsilon^2). \tag{2.113}$$

The geometric decay with respect to the lag n is thus given by a superposition of exponentials with decay constants $\hat{\tau}_i$. Figure 2.6 shows the case, in which the PIF model is driven by two OUPs with well-separated correlation times. These time scales are clearly visible as two separate decays in the serial correlation coefficient (Fig. 2.6B).

Furthermore, using Eq. (2.81) and (2.112), Fano factor for large time windows becomes

$$F_{\text{large}}(t) = 2\epsilon^2 \sum_{i=1}^{d} b_i^2 \hat{\tau}_i^2 \left(\frac{1}{\hat{\tau}_i} - \frac{1 - e^{-t/\hat{\tau}_i}}{t}\right), \qquad t \gg 1. \tag{2.114}$$

For small time windows (smaller than the typical diffusion time), the spike train can be regarded as periodic. In this case, the Fano factor does not depend on the specific correlation function and the generic formula of Middleton et al. [2003] can be used. This formula reads

$$F_{\text{small}}(t) = \frac{\{t\}(1 - \{t\})}{t}, \tag{2.115}$$

where $\{t\} = t - \lfloor t \rfloor$ denotes the difference between t and the largest integer $\lfloor t \rfloor$ not greater than t, i.e. $\{t\}$ is a sawtooth function. A uniform approximation for the Fano factor can be obtained by adding the small and large time behavior [Middleton et al.,

2003], i.e.

$$F(t) \approx F_{\text{small}}(t) + F_{\text{large}}(t). \tag{2.116}$$

Figure 2.6C shows indeed an excellent agreement of this interpolation formula with the result of numerical simulations of a PIF model driven by two OUPs with different correlation times. In the large-time behavior, the Fano factor reveals a small shoulder that is due to the superposition of two individual Fano factors in Eq. (2.114) (cf. also the general relation Eq. (2.110)). Although this effect might not be significant, the superposition still causes a strong increase in the Fano factor over several orders of the observation time t. The presence of multiple time-scales in the noise driving neuronal variabitlity might thus explain the seemingly unbounded growth of the Fano factor in the experiment of Lowen and Teich [1992] (see Fig. 1.10).

2.4. PIF model driven by harmonic noise[5]

As a third example, I consider a PIF neuron that is driven by both Ornstein-Uhlenbeck noise and so-called harmonic noise [Schimansky-Geier and Zülicke, 1990]. The latter represents an underdamped harmonic oscillator driven by a Gaussian white noise force. In contrast to the monotonically decaying Lorentzian spectrum of an Ornstein-Uhlenbeck process, the salient feature of harmonic noise is a pronounced peak in the power spectrum at some characteristic frequency. Such kind of noise can serve as a simple model for a stochastic process that shows a clear periodic behavior albeit with a finite phase coherence. Examples of such stochastic oscillations in the nervous system are abundant, ranging from epithelial oscillations of sensory hair cells to gamma oscillations in the hippocampus.

The model considered in the following has been put forward to describe the activity of afferent neurons in the electro-sensory system of paddlefish [Engel et al., 2009]. These neurons are innervated by a number of sensory epithelia within a skin pore of the electro-sensory system [Neiman and Russell, 2004]. Each epithelium exhibits spontaneous oscillations of epithelial hair cells at a frequency of 26 Hz. As a result the afferent neuron receives an input current that can be described by a superposition of a large number of independent oscillating currents. This suggests to model the epithelial driving by a Gaussian process with a characteristic peak in the power spectrum [6].

The neuron model by Engel et al. [2009] is a PIF model, where the membrane potential V is driven by a constant base current μ and two kinds of noise, $\zeta(t)$ and $\varepsilon(t)$:

$$\dot{V} = \mu + \zeta + \varepsilon. \tag{2.117}$$

Here, $\zeta(t)$ represents the harmonic noise defined as an underdamped harmonic oscillator driven by white Gaussian noise,

$$\ddot{\zeta} + \gamma\dot{\zeta} + \omega_0^2\zeta = \sqrt{2D}\xi_\zeta(t'). \tag{2.118}$$

[5] Parts of this section have been studied together with Christoph Bauermeister [see also Bauermeister, 2012]. All calculations and simulations presented here, have been carried out by myself.

[6] The power spectrum of the epithelial oscillator also shows higher harmonics at multiples of 26 Hz [Neiman and Russell, 2004], which are neglected in the model.

In this equation, γ is the damping constant, ω_0 is the undamped angular frequency and D is the noise intensity. The system exhibits damped oscillations if $\omega_0 > \gamma/2$ ("underdamped regime"). Under this assumption, the harmonic noise has a peak in its power spectrum,

$$S_\zeta(\omega) = \frac{2D}{(\omega^2 - \omega_0^2)^2 + \gamma^2\omega^2}. \tag{2.119}$$

In addition to that, let $\varepsilon(t)$ be an Ornstein-Uhlenbeck noise that obeys the Langevin equation

$$\tau_c\dot{\varepsilon} = -\varepsilon + \sqrt{2D'}\xi_\varepsilon(t') \tag{2.120}$$

(cf. Eq. (2.83b)). This noise is included in the model to account for (fast) intrinsic fluctuations with an approximately Lorentzian spectrum $S_\varepsilon(\omega) = 2D'/(1+\omega^2\tau_c^2)$. This yields a better agreement with experimental data from paddlefish electro-sensory neurons [Bauermeister, 2012].

Following the general strategy, the model is first non-dimensionalized by measuring voltage in units of V_{th} and time in units of V_{th}/μ. This leads to the representation

$$\dot{X} = 1 + \hat{\varepsilon} + \hat{\zeta}, \tag{2.121}$$

$$\hat{\tau}\dot{\hat{\varepsilon}} = -\hat{\varepsilon} + \sqrt{2\hat{D}'}\xi_\varepsilon(t) \tag{2.122}$$

and

$$\ddot{\hat{\zeta}} + \hat{\gamma}\dot{\hat{\zeta}} + \hat{\omega}_0^2\hat{\zeta} = \sqrt{2\hat{D}}\xi_\zeta(t) \tag{2.123}$$

with the dimensionless variables

$$t = \frac{\mu}{V_{\text{th}}}t', \qquad X = \frac{V}{V_{\text{th}}}, \qquad \hat{\varepsilon} = \frac{\varepsilon}{\mu}, \qquad \hat{\zeta} = \frac{\zeta}{\mu}. \tag{2.124}$$

and dimensionless parameters

$$\hat{\tau} = \frac{\mu}{V_{\text{th}}}\tau, \qquad \hat{\gamma} = \frac{V_{\text{th}}}{\mu}\gamma, \qquad \hat{\omega}_0^2 = \frac{V_{\text{th}}^2}{\mu^2}\omega_0^2 \qquad \hat{D}' = \frac{D'}{V_{\text{th}}\mu} \qquad \hat{D} = \frac{V_{\text{th}}^3 D}{\mu^5}. \tag{2.125}$$

Furthermore, in these units the firing threshold is at $X = 1$. Note, that these parameters correspond to setting $\mu = 1$ and $V_{\text{th}} = 1$ in the original equations. Finally, the noise processes are renormalized by their respective standard deviation, so that the renormalized processes exhibit unit variance[7]. This results in a four-dimensional system of first-order

[7] The variances of the OU noise and the harmonic noise are given by $\langle\hat{\varepsilon}^2\rangle = \hat{D}'/\hat{\tau}$ and $\langle\hat{\zeta}^2\rangle = \hat{D}/(\hat{\gamma}\hat{\omega}_0^2)$, respectively. This suggests to introduce the variables

$$Y_1 = \sqrt{\frac{\hat{\tau}}{\hat{D}'}}\hat{\varepsilon}, \qquad Y_2 = \sqrt{\frac{\hat{\gamma}\hat{\omega}_0^2}{\hat{D}}}\hat{\zeta}, \qquad Y_3 = \dot{Y}_2 = \sqrt{\frac{\hat{\gamma}\hat{\omega}_0^2}{\hat{D}}}\frac{\mathrm{d}\hat{\zeta}}{\mathrm{d}t}, \tag{2.126}$$

where Y_1 and Y_2 have unit variance.

differential equations:

$$\dot{X} = 1 + \epsilon \left(bY_1 + \sqrt{1-b^2} Y_2 \right) \tag{2.127a}$$

$$\dot{Y}_1 = -\frac{1}{\hat{\tau}} Y_1 + \sqrt{\frac{2}{\hat{\tau}}} \xi_1(t) \tag{2.127b}$$

$$\dot{Y}_2 = Y_3 \tag{2.127c}$$

$$\dot{Y}_3 = -\hat{\gamma} Y_3 - \hat{\omega}_0^2 Y_2 + \sqrt{2\hat{\gamma}\hat{\omega}_0^2} \xi_3(t), \tag{2.127d}$$

where we changed from the noise intensities $\hat{D}$ and $\hat{D}'$ to the new parameters

$$\epsilon = \sqrt{\frac{\hat{D}}{\hat{\gamma}\hat{\omega}_0^2} + \frac{\hat{D}'}{\hat{\tau}}} = \frac{1}{\mu} \sqrt{\frac{D}{\gamma\omega_0^2} + \frac{D'}{\tau_c}}, \qquad b = \sqrt{\frac{\hat{\tau}\hat{D}}{\hat{\tau}\hat{D} + \hat{\gamma}\hat{\omega}_0^2 \hat{D}'}} = \sqrt{\frac{\tau D}{\tau D + \gamma\omega_0^2 D'}} \tag{2.128}$$

Because Y_1 and Y_2 have unit variance, the variance of the noise $\eta = bY_1 + \sqrt{1-b^2} Y_2$ is also unity. The dimensionless quantity ϵ has the role of a weak noise parameter that depends on both noise intensities $\hat{D}$ and $\hat{D}'$ of harmonic noise and OU noise, respectively. The dimensionless parameter $b \in [0, 1]$ weights the contribution of the two types of noise. In particular, $b = 0$ corresponds to a PIF model that is solely driven by harmonic noise, whereas $b = 1$ yields the special case that has been analyzed in Sec. 2.2, i.e. a PIF model driven by exponentially correlated noise. The weak-noise limit $\epsilon \to 0$, can be achieved if $\hat{D}$ and $\hat{D}'$ both scale like ϵ^2.

In the following, only the (more interesting) case $\hat{\omega}_0 > \hat{\gamma}/2$ is considered, in which the noiseless dynamics of $Y_2(t)$ exhibits damped oscillations (the so-called underdamped case). This regime corresponds to a stable focus at the origin of the phase plane spanned by the variables Y_2 and $Y_3 = \dot{Y}_2$. Furthermore, for the validity of the weak-noise perturbation theory it is assumed that the total standard deviation of the noise driving is much smaller than the deterministic driving force. Since the standard deviation of the total noise is ϵ, it must be required that

$$\epsilon \ll 1. \tag{2.129}$$

Our model (2.127) has the form of the general system (2.5) by choosing A and B as the following 3×3 matrices:

$$\mathrm{A} = \begin{pmatrix} -\frac{1}{\hat{\tau}} & 0 & 0 \\ 0 & 0 & 1 \\ 0 & -\hat{\omega}_0^2 & -\hat{\gamma} \end{pmatrix}, \qquad \mathrm{B} = \begin{pmatrix} \sqrt{\frac{2}{\hat{\tau}}} & 0 & 0 \\ 0 & 0 & 0 \\ 0 & 0 & \sqrt{2\hat{\gamma}\hat{\omega}_0^2} \end{pmatrix}. \tag{2.130}$$

Furthermore, the projection vector must be chosen as $\mathbf{b}^{\mathrm{T}} = \left(b, \sqrt{1-b^2}, 0 \right)$. As shown in the appendix A.4, this yields the following correlation function of the input noise [see also Chandrasekhar, 1943, Wang and Uhlenbeck, 1945, Schimansky-Geier and Zülicke, 1990],

$$C(t) = b^2 e^{-\frac{t}{\hat{\tau}}} + (1-b^2) e^{-\frac{\hat{\gamma}}{2}t} \left(\cos \Omega t + \frac{\hat{\gamma}}{2\Omega} \sin \Omega t \right), \tag{2.131}$$

where

$$\Omega = \sqrt{\hat{\omega}_0^2 - \frac{\hat{\gamma}^2}{4}} \tag{2.132}$$

denotes the damped natural frequency of the oscillator. Using the general relation between correlation function and nth-order variance, Eq. (2.67), yields the leading order of the squared CV (see Sec. A.4, Eq. (A.56)). For small correlation times of the OUP, $\hat{\tau} \ll 1$, the resulting expression reduces to

$$C_V^2 = 2\hat{D}' + \frac{2\hat{D}}{\hat{\gamma}\hat{\omega}_0^4}\left[1 - \frac{\hat{\gamma}^2}{\hat{\omega}_0^2} + \gamma - \frac{a_1 \sin(\Omega) + a_2 \cos(\Omega)}{4\Omega\hat{\omega}_0^2} \exp\left(-\frac{\hat{\gamma}}{2}\right)\right]. \tag{2.133}$$

where

$$a_1 = \frac{\hat{\gamma}}{2}\left(12\Omega^2 - \hat{\gamma}^2\right), \qquad a_2 = \Omega\left(4\Omega^2 - 3\hat{\gamma}^2\right).$$

Here, it is assumed that the noise intensity is sufficiently small, $\hat{D}' \ll \hat{\tau}$, so that ϵ is still a small parameter (cf. discussion at the end of Sec. 2.2). Eq. (2.133) shows that the effect of the OU noise consists simply in an additive increase of the ISI variance. The effect of the harmonic noise on the ISI variability sensitively depends on the ratio of the frequency $\Omega/(2\pi)$ of the damped harmonic oscillations and the firing frequency. Note that the latter is unity in our scaling (time is measured in units of the mean ISI). Figure 2.7A shows an oscillating behavior of the CV as a function of Ω as predicted by the theory, Eq. (2.133) [see also Bauermeister, 2012]. The maxima and minima can be understood as follows: For a high quality factor of the harmonic noise, i.e. for $\Omega/\hat{\gamma} \gg 1$, the sine term can be neglected against the cosine term in Eq. (2.133) because $a_1 \ll a_2$. Hence, the CV has minima at integral values of $\Omega/(2\pi)$ and maxima if $\Omega/(2\pi)$ is an odd multiple of $\frac{1}{2}$. This makes sense because for an integral ratio of damped oscillation frequency and firing frequency, spikes occur close to the maxima of the (almost) periodic driving because the instantaneous firing rate (i.e. the probability to spike) is roughly proportional to the periodic stimulus. This leads to a rather regular firing pattern. In contrast, if the mean ISI is an odd multiple of half of the driving period, then a spike at the crest of the harmonic driving is followed on average by a spike in the trough of the harmonic driving, which in turn is succeeded by a spike at the crest. If such a pattern was regular, the firing rate would not be proportional to the harmonic drive; in particular, the probability to fire close to the maxima would be the same as the probability to fire close to the minima of the driving. Thus, it can be concluded that the spike train cannot be as regular as for the case when the mean ISI is a multiple of the driving period.

Another non-trivial effect of the harmonic noise can be observed for the skewness of the ISI density (Fig. 2.7B). Depending on the frequency of the harmonic driving, the ISI density can be skewed to the left or to the right, in particular the skewness oscillates as a function of Ω. This behavior of the skewness is also predicted by the theory. As shown in Sec. A.4, the rescaled skewness can be calculated by using higher-order perturbation theory. The calculations for the general case of OU noise and harmonic noise are rather cumbersome. However, to capture the principal effect of harmonic noise on the ISI skewness, it is sufficient to consider a purely harmonic noise and disregard the OU noise. This simplification corresponds to setting $b = 0$ (or $\hat{D}' = 0$). In this case, the zeroth-order

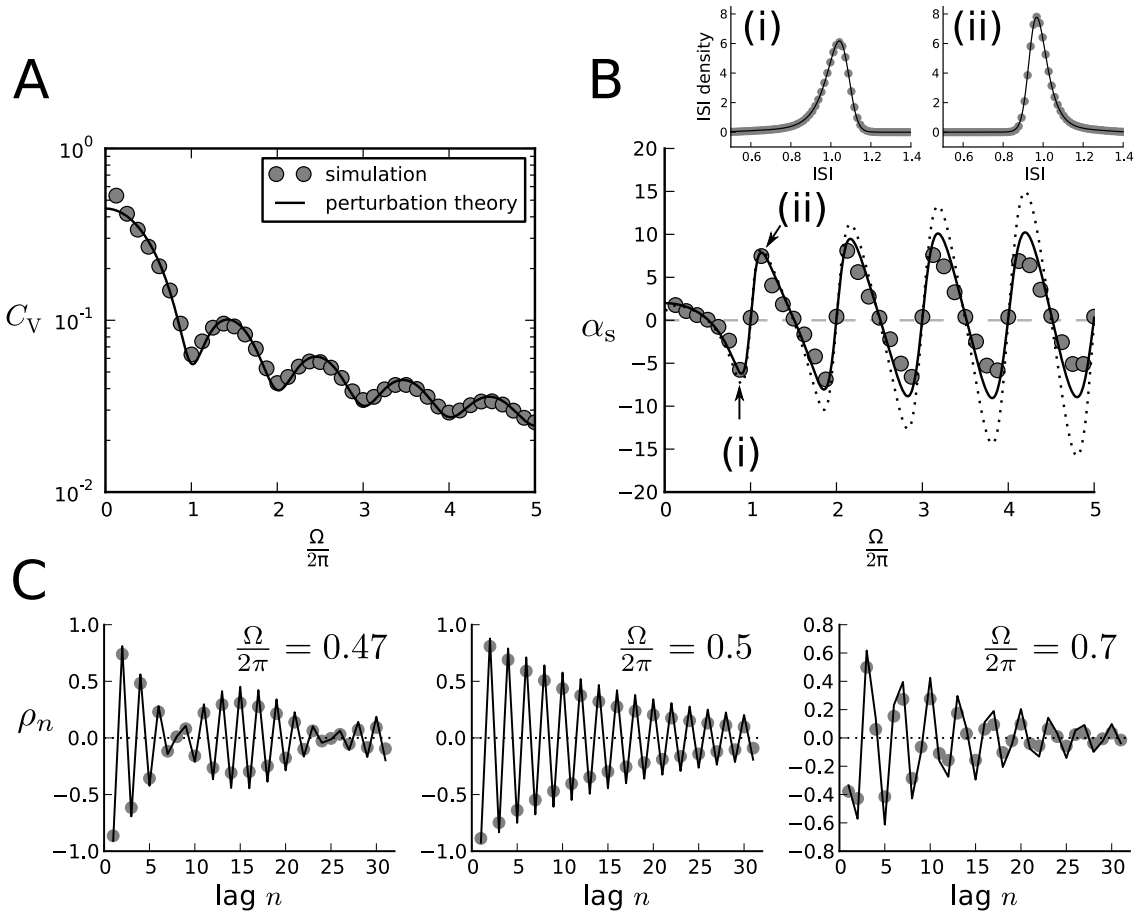

Figure 2.7.: ISI statistics of a PIF neuron driven by harmonic noise. **A** Coefficient of variation as a function of the frequency ratio $w = \Omega/(2\pi r)$ (with unit firing rate, $r = 1$). The circles represent results of simulations, the solid line shows the result of perturbation theory, Eq. (2.133). **B** Rescaled skewness $\alpha_s = \kappa_3/(3\kappa_2^2)$ as a function of the frequency ratio w (circles – simulation, solid line – zeroth-order perturbation theory, Eq. (2.134), dotted line – low damping approximation, Eq. (2.135)). Example ISI densities corresponding to (i) the negative skewness at $\Omega/(2\pi) = 0.875$ and (ii) the positive skewness at $\Omega/(2\pi) = 1.125$ (as indicated by the arrows) are shown in panel **B (i)** and **B (ii)** (circles – simulation, solid line – theory, Eq. (2.74)). **C** The serial correlation coefficient ρ_n is depicted as a function of the lag n for the frequency ratios $w = 0.47, 0.5, 0.7$ (circles – simulation, solid line – zeroth-order perturbation theory, Eq. (2.136)). Parameter values in all graphs: $\epsilon^2 = 0.2$, $Q = \Omega/\hat{\gamma} = 30$ and $\hat{D}' = 0$.

approximation of the rescaled skewness can be calculated, which reads

$$\alpha_s = \frac{2\hat{D}}{\Omega\hat{\gamma}\hat{\omega}_0^4 C_V^2}\left[\hat{\gamma}\Omega\left(1 - e^{-\frac{\hat{\gamma}}{2}}\cos\Omega\right) + \left(\Omega^2 - \frac{\hat{\gamma}^2}{4}\right)e^{-\frac{\hat{\gamma}}{2}}\sin\Omega\right] + \mathcal{O}(\epsilon^2), \tag{2.134}$$

(cf, Eq. (A.70)). Fig. 2.7 shows a rather good agreement between the zeroth-order approximation and simulation results for $\epsilon^2 = 0.2$. An inspection of the ISI densities at negative and positive values of α_s, reveals indeed a left-tailed and a right-tailed ISI density, respectively (Fig. 2.7B.i,ii). A simple criterion for the sign of the skewness can be derived for the case of small damping, $\hat{\gamma} \ll 1$. In this case, the rescaled skewness assumes the form

$$\alpha_s = \frac{2\hat{D}\Omega}{\hat{\gamma}\hat{\omega}_0^4 C_V^2}\sin\Omega. \tag{2.135}$$

Note that the factor in front of the sine function is positive. Thus, the sign of the skewness is simply given by the sign of $\sin\Omega$. The small damping approximation, Eq. (2.135), captures the behavior of the skewness rather well (Fig. 2.7B, dotted line). The deviations at large driving frequencies are due to fact that the damping constant $\hat{\gamma}$ becomes large in this case ($\hat{\gamma}$ grows in proportion with Ω because the quality factor $Q = \Omega/\hat{\gamma}$ was fixed in Fig. 2.7). Nevertheless, the changes of the sign as well as the positions of maxima and minima of the skewness are accurately predicted by the sine wave, Eq. (2.135).

Finally, the zeroth-order approximation of the serial correlation coefficient of a PIF model driven by both noises is derived in the appendix A.4 ((A.63)). For small correlation times of the OU noise, i.e. for $\hat{\tau} \ll 1$, the resulting formula is

$$\rho_n = \frac{\hat{D}}{2\hat{\gamma}\Omega\hat{\omega}_0^6 C_V^2}\left[\lambda_1\sin(\Omega n) + \lambda_2\cos(\Omega n)\right]\exp\left(-\frac{\hat{\gamma}}{2}n\right) \tag{2.136}$$

with

$$\lambda_1 = a_1\left[1 - \cosh(\frac{\hat{\gamma}}{2})\cos\Omega\right] - a_2\sinh(\frac{\hat{\gamma}}{2})\sin\Omega \tag{2.137}$$

$$\lambda_2 = a_2\left[1 - \cosh(\frac{\hat{\gamma}}{2})\cos\Omega\right] + a_1\sinh(\frac{\hat{\gamma}}{2})\sin\Omega. \tag{2.138}$$

Note that the effect of the noise intensity $\hat{D}'$ of the OU noise on the SCC is hidden in the expression for C_V, which is given by Eq. (2.133). Because the OU noise increases the CV, the only effect of this noise is to reduce the magnitude of the correlations globally. In contrast, the dependence of the SCC on the lag is completely determined by the properties of the harmonic noise. Fig. 2.7C shows three examples of the SCC as a function of the lag. In general, the simulation results agree qualitatively with the zeroth-order perturbation theory, Eq. (2.136). Slight deviations for $\epsilon^2 = 0.2$ are due to neglecting higher-order perturbation terms; the deviations disappear at sufficiently small ϵ (data not shown). According to the theory, the SCC shows damped oscillations with damped frequency Ω and damping constant γ if the lag n is regarded as a continuous parameter. Hence, the SCC reflects precisely the input correlation function $C(t)$ except for a phase shift. However, due to the discrete nature of the lag, the damped oscillation is sampled at discrete values. This gives rise to various patterns, which are determined by the driving frequency

Ω [Bauermeister, 2012]: For instance, if $\Omega/(2\pi) = \frac{1}{2}$ in Eq. (2.136) the term $\sin(\Omega n)$ vanishes for integral lags n, whereas the term $\cos(\Omega n)$ is sampled at its maxima and minima. As a consequence, the sign of ρ_n alternates with respect to the lag. Furthermore, the envelope of these oscillations decays with a characteristic correlation lag of $2/\hat{\gamma}$. In the case of a slightly smaller sampling rate, $\Omega/(2\pi) < \frac{1}{2}$, the envelope can show itself slow damped oscillations. For a more detailed discussion of the various patterns of the SCC the reader is referred to Bauermeister [2012].

2.5. Summary

In this chapter, I have generalized the theory of Lindner [2004a] to a multi-dimensional OU noise. By appropriately choosing the drift and diffusion matrices a broad class of correlation functions $C(t)$ of the input noise can be realized. I have demonstrated, how perturbation theory can be used to calculate the cumulants of the nth-order intervals within a Fokker-Planck formalism. As a result, simple relations between the correlation function $C(t)$ and the variance, skewness and probability density of the nth-order intervals have been put forward for the case of weak noise. These results could be used to derive general formulas for the CV and the SCC as a function of the drift and covariance matrix of the OUP. In particular, the decay of the SCC with lag is a superposition of oscillations and exponential decays determined by the (complex and/or real) eigenvalues of the drift matrix.

In the second part, I studied three specific cases to demonstrate the application of the general theory. Firstly, I considered a PIF model driven by a one-dimensional OUP. Here, the results of Lindner [2004a] could be reproduced; in particular, the model exhibits positive serial correlations that decay exponentially. In addition to that, measures that characterize the skewness and kurtosis of the ISIs have been calculated using higher-order perturbation theory. By means of these analytical results and numerical calculations, I have shown that a finite correlation time of the noise leads to ISI densities that are more skewed and more peaked than an inverse Gaussian density with the same variance, where the latter corresponds to the case of a vanishing correlation time. Secondly, the superposition of independent inputs has been investigated, especially the sum of several exponentially-correlated noises. In particular, it has been pointed out that, in leading order, the variance (CV) and covariance are linear functionals of the correlation function $C(t)$, i.e. different contributions to the ISI variance or covariances add up linearly. Consequently, the serial correlation coefficient is, up to a common constant factor, given by the sum of the individual SCCs. Thus, the input correlation structure is still represented in the serial correlation structure of the output. A similar additivity property has also been found for the Fano factor. Thirdly, I analyzed a PIF neuron driven by harmonic noise and exponentially correlated noise – a simple model for electro-sensory afferent neurons of paddlefish. For this model, the CV, the SCC and the skewness as well as the ISI density have been calculated explicitly. As already pointed out in Bauermeister [2012], the CV and the SCC show a non-trivial dependence on the ratio of characteristic frequency of the harmonic noise and the firing rate. In addition to that I find a non-monotonic behavior of the skewness as a function of the frequency ratio, which can be described by a simple sine function. In particular, the skewness alternates between negative and positive values corresponding to left- and right-tailed ISI densities, respectively.

The problem investigated in this chapter also raises the following questions: How should the drift and diffusion matrices be chosen for some given correlation function of the OUP? If the choice is ambiguous, what would be the optimal choice? Certainly, $1/f$ noise with a correlation function that decays algebraically cannot be generated by an OUP. Nevertheless, is it possible to produce such noise in the limit of an infinitely-dimensional OUP. $1/f$-noise in a PIF model has recently been analyzed with respect to the Fano factor [Sobie et al., 2011]. How are other statistics like the ISI density or the SCC influenced by $1/f$-noise? These interesting questions remain for future studies.

Chapter 3.

The adapting perfect integrate-and-fire model driven by white noise

Spike-frequency adaptation, i.e. the transient decrease of the firing rate of a single neuron in response to a sustained stimulus, is an ubiquitous phenomenon throughout the nervous system. As already mentioned in the introduction, an important mechanism for this phenomenon are spike-triggered adaptation currents, which realize a self-inhibitory feedback. It is this negative feedback in conjunction with the stochastic spike generation that makes adapting neuron models difficult to investigate analytically. Here, I conduct a detailed analysis of a tractable model that exhibits the characteristic features of spike-frequency adaptation: the perfect integrate-and-fire (PIF) model driven by white noise and equipped with a spike-triggered adaptation current. This model applies to neurons that operate in the supra-threshold regime (like many sensory neurons) because the PIF model is the canonical model for supra-threshold, periodic firing. Furthermore, it has been demonstrated that integrate-and-fire neurons that possess a spike-triggered adaptation mechanisms can yield highly reliable predictions of the spike responses to a given noisy stimulus [Brette and Gerstner, 2005, Mensi et al., 2011].

This study is mainly focused on the stationary spiking statistics. The response to time-dependent stimuli will be briefly discussed at the end of this chapter. It will be shown that the ISI statistics shows a number of characteristic features which are due to the negative feedback. Perhaps most strikingly are negative correlations in the sequence of ISIs, which are commonly regarded as a signature of spike-frequency adaptation in a stationary spike train. Such serial correlations have been experimentally measured in many types of neurons (for reviews see Farkhooi et al. [2009], Avila-Akerberg and Chacron [2011]) and they are often believed to originate from a self-inhibitory feedback mechanism. Numerical studies of reduced models with an spike-triggered adaptation mechanism have indeed supported the link between negative serial correlations and spike-frequency adaptation [Liu and Wang, 2001, Chacron et al., 2000, 2003, Nesse et al., 2010, Benda et al., 2010]. However, an analytical understanding of negative serial correlations in adapting neuron models has been challenging. Analytical calculations of serial correlations have been approached from different directions. For instance, for subthreshold firing models, hazard function models have been proposed to model the instantaneous firing probability as a function of an internal adaptation state (e.g. a slow conductance), [Muller et al., 2007, Nesse et al., 2010]; I will come back to such an approach in Chap. 5. Furthermore, expansions of the first-passage-time moments of integrate-and-fire models for weak spike-triggered feedback have been developed [Lindner, 2004b] and recently applied to the problem of serial correlations in spike trains [Urdapilleta, 2011].

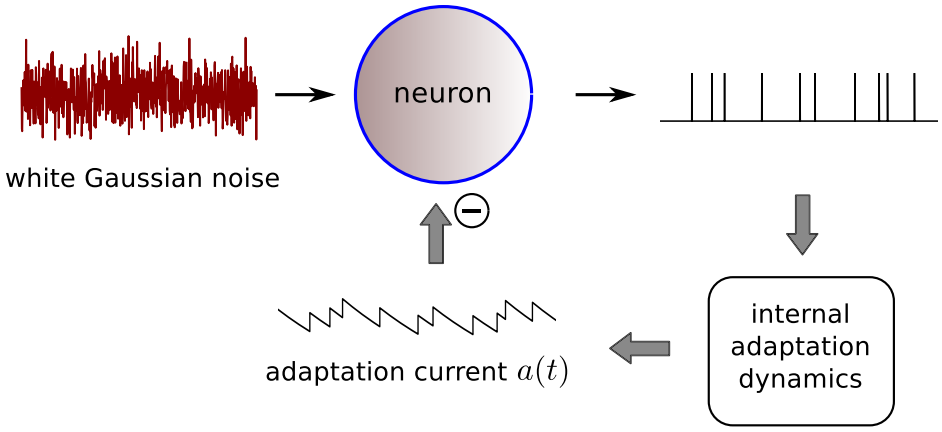

Figure 3.1.: Schematic illustration of the basic setup. A perfect integrate-and-fire neuron is driven by Gaussian white noise and inhibited by an adaptation current. The resulting spike train drives the internal dynamics of the adaptation current, thus realizing a feedback loop. In particular, each output spike causes a jump of the adaptation current, which relaxes exponentially between subsequent spikes.

Here, I pursue another approach that is based on a limit-cycle description of the deterministic system. Much of the intricate dynamics can already be understood from the deterministic dynamics. Afterwards, weak-noise approximation techniques are employed to study the effect of noise. In our approach the noise intensity is a small parameter, but the time scale of the adaptation process and the adaptation strength are arbitrary. This allows us to analyze the full range of dynamical effects of an adaptation current.

A theory for the SCC of an adapting neuron model is desirable because this quantity can be directly measured from a spike train recording. Another observable quantity is the distribution of the subthreshold membrane potential. For both quantities a theory will be put forward in this chapter. In contrast, the statistics of the adaptation state variable is difficult to access from experiments. Hence, the adaptation state can be seen as a hidden variable. Nevertheless, the analysis of the statistics of the adaptation variable is crucial to understand the stochastic spike patterns and in particular the ISI statistics. Therefore, a large part of this chapter is devoted to the statistics of the internal adaptation variable. This also involves the stationary solution of the Fokker-Planck equation.

There are several questions that will be addressed in this chapter:

- How does the stationary statistics depends on the time scale of the adaptation mechanism? In previous analytical studies [Latham et al., 2000, La Camera et al., 2004] the adaptation mechanism was often considered to be slow compared to the time scale of spike generation. However, the case of an adaptation time constant that is comparable to the mean ISI has not been addressed yet.
- How does the stationary statistics depends on the adaptation strength, i.e. on the strength of the negative feedback? In previous studies, the effect of weak feedback has been studied as a weak perturbation of the dynamics [Urdapilleta, 2011]. Pronounced non-renewal spiking statistics is, however, expected for strong negative feedback.
- What is the stationary distribution of the membrane potential and of the adaptation variable upon firing?

- How are the response properties to time-dependent stimuli altered by an adaptation current? What is the effect on the power spectrum of the spontaneous spike train ("noise spectrum")?

To answer these questions I will proceed as follows: After the introduction of the adapting PIF model, the dynamics is first analyzed for the deterministic case. In this case, perturbation theoretical considerations make it possible to obtain the deterministic limit of the serial correlation coefficient. The resulting formula represents a reasonable approximation even in the case of weak noise. The noisy dynamics is further treated as a perturbation of the deterministic dynamics. In particular, the conditional ensemble, in which trajectories start with a given initial adaptation state, will be studied in more detail. This involves the solution of the first-passage-time problem of a time-inhomogeneous stochastic process. Next, the distribution of the adaptation current upon firing is studied. This distribution can be obtained from the solution of the stationary Fokker-Planck equation. To solve this equation taking into account complicated boundary conditions, I will employ a number of weak-noise approximations. This solution yields a Gaussian distribution of the adaptation current upon firing. In particular, a simple, analytical formula for the variance of this distribution is obtained. Finally, the response properties of the model in the presence of a time-dependent stimulus and the spectral properties of the stationary spike train are analyzed. Instead of assuming weak-noise, the approximations used in this part are based on a strong time scale separation due to the slowness of the adaptation current.

3.1. The adapting PIF model

In this chapter the following simple extension of the PIF model is analyzed that includes an inhibitory adaptation current (see Sec. 1.3.2). The model is similar to previous models that contained an adaptation current [Treves, 1993, Stemmler et al., 1995, Liu and Wang, 2001, Dayan and Abbott, 2005, Brette and Gerstner, 2005]. Specifically, I consider the subthreshold dynamics in the form

$$\dot{V} = \mu - a + \sqrt{2D}\xi(t) \tag{3.1}$$

$$\tau_a \dot{a} = -a + \tilde{\Delta}\sum_i \delta(t - t_i), \tag{3.2}$$

where V is the membrane potential, $\mu > 0$ is a positive base current and D is the noise intensity of the white Gaussian noise $\xi(t)$, which obeys $\langle \xi(t)\xi(t')\rangle = \delta(t-t')$. As usual, the subthreshold dynamics is augmented with a fire and reset rule: if V reaches the threshold value V_{th} a spike is triggered and V is reset to zero:

$$\text{if } V = V_{\mathrm{th}}\text{:} \quad V \to V_{\mathrm{r}}. \tag{3.3}$$

In addition to the standard PIF model, Eq. (1.21), the membrane potential is inhibited by an adaptation current $a(t)$, which follows a simple first-order kinetics that is driven by the output spikes of the model. Because of the delta-spikes in Eq. (3.2), the adaptation variable a jumps by an amount $\Delta = \tilde{\Delta}/\tau_a$ at each spiking event. The parameter $\tilde{\Delta}$ determines the strength of feedback and adaptation. Between subsequent spikes, $a(t)$ decays exponentially with a time constant τ_a. In the following, τ_a will be referred to as

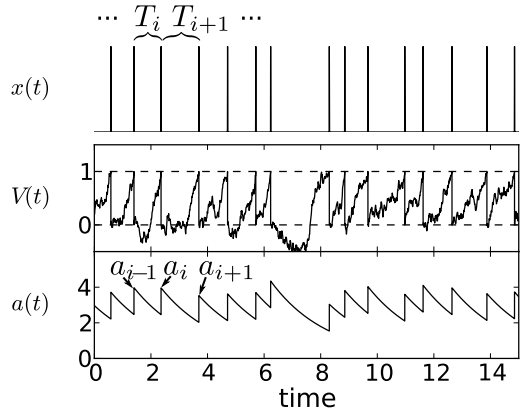

Figure 3.2.: Trajectory of an adapting perfect integrate-and-fire model driven by white Gaussian noise. A typical realization $[V(t), a(t)]$ as a function of time (time in units of the mean interspike interval). Each threshold crossing event of $V(t)$ (middle panel) causes a spike (top panel) and a jump of the adaptation variable $a(t)$ (bottom panel). Between subsequent spikes $a(t)$ decays exponentially. The peaks of the adaptation variable at the moments of firing are denoted by $a_i = a(t_i+)$. Parameter values: $\tau_a = 2$, $\tilde{\Delta} = 3$, $D = 0.1$.

the *adaptation time constant*. This quantity should not be confused with the time constant with which the firing rate adapts (this time constant is generally smaller than τ_a). Note that the adaptation current is solely driven by the output spikes; in particular, it does not explicitly depend on the subthreshold voltage. As shown in Fig. 1.13B, this model exhibits indeed spike-frequency adaptation in response to a step current: following the initial increase of the firing rate, it shows a transient decrease of the firing rate, which eventually saturates in a stationary state. This so-called adapted state will be the subject of the following analysis. A typical realization in the stationary state is shown in Fig. 3.2.

As mentioned in Sec. 1.2.6, the adaptation current can be regarded as a hidden Markov process that keeps a memory of the spiking history and thus renders the spike train nonrenewal. Because the statistics of a particular ISI, say the statistics of T_{i+1}, is completely determined by the initial value $a_i = a(t_i+)$, the sequence of initial values

$$\{\dots, a_{i-1}, a_i, a_{i+1}, a_{i+2}, \dots\} \tag{3.4}$$

is a Markov chain (cf. Sec. 1.2.6). The values a_i, where the index i labels the spike times, will be referred to as the adaptation currents upon firing or the *peak adaptation currents*, a notion that becomes obvious from Fig. 3.2. Because the dynamics of $a(t)$ between subsequent spikes is deterministic (cf. Eq. (3.2)), we find an exponential relationship between subsequent peak adaptation currents given the enclosed interspike interval T_{i+1}:

$$a_{i+1} = a_i \exp\left(-\frac{T_{i+1}}{\tau_a}\right) + \Delta. \tag{3.5}$$

This implies that the conditional mean ISI given the enclosing values of the adaptation current is given by

$$\langle T_{i+1} | a_i, a_{i+1} \rangle = \tau_a \ln\left(\frac{a_i}{a_{i+1} - \Delta}\right) \tag{3.6}$$

for $\Delta < a_{i+1} < a_i + \Delta$. Using this equation, the general relation Eq. (1.76) for the cross-moments can be written as

$$\langle T_i T_{i+n} \rangle = \int \mathrm{d}a_{i-1}\, P_f(a_{i-1}) \int \left(\prod_{k=0}^{n-1} \mathrm{d}a_{i+k} p_{tr}(a_{i+k} | a_{i+k-1}) \right) \langle T_{i+n} | a_{i+n-1} \rangle \tau_a \ln\left(\frac{a_{i-1}}{a_i - \Delta}\right), \tag{3.7}$$

for $n \geq 1$. This formula shows that a general expression for the serial correlation coefficient (which essentially requires the calculation of $\langle T_i T_{i+n} \rangle$ and $\langle T_i^2 \rangle$, cf. Eq. (1.46)), can in principle be obtained by knowing the distribution of the adaptation current upon firing $P_\mathrm{f}(a)$, the transition probability density $p_\mathrm{tr}(a_i|a_{i-1})$ and the conditional moments $\langle T_{i+1}|a_i \rangle$ and $\langle T_{i+1}^2|a_i \rangle$. I will demonstrate in Sec. 3.3.1 and 3.3.5 how these quantities can be calculated explicitly. However, it turns out that for not too strong noise, the deterministic limit of the SCC, which can be computed in a much simpler way, yields already a reasonable approximation. For this reason, Eq. (3.7) will not be used here to calculate the SCC.

3.2. The deterministic limit

The adapting PIF model operates in the supra-threshold regime, which can be seen as follows: Without adaptation and noise (i.e. setting $\tilde{\Delta} = 0$ and $D = 0$), the model fires repetitively with period V_th/μ as long as $\mu > 0$ and is thus supra-threshold (PIF model). If we switch on the adaptation dynamics by setting $\tilde{\Delta} > 0$, we still are in the supra-threshold regime because without spikes the adaptation variable eventually decays to zero, for which we already know that the model generates spikes unless $\mu \leq 0$. If a small amount of noise is present, the dynamics will be still close to the deterministic dynamics because spiking is mainly driven by the mean driving current (cf. Sec. 1.1.2). Therefore, much of the stochastic dynamics of the system can be already understood by studying the deterministic case. Parts of the results of this section have been published in Schwalger et al. [2010].

3.2.1. Limit cycle

Let us assume that at time $t = t_i$ the neuron has just fired a spike and has been reset instantaneously. Accordingly, the state of the neuron is $V(t_i) = 0$ and $a(t_i) = a_i$ (Fig. 3.3A). Without noise the integration of the system (3.1) yields

$$a(t) = a_i \exp\left(-\frac{t - t_i}{\tau_\mathrm{a}}\right), \tag{3.8}$$

$$V(t) = \int_{t_i}^{t} (\mu - a(t))\,\mathrm{d}t = \mu(t - t_i) - \tau_\mathrm{a} a_i \left[1 - \exp\left(-\frac{t - t_i}{\tau_\mathrm{a}}\right)\right]. \tag{3.9}$$

This deterministic trajectory holds in the time segment $t \in [t_i, t_i + T_\mathrm{det}(a_i)]$, where $T_\mathrm{det}(a_i)$ is the time to reach the threshold (i.e. $V(t) = V_\mathrm{th}$ at time $t = t_i + T_\mathrm{det}(a_i)$). In other words, the interspike interval T_{i+1} that follows spike time t_i is given by $T_\mathrm{det}(a_i)$. From (3.9) it can be seen that $T_\mathrm{det}(a_i)$ is the solution of the transcendental equation

$$V_\mathrm{th} = \mu T_\mathrm{det}(a_i) - \tau_\mathrm{a} a_i \left[1 - \exp\left(-\frac{T_\mathrm{det}(a_i)}{\tau_\mathrm{a}}\right)\right]. \tag{3.10}$$

How does the deterministic dynamics proceeds after the next spike time $t_{i+1} \equiv t_i + T_\mathrm{det}(a_i)$? First of all, $a(t)$ is incremented by an amount Δ and V is reset to zero. This results in the new initial values $a(t_{i+1}) = a_{i+1}$ and $V(t_{i+1}) = 0$. The initial value a_{i+1} is

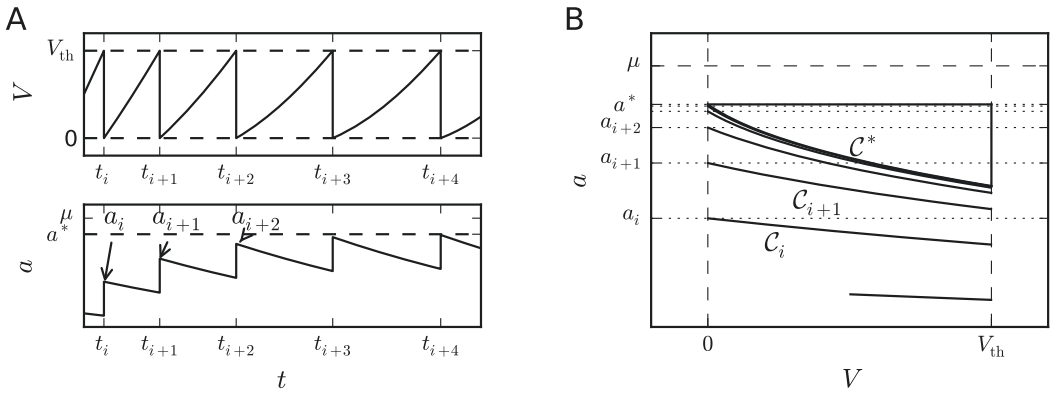

Figure 3.3.: Deterministic dynamics and limit cycle. A Typical trajectories $V(t)$ and $a(t)$: upper panel shows the voltage reset to the reset potential (lower dashed line) when V reaches the threshold (upper dashed line). The lower panel shows the exponential decay of $a(t)$ between threshold events and the jump at the firing times $\{t_i\}$. The values of $a(t)$ immediately after the jumps define the sequence $\{a_i\}$. This sequence converges to the fixed point a^* (dashed line). Note that in this example $a^* < \mu$. **B** The corresponding trajectory in the phase plane: the system moves along the curves $\mathcal{C}_i$ that start at a_i on the reset line and end at the threshold line (vertical dashed lines). At this point a jump occurs to the initial values of the successive curve $\mathcal{C}_{i+1}$. The curves converge to the limit cycle $\mathcal{C}^*$. Parameter values: $\tau_{\rm a} = 3$, $\tilde{\Delta} = 3$, $D = 0$.

related to the initial value a_i of the previous segment by

$$a_{i+1} = a_i \exp\left(-\frac{T_{\rm det}(a_i)}{\tau_{\rm a}}\right) + \Delta, \tag{3.11}$$

which is a special case of Eq. (3.5). From this the trajectory in the next time segment $t \in [t_{i+1}, t_{i+1} + T_{\rm det}(a_{i+1})]$ is obtained in the same manner as before: $a(t)$ and $V(t)$ are again given by (3.8) and (3.9) with the index i replaced by $i+1$. By repeating this procedure the whole trajectory can be constructed segment by segment.

It is useful to visualize the trajectory in the phase-plane spanned by the state variables V and a (Fig. 3.3B). The trajectory $(V(t), a(t))$ in the i-th time segment is a curve from reset potential to threshold. This curve will be denoted by $\mathcal{C}_i$ and it is given in the parametric form (3.8), (3.9). The reset potential and the threshold become lines in the phase plane defined by $V = 0$ and $V = V_{\rm th}$, respectively. For the visualization of a continuous trajectory, the instantaneous jump and reset are drawn by straight lines in the phase plane. Each curve $\mathcal{C}_i$ is completely determined by its initial value a_i. In the following, it is more convenient to study the sequence $\{a_i\}$ instead of the full dynamics $a(t)$ and $V(t)$. In the deterministic case, the dynamics of a_i is given by the deterministic map (3.11).

The sequence of curves $\mathcal{C}_i$ converges to a limit curve $\mathcal{C}^*$ as $i \to \infty$. An example of such a limit curve is shown in Fig. 3.3B. It can be interpreted as a limit cycle, which emphasizes the oscillatory nature of our model. The attraction of trajectories to $\mathcal{C}^*$ is equivalent to the convergence of the sequence $\{a_i\}$ to a limiting value a^*. Thus, $\mathcal{C}^*$ is attracting if the map (3.11) possesses a stable fixed point a^*. The fixed point condition requires that $a_{i+1} = a_i = a^*$, or

$$a^* = a^* \exp\left(-\frac{T^*}{\tau_{\rm a}}\right) + \Delta. \tag{3.12}$$

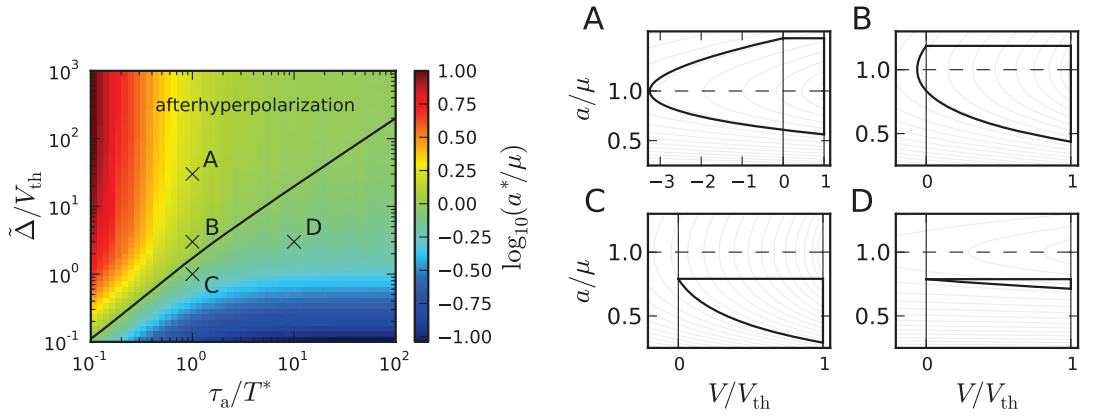

Figure 3.4.: Dependence of the limit cycle on the system parameters. The left panel depicts the fixed point a^* normalized by $\mu = (V_{\mathrm{th}} + \tilde{\Delta})/T^*$ in the parameter space spanned by the adaptation time constant τ_{a} and the adaptation strength $\tilde{\Delta}$. The solid line divides the parameter space into two regions corresponding to $a^* > \mu$ (afterhyperpolarization regime, upper region) and $a^* < \mu$ (lower region). Examples of limit cycles are shown in the phase plane (right panel) by solid lines for the parameter sets A–D as indicated in the left panel . The reset and threshold lines are displayed by thin solid lines, the dashed line represents the nullcline $a = \mu$, where $\dot{V} = 0$.

Here, the notation $T^* \equiv T_{\mathrm{det}}(a^*)$ for the time period of the limit cycle (time on the limit curve $\mathcal{C}^*$) was introduced. The time T^* yields the limiting value of the deterministic ISI sequence because the i-th ISI is given by $T_{\mathrm{det}}(a_i)$. Moreover, T^* has to fulfill Eq. (3.10) evaluated at $a_i = a^*$, thus

$$V_{\mathrm{th}} = \mu T^* - \tau_{\mathrm{a}} a^* \left[1 - \exp\left(-\frac{T^*}{\tau_{\mathrm{a}}}\right)\right]. \tag{3.13}$$

The two equations (3.12) and (3.13) can now be solved for the limit cycle parameters T^* and a^* resulting in

$$\boxed{T^* = \frac{V_{\mathrm{th}} + \tilde{\Delta}}{\mu}, \qquad a^* = \frac{\Delta}{1 - \exp(-T^*/\tau_{\mathrm{a}})}.} \tag{3.14}$$

With these quantities, the limit curve $\mathcal{C}^*$ can be parametrized as follows:

$$\mathcal{C}^*: \qquad a(t) = a^* e^{-t/\tau_{\mathrm{a}}}, \quad V(t) = \mu t - \tau_{\mathrm{a}} a^* (1 - e^{-t/\tau_{\mathrm{a}}}), \qquad 0 \le t \le T^*. \tag{3.15}$$

The deterministic limit period T^* and the fixed point a^* are of particular importance for the following analysis. First of all, to a very good approximation the deterministic period T^* also yields the mean ISI in the stochastic case unless the noise intensity is exceedingly large, as will be shown in Sec. 3.3.1. Thus, T^* determines the typical time scale of the spike generator[1]. It is therefore convenient to measure time in units of T^*. Similarly, the typical scale of the membrane potential is V_{th}, hence it is reasonable to measure voltages

[1] In contrast to the LIF model, the PIF model has no intrinsic time scale like the membrane time constant of the LIF model.

in units of V_{th}. Doing so, one can pass to the non-dimensional variables $\bar{V} = V/V_{\mathrm{th}}$, $\bar{t} = t/T^*$ and $\bar{a} = aT^*/V_{\mathrm{th}}$ to obtain the equivalent non-dimensional dynamics

$$\dot{\bar{V}} = 1 + \bar{\Delta} - \bar{a} + \sqrt{2\bar{D}}\xi(\bar{t}), \qquad \bar{\tau}_{\mathrm{a}}\dot{\bar{a}} = -\bar{a} + \bar{\Delta}\sum\delta(\bar{t} - \bar{t}_i) \tag{3.16}$$
$$\text{if } \bar{V}(\bar{t}^-) = 1\text{:} \quad \bar{V}(\bar{t}^+) \to 0.$$

Here, the dimensionless parameters

$$\bar{\tau}_{\mathrm{a}} = \frac{\tau_{\mathrm{a}}}{T^*}, \quad \bar{\Delta} = \frac{\tilde{\Delta}}{V_{\mathrm{th}}}, \quad \bar{D} = D\frac{T^*}{V_{\mathrm{th}}^2} \tag{3.17}$$

were introduced. This form points out that the adapting PIF model is completely determined by the three parameters $\bar{\tau}_{\mathrm{a}}$, $\bar{\Delta}$ and $\bar{D}$.

Secondly, the initial value of a on the limit cycle, a^*, is important because it sets the order of magnitude of the peak currents a_i, which are distributed in the neighborhood of a^*. Furthermore, a^* defines two regimes depending on whether a^* is smaller or larger than the base current $\mu = (V_{\mathrm{th}} + \tilde{\Delta})/T^*$. It will turn out that these regimes have distinct statistical and dynamical properties. In Fig. 3.4 the magnitude of a^* normalized by μ is displayed as a function of the system parameters τ_{a}/T^* and $\tilde{\Delta}/V_{\mathrm{th}}$ of the deterministic system. It can be seen that the conditions $a^*/\mu < 1$ and $a^*/\mu > 1$ correspond to two regions in the parameter space. The separating line, on which $a^*/\mu = 1$, is given by

$$\frac{\tilde{\Delta}}{V_{\mathrm{th}}} = \frac{1 - e^{-\delta}}{\delta - 1 + e^{-\delta}}, \qquad \delta = \frac{T^*}{\tau_{\mathrm{a}}}. \tag{3.18}$$

Above this line, i.e. for sufficiently strong adaptation, the limit cycle exhibits an excursion to negative membrane potentials $V(t)$ (afterhyperpolarization, Fig. 3.4A,B). The reason for this is that the drift $\dot{V} = \mu - a(t)$ is negative immediately after the reset because in this region $a(t_i) = a^* > \mu$. Consequently, $V(t)$ decreases after the reset until $a(t)$ reaches μ. Below the separating line, i.e. for $a^*/\mu < 1$, the drift on the limit-cycle is always positive (Fig. 3.4C,D). Hence, the limit-cycle does not enter the region of negative membrane potentials.

The effect of increasing the adaptation time constant τ_{a} is twofold (cf. Fig. 3.4B,D): Firstly, the phase-space is stretched horizontally because the variable a is proportional to $e^{-t/\tau_{\mathrm{a}}}$, i.e. a decreases more slowly. Secondly, the jump size $\Delta = \tilde{\Delta}/\tau_{\mathrm{a}}$ scales inversely to the adaptation time constant, hence the jump becomes smaller with increasing τ_{a}.

3.2.2. Dynamics close to the limit cycle

The solution of Eq. (3.10) cannot be obtained in closed form if $a_i \neq a^*$ [2]. However, if a_i is close to a^*, i.e. if $a_i = a^* + \delta a_i$ with $\delta a_i \ll a^*$, one can obtain $T_{\mathrm{det}}(a_i)$ by a perturbation

[2] Note that the solution to Eq. (3.10) can be expressed using the Lambert W function as

$$T_{\mathrm{det}}(a_i) = \tau_{\mathrm{a}}\left[W_0\left(-\frac{a_i}{\mu}\exp\left(-\frac{V_{\mathrm{th}} + \tau_{\mathrm{a}}a_i}{\mu\tau_{\mathrm{a}}}\right)\right) + \frac{V_{\mathrm{th}} + \tau_{\mathrm{a}}a_i}{\mu\tau_{\mathrm{a}}}\right], \tag{3.19}$$

where $W_0(x)$ denotes the principle branch of the Lambert W function [Weisstein, 2012].

expansion in the small parameter $\epsilon_a = \delta a_i / a^*$. To this end, I substitute the expansion

$$T_{\text{det}}(a_i) = T^{(0)} + T^{(1)}\epsilon_a + T^{(2)}\epsilon_a^2 + \dots \tag{3.20}$$

into Eq. (3.10) and collect terms with equal powers in ϵ_a. The resulting equation must be balanced with respect to each power in ϵ_a, which yields equations that can be solved order-by-order for the coefficients $T^{(k)}$, $k \geq 0$. In particular, substituting the expansion (3.20) into (3.10) leads to

$$V_\text{th} = \mu \sum_{k=0}^{\infty} T^{(k)} \epsilon_\text{a}^k - \tau_\text{a} a^* (1+\epsilon_\text{a}) \left[1 - \exp\left(-\frac{1}{\tau_\text{a}} \sum_{k=0}^{\infty} T^{(k)} \epsilon_\text{a}^k \right) \right]. \tag{3.21}$$

Next, we perform a Taylor expansion of the exponential term up to second order:

$$\exp\left(-\frac{1}{\tau_\text{a}} \sum_{k=0}^{\infty} T^{(k)} \epsilon_\text{a}^k \right) = e^{-T^{(0)}/\tau_\text{a}} \left\{ 1 - \frac{T^{(1)}}{\tau_\text{a}} \epsilon_\text{a} + \left[\frac{1}{2} \left(\frac{T^{(1)}}{\tau_\text{a}} \right)^2 - \frac{T^{(2)}}{\tau_\text{a}} \right] \epsilon_\text{a}^2 + \mathcal{O}(\epsilon_\text{a}^3) \right\}. \tag{3.22}$$

Inserting this expression back into Eq. (3.21) and collecting like powers in ϵ_a the equations up to second order read

$$\epsilon_\text{a}^0 : \qquad V_\text{th} = \mu T^{(0)} - \tau_\text{a} a^* \left(1 - e^{-T^{(0)}/\tau_\text{a}} \right) \tag{3.23}$$

$$\epsilon_\text{a}^1 : \qquad 0 = \mu T^{(1)} - \tau_\text{a} a^* \left[1 - e^{-T^{(0)}/\tau_\text{a}} \left(1 - \frac{T^{(1)}}{\tau_\text{a}} \right) \right] \tag{3.24}$$

$$\epsilon_\text{a}^2 : \qquad 0 = \mu T^{(2)} - \tau_\text{a} a^* e^{-T^{(0)}/\tau_\text{a}} \left[\frac{T^{(2)}}{\tau_\text{a}} - \frac{1}{2} \left(\frac{T^{(1)}}{\tau_\text{a}} \right)^2 + \frac{T^{(1)}}{\tau_\text{a}} \right] \tag{3.25}$$

The zeroth order equation is identical to the limit cycle equation (3.13). Thus, to zeroth order the ISI of the deterministic dynamics is equal to the period of the deterministic limit cycle, i.e. $T^{(0)} = T^*$, as it should be. The first and second-order corrections are given by

$$T^{(1)} = \tau_\text{a} a^* \frac{1 - e^{-T^*/\tau_\text{a}}}{\mu - a^* e^{-T^*/\tau_\text{a}}}, \qquad T^{(2)} = \frac{a^* - \Delta}{\mu - a^* + \Delta} T^{(1)} \left(1 - \frac{T^{(1)}}{2\tau_\text{a}} \right). \tag{3.26}$$

The first- and second order approximations are shown in Fig. 3.5 as a function of the adaptation time constant for a relatively large deviation $\epsilon_a = \pm 0.1$ from the limit-cycle. As can be seen, the perturbation approximation works well for τ_a of the order of the mean ISI or smaller. For large τ_a the approximations become generally worse. In section 3.3.1, I will discuss the approximations for $T_{\text{det}}(a_i)$ for typical δa_i that are of the order of the standard deviation of the stationary sequence $\{a_i\}$. In this case, the approximations compare well with the exact solution $T_{\text{det}}(a_i)$ even for large τ_a because the standard deviation of a_i decreases with τ_a, as I will show below.

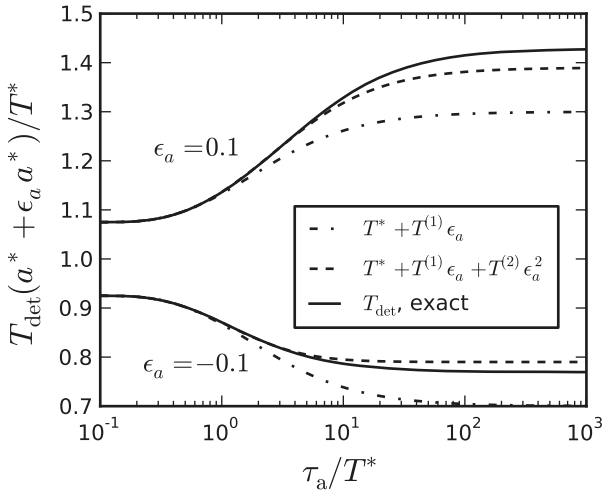

Figure 3.5.: First- and second-order approximation of the deterministic period $T_{\mathbf{det}}(a_i)$ for $\epsilon_a = \delta a_i/a^* = \pm 0.1$. The solid lines represent the exact numerical solution of the transcendental eq. (3.10), dashed-dotted and dashed lines represent the first- and second order approximation, respectively. The parameters are $\tilde{\Delta} = 3$, $T^* = 1$.

3.2.3. The serial correlation coefficient

In the deterministic limit both the covariance and the variance of two ISIs with a given lag vanish. Thus, the asymptotic behavior of the serial correlation coefficient, i.e. the ratio of covariance and variance, cannot not be explained by the purely deterministic limit cycle dynamics. To obtain the correct limit, it is necessary to account for the effect of an infinitesimally small amount of noise. This leads to stochastic trajectories that deviate slightly from the deterministic limit cycle $\mathcal{C}^*$. In particular, the sequence $\{a_i\}$ becomes a stochastic process and a_i generally deviates from a^* even in the limit $i \to \infty$, where a_i becomes a stationary process. Similarly, noise leads to stochastic interspike intervals T_i that deviate from the deterministic limit period T^*. In the following, the deviations will be denoted by δa_i and δT_i, hence

$$a_i = a^* + \delta a_i \tag{3.27}$$

$$T_i = T^* + \delta T_i. \tag{3.28}$$

In order to calculate the serial correlation coefficient, I will first derive an expression for the covariance $\langle \delta a_i \delta a_{i+k} \rangle$ of the peak adaptation currents. The result will then be used to find an expression for the covariance $\langle \delta T_i \delta T_{i+k} \rangle$ of the interspike intervals, which is required for the computation of the SCC.

To start with, let us consider the relationship Eq. (3.5), which represents the stochastic analog of the deterministic map (3.11). Indeed, equation (3.5) can be regarded as a stochastic map $a_{i+1} = f(a_i)$ because a_{i+1} can be generated from a_i and a random number T_{i+1} that is drawn from the conditional distribution $P(T_{i+1}|a_i)$ (an expression for this distribution will be derived in Sec. 3.3.1). For weak noise, the stochastic map (3.5) can be linearized about the limit cycle by substituting $a_i = a^* + \delta a_i$ and $T_{i+1} = T^* + \delta T_{i+1}$ and retaining only terms that are first order in δa_i and δT_{i+1}. As a result the linearized

stochastic map reads

$$\delta a_{i+1} = \alpha \left(\delta a_i - a^* \frac{\delta T_{i+1}}{\tau_a} \right), \tag{3.29}$$

where I have introduced the non-dimensional parameter

$$\alpha = \exp\left(-\frac{T^*}{\tau_a} \right) = \frac{a^* - \Delta}{a^*}. \tag{3.30}$$

In the appendix, Sec. B.1.1, it is shown that for weak noise the conditional ISI T_{i+1} is Gaussian distributed with mean $T_{\mathrm{det}}(a_i)$ and variance $\sigma_T^2(a_i)$, which is given by Eq. (B.1). This enables us to assume that the variable T_{i+1} can be generated from the stochastic map

$$T_{i+1} = T_{\mathrm{det}}(a_i) + \sigma_T(a_i) X_i, \qquad X_i \sim \mathcal{N}(0,1), \tag{3.31}$$

where X_i is a Gaussian random number with unit variance that is independent of a_i. Expanding $T_{\mathrm{det}}(a_i)$ to first order in the small deviation δa_i (cf. Eq. (3.20)), the last equation reads

$$\delta T_{i+1} = T^{(1)} \frac{\delta a_i}{a^*} + \sigma_T(a_i) X_i. \tag{3.32}$$

Inserting δT_{i+1} into (3.29) and using the expression (3.26) for $T^{(1)}$ yields a stochastic map that only contains δa_i:

$$\delta a_{i+1} = \alpha \left(\vartheta \delta a_i - a^* \frac{\sigma_T(a_i)}{\tau_a} X_i \right) \tag{3.33}$$

with

$$\vartheta = \frac{\mu - a^*}{\mu - a^* + \Delta}. \tag{3.34}$$

Applying the stochastic map to δa_{i+k} the covariance $c_k = \langle \delta a_i \delta a_{i+k} \rangle$ can be calculated:

$$c_k = \alpha \left\langle \delta a_i \left(\vartheta \delta a_{i+k-1} - a^* \frac{\sigma_T(a_{i+k-1})}{\tau_a} X_{i+k-1} \right) \right\rangle \tag{3.35}$$

$$= \alpha \left(\vartheta c_{k-1} - \frac{a^*}{\tau_a} \left\langle \delta a_i \sigma_T(a_{i+k-1}) X_{i+k-1} \right\rangle \right). \tag{3.36}$$

We can now benefit from the representation (3.31): the random variable X_{i+k-1} is independent of δa_i and a_{i+k-1} for $k \geq 1$ and its mean is zero. Hence, the average in Eq. (3.36) decouples into $\langle \delta a_i \sigma_T(a_{i+k-1}) \rangle \langle X_{i+k-1} \rangle$ and consequently vanishes, because $\langle X_{i+k-1} \rangle = 0$. We are left with

$$c_k = \alpha \vartheta c_{k-1} = (\alpha \vartheta)^k c_0, \qquad k \geq 1. \tag{3.37}$$

This reveals that the covariance of the peak currents a_i is a geometric sequence with respect to the lag k. The dependence on the noise intensity D or respectively the ISI variance $\sigma_T^2(a_i)$ is completely shifted into the variance of peak currents $c_0 = \langle \delta a_i^2 \rangle$. This has a surprising consequence: in the correlation coefficient defined as the covariance divided by the variance the dependence on the noise cancels out:

$$\rho_k^a \equiv \frac{c_k}{c_0} = (\alpha \vartheta)^k. \tag{3.38}$$

As a result, the correlation coefficient ρ_k^a has a finite deterministic limit, simply because it does not depend on D if the noise is sufficiently weak.

The covariance of ISIs can be reduced to the covariance of peak adaptation currents. To this end, I solve the linearized stochastic map (3.29) for δT_{i+1} and shift the index by one:

$$\delta T_i = \frac{\tau_a}{\alpha a^*} \left(\alpha \delta a_{i-1} - \delta a_i \right). \tag{3.39}$$

Averaging the product of δT_i and δT_{i+k} yields

$$\begin{aligned} \langle \delta T_i \delta T_{i+k} \rangle &= \left(\frac{\tau_a}{\alpha a^*} \right)^2 \langle \left(\alpha \delta a_{i-1} - \delta a_i \right) \left(\alpha \delta a_{i+k-1} - \delta a_{i+k} \right) \rangle \\ &= \left(\frac{\tau_a}{\alpha a^*} \right)^2 \left[(\alpha^2 + 1) c_k - \alpha (c_{k+1} + c_{k-1}) \right]. \end{aligned} \tag{3.40}$$

Inserting the geometric series (3.37) for c_k results in

$$\langle \delta T_i \delta T_{i+k} \rangle = -c_0 \left(\frac{\tau_a}{\alpha a^*} \right)^2 \alpha (1 - \vartheta)(1 - \alpha^2 \vartheta)(\alpha \vartheta)^{k-1} \tag{3.41}$$

for $k \geq 1$. Similarly, for $k = 0$ the variance is

$$\langle \delta T_i^2 \rangle = c_0 \left(\frac{\tau_a}{\alpha a^*} \right)^2 \left(1 + \alpha^2 - 2\alpha^2 \vartheta \right), \tag{3.42}$$

where the symmetry $c_{-1} = c_1$ was used. Finally, dividing the covariance by the variance leads to the serial correlation coefficient for $k \geq 1$:

$$\boxed{\rho_k = \rho_1 (\alpha \vartheta)^{k-1}, \qquad \rho_1 = -\frac{\alpha (1 - \vartheta)(1 - \alpha^2 \vartheta)}{1 + \alpha^2 - 2\alpha^2 \vartheta}.} \tag{3.43}$$

This result constitutes the weak-noise limit of the SCC. It can be expected that this expression also holds for moderate noise intensities because both covariance and variance depend on the noise only through the common factor c_0. The factor drops out in the SCC, so that our formula does not contain the noise intensity at all. This indicates that the SCC depends only weakly on the noise intensity.

The expression (3.43) shows that the SCC has the form of a geometric sequence. The SCC at lag 1, ρ_1, is negative in the whole parameter space[3]. Fig. 3.6A shows that the magnitude of the negative correlations increases monotonously with the adaptation strength $\tilde{\Delta}$ and exhibits a minimum with respect to the time-scale ratio τ_a / T^*. This behavior has also been pointed out in the numerical study of Liu and Wang [2001]. At the minimum, adjacent ISIs are maximally anti-correlated. It occurs at a certain "optimal" τ_a, which is of the order of T^*. For $\tau_a \ll T^*$ the anti-correlations vanish because the memory kept in $a(t)$ does not extend over the duration of a single ISI. In the extreme case $\tau_a \to 0$, the spike-triggered jumps of $a(t)$ become infinitely large and the exponential decay, and hence the memory loss, becomes infinitely fast. In this limit, the $a(t)$ resembles a delta-spike train, the effect of which is merely a shift of the reset potential to negative values. The result is a

[3] In fact, if $a^* < \mu$ it holds $0 < \vartheta < 1$ from the definition (3.34). Moreover, from the definition (3.30) it holds $0 < \alpha < 1$. Thus, I find $1 - \alpha^2 \vartheta > 0$ and $1 + \alpha^2 - 2\alpha^2 \vartheta = (1 - \alpha)^2 + 2\alpha(1 - \alpha\vartheta) > 0$, so $\rho_1 < 0$. On the other hand, if $a^* \geq \mu$ it follows $\vartheta \leq 0$ because $\mu - a^* + \Delta$ is always positive ($\mu - a^* + \Delta = \mu - a^* e^{-T^*/\tau_a}$ is the velocity of the membrane potential on $\mathcal{C}^*$ when reaching the threshold, which must be positive).

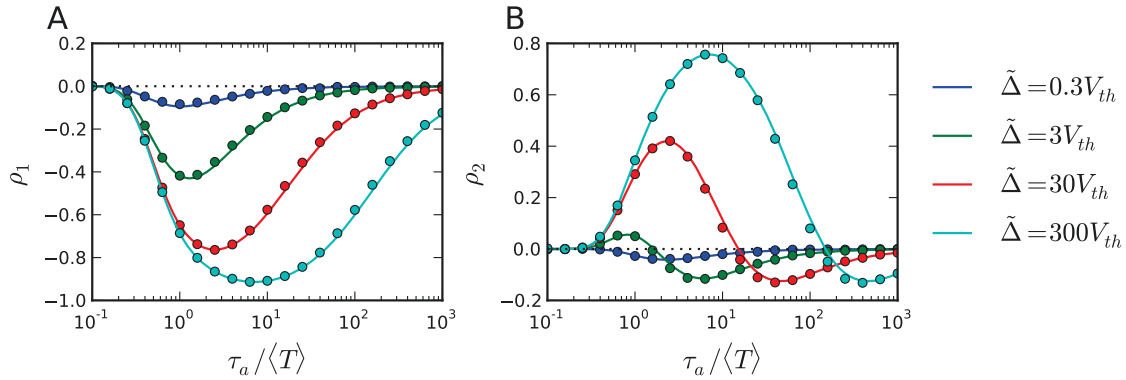

Figure 3.6.: SCC as a function of the time-scale separation τ_a/T^* at lag 1 and lag 2. Weak-noise theory (solid lines) and simulations (circles) of **A** ρ_1 and **B** ρ_2 are displayed for different adaptation strength as indicated on the right-hand side. The dashed line indicates the zero line. The noise intensity was chosen as $D = 0.1$.

PIF model without adaptation but with a lowered firing rate, thus resulting in a renewal model. In the opposite limit, $\tau_a/T^* \to \infty$, ρ_1 also vanishes. Here, the linear filter dynamics of $a(t)$ acts as a temporal average over an infinitely long time scale. As a result, $a(t)$ converges to its constant mean value, the effect of which is merely to reduce the effective base current. A constant adaptation variable, has no capacity to remember the deviations of previous ISIs from its mean value. In a sense, the adaptation variable keeps too much memory of the ISI history, i.e. it remembers infinitely many ISI, at the price of vanishing correlations at any given lag. In fact, it will become clear in a moment that the sum of ρ_k over all lags does not vanish.

The change of the SCCs at higher lags, $k > 1$, is determined by the factor $(\alpha\vartheta)^{k-1}$. At odd lags, this factor is positive, hence, the corresponding SCC is always negative (since $\rho_1 < 0$). The sign of the SCC at even lags depends on the sign of ϑ because $\alpha = e^{-T^*/\tau_a}$ is a positive number (more precisely, $0 < \alpha < 1$ for any parameter set). For $a^* < \mu$, it holds $0 < \vartheta < 1$, whereas in the afterhyperpolarization regime $a^* > \mu$ we have $-1 < \vartheta < 0$. Thus, SCCs at even lags are negative if $a^* < \mu$ and positive if $a^* > \mu$. This theoretical prediction is in excellent agreement with simulation results. In particular, ρ_2 is positive below a critical time-scale ratio τ_a/T^* that corresponds to $a^* = \mu$; and it becomes negative for larger time-scale ratios (Fig. 3.6B). By the same reasoning as for ρ_1, the SCC at lag 2 vanishes in the limits $\tau_a \to 0$ and $\tau_a \to \infty$. The maximum of ρ_2 strongly depends on the adaptation strength $\tilde{\Delta}$. For sufficiently large $\tilde{\Delta}$ the maximum can become arbitrarily close to unity.

Figure 3.7A–D shows ρ_k as a function of the lag. For small τ_a corresponding to the afterhyperpolarization regime $a^* > \mu$, the SCC shows damped oscillations, Fig. 3.7A,B. If the adaptation is not too strong (Fig. 3.7A, parameter set B in Fig. 3.4) the correlations decay quickly yielding significant correlations only at lag 1. Such a pattern resembles experimentally observed patterns of P-units of weakly electric fish (see e.g. Chacron et al. [2001]). For stronger adaptation, oscillations can be observed that extend over about 5 lags, Fig. 3.7B. Similar patterns have also been found in P-units of weakly electric fish [Ratnam and Nelson, 2000]. For larger τ_a (corresponding to $a^* < \mu$), the SCC decays more slowly, but without oscillations, Fig. 3.7C,D.

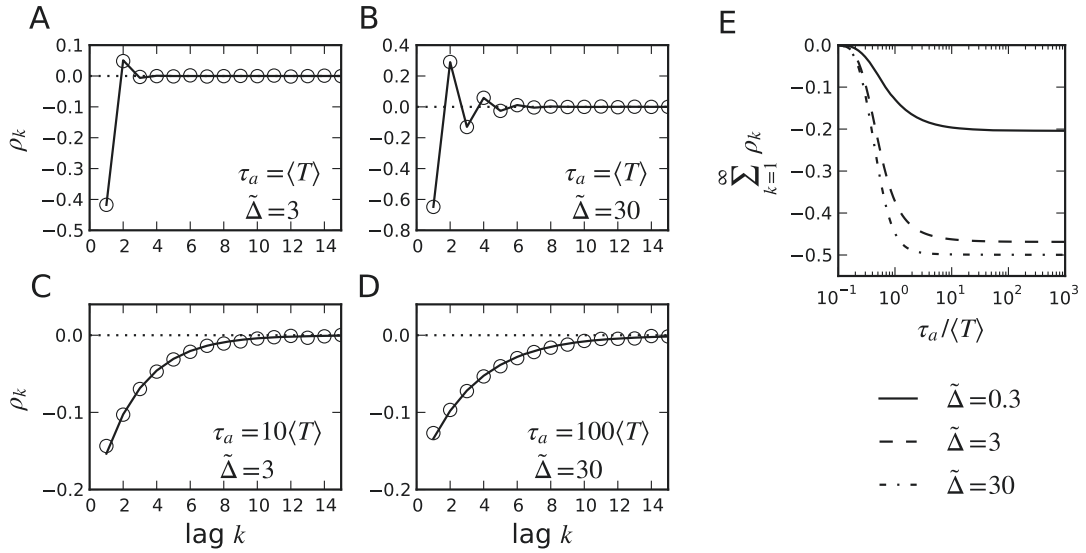

Figure 3.7.: SCC as a function of the lag k and sum of ρ_k. A–D Theory (solid lines) and simulation (circles) for four different parameter sets as indicated in the panels. The noise intensity was chosen as $D = 0.1$. The dashed line indicates the zero line. **E** The sum $\sum_{k=1}^{\infty} \rho_k = \rho_1/(1 - \alpha\vartheta)$ is shown as a function of the time-scale ratio τ_a/T^* for different adaptation strength $\tilde{\Delta}$ as indicated below the panel.

Although for any given lag the SCC vanishes in the limit $\tau_a \to \infty$, the sum of the SCCs over all lags converges to a finite, non-vanishing limit (Fig. 3.7E). The summation of the geometric series (3.43) yields $\rho_1/(1 - \alpha\vartheta)$, which in the limit $\tau_a \to \infty$ saturates at

$$\lim_{\tau_a/T^* \to \infty} \sum_{k=1}^{\infty} \rho_k = -\frac{\tilde{\Delta}(\tilde{\Delta} + 2V_{\text{th}})}{2(\tilde{\Delta} + V_{\text{th}})^2}. \tag{3.44}$$

The vanishing serial correlation coefficients, on the one hand, and the non-vanishing sum, on the other hand, may seem contradictory. The apparent difference is due to the order of the limiting procedure. In deriving Eq. (3.44) it is important that one first computes the infinite series and only then performs the limit $\tau_a \to \infty$ – the reverse limiting order would yield zero because all terms in the sum vanish. The limit (3.44) is negative and its absolute value grows with the adaptation strength $\tilde{\Delta}$. In the limit of large $\tilde{\Delta}$ the saturation level converges to $-1/2$. The sum $\sum_k \rho_k$ is of interest because it relates to the power spectrum of the spike train $y(t) = \sum_i \delta(t - t_i)$ at zero frequency:

$$S_y(0) = \frac{C_V^2}{\langle T_i \rangle} \left(1 + 2 \sum_{k=1}^{\infty} \rho_k \right). \tag{3.45}$$

In Sec. 3.4 the limit $\tau_a \to \infty$ is reconsidered: in this case, the variable $a(t)$ converges to its constant mean value $\langle a \rangle$. It seems thus reasonable to replace $a(t)$ by the constant $\langle a \rangle$ resulting in the standard white-noise driven PIF model, however, with a reduced drift current $\tilde{\mu} = \mu - \langle a \rangle$ ("mean-adaptation approximation"). In other words, it seems that in the limit $\tau_a \to \infty$, the model converges to a renewal process. As will be shown below, the mean ISI and the CV are indeed well-captured by the approximate renewal model for large τ_a. Nevertheless, the limit $\tau_a \to \infty$ of the sum of the SCCs and hence the power

spectrum at zero frequency will be rather different from the approximate renewal model, which predicts $\sum_k \rho_k = 0$ and $S_y(0) = C_V^2 / \langle T_i \rangle$. In short, the spike train does not converge to a renewal process in the large τ_a limit. This paradox is similar to the one studied in Lindner [2006].

Finally, it is worth to note that the serial correlations in the sequence of adaptation peak currents a_i are essential to generate ISI correlations, which follows directly from Eq. (3.40). This is in marked contrast to the study of Nesse et al. [2010]. The authors of that study have argued that the correlations between peak conductances of adaptation currents are independent despite the presence of pronounced serial ISI correlations. It has been suggested that this independence property may be beneficial for neural coding. Our opposite finding may be explained by the fact that the present model operates in the supra-threshold firing regime, whereas the model of Nesse et al. [2010] operates in the subthreshold, excitable regime.

3.3. Weak noise

We now turn to the stochastic system. For weak noise, trajectories will fluctuate about the deterministic limit-cycle dynamics. Furthermore, the neuron does not fire strictly periodically as in the deterministic case, but the ISIs are distributed according to some ISI density. The fluctuations about the limit-cycle can be described by the distribution of the peak adaptation current a_i about its deterministic value a^*. This upon firing distribution, $P_f(a_i)$, will be considered in Sec. 3.3.2 – 3.3.5. The ISI statistics – such as the ISI density and the coefficient of variation – is then approximated by averaging the conditional ISI statistics for a given initial value a_i with respect to $P_f(a_i)$ (Sec. 3.3.6). Therefore, we will begin this section with the analysis of the conditional ISI statistics.

3.3.1. The conditional ensemble and the time-inhomogeneous first-passage-time problem

The random variables a_i and T_{i+1}, or respectively δa_i and δT_{i+1}, are not statistically independent. This becomes apparent if one considers the ensemble of trajectories $\{(V(t), a(t))\}$ that start at time t_i at the reset potential with a fixed value $a_i = a$. In this *conditional ensemble*, the interspike interval T_{i+1} can be interpreted as a first-passage time, i.e. the time it takes for a trajectory that starts at $V(t_i) = 0$ and $a(t_i) = a_i$ to reach the threshold line for the first time. The statistics of the first-passage time strongly depends on the initial value a_i. For instance, for large a_i a large first-passage time can be expected because the drift current $\mu - a$ that drives the trajectory towards the threshold is initially small (it can be even negative) and only gradually recovers to the stronger drift that corresponds to smaller a_i.

The conditional ISI density $P(T_{i+1}|a_i)$

In the next two section, I want to derive approximations for the statistics of T_{i+1} and a_{i+1} in the conditional ensemble, i.e. for a fixed value of a_i. Mathematically, this corresponds to a first-passage-time problem in the two-dimensional phase space: When does a trajectory that starts at $V(0) = 0$, $a(0) = a_i$ reach the threshold line $V = V_{th}$ for the first

time? Equivalently, this situation can be regarded as a one-dimensional first-passage-time problem, but with time-dependent drift: When does the process $V(t)$ defined by

$$\dot{V} = \mu - a_i e^{-t/\tau_a} + \sqrt{2D}\xi(t), \qquad V(0) = 0 \tag{3.46}$$

reach the threshold V_{th} for the first time? In the following, I will adopt the latter point of view.

The first-passage-time statistics can be quantified by the FPT density or conditional ISI density $P(T_{i+1}|a_i)$. Recall that the first and second moment of this conditional probability density are denoted by $\langle T_{i+1}|a_i\rangle$ and $\langle T_{i+1}^2|a_i\rangle$, respectively. An associated problem concerns the distribution of the variable $a(t)$ at the time of the first threshold crossing T_{i+1}. Equivalently, the distribution of a_{i+1} can be considered, where the jump of $a(t)$ at threshold crossing is taken into account. This conditional distribution will be called transition probability density and will be denoted by $p_{tr}(a_{i+1}|a_i)$.

In general, the first-passage-time problem in the time-inhomogeneous case is a difficult problem. Approximations for the moments of the first-passage-time have been developed in Lindner [2004b], Lindner and Longtin [2005] for the case that the exponential term in Eq. (3.46) can be treated as a small perturbation. In that work, the FPT moments could be obtained as a perturbation expansion in the small parameter $a_i/\mu \ll 1$. Here, an approximation for the first-passage-time density is put forward that is valid for arbitrary a_i but assumes sufficiently weak noise. The approximation is based on a linearization of the dynamics about the deterministic time $T_{det}(a_i)$. For weak noise, trajectories will be close to the noiseless dynamics and the shape of the first-passage-time density is approximately determined by the dynamics in the vicinity of $T_{det}(a_i)$. An instructive way to achieve this, is to regard an equivalent system, in which the stochastic dynamics of the membrane potential is time-homogeneous (autonomous) and the threshold becomes time-dependent. To this end, I consider the deterministic dynamics $\dot{\bar{V}}(t) = \mu - a_i e^{-t/\tau_a}$, $\bar{V}(0) = 0$, and introduce the variables $x = V - \bar{V}$ and $x_{th}(t) = V_{th} - \bar{V}(t)$. Then the model (3.46) is equivalent to

$$\dot{x} = \sqrt{2D}\xi(t), \qquad x(0) = 0, \qquad x_{th}(t) = V_{th} - \left[\mu t - a_i\tau_a\left(1 - e^{-t/\tau_a}\right)\right] \tag{3.47}$$

and the first-passage time is the first time that $x(t) = x_{th}(t)$ (Fig. 3.8). The time-dependent threshold can be linearized yielding $x_{th,lin}(t) = -\dot{\bar{V}}(T_{det}(a_i))\,(t - T_{det}(a_i))$. For weak noise, it is unlikely that trajectories cross $x_{th}(t)$ outside the linear regime. Transforming the system back to a constant threshold ϑ_0 results in the approximate dynamics

$$\dot{V}_{lin} = \mu_{eff}(a_i) + \sqrt{2D}\xi(t) \tag{3.48}$$

with an effective base current

$$\mu_{eff}(a_i) = \mu - a_i \exp\left(-\frac{T_{det}(a_i)}{\tau_a}\right). \tag{3.49}$$

and an effective threshold $\vartheta_0(a_i) = \mu_{eff}(a_i)T_{det}(a_i)$.

Equation (3.48) represents a PIF model with a constant base current $\mu_{eff}(a_i)$ and an effective firing threshold $\vartheta_0(a_i)$. The conditional ISI density is thus given by the inverse

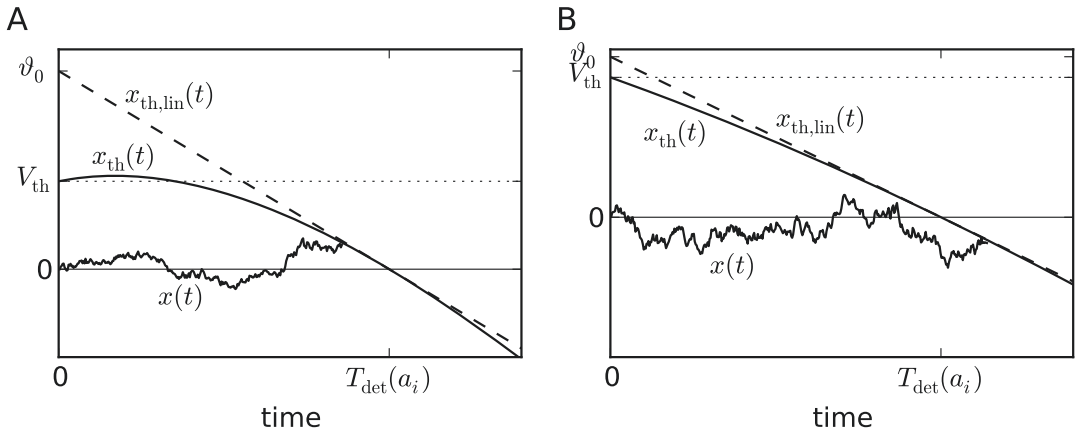

Figure 3.8.: Illustration of the weak-noise approximation of the first-passage-time to a time-dependent boundary. The original dynamics with the time-dependent drift $\mu - a_i e^{-t/\tau_a}$ and a constant threshold $V_{\rm th}$ can be mapped to the time-homogeneous Wiener process $x(t)$ and a time-dependent threshold $x_{\rm th}(t)$, which exhibits a zero crossing at time $T_{\rm det}(a_i)$. The approximation consists in a linearization of the threshold about $T_{\rm det}(a_i)$. At $t = 0$ the resulting line $x_{\rm th,lin}(t)$ yields the effective threshold ϑ_0. **A** $a_i > \mu$ (this is the condition for the presence of a maximum of $x_{\rm th}(t)$), $\tau_a = T_{\rm det}(a_i)$, **B** $a_i < \mu$, $\tau_a = 10 T_{\rm det}(a_i)$.

Gaussian

$$P(T_{i+1}|a_i) = \frac{\vartheta_0(a_i)}{\sqrt{4\pi D T_{i+1}^3}} \exp\left[-\frac{(T_{i+1} - T_{\rm det}(a_i))^2}{4[D/\mu_{\rm eff}^2(a_i)]T_{i+1}}\right] \tag{3.50}$$

with the conditional mean ISI

$$\langle T|a_i\rangle = T_{\rm det}(a_i) \tag{3.51}$$

and the conditional coefficient of variation

$$C_V(a_i) = \frac{1}{\mu_{\rm eff}(a_i)}\sqrt{\frac{2D}{T_{\rm det}(a_i)}}. \tag{3.52}$$

In deriving the conditional ISI statistics, two approximations have been applied: one concerns the linearization of the dynamics about the deterministic period $T_{\rm det}(a_i)$, which is expected to yield a faithful approximation if the standard deviation of the FPT is much smaller than τ_a. The second approximation, concerns the approximate solution of the transcendental equation (3.10) for $T_{\rm det}(a_i)$ to first- and second-order in the perturbation parameter $\delta a_i/a^*$. According to perturbation theory, the corrections (3.26) are valid if $|\delta a_i| \ll a^*$, i.e. if the trajectories are sufficiently close to the limit-cycle. In the following, the validity of the two approximations will be discussed separately by using first the exact numerical solution for $T_{\rm det}(a_i)$ and investigate then the effect of the first- and second-order approximation of $T_{\rm det}(a_i)$.

For weak noise, these conditional mean ISI and CV agree well with simulations (Fig. 3.9). In particular, the usage of the exact solution $T_{\rm det}(a_i)$ (obtained by numerically solving Eq. (3.10)) in Eq. (3.51) and (3.52) results in quite accurate predictions. This supports the approximation based on the linearization of the time-dependent threshold for weak noise. For strong noise, the performance of the weak-noise theory is expected to be poor. Still, for $D = 1$ (leading to CVs comparable to a Poisson process) the weak-noise the-

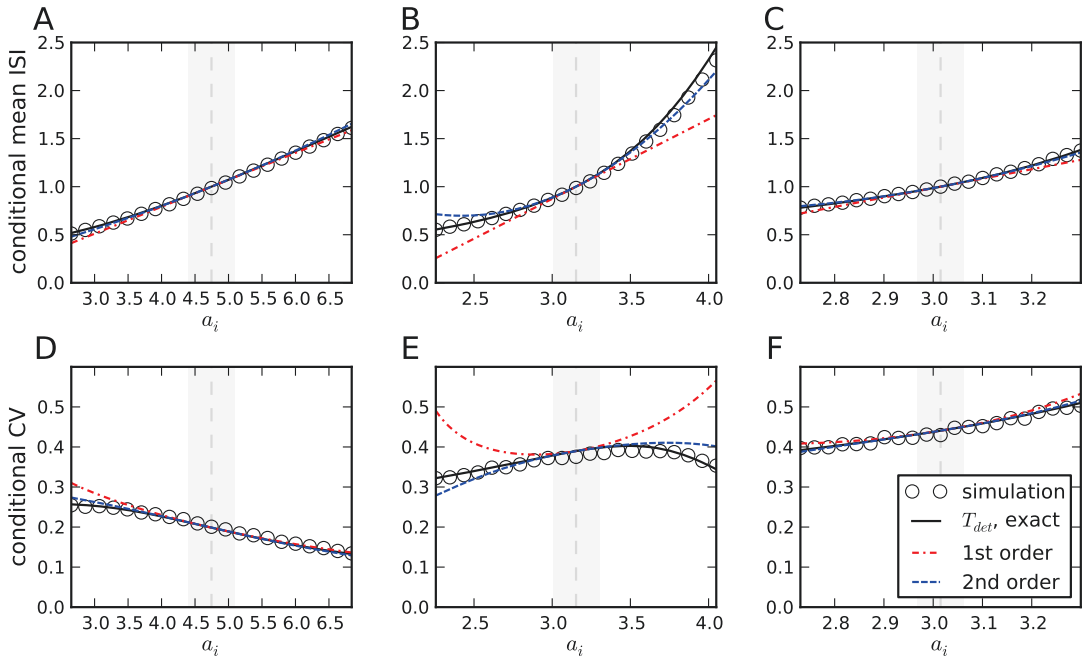

Figure 3.9.: Mean and CV of the conditional ISI for moderate noise intensity. The conditional mean ISI or mean first-passage-time $\langle T|a_i\rangle$ as a function of the initial value a_i for $D = 0.1$, $\tilde{\Delta} = 3V_{\text{th}}$ and $T^* = 1$ (corresponds to $\mu = 4$). The adaptation time constant is **A** $\tau_{\text{a}} = T^*$, **B** $\tau_{\text{a}} = 10T^*$ and **C** $\tau_{\text{a}} = 100T^*$. Circles represent the average over 10^4 first-passage times, the black solid lines display the weak-noise theory Eq. (3.51), where $T_{\text{det}}(a_i)$ is obtained from a numerical solution of Eq. (3.10) using the Newton-Raphson method. The first and second-order approximations of $T_{\text{det}}(a_i)$ (Eqs. (3.20), (3.26)) are displayed by the red dashed-dotted line and the blue dotted line, respectively. The dashed vertical line and the gray-shaded area indicate the mean a^* and standard deviation σ_a of the stationary sequence $\{a_i\}$, i.e. the typical range of a_i. **D-F** show the corresponding conditional coefficients of variations for $\tau_{\text{a}} = T^*, 10T^*, 100T^*$, respectively. The theoretical curves are based on Eq. (3.52).

ory yields reasonable results for typical values of the stationary sequence $\{a_i\}$, i.e. for initial values that lie within a one-standard-deviation interval about a^* (Fig. 3.10). The agreement is particularly good for small initial values a_i. However, for $a_i > a^*$ the weak noise theory significantly deviates from the conditional mean ISI and CV obtained from simulations with strong noise. In this case, trajectories are likely to hit the threshold at times not close to the deterministic FPT $T_{\text{det}}(a_i)$, where the time-dependent threshold is not captured by the linear approximation about $T_{\text{det}}(a_i)$. It is worth to note that the CV exhibits a maximum. In particular, for large a_i the conditional CV decreases (Fig. 3.9E, Fig. 3.10D,E), an effect that is qualitatively captured by the weak-noise theory. A strong initial adaptation value has a strong hyperpolarizing effect which acts essentially as a refractory period, in which the neuron is unlikely to fire. This refractory period has a regularizing effect on the spike train. In fact, Fig. 3.9E and Fig. 3.10D,E suggest that the decrease sets in approximately when $a_i \sim \mu$. As discussed above, $V(t)$ hyperpolarizes on average if and only if $a_i > \mu$.

The second approximation based on the first- and second-order corrections of $T_{\text{det}}(a_i)$ for small δa_i provides analytical expressions for the ISI statistics. For weak noise, the typical deviations δa_i are small enough so that the first-order approximations matches ex-

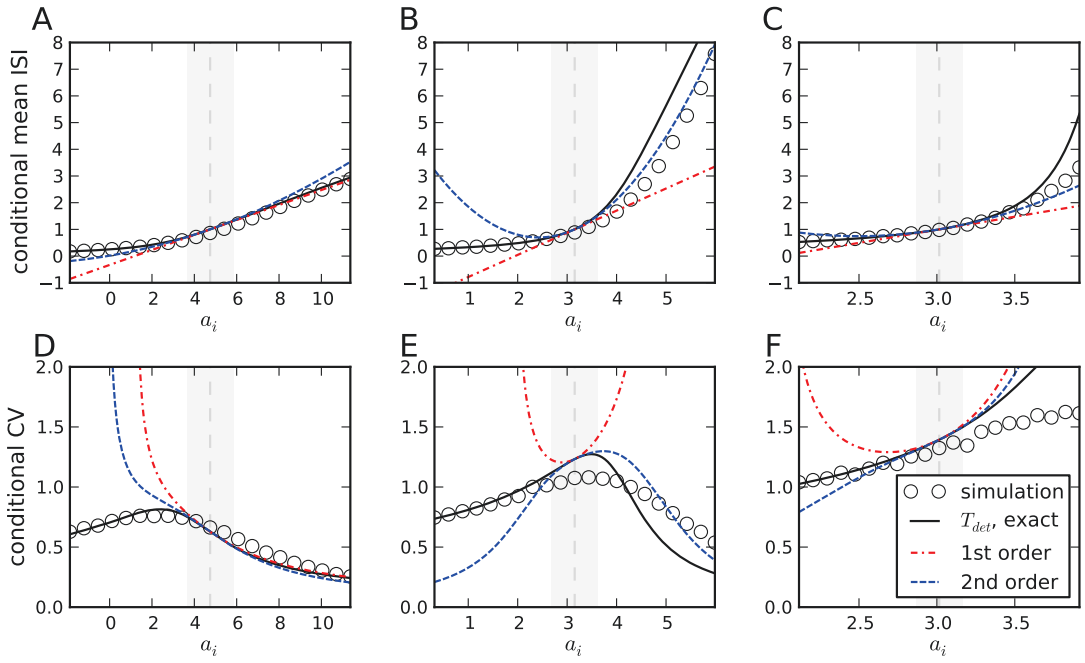

Figure 3.10.: Mean and CV of the conditional ISI for strong noise. Same as Fig. 3.9, but $D = 1$.

cellently with the exact function $T_{\mathrm{det}}(a_i)$ (Fig. 3.9A,C). Small deviations can be observed for intermediate adaptation time constants and large δa_i (Fig. 3.9B), although in the $1\sigma_a$-interval about a^* the match is still excellent. Inserting the first- and second-order approximations into the expression for the conditional CV, Eq. (3.52), the match with the result obtained by using the exact values of $T_{\mathrm{det}}(a_i)$ is still reasonable (Fig. 3.9D–E). The worse agreement at intermediate adaptation time constants can be explained as follows: on the one hand, the perturbation theory becomes less accurate for increasing τ_{a} under the condition that the perturbation parameter $\epsilon_a = \delta a_i / a^*$ is fixed to some small value (Fig. 3.5). On the other hand, the typical value of ϵ_a, determined by the standard deviation σ_a of the sequence $\{a_i\}$, also depends on τ_{a}. In fact, I will show in Sec. 3.3.5 that σ_a decreases with increasing τ_{a} so that the first-order correction correctly describes the behavior of $T_{\mathrm{det}}(a_i)$ in the large τ_{a} limit.

For strong noise, the deviations of trajectories from the limit-cycle increase. On this larger scale of $\delta a_i \sim \sigma_a$, the first-order approximation of $T_{\mathrm{det}}(a_i)$ is not expected to be valid (Fig. 3.10). One obvious shortcoming is that the conditional mean ISI can become negative in the linear approximation for large deviations δa_i. Moreover, the disagreement is particularly severe when the first-order approximation is applied to the conditional CV. In this case, $C_{\mathrm{V}}(a_i)$ diverges if either $T_{\mathrm{det}}(a_i)$ or $\mu_{\mathrm{eff}}(a_i)$ becomes zero. As mentioned above, the linearization of $T_{\mathrm{det}}(a_i)$ generally leads to negative values involving a zero crossing at some a_i. Similarly, there is the possibility that the effective base current $\mu_{\mathrm{eff}}(a_i) = \mu - a_i e^{-T_{\mathrm{det}}(a_i)/\tau_{\mathrm{a}}}$ changes sign at some large value of a_i. Consequently, the conditional CV diverges at this a_i according to Eq. (3.52) (Fig. 3.10E, sign changes at approximately $a_i \approx 5.3$). This artifact is not possible when the exact $T_{\mathrm{det}}(a_i)$ is employed, but it can happen when $T_{\mathrm{det}}(a_i)$ is linearized. The region of validity can be slightly improved by the use of the second-order approximation. However, the weak noise approximation

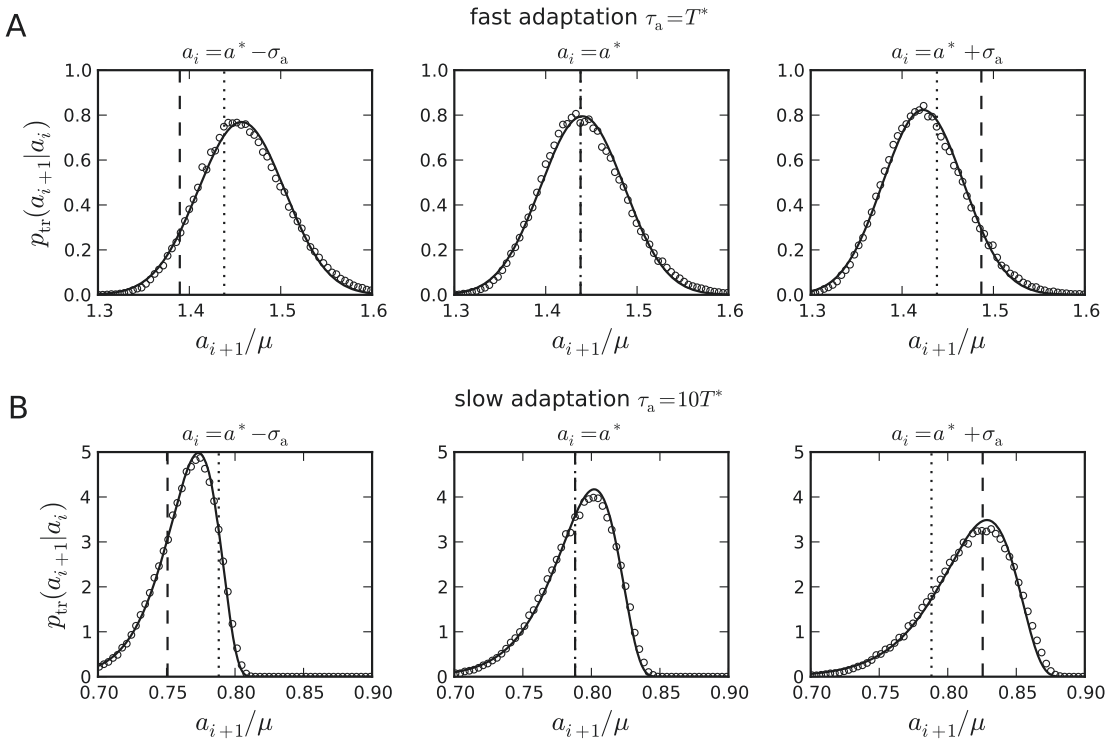

Figure 3.11.: Transition probability density for $D = 0.1$. For the initial values $a_i = a^*$ and $a^* \pm \sigma_a$ with σ_a being the standard deviation of the stationary sequence $\{a_i\}$ (position of a_i indicated by the dashed vertical line), the density of the subsequent value $a_{i+1} = a_i e^{-T_i/\tau_a} + \Delta$ is displayed by circles (simulation) and solid lines (weak-noise theory Eq. (3.53) using the exact value of $T_{det}(a_i)$). The position of the mean value a^* is depicted by a dotted vertical line. **A** $\tau_a = T^*$, $\tilde{\Delta} = 10V_{th}$ (afterhyperpolarization regime $a^* > \mu = 11$), **B** $\tau_a = 10T^*$, $\tilde{\Delta} = 3V_{th}$ ($a^* < \mu = 4$).

of the conditional ISI statistics should be generally used with caution when the noise is not weak.

The transition probability density $p_{tr}(a_{i+1}|a_i)$

The statistics of a_{i+1} for a given a_i can easily be obtained from the distribution $P(T_i|a_i)$ because a_{i+1} is related to the random variable T_i by the nonlinear transformation Eq. (3.5).

Eq. (3.50) leads then to

$$p_{tr}(a_{i+1}|a_i) = \left|\frac{da_{i+1}}{dT_i}\right|^{-1} P(T_i|a_i)\Big|_{T_i=\tau_a \ln\left(\frac{a_i}{a_{i+1}-\Delta}\right)} \tag{3.53}$$

$$= \frac{\vartheta_0(a_i)\tau_a/(a_{i+1}-\Delta)}{\sqrt{4\pi D\tau_a \ln\frac{a_i}{a_{i+1}-\Delta}}} \exp\left\{-\frac{\left[\tau_a \ln\left(\frac{a_i}{a_{i+1}-\Delta}\right) - T_{det}(a_i)\right]^2}{4[D/\mu_{eff}^2(a_i)]\tau_a \ln\left(\frac{a_i}{a_{i+1}-\Delta}\right)}\right\}. \tag{3.54}$$

This distribution is defined on the finite interval $a_{i+1} \in (\Delta, a_i + \Delta)$. Fig. 3.11 shows transition probability densities for different initial adaptation states a_i in the case of weak

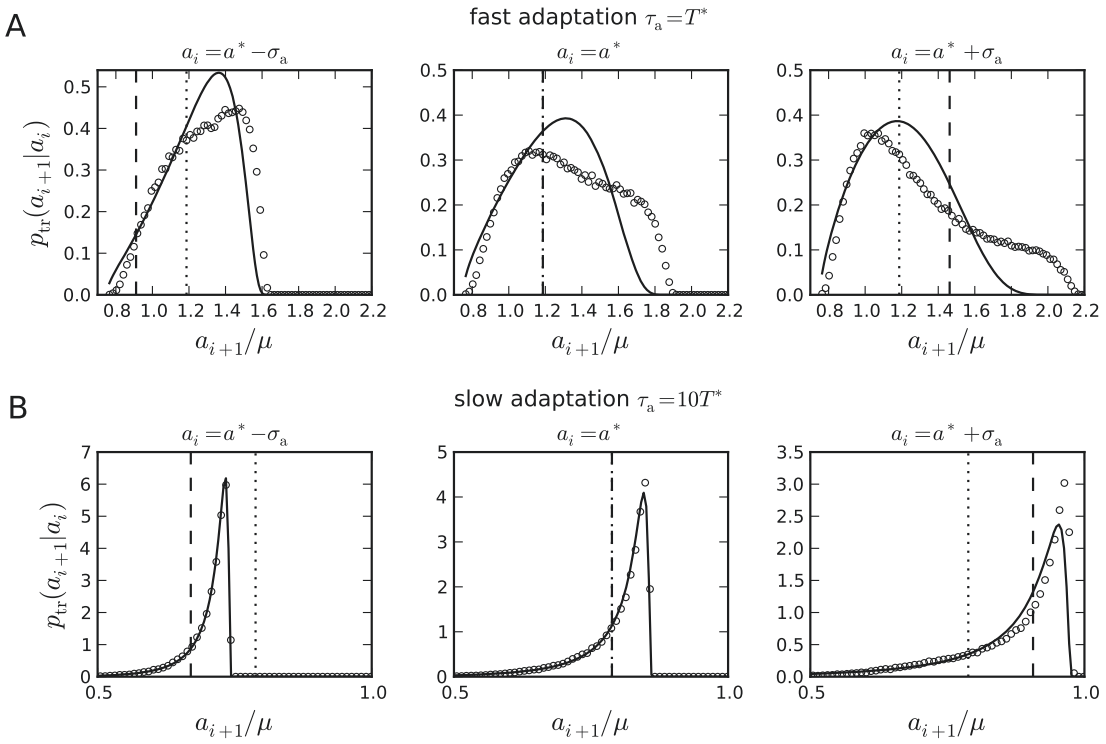

Figure 3.12.: Transition probability density for strong noise, $D = 1$**.** Same as Fig. 3.11, but **A** $\tau_a = T^*$, $\tilde{\Delta} = 3V_{th}$ (afterhyperpolarization regime $a^* > \mu = 4$) **B** $\tau_a = 10T^*$, $\tilde{\Delta} = 3V_{th}$ ($a^* < \mu = 4$).

noise. The normalized histograms of a_{i+1} obtained from simulations are well captured by the weak-noise theory, Eq. (3.53). For the chosen parameters the transition probability densities show a unimodal shape located close to a^*. The skewness can be either positive or negative depending on the parameters. Interestingly, the position of the mean a_{i+1} seems to be correlated with the initial adaptation state a_i in a distinct manner. For $a^* > \mu$ (afterhyperpolarization regime) and not a too large δa_i, the mean a_{i+1} is above a^* if a_i is below a^*, and vice versa (Fig. 3.11A). In other words, a_i and a_{i+1} seem to be anti-correlated for $a^* > \mu$. In contrast, a_{i+1} seems to be positively correlated with a_i for $a^* < \mu$ (Fig. 3.11B). This is intuitively plausible from the deterministic picture. Consider the case that a^* is well below μ (e.g. Fig. 3.4C,D). Then a small positive initial deviation δa_i of a trajectory will be transported along $\mathcal{C}^*$ leading to a positive deviation at the threshold. Likewise, a negative deviation leads to a negative deviation at the threshold. The situation is, however, different if a^* is well above μ (see e.g. Fig. 3.4A,B). In this case, an initial deviation δa_i reverts its sign at the vertex of $\mathcal{C}^*$ when transported along the limit-cycle. As a result, the sign of the deviation at the threshold will be reverted, too. A thorough quantitative description of the correlations in the sequence $\{a_i\}$ will be given in the next section.

Let us conclude with two remarks. First, Fig. 3.11 also illustrates that the main effect of increasing the adaptation time constant consists of shrinking the width of the distribution. We return to this issue in Sec. 3.3.5. Second, increasing the noise intensity by a factor 10, deviations appear that are due to non-linear effects that are not captured by

the linearized threshold (Fig. 3.12A, corresponding to the parameter set B in Fig. 3.4 and reflecting the threshold dynamics depicted in Fig. 3.8A). Specifically, using the moving threshold picture (cf. Fig. 3.8), strong noise facilitates short ISIs, which can lead to effects that are sensitive to the short-time dynamics of the moving threshold. Indeed, the moving threshold $x_{\mathrm{th}}(t)$ is a concave function, i.e. $x_{\mathrm{th}}(t)$ lies below the linearized threshold $x_{\mathrm{th,lin}}(t)$ (Fig. 3.8). Thus, short FPTs become more likely, simply because the true threshold $x_{\mathrm{th}}(t)$ is closer to the reset than $x_{\mathrm{th,lin}}$. Short FPTs, however, entail large values of a_{i+1}, which should be reflected in the distribution of a_{i+1}. In fact, Fig. 3.12A shows that the distributions have additional weight close to the maximally possible value $a_i + \Delta$ (which would correspond to $T_i = 0$). This additional probability is compensated by the lack of probability at moderate values of a_{i+1}. Another consequence of a larger noise intensity are larger initial deviations, which can cause surprising effects: In Fig. 3.12B (corresponding to the parameter set D in Fig. 3.4), the weak-noise approximation works well for $a_i < \mu$ even for strong noise. In this case, $a_i < \mu$, which ensures a monotonically decreasing threshold $x_{\mathrm{th}}(t)$. Moreover, $x_{\mathrm{th}}(t)$ is almost linear due to the large adaptation time constant τ_{a}. This situation is depicted in Fig. 3.8B (note that ϑ_0 is close to V_{th}). Thus, linearization about $T_{\mathrm{det}}(a_i)$ does not lead to large errors at short ISIs. However, if a_i becomes larger than μ a maximum in x_{th} appears and the discrepancy between $x_{\mathrm{th}}(t)$ and $x_{\mathrm{th,lin}}(t)$ rises rapidly. This explains the failure of the linearization in the rightmost panel of Fig. 3.12B: The true distribution of a_{i+1} has a sharp maximum at the right boundary of the domain corresponding to very short ISIs. Intermediate ISIs are actually inhibited because of the maximum of $x_{\mathrm{th}}(t)$.

3.3.2. The Fokker-Planck equation

So far, we have analyzed the conditional ISI statistics. As explained in Sec. 1.2.6, the full ISI statistics can be obtained by averaging the conditional ISI statistics with respect to the distribution of the adaptation current upon firing $P_{\mathrm{f}}(a_i)$, i.e. the stationary distribution of the sequence $\{a_i\}$. How can this distribution be computed analytically? One way to obtain $P_{\mathrm{f}}(a_i)$ is to calculate the stationary solution of the Fokker-Planck equation associated with the adapting PIF model. In the following, I will introduce the Fokker-Planck equation and derive the stationary distribution of the membrane potential $P_0(V)$ as well as the upon firing distribution $P_{\mathrm{f}}(a_i)$.

Formulation of the boundary value problem

The stochastic differential equation (3.1) of the PIF model can be reformulated in terms of the joint probability density $P(V,a,t)$ in the domain $V < V_{\mathrm{th}}$, $a > 0$. The function $P(V,a,t)$ must satisfy the continuity equation

$$\partial_t P(V,a,t) + \partial_V J_V(V,a,t) + \partial_a J_a(V,a,t) = \underbrace{-J_V(V_{\mathrm{th}}-,a,t)\delta(V-V_{\mathrm{th}})}_{\text{absorption at } V=V_{\mathrm{th}}} + \underbrace{J_V(V_{\mathrm{th}}-,a-\Delta,t)\delta(V)}_{\text{jump and reinsertion at } V=0}. \quad (3.55)$$

As in Chap. 2, the notation $f(x-)$ and $f(x+)$ stands for the left and right-sided limit, respectively. Furthermore, $J_V(V,a,t)$ and $J_a(V,a,t)$ are the components of the two-dimensional

probability current $\mathbf{J} = (J_V, J_a)$, which are given by

$$J_V(V,a,t) = [(\mu - a) - D\partial_V]P(V,a,t), \tag{3.56}$$

$$J_a(V,a,t) = -\frac{a}{\tau_\mathrm{a}}P(V,a,t). \tag{3.57}$$

The right side of Eq. (3.55) represents the source and sink terms: trajectories that reach the threshold at the point $(V_\mathrm{th}, a - \Delta)$ are taken out of the system (sink) and are reinserted at the point $(0, a)$ (source). In other words, the sink and source terms realize the absorbing boundary at $V = V_\mathrm{th}$, the jump of the adaptation variable by an amount Δ and the reset to $V = 0$.

Alternatively, the continuity equation can be written without source and sink terms, but with explicit boundary conditions that realize the jump and reset condition. Using (3.56) and (3.57), the continuity equation attains the form of a Fokker-Planck equation:

$$\partial_t P(V,a,t) = [-(\mu - a)\partial_V + \frac{1}{\tau_\mathrm{a}}\partial_a a + D\partial_V^2]P(V,a,t). \tag{3.58}$$

The initial condition at $t = 0$ are not specified further, however, I require that the trajectory is initially in the domain $\{V, a | V \leq V_\mathrm{th}, a > 0\}$, in particular $P(V,a,0) = 0$ for $V > V_\mathrm{th}$. The boundary conditions can be derived from the continuity equation (3.55). First, the diffusion current in the variable V precludes any discontinuity of the probability density. In particular, $P(V,a,t)$ must be continuous at the reset,

$$P(0-,a,t) = P(0+,a,t). \tag{3.59}$$

The boundary conditions induced by the singular sink and source terms can be obtained by integrating the continuity equation with respect to V over an infinitesimal interval containing the threshold or the reset, respectively. In particular, the integral from $V_\mathrm{th} - \epsilon$ to $V_\mathrm{th} + \epsilon$ of $P(V,a,t)$ and $J_a(V,a,t) = -aP(V,a,t)/\tau_\mathrm{a}$ vanishes in the limit $\epsilon \to 0$ due to the continuity of $P(V,a,t)$ in the variable V. Furthermore, $J_V(V_\mathrm{th}-,a,t)$ cancels from both sides of the integrated continuity equation. This leaves the condition $J_V(V_\mathrm{th}+,a,t) = 0$, from which follows $P(V,a,t) = 0$ for all $V > V_\mathrm{th}$ and from continuity one must conclude the absorbing boundary condition

$$P(V_\mathrm{th},a,t) = 0 \tag{3.60}$$

Similarly, integrating the continuity equation about the reset potential from $V = -\epsilon$ to $V = \epsilon$ and letting $\epsilon \to 0$ yields the condition

$$J_V(0+,a,t) - J_V(0-,a,t) = J_V(V_\mathrm{th},a-\Delta,t).$$

Using the definition of the current J_V, Eq. (3.56), and accounting for the continuity and the absorbing boundary, Eq. (3.59) and Eq. (3.60), the latter condition becomes

$$\partial_V P(0+,a,t) - \partial_V P(0-,a,t) = \partial_V P(V_\mathrm{th},a-\Delta,t). \tag{3.61}$$

This discontinuity in the derivative $\partial_V P$ realizes the jump and reset. Furthermore, all probability and currents should vanish at infinity, which leads to the natural boundary

conditions

$$\lim_{V\to-\infty} P(V,a,t) = 0, \quad \lim_{a\to\infty} P(V,a,t) = 0, \quad \lim_{V\to-\infty} \partial_V P(V,a,t) = 0. \tag{3.62}$$

Finally, the probability density must be normalized,

$$\int_{-\infty}^{V_{\text{th}}} \mathrm{d}V \int_0^\infty \mathrm{d}a\, P(V,a,t) = 1. \tag{3.63}$$

The Fokker-Planck equation (3.58) together with the initial and boundary conditions Eq. (3.59)– (3.63) completely determine the boundary value problem.

The stationary Fokker-Planck equation

In the limit $t \to \infty$ the probability density $P(V,a,t)$ converges to a stationary probability density $P_0(V,a)$. This function is the unique solution of the boundary value problem (3.58)– (3.63) with $\partial_t P(V,a,t) = 0$. Knowing the stationary solution, one can derive the following quantities:

1. The stationary firing rate

$$r_0 = \int_0^\infty \mathrm{d}a\, J_V^{(s)}(V_{\text{th}},a) = -D\int_0^\infty \mathrm{d}a\, \partial_V P_0(V_{\text{th}},a), \tag{3.64}$$

   where the stationary probability current $J_V^{(s)} = [(\mu - a) - D\partial_V]P_0(V,a)$ and Eq. (3.60) has been used.

2. The distribution of the subthreshold membrane potential

$$P_0(V) = \int_0^\infty \mathrm{d}a\, P_0(V,a). \tag{3.65}$$

3. The distribution of the adaptation current upon firing

$$P_{\text{f}}(a) \propto J_V^{(s)}(V_{\text{th}}, a-\Delta) = -D\partial_V P_0(V_{\text{th}}, a-\Delta). \tag{3.66}$$

The two-dimensional Fokker-Planck equation for the stationary probability density cannot be solved exactly. To still find an approximate solution, I assume that the noise is weak. Specifically, the aim is to derive an asymptotic solution for the limit of weak noise. To this end, a small, non-dimensional parameter ϵ is introduced that scales the noise intensity as follows:

$$D = \epsilon\hat{D}, \tag{3.67}$$

where $\hat{D}$ is some characteristic noise intensity. Setting $\partial_t P_0(V,a) = 0$, the Fokker-Planck equation for the stationary probability density thus reads

$$-(\mu - a)\partial_V P_0 + \frac{1}{\tau_{\text{a}}}\partial_a(aP_0) + \epsilon\hat{D}\partial_V^2 P_0 = 0. \tag{3.68}$$

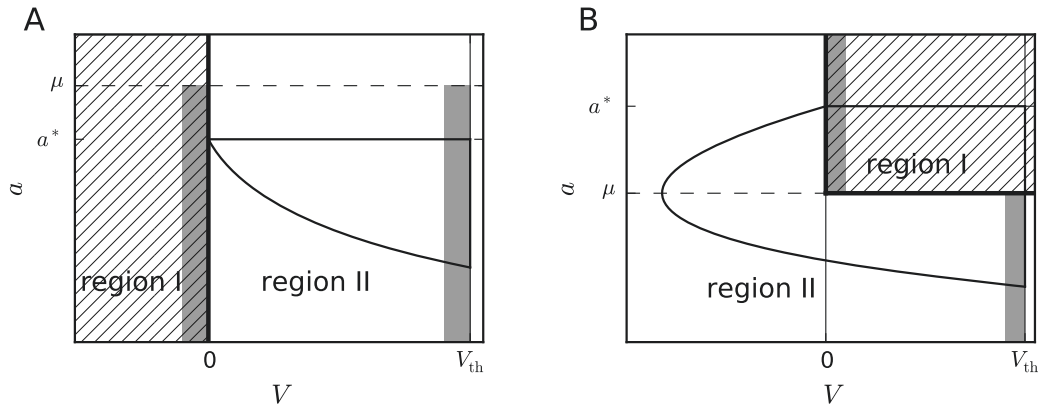

Figure 3.13.: Different regions of solutions and locations of the boundary layers. (A) Case $a^* < \mu$, **(B)** case $a^* > \mu$. The solution is calculated separately for region I (hatched area) and region II (white area). In the boundary layers of thickness $\mathcal{O}(\epsilon)$ (indicated by the gray-shaded areas) the solution drops off rapidly.

According to Eq. (3.59) – (3.62), the stationary solution has to fulfill the following boundary conditions

$$P_0(V_{\text{th}}, a) = 0, \tag{3.69}$$

$$P_0(0-, a) = P_0(0+, a), \tag{3.70}$$

$$\partial_V P_0(0+, a) - \partial_V P_0(0-, a) = \partial_V P_0(V_{\text{th}}, a - \Delta), \tag{3.71}$$

which express the absorption at the threshold, the continuity at the reset and the resetting of trajectories, respectively. In the stationary case, the natural boundary conditions become

$$\lim_{V \to -\infty} P_0(V, a) = 0, \quad \lim_{a \to \infty} P_0(V, a) = 0, \quad \lim_{V \to -\infty} \partial_V P_0(V, a) = 0. \tag{3.72}$$

The stationary solution is determined by the boundary-value problem Eq. (3.68) – (3.72) up to a constant factor that can be fixed by the normalization condition (3.63). For the weak-noise approximation method it is, however, more convenient to determine the multiplicative factor in another way: We already know that in the limit $\epsilon \to 0$ the firing rate is asymptotic to $1/T^*$. Together with Eq. (3.64), this yields the additional boundary condition

$$-\epsilon \hat{D} \int_0^\infty \mathrm{d}a \, \partial_V P_0(V_{\text{th}}, a) = \frac{1}{T^*}, \tag{3.73}$$

which completes the formulation of the boundary value problem for $P_0(V, a)$.

The Fokker-Planck equation (3.68) is solved in different regions, which depend on whether $a^* < \mu$ or $a^* > \mu$ (Fig. 3.13). The solutions are then patched together according to the continuity and reset condition. In particular, for $a^* < \mu$ (Fig. 3.13A) the Fokker-Planck equation is solved below the reset line ($V < 0$) and between reset and threshold line ($0 < V \leq V_{\text{th}}$) separately. These regions are referred to as region I and region II, respectively. Slightly differently, for $a^* > \mu$ the plane is divided into region I and region II as indicated in Fig. 3.13B. The solution in region II has to be further subdivided into

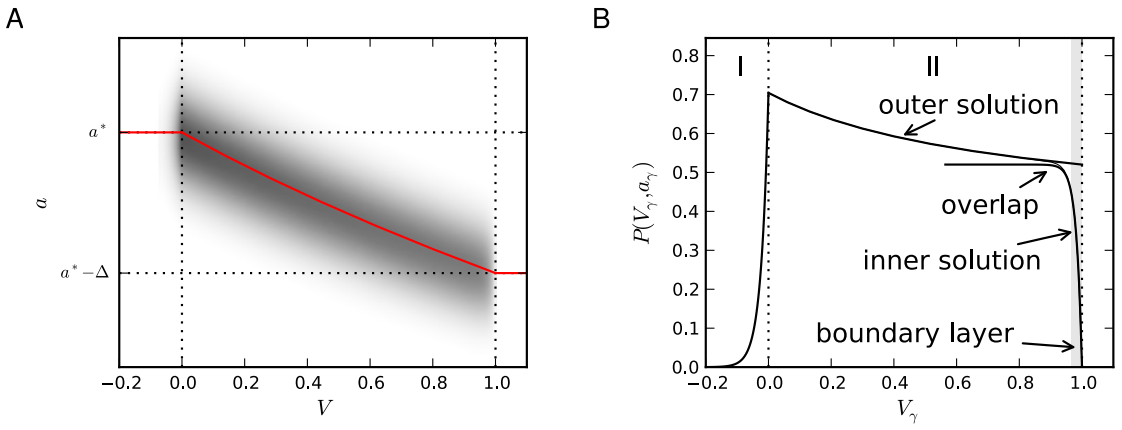

Figure 3.14.: Structure of the stationary solution of the Fokker-Planck equation. A illustrates the stationary probability density in the environment of the limit-cycle. The density along the red path γ is shown in **B**. It illustrates the different regions of solutions and indicates how the solutions are patched together. In region I (corresponding to $V < 0$ in the case $a^* < \mu$) the solution rises steeply in a boundary layer of thickness $\mathcal{O}(\epsilon)$ below the reset. In region II, I use a WKB ansatz for the solution which must be continuous at $V = 0$. This ansatz cannot, however, capture the steep decline to zero in a second boundary layer close to the threshold (absorbing boundary). The inner solution of this boundary layer is asymptotically matched to the WKB solution (outer solution).

a solution within a thin boundary layer close to the threshold ("inner solution") and a solution outside the boundary layer ("outer solution"). The outer solution will be obtained using WKB theory, which yields the asymptotic form of the probability density around the deterministic limit-cycle $\mathcal{C}^*$. In the deterministic limit, the probability density is proportional to a δ-function, which ensures that all probability is concentrated on the limit cycle. Intuitively speaking, the WKB solution can be seen as a noise-induced softening of this δ-singularity by approximating the local shape of the probability density (perpendicular to the limit-cycle) by a Gaussian, the variance of which is proportional to ϵ.

3.3.3. Stationary solution of the Fokker-Planck equation

The detailed derivation of the stationary solution is presented in the appendix, Sec. B.2. Here, I will provide a brief overview of the derivation in order to illustrate the main idea of solution. In region I, the Fokker-Planck equation can be solved in perturbation theory by using the stretched variable $x = V/\epsilon$. This transformation removes the singular behavior of the probability density at $V = 0$ (reset) in the limit $\epsilon \to 0$ (Fig. 3.14). As a result (Sec. B.2.1), the leading-order solution in region I can be written as

$$P_{0,\mathrm{I}}(V, a) = \frac{M(a)}{\sqrt{\epsilon}\lambda(a)} \exp\left(\frac{\lambda(a)V}{\epsilon}\right), \tag{3.74}$$

where

$$\lambda(a) = \frac{\mu - a}{\hat{D}} \tag{3.75}$$

and $M(a)$ is some function of a that is determined by continuity condition (3.70).

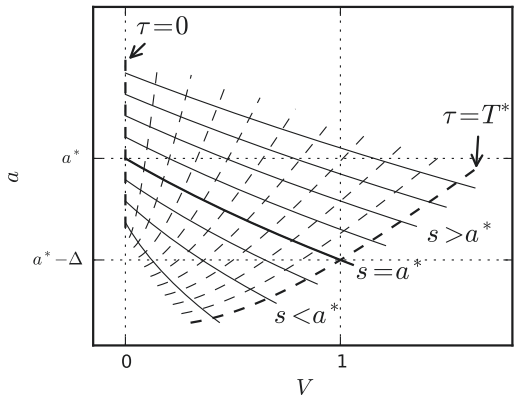

Figure 3.15.: Parametrization of region II by the characteristic coordinates τ and s. For each value of s there is a characteristic curve parametrized by the coordinate τ (solid lines). Along these curves the functions $\Phi(V,a)$ and $\Psi(V,a)$ obey ordinary differential equations with respect to the "time" τ. The parameter s corresponds to the initial condition at "time" $\tau = 0$, where in the original coordinates $V = 0$ and $a = s$. A particular important characteristic is given by the initial value $s = a^*$: this curve is identical to the limit curve $\mathcal{C}^*$, where all probability is concentrated in the deterministic limit. Because the deterministic period is T^*, the characteristic curve for $s = a^*$ crosses the threshold $V = V_{\text{th}}$ at "time" $\tau = T^*$. The dashed lines are isochrons, where $\tau = \text{const.}$.

In region II, a perturbation expansion of the Fokker-Planck equation cannot yield a solution that satisfies the boundary conditions at both $V = 0$ and $V = V_{\text{th}}$. This is related to the fact that the solution drops off rapidly within a boundary layer of thickness $\mathcal{O}(\epsilon)$ close to the threshold (Fig. 3.14). However, boundary layer theory can be used to find separate solutions outside and inside the boundary layer, which are then matched asymptotically [see e.g. Bender and Orszag, 1999]. These solutions are usually called *outer* and *inner solution*, respectively. The inner solution, i.e. the solution close to the threshold ($0 \ll V \leq V_{\text{th}}$), can be obtained analogously as in region I; in particular, using the stretched variable $x = (V - V_{\text{th}})/\epsilon$ the Fokker-Planck equation can be solved perturbatively resulting in (Sec. B.2.2)

$$P_{0,\text{II,in}}(V,a) = \frac{N(a)}{\sqrt{\epsilon}\lambda(a)} \left[\exp\left(\frac{\lambda(a)(V - V_{\text{th}})}{\epsilon} \right) - 1 \right]. \tag{3.76}$$

Here, $N(a)$ is a function that has to be determined by the reset condition, Eq. (3.71).

The outer solution can be obtained by using the WKB approximation [see e.g. Schuss, 2009]. This approximation assumes the following ansatz for the outer solution:

$$P_{0,\text{II,out}}(V,a) = \frac{1}{\sqrt{2\pi\epsilon}} \Psi(V,a) \exp\left(-\frac{\Phi(V,a)}{\epsilon} \right), \tag{3.77}$$

where the functions $\Phi(V,a)$ and $\Psi(V,a)$ can be interpreted as a non-equilibrium potential [Graham and Tél, 1984] and a modulation function, respectively. These functions satisfy first-order, nonlinear partial differential equations, which can be solved by the method of characteristics. In this solution further constraints for $\Phi(V,a)$ have to be taken into account that guarantee that the non-equilibrium potential has a local minimum along the limit curve $\mathcal{C}^*$. Moreover, it is advantageous to change to a coordinate system that is given by the characteristics of the system (see Fig. 3.15 for an illustration of the new coordinate system). These coordinates are denoted by s and τ and have the following interpretation: s labels the characteristic curves $\gamma(s) = (V(\tau;s), a(\tau;s))$ of the system as an initial condition of a for $\tau = 0$.[4] On the other hand, τ parametrizes a characteristic

[4] The initial conditions are $a(\tau = 0;s) = s$ and $V(\tau = 0;s) = 0$ (see Fig. 3.15 and Sec. B.2.2 for more details).

curve, i.e. it can be seen as the "time" along such a curve. The particular characteristic curve for $s = a^*$ coincides with the deterministic limit curve $\mathcal{C}^*$. On this characteristic, the parameter τ coincides indeed with the time t that elapses for a real trajectory on the limit-cycle. For $s \neq a^*$, the characteristic curve does, in general, not coincide with a trajectory that starts at $V = 0$ and $a = s$. As a result (Sec. B.2.2), the WKB solution yields the transformation law

$$V(\tau, s) = \left[\mu + 2\hat{D}p_0(s)\right]\tau - \tau_a s\left(1 - e^{-\tau/\tau_a}\right), \tag{3.78}$$

$$a(\tau, s) = se^{-\tau/\tau_a} \tag{3.79}$$

as well as the solution parametrized by τ and s:

$$\Phi(V, a) \equiv \phi(\tau, s) = \hat{D}p_0^2(s)\tau + \phi_0(s) \tag{3.80}$$

$$\Psi(V, a) \equiv \psi(\tau, s) = \psi_0(s)e^{\tau/\tau_a}\sqrt{\frac{\mu - s + 2\hat{D}p_0(s)}{2\hat{D}p_0{}'(s)s\tau/\tau_a + \mu - s + 2\hat{D}p_0(s)}}, \tag{3.81}$$

where

$$p_0(s) = -\frac{\mu - s}{2\hat{D}} + \mathrm{sgn}(\mu - a^*)\sqrt{\frac{(\mu - s)^2}{4\hat{D}^2} + \frac{s}{\hat{D}\tau_a}\phi_0'(s)}. \tag{3.82}$$

The "initial" functions $\phi_0(s) = \phi(0, s)$ and $\psi_0(s) = \psi(0, s)$ have to be determined by the reset condition and normalization condition, respectively. However, satisfying these boundary conditions for all $s > 0$ is analytically infeasible. Therefore, I will require these conditions only in the vicinity of the limit cycle ($s = a^*$). This local implementation of the boundary conditions about $s = a^*$ is justified for sufficiently weak noise. To obtain the local boundary conditions, I only consider the leading-order behavior

$$\phi_0(s) = \frac{\phi_0''(a^*)}{2}(s - a^*)^2 + \mathcal{O}((s - a^*)^3), \qquad \psi_0(s) = \psi_0(a^*) + \mathcal{O}(s - a^*), \tag{3.83}$$

where I used the fact that $\phi_0(a)$ and $\phi_0'(a)$ must vanish on the limit cycle ($a = a^*$) to ensure the correct deterministic limit (cf. Sec. B.2.2, Eqs. (B.40), (B.42)). Thus, it remains to determine the numbers $\phi_0''(a^*)$ and $\psi_0(a^*)$ from the reset and normalization condition, respectively. Furthermore, since the reset condition also involves the behavior of the probability density at the threshold, the inner and outer solution have to be matched asymptotically in a common overlap region (Fig. 3.14). As the final result of the reset condition (Sec. B.2.3), we obtain

$$\boxed{\phi_0''(a^*) = \frac{\tau_a^2\mu\Delta\left[2a^*(\mu - a^* + \Delta) - \mu\Delta\right]}{2\hat{D}a^{*2}T^*(a^* - \Delta)^2}.} \tag{3.84}$$

Note that this expression of the curvature of the non-equilibrium potential is directly related to the variance of a upon firing (see below). Finally, the normalization condition yields

$$\boxed{\psi_0(a^*) = \frac{\sqrt{\phi_0''(a^*)}}{|\mu - a^*|T^*},} \tag{3.85}$$

(Sec. B.2.4) and the functions

$$M(a) = \frac{\mu - a}{\sqrt{2\pi}\hat{D}} \psi_0(a^*) \exp\left[-\frac{\phi_0''(a^*)}{2\epsilon}(a-a^*)^2\right] \tag{3.86}$$

$$N(a) = -\frac{\lambda(a)}{\sqrt{2\pi}} \frac{|\mu - a^*|}{\mu - a^* + \Delta} \psi_0(a^*) \exp\left(-\frac{\phi_0''(a^*)}{2\epsilon}(a-a^*+\Delta)^2\right), \tag{3.87}$$

which completes the solution of the stationary Fokker-Planck equation.

Summary

Let me summarize the full solution. Using Eq. (3.74) and (3.86), the solution in region I can be written as

$$P_{0,\mathrm{I}}(V,a) = \frac{\psi_0(a^*)}{\sqrt{2\pi\epsilon}} \exp\left(\frac{\mu - a^*}{\epsilon\hat{D}} V - \frac{\phi_0''(a^*)}{2\epsilon}(a-a^*)^2\right). \tag{3.88}$$

In region II, the inner solution (close to the threshold) reads

$$P_{0,\mathrm{II,in}}(V,a) = \frac{\psi_0(a^*)}{\sqrt{2\pi\epsilon}} \frac{|\mu - a^*|}{\mu - a^* + \Delta} \left[1 - \exp\left(\frac{\mu - a^* + \Delta}{\epsilon\hat{D}}(V - V_{\mathrm{th}})\right)\right] \times \exp\left[-\frac{\phi_0''(a^*)}{2\epsilon}(a-a^*+\Delta)^2\right], \tag{3.89}$$

where Eq. (3.76) and (3.87) have been used. The outer solution in the neighborhood of the limit cycle has the parametric representation

$$P_{0,\mathrm{II,out}}(V,a) = \frac{\psi_0(a^*)e^{\tau/\tau_{\mathrm{a}}}}{\sqrt{2\pi\epsilon}} \sqrt{\frac{\mu - s + 2\hat{D}p_0(s)}{2\hat{D}p_0{}'(s)s\tau/\tau_{\mathrm{a}} + \mu - s + 2\hat{D}p_0(s)}} \tag{3.90}$$

$$\times \exp\left[-\frac{1}{\epsilon}\left(\hat{D}p_0^2(s)\tau + \frac{\phi_0''(a^*)}{2}(s-a^*)^2\right)\right] \tag{3.91}$$

$$V(\tau,s) = \left[\mu + 2\hat{D}p_0(s)\right]\tau - \tau_{\mathrm{a}} s\left(1 - e^{-\tau/\tau_{\mathrm{a}}}\right) \tag{3.92}$$

$$a(\tau,s) = se^{-\tau/\tau_{\mathrm{a}}} \tag{3.93}$$

for $0 \le \tau \le T^*$. Here, the function $p_0(s)$ is given by

$$p_0(s) = -\frac{\mu - s}{2\hat{D}} + \mathrm{sgn}(\mu - a^*)\sqrt{\frac{(\mu-s)^2}{4\hat{D}^2} + \frac{s(s-a^*)}{\hat{D}\tau_{\mathrm{a}}}\phi_0''(a^*)}. \tag{3.94}$$

The parameter s is varied in a small environment of $s = a^*$, e.g. $s \in [a^* - \mathcal{O}(\epsilon^{\frac{1}{2}}), a^* + \mathcal{O}(\epsilon^{\frac{1}{2}})]$. Outside this environment the probability density is exponentially small. The range of s should not include the critical point $s = \mu$, but must be either below or above this point. Note that the weak-noise theory developed here is not applicable to the singular case $a^* = \mu$.

Stationary solution evaluated on the limit cycle

On the limit-cycle, the solution simplifies considerably because $p_0(s)$ vanishes for $s = a^*$. In region I, the solution is concentrated about $a = a^*$. Specifically, the solution at $a = a^*$ reads

$$P_{0,\mathrm{I}}(V, a^*) = \frac{\psi_0(a^*)}{\sqrt{2\pi\epsilon}} \exp\left(\frac{\mu - a^*}{\epsilon\hat{D}} V\right). \tag{3.95}$$

In region II, the inner solution close to the threshold is concentrated about $a = a^* - \Delta$. Here, the solution reads

$$P_{0,\mathrm{II,in}}(V, a^*) = \frac{\psi_0(a^*)}{\sqrt{2\pi\epsilon}} \frac{|\mu - a^*|}{\mu - a^* + \Delta} \left[1 - \exp\left(\frac{\mu - a^* + \Delta}{\epsilon\hat{D}}(V - V_{\mathrm{th}})\right)\right]. \tag{3.96}$$

Using Eqs. (B.93) and (B.92) (appendix) yields a simple expression for the outer solution in parametric form:

$$P_{0,\mathrm{II,out}}(V(\tau), a(\tau))|_{\mathcal{C}^*} = \frac{\psi_0(a^*) e^{\tau/\tau_{\mathrm{a}}}}{\sqrt{2\pi\epsilon(\nu\tau + 1)}}, \qquad 0 \le \tau \le T^*, \tag{3.97}$$

$$a(\tau) = a^* e^{-\tau/\tau_{\mathrm{a}}}, \qquad V(\tau) = \mu\tau - \tau_{\mathrm{a}} a^* (1 - e^{-\tau/\tau_{\mathrm{a}}}), \tag{3.98}$$

where

$$\nu = \frac{2\hat{D} a^{*2} \phi_0''(a^*)}{\tau_{\mathrm{a}}^2 (\mu - a^*)^2}. \tag{3.99}$$

Fig. 3.16B,D show the stationary probability density along the limit-cycle. For weak-noise, the expression (3.97) agrees well with the simulation result, Fig. 3.16B. For larger noise intensity, the overall magnitude deviates between theory and simulation, although the shape is qualitatively similar, Fig. 3.16D. This is likely due to the fact that the maximum of the p.d.f. is off the deterministic limit-cycle, which seems to be indeed the case (Fig. 3.16A,C). Thus, the p.d.f. sampled along the limit-cycle is smaller than the theoretically predicted maximum. Note, that in the leading order WKB approximation, the maximum coincides with the deterministic limit-cycle. A shift of the maximum off the limit-cycle, could e.g. appear if higher-order terms of Ψ were taken into account. In the case $a^* > \mu$, the density along $\mathcal{C}^*$ is not a unique function of V: Figure 3.16E,F illustrates that this case can also be captured by the theory, Eq. (3.97).

3.3.4. Distribution of the membrane potential

From the general two-dimensional solution, it is possible to derive the stationary distribution of the (subthreshold) membrane potential. Such a distribution can be measured in experimental recordings of real neurons. Here, we are interested in how adaptation currents might shape the distribution of the subthreshold membrane potential. To this end, the distribution can be compared to the respective distribution of a PIF neuron without adaptation current, which has been already derived in the literature [Abbott and van Vreeswijk, 1993]. Specifically, the distribution of the non-adapting PIF model is given by

$$P_{\mathrm{PIF}}(V) = \frac{1}{V_{\mathrm{th}}} \begin{cases} 1 - e^{\frac{\mu}{D}(V - V_{\mathrm{th}})}, & 0 \le V \le V_{\mathrm{th}} \\ e^{\frac{\mu}{D}V} \left(1 - e^{-\frac{\mu}{D}V_{\mathrm{th}}}\right), & V < 0. \end{cases} \tag{3.100}$$

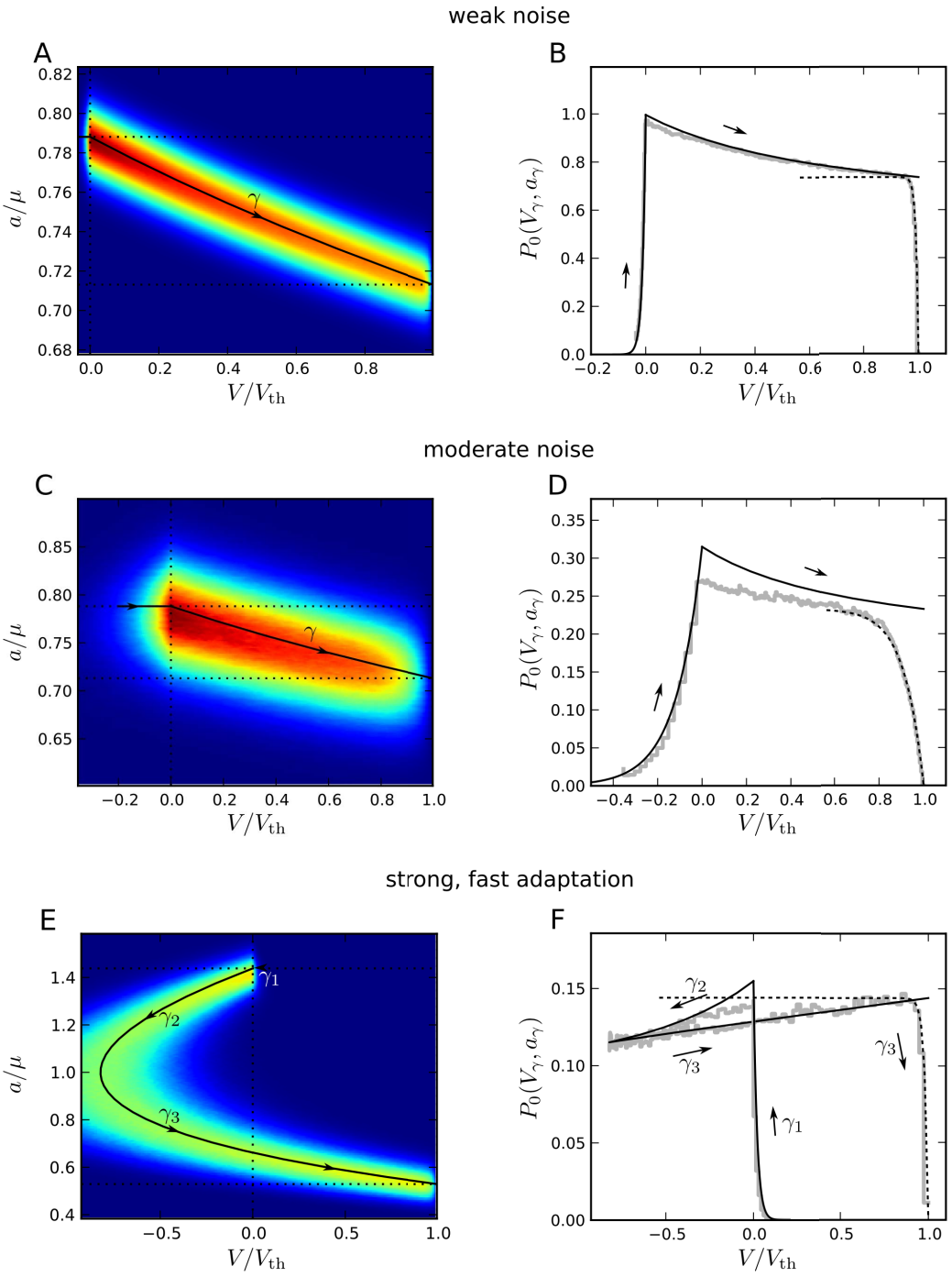

Figure 3.16.: Stationary probability density $P_0(V,a)$. **A** $P_0(V,a)$ obtained from numerical simulations for weak-noise ($D = 0.01$). Dark blue and dark red colors indicate low and high density, respectively. The black solid line indicates the limit-cycle in the region $0 \leq V \leq V_{\rm th}$, the dashed vertical line indicates the reset line and the dashed horizontal lines indicate the locations of a^* and $a * -\Delta$. A cross-section of $P_0(V,a)$ along the black solid curve γ is depicted in **B** by a gray line (simulation). The theory based on the WKB solution, Eq. (3.97), and the solution in region I, Eq. (3.95), are displayed by the solid line. The inner solution of the threshold layer, Eq. (3.96), is depicted by the dashed line. **C**,**D** show the corresponding curves for $D = 0.1$. In panels **A–D**, $\tau_{\rm a} = 10T^*$, $\tilde{\Delta} = 3V_{\rm th}$, for which $a^* < \mu$; in panels **E**,**F** $D = 0.1V_{\rm th}^2/T^*$, $\tau_{\rm a} = T^*$, $\tilde{\Delta} = 10V_{\rm th}$, which corresponds to the case $a^* > \mu$. Arrows indicate how the stationary solution is traced out.

I.e. the solution is given by an exponential function below and above reset.

In the case of the adapting PIF model, the stationary distribution can be integrated over the variable a, yielding the marginal distribution $P_0(V)$. For instance, in region II, the WKB solution can be used outside the boundary layer at the threshold:

$$P_{0,\mathrm{II,out}}(V) = \int \mathrm{d}a\, P_{0,\mathrm{II,out}}(V,a) = \frac{1}{\sqrt{2\pi\epsilon}} \int \mathrm{d}a\, \Psi(V,a) \exp\left[-\frac{\Phi(V,a)}{\epsilon}\right]. \tag{3.101}$$

For weak noise, $\epsilon \ll 1$, the probability density $P_{0,\mathrm{II,out}}(V,a)$ is strongly peaked about $\mathcal{C}^*$. This permits to employ Laplace's method [see e.g. Bender and Orszag, 1999] in order to obtain an asymptotic approximation for $P_0(V)$. To this end, the minimum of $\Phi(V,a)$ and its second derivative $\Phi_{aa}(V,a)$ at the minimum for a given membrane potential V is needed.

The case $a^* < \mu$. For $a^* < \mu$, the theoretical solution exhibits only one minimum, which is on the limit cycle. In this case, Laplace's method yields the parametric representation

$$P_{0,\mathrm{II,out}}(V) \approx \frac{\psi(\tau,a^*)}{\sqrt{\phi_{aa}(\tau,a^*)}}, \qquad V = \mu\tau - \tau_\mathrm{a} a^* \left(1 - e^{-\tau/\tau_\mathrm{a}}\right) \tag{3.102}$$

for $0 \le \tau \le T^*$. Using Eq. (B.108) and (B.110), results in the simple expression

$$P_{0,\mathrm{II,out}}(V) = \frac{1}{T^*(\mu - a^* e^{-\tau/\tau_\mathrm{a}})}, \qquad 0 \le V < V_\mathrm{th} - \mathcal{O}(\epsilon). \tag{3.103}$$

Note that this expression is independent of the noise intensity. In particular, it is equal to the inverse drift velocity $(\mu - a^* e^{-\tau/\tau_\mathrm{a}})T^*$ of a trajectory that starts at $a_i = a^*$. As for the two-dimensional probability density, the WKB solution Eq. (3.103) does not satisfy $P_0(V_\mathrm{th}) = 0$. Rather, it limits at $1/[T^*(\mu - a^* + \Delta)] > 0$ for $\tau \to T^*$. In the boundary layer close to the threshold, the probability density drops-off as in Eq. (3.96). The threshold layer solution that asymptotically matches the limit is

$$P_{0,\mathrm{II,in}}(V) = \frac{1}{T^*(\mu - a^* + \Delta)} \left\{1 - \exp\left[\frac{\mu - a^* + \Delta}{D}(V - V_\mathrm{th})\right]\right\}, \qquad V \sim V_\mathrm{th} - \mathcal{O}(\epsilon). \tag{3.104}$$

A uniform approximation in region II can be obtained by adding the WKB solution Eq. (3.103) and the threshold layer solution Eq. (3.104) and subtracting the common limit for $V \to V_\mathrm{th}$, or equivalently for $\tau \to T^*$. As a result, the distribution of the membrane potential in region II, $0 \le V \le V_\mathrm{th}$, has the parametric representation

$$P_{0,\mathrm{II}}(V(\tau)) = \frac{1}{T^*}\left(\frac{1}{\mu - a^* e^{-\tau/\tau_\mathrm{a}}} - \frac{\exp\left[\frac{\mu - a^* + \Delta}{D}(V - V_\mathrm{th})\right]}{\mu - a^* + \Delta}\right) \tag{3.105}$$

$$V(\tau) = \mu\tau - \tau_\mathrm{a} a^* \left(1 - e^{-\tau/\tau_\mathrm{a}}\right), \qquad 0 \le \tau \le T^*. \tag{3.106}$$

Alternatively, the distribution in region II can be expressed explicitly (i.e. in a non-parametric form) by using the inverse relation $\tau = \tau(V)$, which can be expressed in terms of the Lambert W function [Weisstein, 2012]: For $a^* < \mu$, the inverse relation is

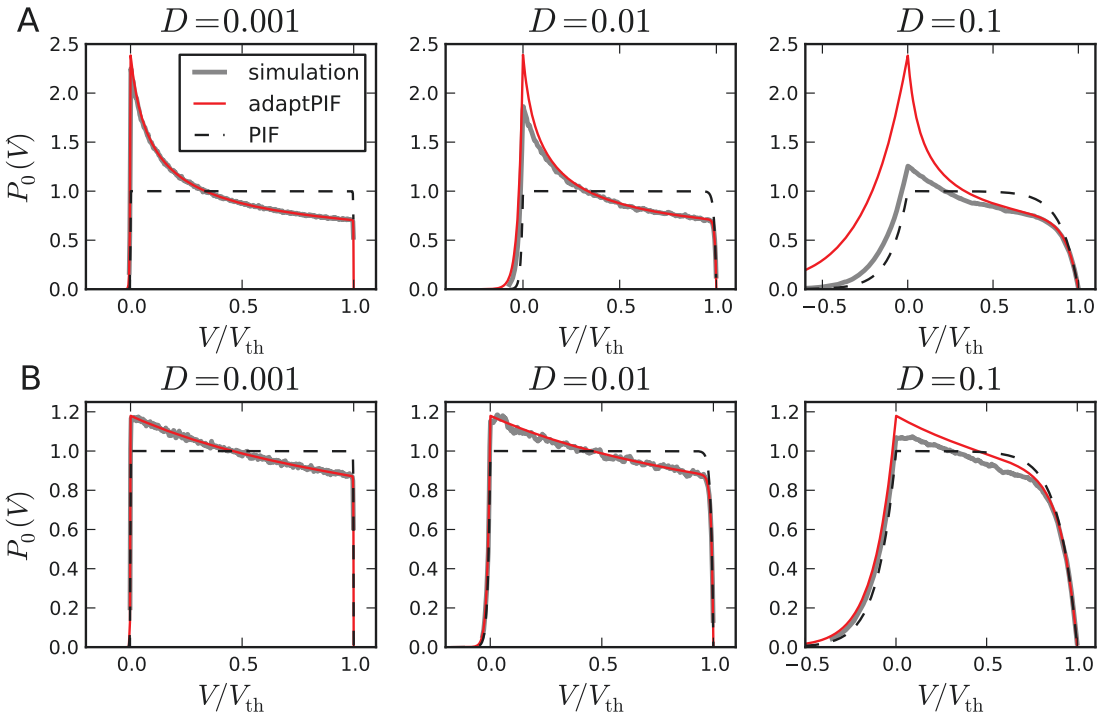

Figure 3.17.: Distribution of the membrane potential in the case $a^* < \mu$. The probability density $P_0(V)$ is shown for different noise intensities (as indicated on top of each panel, D in units of V_{th}^2/T^*). The gray curves display the histograms obtained from simulations, the red line displays the weak-noise theory given by Eq. (3.105) and (3.109). The dashed line indicates the probability density of the corresponding non-adapting PIF model, Eq. (3.100). **A** Fast adaptation current with $\tau_{\mathrm{a}} = T^*$, $\tilde{\Delta} = 1V_{\mathrm{th}}$, **B** slow adaptation current with $\tau_{\mathrm{a}} = 10T^*$, $\tilde{\Delta} = 3V_{\mathrm{th}}$.

given by

$$\tau(V) = \tau_+(V, a^*) \equiv \tau_{\mathrm{a}} \left[W_0\left(-\frac{a^*}{\mu} \exp\left(-\frac{V + \tau_{\mathrm{a}} a^*}{\mu \tau_{\mathrm{a}}} \right) \right) + \frac{V + \tau_{\mathrm{a}} a^*}{\mu \tau_{\mathrm{a}}} \right], \tag{3.107}$$

with $W_0(y)$ being the upper branch of the Lambert W function, where $W_0(y)$ is the inverse of the function $y = xe^x$. Using the function $\tau_+(V, a^*)$ the distribution of the membrane potential can be rewritten as

$$P_{0,\mathrm{II}}(V) = \frac{1}{T^*} \left(\left| \mu - a^* \exp\left(-\frac{\tau_+(V, a^*)}{\tau_{\mathrm{a}}} \right) \right|^{-1} - \frac{\exp\left[\frac{\mu - a^* + \Delta}{D} (V - V_{\mathrm{th}}) \right]}{\mu - a^* + \Delta} \right). \tag{3.108}$$

For $V < 0$ the solution in region I must be used, which yields the exponential drop-off below the reset:

$$P_{0,\mathrm{I}}(V) = \frac{1}{T^*(\mu - a^*)} \exp\left(\frac{\mu - a^*}{D} V \right). \tag{3.109}$$

The theory Eq. (3.105), (3.109) yields an excellent fit to the simulations in the limit of weak noise (Fig. 3.17). In this limit the distribution in region II is not constant as in the case of the non-adapting PIF model (the distribution, Eq. (3.100), converges to a "box", $P_{\mathrm{PIF}}(V) \to V_{\mathrm{th}}^{-1} \theta(V) \theta(V_{\mathrm{th}} - V)$). Close to the reset, the distribution for the adapting model is larger than for the non-adapting one. The distribution decreases with rising V

and falls below $1/V_{\mathrm{th}}$ at an intermediate membrane potential. This decrease reflects exactly the above-mentioned observation that the outer solution $P_{0,\mathrm{II},\mathrm{out}}(V)$ is equal to the inverse mean drift current $\mu - a^* \exp(-\tau(V)/\tau_{\mathrm{a}})$ for a given $V(t)$: after firing the drift velocity is small due to a large adaptation current $a(t) \sim a^*$. This increases the probability to stay close to the reset. As $a(t)$ decays, both the membrane potential and the drift velocity increase leading to a reduced probability for larger membrane potentials. Thus, for a slow adaptation current the decay of the distribution is also slow (compare Figs. 3.17A and B). Furthermore, the acceleration of the membrane potential towards the threshold leads to a convex shape of the membrane potential distribution if V is sufficiently below the threshold (in the threshold layer the distribution is a concave function). It would be interesting to observe such convex voltage distributions in experimental recordings.

At larger noise intensities, there are significant deviations between theory and simulations. In particular, the probability density is overestimated. This deviation might be related to the deviation of $P_0(V,a)$ taken on the limit cycle: In Figure 3.16 it became clear that the maximum of $P_0(V,a)$ for a fixed V is not, as assumed, on the limit cycle, but is shifted to smaller values of a. Therefore, the asymptotic approximation based on Laplace's method yields poor results because the maximum moves with ϵ. Still, the pronounced decay of $P_0(V)$ is in qualitative agreement with the weak-noise theory. It should be also noted that the weak noise approximation of $P_0(V)$ is generally not normalized as becomes apparent in Fig. 3.17 for large D. The probability density is only normalized in the asymptotic limit of weak noise, for which the approximations become exact.

It is interesting to investigate, whether the weak-noise theory contains the exact theoretical distribution, Eq. (3.100), for the non-adapting model as a limit case. To this end, one can consider two limits: firstly, the limit $\tau_{\mathrm{a}} \to \infty$, $\tilde{\Delta} = \text{const.}$ leads to a constant drift velocity, because the exponential decay of $a(t)$ becomes infinitely slow and the jump size $\Delta = \tilde{\Delta}/\tau_{\mathrm{a}}$ vanishes. Thus, the distribution of a non-adapting PIF model with an effective (constant) drift current might be expected in this limit. In fact, a simple calculation reveals that the expressions Eq. (3.105), (3.109) converge exactly to Eq. (3.100) with μ replaced by the effective base current V_{th}/T^*. Secondly, the limit of a vanishing adaptation current, $\tilde{\Delta} \to 0$, $\tau_{\mathrm{a}} = \text{const.}$, should recover the probability density of the non-adapting PIF model with the same parameters μ and D. Indeed, this limit can be readily seen from Eq. (3.105). In conclusion, the weak-noise theory includes two known limit cases even for arbitrary noise intensities D, which supports the weak-noise theory for $P_0(V,a)$.

The case $a^* > \mu$. In this case, the application of Laplace's method for the integral (3.101) is slightly more complicated because for a given V in the range $V_{\mathrm{vertex}} < V \leq 0$, the stationary probability density possesses two maxima with respect to a (Fig. 3.16E). Here, V_{vertex} denotes the value of V at the vertex of the limit cycle, i.e. the extremal value of $V(\tau, a^*)$. The vertex is determined by the condition $\dot{V} = 0$ or $a^* e^{\tau/\tau_{\mathrm{a}}} = \mu$, from which follows

$$V_{\mathrm{vertex}} = \tau_{\mathrm{a}} \left[\mu - a^* + \mu \ln\left(\frac{a^*}{\mu}\right) \right]. \tag{3.110}$$

The two maxima correspond to the two branches of $\mathcal{C}^*$ that exist for $a^* > \mu$: the upper branch $\mathcal{C}^*_-$ (where $a(\tau, a^*) > \mu$) and the lower branch $\mathcal{C}^*_+$ (where $a(\tau, a^*) < \mu$). For weak noise, the integral (3.101) is the sum of the contributions from the neighborhood of each

branch. Laplace's method yields for the lower branch the contribution

$$P_+(V) = \frac{1}{T^*}\left(\left|\mu - a^* \exp\left(-\frac{\tau_+(V,a^*)}{\tau_a}\right)\right|^{-1} - \frac{\exp\left[\frac{\mu-a^*+\Delta}{D}(V-V_{th})\right]}{\mu - a^* + \Delta}\right) \tag{3.111}$$

as was already found in Eq. (3.108). The function $\tau_+(V,a^*)$ given in Eq. (3.107) provides the parameter τ as a function of V on the lower branch of the limit cycle. The application of Laplace's method to the upper branch yields

$$P_-(V) = \frac{1}{T^*}\left|\mu - a^* \exp\left(-\frac{\tau_-(V,a^*)}{\tau_a}\right)\right|^{-1}, \tag{3.112}$$

which corresponds to Eq. (3.103) but with $\tau(V)$ taken on $\mathcal{C}_-^*$: $\tau(V) = \tau_-(V,a^*)$ with

$$\tau_-(V,a^*) = \tau_a\left[W_{-1}\left(-\frac{a^*}{\mu}\exp\left(-\frac{V+\tau_a a^*}{\mu\tau_a}\right)\right) + \frac{V+\tau_a a^*}{\mu\tau_a}\right]. \tag{3.113}$$

In this equation, $W_{-1}(y)$ denotes the lower branch of the Lambert W function.

Finally, the probability contribution from the lower branch for $V > 0$ is augmented by the probability in region I (Fig. 3.13B). This contribution is given by (cf. Eq. (3.109))

$$P_{0,I}(V) = \frac{1}{T^*(a^*-\mu)}\exp\left(\frac{\mu-a^*}{D}V\right), \qquad V \geq 0. \tag{3.114}$$

Adding all parts together, results in the following distribution of the membrane potential

$$P_0(V) = \theta(V - V_{vertex})\left[P_+(V) + \theta(-V)P_-(V) + \theta(V)P_I(V)\right]. \tag{3.115}$$

Close to the vertex, the maxima approach each other and the curvature $\Phi_{aa}(V,a)|_{\mathcal{C}^*}$ becomes small. At the vertex, the curvature vanishes: $\Phi_{aa}(V_{vertex},\mu) = 0$. As a consequence, the approximation Eq. (3.102) diverges, which is obviously wrong. To prevent the divergence in the case $\Phi_{aa}(V,a)|_{\mathcal{C}^*} = 0$, higher-order terms (such as $\partial_a^4\Phi$) must be taken into account for a faithful application of Laplace's method, even in the asymptotic limit of weak noise. Another problem associated with the divergence is that it is difficult to obtain a solution for $V < V_{vertex}$ that is continuous at V_{vertex}. For this reason, in Eq. (3.115) the probability density was set to zero in the range $V < V_{vertex}$.

Apart from the divergence at $V = V_{vertex}$ the theoretical prediction given by Eq. (3.115) agrees well with simulations if the noise is sufficiently weak (Fig. 3.18). In contrast, the corresponding PIF model without adaptation fails clearly. The probability density has a maximum for negative membrane potentials close to the vertex, i.e. close to the turning point of the negative current excursion. Generally, negative values of V attract most probability, firstly because the deterministic velocity of V is small in that region and secondly because the contributions from the two branches of the limit cycle are superimposed. This leads to roughly a doubled probability to observe a trajectory at some V slightly below the reset as compared to V slightly above the reset. In the latter case, only the lower branch and the (small) probability of region I matters (see Fig. 3.13B). Although the membrane potential of the adapting PIF model has a somewhat artificial shape, the typical feature of a strong adaptation current (that leads to $a^* > \mu$) seems to be a pro-

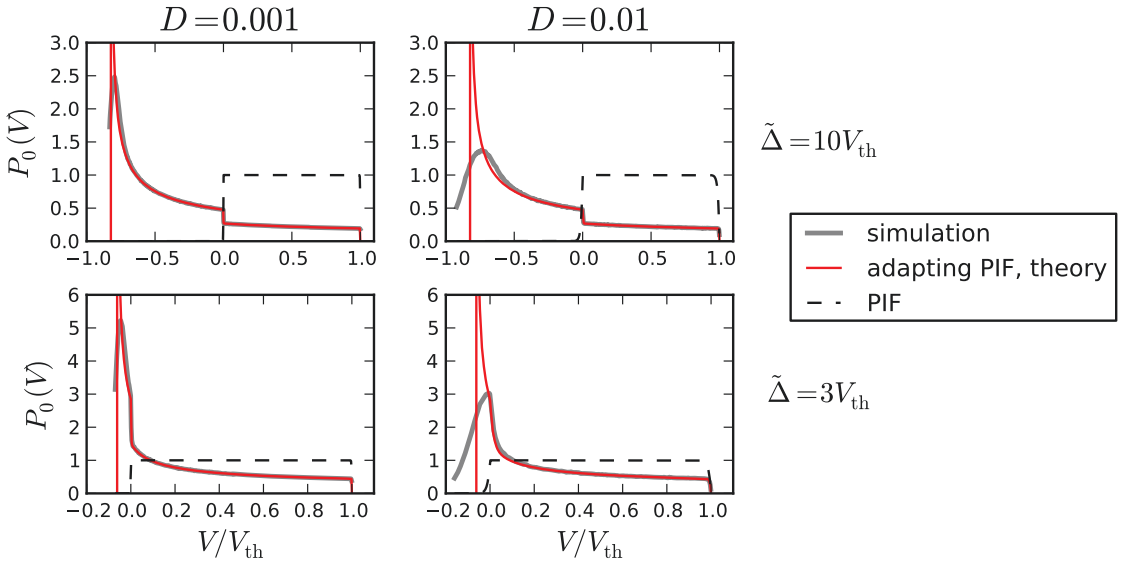

Figure 3.18.: Distribution of the membrane potential for $a^* > \mu$. As in Fig. 3.17, the probability density $P_0(V)$ is shown for different noise intensities (as indicated). The gray curves display the histograms obtained from simulations, the red line displays the weak-noise theory given by Eq. (3.105) and (3.109). The dashed line indicates the probability density of the corresponding non-adapting PIF model, Eq. (3.100). In the top row, the case of a strong adaptation current is shown ($\tilde{\Delta} = 10V_{\rm th}$), which leads to a strong negative excursion of the membrane potential (cf. Fig. 3.16C). In the bottom row, the adaptation current is weaker (($\tilde{\Delta} = 3V_{\rm th}$) leading only to a small negative excursion (cf. Fig. 3.4B). In all cases, $\tau_{\rm a} = 3T^*$.

nounced increase of probability at small membrane potentials.

3.3.5. Distribution of the adaptation variable upon firing

The probability density of $a(t)$ sampled immediately *before* firing, $P_{\rm f,pre}(a)$, is proportional to the out-flux at the threshold:

$$P_{\rm f,pre}(a) \sim \partial_V P(V_{\rm th}, a) \sim (\mu - a)\Psi(V_{\rm th}, a) \exp\left(-\frac{\Phi(V_{\rm th}, a)}{\epsilon}\right). \tag{3.116}$$

For asymptotically weak noise, $P_{\rm f,pre}(a)$ becomes a Gaussian with mean $a^* - \Delta$ and variance $\epsilon/\phi_0''(a^*)$. For the distribution of $a(t)$ sampled immediately *after* firing, $P_{\rm f}(a) = P_{\rm f,pre}(a - \Delta)$, the asymptotic distribution is thus

$$\boxed{P_{\rm f}(a) = \frac{1}{\sqrt{2\pi\sigma_a}} \exp\left(-\frac{(a - a^*)^2}{2\sigma_a^2}\right)} \tag{3.117}$$

with the variance of a_i given by

$$\boxed{\sigma_a^2 = \frac{2\epsilon\hat{D}a^{*2}T^*(a^* - \Delta)^2}{\tau_{\rm a}^2\mu\Delta[2a^*(\mu - a^* + \Delta) - \mu\Delta]}.} \tag{3.118}$$

For weak noise, figure 3.19A shows indeed a good agreement between our approxima-

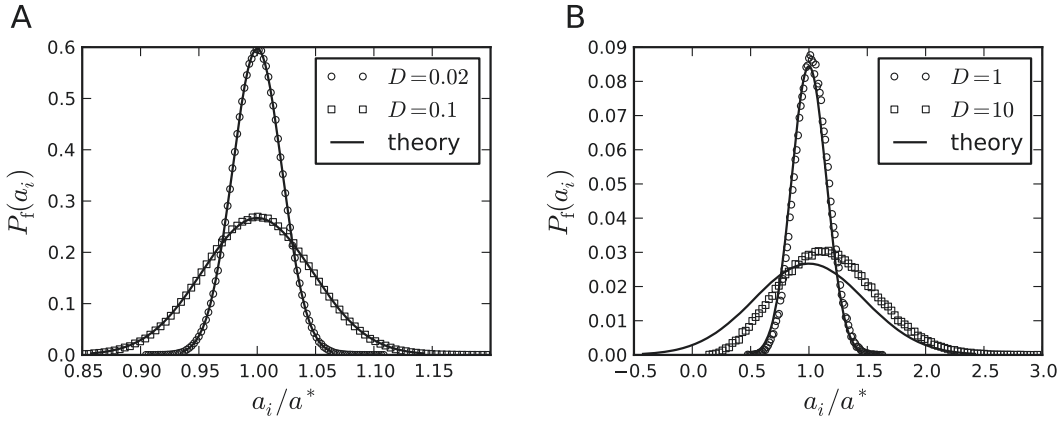

Figure 3.19.: Stationary probability density of the peak adaptation currents. The stationary probability density $P_\mathrm{f}(a)$ is shown for $\tau_\mathrm{a} = 10T^*$, $\tilde{\Delta} = 3V_\mathrm{th}$ and different noise intensities as indicated in the legends. The theoretical curves are based on the Gaussian approximation, Eq. (3.117).

tion and simulations. For strong noise, the distribution becomes slightly shifted to larger values of a_i than predicted by the theory, although the Gaussian shape is still preserved (Fig. 3.19B).

The standard deviation of a_i is compared to simulations in Fig. 3.20. It can be seen that the weak-noise theory yields reasonable results up to relatively large noise intensities. Moreover, the standard deviation exhibits a maximum with respect to the adaptation time constant. This can be understood as follows: on the one hand, for $\tau_\mathrm{a} \to 0$ the value a^* diverges to infinity and σ_a converges to zero (because $a(t)$ has decayed to zero when the trajectories reach the threshold). Consequently, σ_a/a^* is zero in the limit $\tau_\mathrm{a} \to 0$. On the other hand, for $\tau_\mathrm{a} \to \infty$, $a(t)$ becomes a constant (equal to a^*) because the jump size $\Delta = \tilde{\Delta}/\tau_\mathrm{a}$ vanishes and and the decay of $a(t)$ is infinitely slow. Hence, the variability of the peak adaptation currents also vanishes in the limit $\tau_\mathrm{a} \to \infty$. We conclude that σ_a/a^* as a function of τ_a possesses at least one maximum.

3.3.6. Coefficient of variation and ISI density

As discussed in Sec. 1.2.6, the moments and the probability density of the interspike intervals can be obtained by averaging the conditional ISI statistics with respect to the stationary distribution upon firing:

$$\langle T_i \rangle = \int \mathrm{d}a\, P_\mathrm{f}(a) \langle T_i | a \rangle \tag{3.119}$$

$$\langle T_i^2 \rangle = \int \mathrm{d}a\, P_\mathrm{f}(a) \langle T_i^2 | a \rangle \tag{3.120}$$

$$P(T_i) = \int \mathrm{d}a\, P_\mathrm{f}(a) P(T_i | a). \tag{3.121}$$

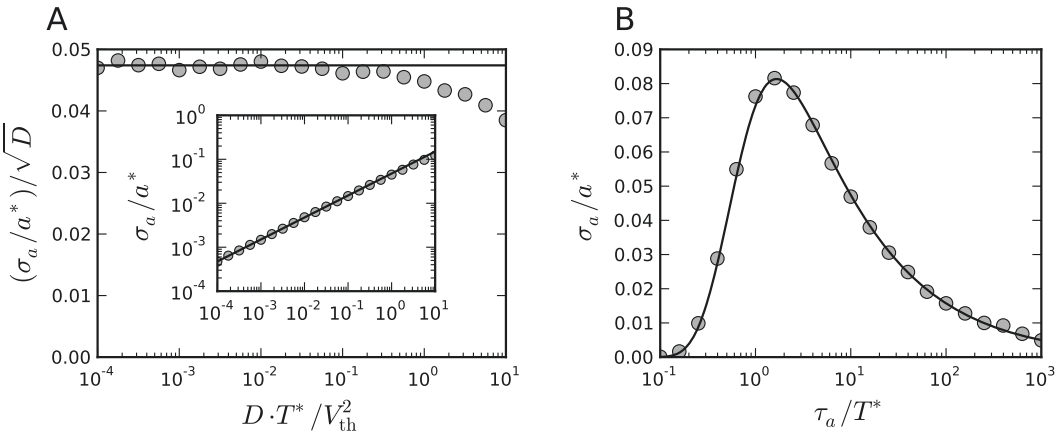

Figure 3.20.: Standard deviation of the peak adaptation currents. **A** The standard deviation σ_a normalized by a^* and $\sqrt{D}$ as a function of the noise intensity D for $\tau_a = 10T^*$. Inset: σ_a normalized by a^* as a function of D in a double-logarithmic plot. **B** σ_a as a function of the adaptation time constant. In both panels, the theory, Eq. (3.118), is depicted by the solid line, the circles represent the simulations. The adaptation strength was $\tilde{\Delta} = 3$

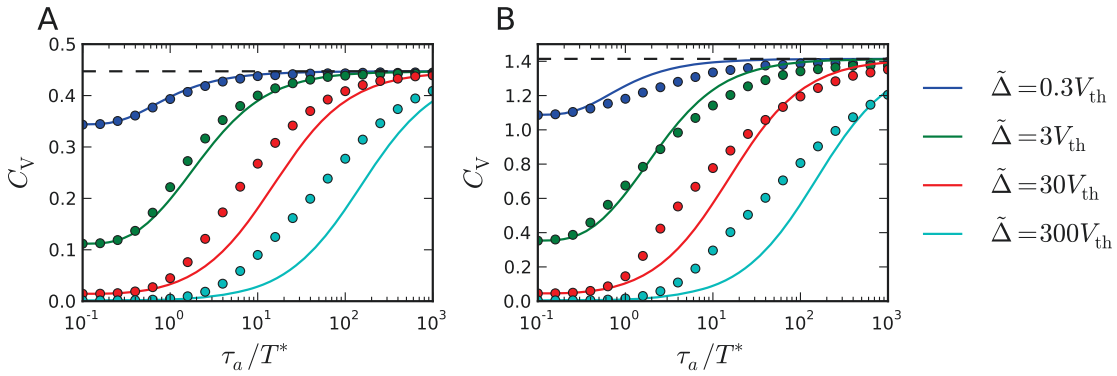

Figure 3.21.: The coefficient of variation as a function of the time-scale separation τ_a/T^*. **A** $D = 0.1$, **B** $D = 1$. The solid lines corresponds to the conditional CV with $a_i = a^*$, Eq. (3.52). The dashed line corresponds to the mean adaptation approximation, Eq. (3.134).

For weak noise, Laplace's method can be again applied because $P_f(a)$ is sharply peaked at $a = a^*$. Thus, one finds the rough approximation

$$\langle T_i\rangle \approx \langle T_i|a^*\rangle, \quad \langle T_i^2\rangle \approx \langle T_i^2|a^*\rangle, \tag{3.122}$$

$$P(T_i) \approx P(T_i|a^*), \tag{3.123}$$

where the conditional statistics $\langle T_i|a^*\rangle$, $\langle T_i^2|a^*\rangle = \langle T_i|a^*\rangle^2\left[C_V^2(a^*)+1\right]$ and $P(T_i|a^*)$ is given by Eqs. (3.50)–(3.52). From Eq. (3.122) follows that the CV can also be approximated by the conditional CV given that $a_i = a^*$ and using Eqs. (3.12), (3.49) and (3.52) yields:

$$C_V \approx C_V(a^*) = \frac{\sqrt{2D/T^*}}{\mu - a^* + \Delta}. \tag{3.124}$$

The CV is shown in Fig. 3.21 as a function of τ_a. Generally, one finds a monotonic increase

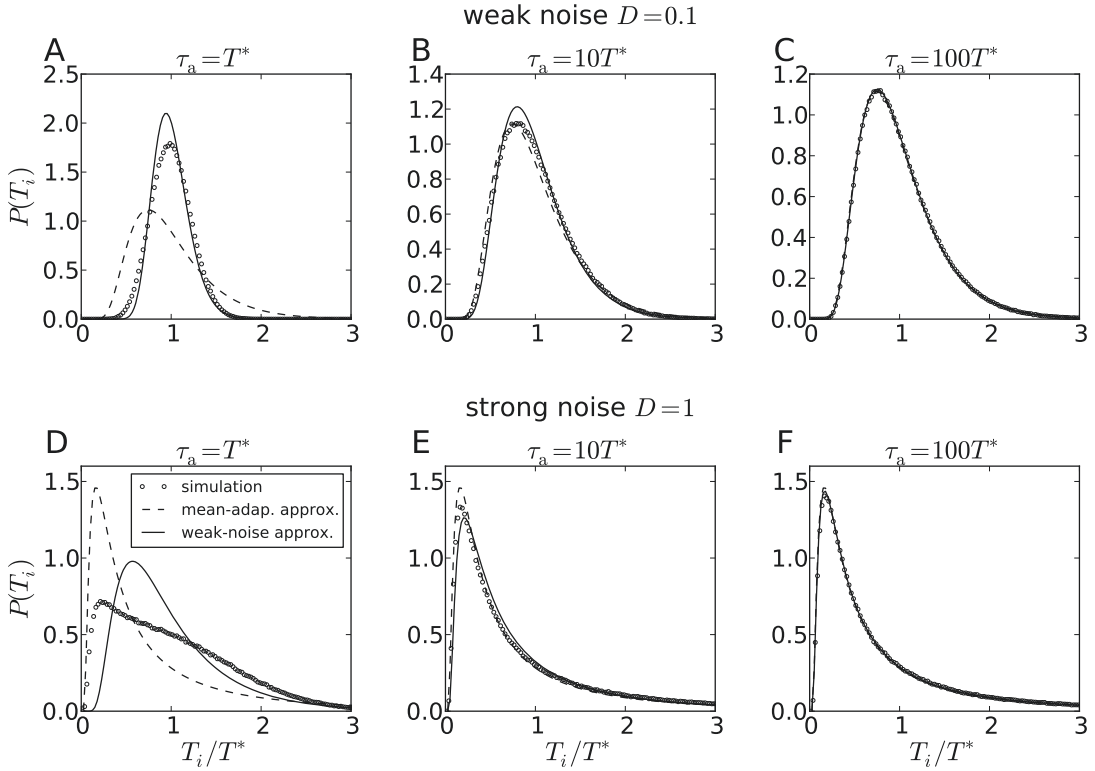

Figure 3.22.: ISI densities for different τ_a. **A-C** For a noise intensity $D = 0.1$ the ISI densities are shown for **A** $\tau_a = T^*$, **B** $\tau_a = 10T^*$ and **C** $\tau_a = 100T^*$. **D-F** Analogous ISI densities for strong noise, $D = 1$. The symbols depict the results of simulations, the dashed line depicts the mean-adaptation approximation valid for large τ_a, Eq. (3.133), and the solid line displays the weak-noise theory, Eq. (3.123). In all cases, the adaptation strength was $\tilde{\Delta} = 3$.

of the CV with increasing τ_a and a saturation at a minimal value in the limit $\tau_a \ll T^*$. Both limits are well captured by the conditional CV, $C_V(a^*)$. At intermediate values of τ_a and strong adaptation, however, deviations from the simulation results can be observed. For weak and moderate adaptation strengths' the deviations are not as pronounced.

The approximation of the ISI density, Eq. (3.123), is compared to simulations in Fig. 3.22. It generally agrees well with the simulations results except for fast adaptation in the presence of strong noise (Fig. 3.22D). An alternative expression for the ISI density, based on a slow-adaptation approximation, is derived in the next section. Let me finally note that the SCC can be computed semi-analytically using Eq. (3.7) for moderate noise, although the formula for the deterministic limit, Eq. (3.43), often yields reasonable results even for moderate noise. As a proof of principle, I have computed the double integral involved in Eq. (3.7) numerically using the analytically known expressions for $p_{tr}(a_{i+1}|a_i)$, $P_f(a_i)$ and $\langle T_i|a^*\rangle$. As a result, the noise-corrections of ρ_1 could be indeed correctly recovered by the semi-analytical approach (data not shown).

3.4. Slow adaptation approximations

Another approach for approximations of the firing statistics is to assume that the adaptation current is slow. More precisely, I assume here that $\tau_a \gg \langle T \rangle$, i.e. that a large time-scale separation holds. Note that in this approach the noise intensity can be arbitrarily large. For slow adaptation, approximations for the response properties to time-dependent stimuli are feasible. Therefore an additional current $s(t)$ is introduced into the right-hand-side of the equation for the membrane potential. Hence, the more general setup

$$\dot{V} = \mu - a + s(t) + \sqrt{2D}\xi(t) \tag{3.125}$$

$$\tau_a \dot{a} = -a + \tilde{\Delta} y(t) \tag{3.126}$$

is considered, where $y(t) = \sum_i (t - t_i)$ is the output spike train (cf. Eq. (3.1), (3.2)).

3.4.1. Stationary ISI statistics: mean adaptation approximation

At first, the stationary case is considered, where the signal is switched off ($s(t) \equiv 0$). For $\tau_a \gg \langle T \rangle$, the trajectory $a(t)$ is effectively smoothed by the linear filter equation (3.126). As a consequence, the relative deviations of $a(t)$ from its mean value $\langle a \rangle$ are small[5], which allows us to replace $a(t)$ by its mean value $\langle a \rangle$. In this so-called *mean adaptation approximation*, the membrane potential is effectively driven by the drift current $\mu - \langle a \rangle$ and by the Gaussian white noise. Averaging equation (3.126) leads to $\langle a \rangle = \tilde{\Delta} \langle y \rangle = \tilde{\Delta} r$. On the other hand, $r = (\mu - \langle a \rangle)/V_{\text{th}}$, so that the firing rate and the mean adaptation current can be determined self-consistently as

$$r = \frac{\lambda \mu}{V_{\text{th}}} = \frac{1}{T^*} \tag{3.129}$$

and

$$\langle a \rangle = \frac{\lambda \mu \tilde{\Delta}}{V_{\text{th}}} = \frac{\tilde{\Delta}}{T^*} \tag{3.130}$$

with

$$\lambda = \frac{V_{\text{th}}}{V_{\text{th}} + \tilde{\Delta}}. \tag{3.131}$$

[5] It can be shown that the variance of $a(t)$ vanishes in the limit $\tau_a \to \infty$: In the Fourier domain, the dynamics of $a(t)$, Eq. (3.126) reads

$$\tilde{a}(\omega) = \frac{\tilde{\Delta}}{1 - i\tau_a \omega} \tilde{y}(\omega), \tag{3.127}$$

where $\tilde{a}(\omega) = \int \mathrm{d}t\, e^{i\omega t} a(t)$ and $\tilde{y}(\omega) = \int \mathrm{d}t\, e^{i\omega t} y(t)$ are the Fourier transforms of the adaptation variable and the spike train, respectively. Thus, the power spectrum of the adaptation variable, $S_a(\omega)$ is related to the spike train power spectrum $S_y(\omega)$ by

$$S_a(\omega) = \frac{\tilde{\Delta}^2}{1 + \tau_a^2 \omega^2} S_y(\omega). \tag{3.128}$$

The cut-off frequency of this low-pass filter becomes arbitrarily small as τ_a becomes large. Moreover, from Eq. (3.45), we already know that $S_y(\omega)$ saturates at a finite value in the limit $\omega \to 0$. Hence, at low frequencies the large τ_a behavior is $S_a(\omega) \propto 1/(1 + \tau_a^2 \omega^2)$. The variance of a is related to the integral over the power spectrum, which yields the scaling $\langle \Delta a^2 \rangle \propto \int \mathrm{d}\omega\, S_a(\omega)/(2\pi) \propto \tau_a^{-1}$. Thus, the fluctuations indeed vanish in the limit $\tau_a \to \infty$.

Thus, in the mean-adaptation approximation the subthreshold dynamics reduces to

$$\dot{V} = \lambda\mu + \sqrt{2D}\xi(t). \tag{3.132}$$

This is the standard (non-adapting) PIF model, but with a reduced driving current $\lambda\mu$ (note that $\lambda < 1$). Hence, the main effect of a slow adaptation current is to reduce statically the firing rate. The firing rate in the mean-adaptation approximation, Eq. (3.129), is consistent with the deterministic limit, which must be $1/T^*$.

Because for $\tau_a \gg \langle T \rangle$ the model reduces to a standard PIF model, the ISI density can be immediately stated: according to Eq. (1.68) the ISI density is given by the inverse Gaussian

$$P(T) = \frac{V_{th}}{\sqrt{4\pi D T^3}} \exp\left[-\frac{(\lambda\mu T - V_{th})^2}{4DT}\right]. \tag{3.133}$$

Fig. 3.22 shows indeed that this approximation agrees rather well with simulations if $\tau_a \ll T^*$. Furthermore, according to Eq. (1.67) the coefficient of variation is given by

$$C_V = \sqrt{\frac{2D}{V_{th}\lambda\mu}}. \tag{3.134}$$

Fig. 3.21 shows that this result indeed captures the limit $\tau_a \gg T^*$. However, this expression yields a rather poor approximation in the absence of a strong time scale separation. In those cases, the approximation Eq. (3.124) is more appropriate.

The serial correlation coefficient vanishes in the limit $\langle T \rangle / \tau_a \to 0$ because the spike train generated by (3.132) reduces to a renewal process. But note Sec. 3.2.3, where it was shown that the sum over all ρ_k does not vanish. Thus, the model does not converge to a renewal process in the limit $\tau_a \to \infty$.

3.4.2. Response to time-dependent stimuli

What is the effect of a time-dependent stimulus $s(t)$ on the instantaneous firing rate $r(t) = \langle y(t) \rangle$? In linear response the firing rate is given by

$$\langle y(t) \rangle = \frac{1}{T^*} + \int_{-\infty}^{t} \mathrm{d}t' \, \chi_{\mathrm{adap}}(t - t') s(t'), \tag{3.135}$$

or in the frequency domain

$$\langle \tilde{y}(\omega) \rangle = \frac{2\pi}{T^*}\delta(\omega) + \tilde{\chi}_{\mathrm{adap}}(\omega)\tilde{s}(\omega). \tag{3.136}$$

Here, $\tilde{\chi}_{\mathrm{adap}}(\omega)$ and $\tilde{s}(\omega)$ are the Fourier transforms of the linear response function $\chi_{\mathrm{adap}}(t)$ and the stimulus $s(t)$, respectively. In order to calculate the linear response function, also called susceptibility, the negative feedback mediated by adaptation and the stimulus are treated as a small perturbation. The response to this perturbation can then also be calculated applying linear response theory. To this end, the stationary mean adaptation $\tilde{\Delta}/T^*$

(see Eq. (3.130)) is subtracted and added in the equation for the membrane potential:

$$\dot{V} = \mu - \frac{\tilde{\Delta}}{T^*} - \left(a - \frac{\tilde{\Delta}}{T^*}\right) + s(t) + \sqrt{2D}\xi(t) \tag{3.137}$$

$$\approx \lambda\mu \underbrace{- \left(a - \frac{\tilde{\Delta}}{T^*}\right) + s(t)}_{\text{perturbation}} + \sqrt{2D}\xi(t). \tag{3.138}$$

In the last line, the definition of T^* and λ, Eq. (3.14), (3.131), have been used. If both the stimulus $s(t)$ and the fluctuations $a(t) - \tilde{\Delta}/T^*$ of the adaptation current about its stationary mean value are small (weak feedback), the sum of both can be treated as a small perturbation. Thus, the response of the adapting PIF model can be approximated by the response of a renewal PIF model with reduced base current $\lambda\mu = V_{\text{th}}/T^*$ and noise intensity D to the perturbation indicated in Eq. (3.138). This response is determined by the susceptibility $\tilde{\chi}_{\text{PIF}}(\omega, \mu, D)$ of the non-adapting PIF model ($\tilde{\Delta} = 0$), which is given by

$$\chi_{\text{PIF}}(\omega, \mu, D) = \frac{1 - \sqrt{1 - 2i\tau_e\omega}}{V_{\text{th}} i\tau_e\omega} \tag{3.139}$$

with $\tau_e = 2D/\mu^2$ (see, e.g. Fourcaud and Brunel [2002]). According to linear response theory, it follows that

$$\langle\tilde{y}\rangle = \frac{2\pi}{T^*}\delta(\omega) + \tilde{\chi}_{\text{PIF}}(\omega, \lambda\mu, D)\left(\frac{2\pi\tilde{\Delta}}{T^*}\delta(\omega) - \tilde{a} + \tilde{s}\right). \tag{3.140}$$

Note that linear response theory with respect to a perturbation that depends on the specific realization of the noise is somewhat problematic because the left hand side of the equation is independent of the noise, whereas the right hand side depends on the noise through the feedback $\tilde{a}$. Nevertheless, if the feedback is weak it can be treated as an external perturbation that must be determined self-consistently from the linear response. To this end, $\tilde{a}$ is expressed in terms of $\tilde{y}$ by means of Eq. (3.127):

$$\langle\tilde{y}\rangle = \frac{2\pi}{T^*}\delta(\omega) + \tilde{\chi}_{\text{PIF}}(\omega, \lambda\mu, D)\left(\frac{2\pi\tilde{\Delta}}{T^*}\delta(\omega) - \frac{\tilde{\Delta}}{1 - i\tau_{\text{a}}\omega}\tilde{y}(\omega) + \tilde{s}\right). \tag{3.141}$$

Averaging the whole equation and solving for $\langle\tilde{y}\rangle$ results in the self-consistent response

$$\langle\tilde{y}\rangle = \frac{2\pi}{T^*}\delta(\omega) + \left(\frac{1}{\tilde{\chi}_{\text{PIF}}} + \frac{\tilde{\Delta}}{1 - i\tau_{\text{a}}\omega}\right)^{-1}\tilde{s}. \tag{3.142}$$

Comparing the last equation with Eq. (3.136), the susceptibility is found as

$$\boxed{\tilde{\chi}_{\text{adap}}(\omega) = \left(\frac{1}{\tilde{\chi}_{\text{PIF}}(\omega, \lambda\mu, D)} + \frac{\tilde{\Delta}}{1 - i\tau_{\text{a}}\omega}\right)^{-1}.} \tag{3.143}$$

Fig. 3.23 shows the susceptibility as a function of the frequency $f = 2\pi\omega$ (in units of $1/T^*$). The linear response approximation, Eq. (3.143), reveals indeed an excellent agreement with simulations for slow and weak adaptation (Fig. 3.23A). The approxima-

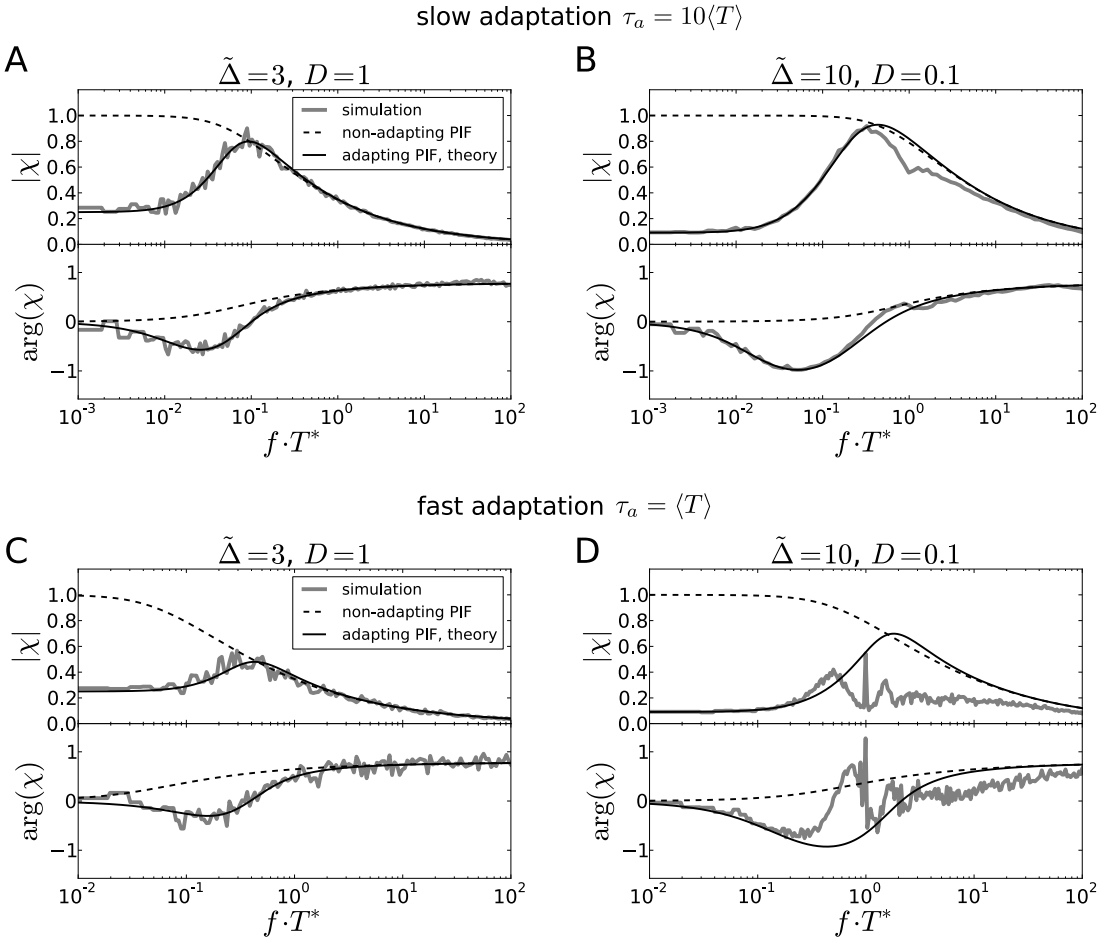

Figure 3.23.: Susceptibility of the adapting PIF model. The upper panels and lower panels show respectively the absolute value and the complex argument of the susceptibility $\tilde{\chi}_{\mathrm{adap}}(\omega)$ as a function of the frequency $f = \omega/(2\pi)$ (in units of $1/T^*$). Simulations (gray lines) were performed using a band-limited white-noise signal with standard deviation $\epsilon = 0.8$ and a cut-off frequency of $500(T^*)^{-1}$. The linear response theory for weak adaptation is depicted by the solid line. For slow adaptation (**A,B**), the susceptibility shows the high-pass filter property of a slow adaptation mechanism. At high frequencies, the response decays again like the corresponding renewal PIF model with the same firing rate and noise intensity (dashed line). Parameter values as indicated in the panels. **A,C** moderate adaptation strength and noise intensity, **B,D** strong adaptation and low noise intensity, for which linear response theory is expected to fail.

tion works still reasonably well, for strong adaptation and low noise, where the linear response could be expected to fail (Fig. 3.23B), as well as for fast adaptation if the adaptation is not too strong (Fig. 3.23C). However, limitations of the linear response theory are observed for fast and strong adaptation, where response shows resonances that are not captured by the theory (Fig. 3.23D). Interestingly, the response in the vicinity of the resonance is reduced as if the resonance draws off power from its neighboring frequencies. Note that the low-frequency behavior is still correctly predicted by the theory even for fast and strong adaptation.

Eq. (3.143) determines the response properties of a PIF neuron *with* adaptation. Let me compare this result with the susceptibility $\tilde{\chi}_{\mathrm{PIF}}(\omega, \lambda\mu, D)$ of the corresponding PIF neuron *without* adaptation. At high frequencies, the second term in Eq. (3.143) can be neglected, hence $\tilde{\chi}_{\mathrm{adap}}(\omega) = \tilde{\chi}_{\mathrm{PIF}}(\omega, \lambda\mu, D)$ for $\omega \gg \tau_{\mathrm{a}}^{-1}$. Thus, the susceptibility at high frequencies for the model with adaptation is simply set by the low-pass behavior of a PIF model without adaptation but with reduced base current $\lambda\mu$ (Fig. 3.23). The single effect of an adaptation current on the high-frequency response is to statically reduce the mean firing rate from μ/V_{th} to $\lambda\mu/V_{\mathrm{th}} = 1/T^*$.

In contrast, adaptation has a strong dynamical effect on the low-frequency response. In this case, the susceptibility of the PIF model without adaptation becomes constant: $\tilde{\chi}_{\mathrm{PIF}}(\omega, \lambda\mu, D) = 1/V_{\mathrm{th}}$. Inserting this asymptotic limit into Eq. (3.143), the response to low-frequency stimuli can be obtained as

$$\tilde{\chi}_{\mathrm{adap}}(\omega) = \frac{1 - i\tau_{\mathrm{a}}\omega}{V_{\mathrm{th}}(1 - i\tau_{\mathrm{a}}\omega) + \tilde{\Delta}}. \tag{3.144}$$

The absolute value is given by

$$|\tilde{\chi}_{\mathrm{adap}}(\omega)| = \frac{\lambda}{V_{\mathrm{th}}} \sqrt{\frac{1 + \tau_{\mathrm{a}}^2\omega^2}{1 + \lambda^2\tau_{\mathrm{a}}^2\omega^2}}, \tag{3.145}$$

which reveals a suppressed low-frequency response: for moderate and strong adaptation, it holds $\lambda^2 \ll 1$, which shows that $|\tilde{\chi}_{\mathrm{adap}}(\omega)| \simeq \frac{\lambda}{V_{\mathrm{th}}}\sqrt{1 + \tau_{\mathrm{a}}^2\omega^2}$ for $\omega \ll (\lambda\tau_{\mathrm{a}})^{-1}$ (Fig. 3.23). In the limit $\omega \to 0$ Eq. (3.144) converges to $\tilde{\chi}_{\mathrm{adap}}(0) = 1/(V_{\mathrm{th}} + \tilde{\Delta})$. Thus, the ratio of the responses of the adapting and the non-adapting model to low-frequency signals is

$$\frac{\tilde{\chi}_{\mathrm{adap}}(0)}{\tilde{\chi}_{\mathrm{PIF}}(0, \lambda\mu, D)} = \frac{V_{\mathrm{th}}}{V_{\mathrm{th}} + \tilde{\Delta}} = \lambda. \tag{3.146}$$

In words, the response at low frequencies is reduced by the factor λ. This reveals the main dynamical effect of adaptation: slow changes in the stimuli are "adapted away", whereas fast changes in the stimuli are transmitted as in the non-adapting PIF neuron. In this sense, adaptation exhibits the property of a high-pass filter [Benda and Herz, 2003].

Response to a step current

In experiments, firing rate adaptation is typically characterized by the response to a step current stimulus as a function of time. Therefore, the response of the adapting PIF model in the time domain is also worth considering. To study the slow decay following the

initial increase of the firing rate it is sufficient to start from the adiabatic expression for the susceptibility, Eq. (3.144). The inverse Fourier transform yields the linear response function

$$\chi_{\text{adap}}(t) = \frac{1}{V_{\text{th}}}\delta(t) - \frac{\tilde{\Delta}}{V_{\text{th}}^2\tau_{\text{a}}}\theta(t)\exp\left(-\frac{t}{\lambda\tau_{\text{a}}}\right). \tag{3.147}$$

The firing rate is thus

$$r(t) = \frac{1}{V_{\text{th}}}\left(\lambda\mu + s(t) - \frac{\tilde{\Delta}}{V_{\text{th}}\tau_{\text{a}}}\int_{-\infty}^{t} \mathrm{d}t' \exp\left(-\frac{t-t'}{\lambda\tau_{\text{a}}}\right) s(t')\right). \tag{3.148}$$

Let us now consider a step of the base current of size A_{s} at time t_{s}: $s(t) = A_{\text{s}}\theta(t - t_{\text{s}})$. Inserting into Eq. (3.147) yields

$$r(t) = \frac{\lambda\mu}{V_{\text{th}}} + \frac{\lambda A_{\text{s}}}{V_{\text{th}}}\theta(t-t_{\text{s}})\left[1 + \frac{\tilde{\Delta}}{V_{\text{th}}}\exp\left(-\frac{t-t_{\text{s}}}{\lambda\tau_{\text{a}}}\right)\right] \tag{3.149}$$

This represents the exponential decay of the firing rate in response to a step stimulus, which is typical for firing rate adaptation. Interestingly, the decay time of the firing rate is $\lambda\tau_{\text{a}}$, i.e. it is not equal to the adaptation time constant τ_{a}, but the time-scale is reduced by the factor λ. Figure 4.6B shows that the theory Eq. (3.149) agrees well with numerical simulations.

The meaning of the parameter λ We have already seen in Eq. (3.146) that the factor λ describes the reduction of the response at low frequencies of the stimulus due to adaptation. Another, albeit related, interpretation of the factor λ is provided by Eq. (3.149). To this end, let us consider the firing rate before the step, $r_0 = \lambda\mu/V_{\text{th}}$, the firing rate immediately after the step, $r_{\text{s}} = r_0 + A_{\text{s}}/V_{\text{th}}$ and the adapted firing rate $r(\infty) = r_0 + \lambda A_{\text{s}}/V_{\text{th}}$. Then the ratio between the gain in firing rate after adaptation (i.e. at $t = \infty$) and directly after the stimulus onset (at $t = t_{\text{s}}+$) is

$$\frac{r(\infty) - r_0}{r_{\text{s}} - r_0} = \lambda. \tag{3.150}$$

This means that λ quantifies the "percentage adaptation" or the "degree of adaptation" [Wang, 1998].

3.4.3. The power spectrum of the spike train

What is the effect of adaptation on the power spectrum of the spike train? We have already seen in Eq. (3.45) that the power at zero frequency is strongly reduced by adaptation compared to a renewal model with the same rate and CV. The reason for this was that the total sum of the ISI serial correlations does not vanish (as it does in a renewal model) but is markedly negative. The same effect has been theoretically investigated in Lindner et al. [2005a]. In that paper it has been argued that a reduced power of the spontaneous spike train ("noise power") at low frequencies leads to a larger signal-to-noise ratio for low frequency signals, and hence to a larger information transfer in the low frequency range. It is thus of considerable interest to find analytical expressions for the power spectral density of the spontaneous spike train in the presence of adaptation. For

non-renewal processes including any adapting neuron model, the power spectral density is difficult to calculate because this is equivalent to finding the conditional firing rate defined as the time-dependent firing rate of an ensemble of neurons that all fired at time $t = 0$. This conditional firing rate, however, cannot be deduced from the statistics of a single ISI unless the spike train is a renewal process.

An elegant method to approximate the power spectrum in the presence of negative feedback has been proposed in Lindner et al. [2005b]. The idea is based on a linear ansatz for a single realization $\tilde{y}(\omega)$ of the spike train that is perturbed by a weak negative feedback. In our case, the perturbed PIF model reads

$$\dot{V} = \lambda\mu \underbrace{- \left(a - \frac{\tilde{\Delta}}{T^*} \right)}_{\text{perturbation}} + \sqrt{2D}\xi(t), \tag{3.151}$$

where $a - \tilde{\Delta}/T^*$ is the fluctuation of the adaptation current about its stationary mean value (cf. Eq. (3.138)). According to the linear ansatz, one can write

$$\tilde{y} = \tilde{y}_0 - \tilde{\chi}_{\text{PIF}}(\omega, \lambda\mu, D) \left(\tilde{a} - \frac{2\pi\tilde{\Delta}}{T^*}\delta(\omega) \right), \tag{3.152}$$

where $\tilde{y}_0(\omega)$ is the Fourier transform of the unperturbed spike train. Note that the relation (3.152) is exact when averaged over an ensemble and the perturbation is infinitesimally small (linear response theory). However, it is assumed that this relation holds even for a single realization of the process. Substituting the expression for $\tilde{a}$, Eq. (3.127), and solving for $\tilde{y}$ yields the representation

$$\tilde{y} = \frac{\tilde{y}_0 + \tilde{\chi}_{\text{PIF}}(\omega, \lambda\mu, D)\frac{2\pi\tilde{\Delta}}{T^*}\delta(\omega)}{1 + \tilde{\chi}_{\text{PIF}}(\omega, \lambda\mu, D)\frac{\tilde{\Delta}}{1 - i\tau_a\omega}}. \tag{3.153}$$

Using this result, one can compute the power spectral density $S_{yy}(\omega)$ defined by $\langle \tilde{y}^*(\omega')\tilde{y}(\omega)\rangle = S_{yy}(\omega)\delta(\omega - \omega')$. For $\omega > 0$ it follows

$$\langle \tilde{y}^*(\omega')\tilde{y}(\omega)\rangle = \frac{\langle \tilde{y}_0^*(\omega')\tilde{y}_0(\omega)\rangle}{\left(1 + \tilde{\chi}_{\text{PIF}}(\omega', \lambda\mu, D)\frac{\tilde{\Delta}}{1 - i\tau_a\omega'}\right)^* \left(1 + \tilde{\chi}_{\text{PIF}}(\omega, \lambda\mu, D)\frac{\tilde{\Delta}}{1 - i\tau_a\omega}\right)}. \tag{3.154}$$

The nominator of this expression is $\langle \tilde{y}_0^*(\omega')\tilde{y}_0(\omega)\rangle = S_0(\omega)\delta(\omega' - \omega)$, where $S_0(\omega)$ denotes the spontaneous spectrum. The power spectral density of the non-adapting PIF model is given by the renewal formula, Eq. (1.58),

$$S_0(\omega) = \frac{1 - |\tilde{P}(\omega)|^2}{T^*|1 - \tilde{P}(\omega)|^2} \tag{3.155}$$

with the characteristic function of ISIs (Fourier transform of the inverse Gaussian, Eq. (3.133))

$$\tilde{P}(\omega) = \exp\left[\frac{V_{\text{th}}\lambda\mu}{2D} \left(1 - \sqrt{1 - \frac{4iD\omega}{\lambda^2\mu^2}} \right) \right] \tag{3.156}$$

(see e.g. [Holden, 1976, Bulsara et al., 1994, Chacron et al., 2005b]). From Eq. (3.154)

follows the power spectrum of the adapting PIF model as

$$\boxed{S_{yy}(\omega) = \frac{S_0(\omega)}{\left|1 + \tilde{\chi}_{\mathrm{PIF}}(\omega, \lambda\mu, D)\frac{\tilde{\Delta}}{1-i\tau_a\omega}\right|^2}.} \tag{3.157}$$

This formula shows nicely the relation between the power spectra $S_0(\omega)$ and $S_{yy}(\omega)$ of the non-adapting and adapting model, respectively. At high frequencies, the denominator becomes unity, hence adaptation does not effect the power at high frequencies. At low frequencies, however, adaptation strongly reduces the power as expected. In the limit $\omega \to 0$, the susceptibility of the PIF model converges to $1/V_{\mathrm{th}}$, thus this limit leads to

$$S_{yy}(0+) = \lambda^2 S_0(0+). \tag{3.158}$$

The reduction of power at low frequencies is thus again determined by the parameter λ.

For slow adaptation, Fig. 3.24A shows a perfect match of simulations and the theory, Eq. (3.157), based on the linear ansatz. It also demonstrates the reduction of power at low frequencies compared to the corresponding renewal model (non-adapting PIF model). For fast adaptation the power spectrum exhibits features that are not captured by the theory Fig. 3.24B–D. This includes resonance peaks at multiples of the firing rate. However, the reduction of power at low frequencies is still well described by the theory.

3.5. Summary

In this chapter, a detailed analysis of the adapting perfect integrate-and-fire neuron model driven by white Gaussian noise has been carried out. This neuron model operates in the supra-threshold regime: Without noise, deterministic trajectories converge to a limit curve that can be interpreted as a limit-cycle, which gives rise to sustained periodic firing. In the first part of this chapter, this deterministic dynamics has been studied. As a result, two different dynamical regimes have been identified, one in which the initial adaptation current is weaker than the positive base current and another one in which the initial adaptation current exceeds the base current leading to a strong initial inhibition (afterhyperpolarization). The latter regime corresponds to strong feedback and fast adaptation. From the deterministic dynamics, analytical formulas for the mean ISI, the mean adaptation current upon firing and the serial correlation coefficient (SCC) have been found, which appear to be a reasonable approximation even in the stochastic case. In particular, studying the effect of infinitesimally small deviations of the deterministic trajectories from the limit-cycle has lead to a simple formula for the SCC. Using this quasi-deterministic theory, it has been found that ISIs with an odd lag are always negatively correlated, whereas ISIs with even lags can be positively correlated if the negative feedback is sufficiently strong (afterhyperpolarization regime), in which case the SCC exhibits an alternation in sign. Furthermore, the magnitude of the serial correlations (positive or negative) is maximized at a certain optimal time scale of the adaptation which is close to the intrinsic time-scale of the neuron. In the limit of large adaptation time constants the SCC vanishes at each given lag. However, the infinite sum of the correlations with respect to the lag does not vanish, but saturates at a finite value.

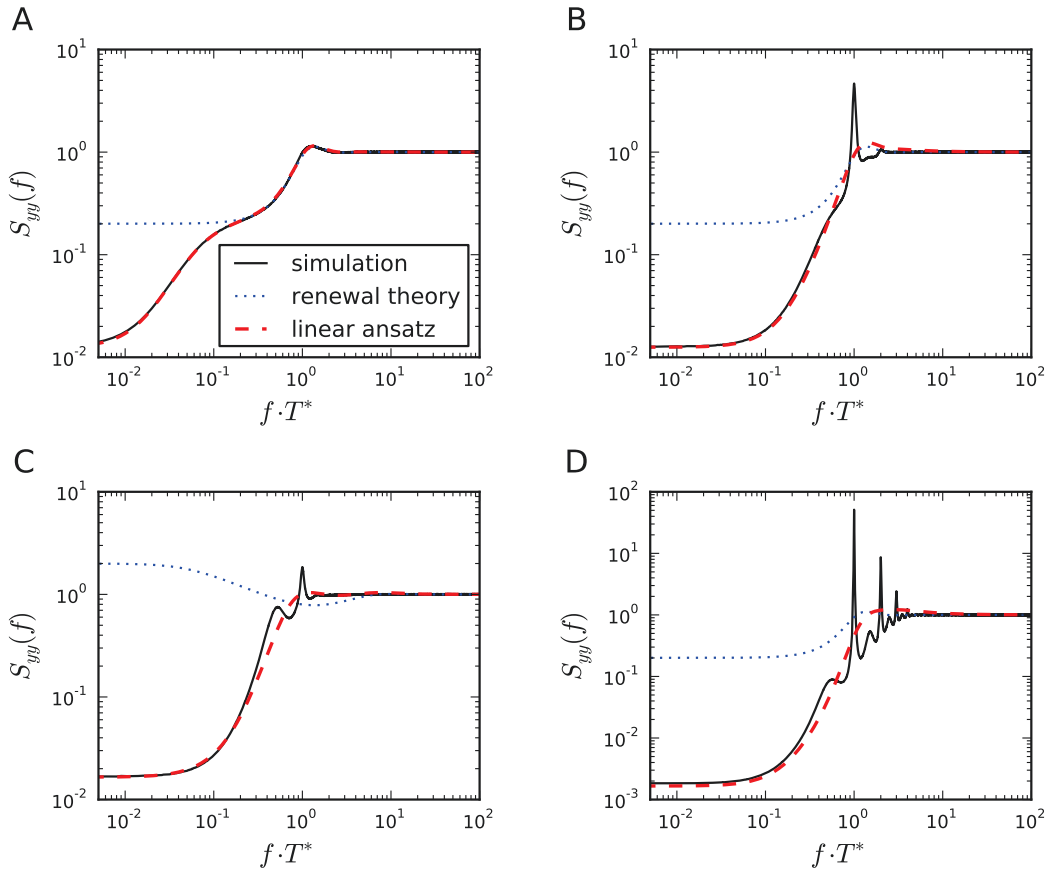

Figure 3.24.: Power spectral densities – reduction of power at low frequencies. The power spectrum obtained from numerical simulations is depicted by the black solid line. The theory, Eq. (3.157), based on the linear ansatz (red dashed line) works well for not too strong adaptation. At low frequencies this theory agrees generally well, where it shows a strong reduction of power compared to the corresponding renewal theory, Eq. (3.155) (blue dotted line). **A** Slow adaptation $\tau_a = 10T^*$, $\tilde{\Delta} = 3V_{th}$, $D = 0.1V_{th}^2/T^*$. Fast adaptation: **B** $\tau_a = 1T^*$, $\tilde{\Delta} = 3V_{th}$, $D = 0.1V_{th}^2/T^*$, Strong adaptation: **C** $\tau_a = T^*$, $\tilde{\Delta} = 10V_{th}$, $D = 1V_{th}^2/T^*$, **D** $\tau_a = T^*$, $\tilde{\Delta} = 10V_{th}$, $D = 0.1V_{th}^2/T^*$

In the second part, the effect of noise was studied using different weak-noise approximation methods. These methods were based on the assumption that the stochastic dynamics is still close to the deterministic limit cycle, which is true for weak noise. In particular, the conditional ISI statistics for a given initial value of the adaptation current has been analyzed, which is equivalent to a first-passage-time problem in a non-stationary setup. This has yielded approximations for the conditional ISI density, the conditional mean ISI, the conditional CV and the transition probability density of subsequent peak adaptation currents, which agree well with simulations for not too strong noise. To obtain the full ISI statistics, the conditional statistics have to be averaged with respect to the stationary distribution of the peak adaptation currents. The distribution has been computed from the stationary solution of the Fokker-Planck equation. To this end, the stationary Fokker-Planck equation has been solved using a WKB ansatz. As a result, I have shown that the variability of the peak adaptation currents becomes maximal at a finite value of the adaptation time constant. Furthermore, the stationary solution of the Fokker-Planck equation could be used to derive an expressions for the distribution of the membrane potential. In contrast to the non-adapting PIF model, the distribution varies more strongly across membrane potentials and is a convex function except for a small region close to the threshold.

In the third part of this chapter, it was assumed that the adaptation current is slow on the time scale of the mean interspike interval, whereas the noise intensity could be arbitrary. Under this assumption, it was possible to derive approximations for the ISI density (inverse Gaussian), the linear response function (or susceptibility) showing the typical high-pass properties of adaptation as well as the power spectrum, which revealed a clear reduction of power at low frequencies due to negative serial correlations.

Chapter 4.

How a stochastic adaptation current affects the interspike interval statistics of a sensory receptor neuron

In many sensory systems, the response of neurons to repeated presentation of the very same stimulus reveals a great variability in both timing of action potentials and spike counts, especially if stimuli are static [van Steveninck et al., 1997, Kreiman et al., 2000, Ronacher et al., 2004]. This trial-to-trial variability may have profound implications on subsequent signal processing, constrains the neural code and sets fundamental limits on the reliability of behavioral responses to external stimuli. The variability is caused by noise sources at all levels of the sensory pathway [Faisal et al., 2008]: e.g. uncertainty in the external stimulus, sensory noise in the transduction and amplification processes, channel noise due to the random gating kinetics of ion channels and synaptic noise due to synaptic background activity and stochastic vesicle release. To understand how the nervous system can cope with noise and can achieve the remarkable reliability on the behavioral level, it is important to first assess the impact of each of these sources of noise on the variability.

Here, we pose the following question: Can we learn about the origin of noise by just looking at the input-output relationship of a neuron? Using stochastic neuron models, we show by theoretical analysis that different sources of noise leave a characteristic trace in the interspike-interval statistics. This suggests a method to uncover the dominating sources of noise from experiments. The method is then applied to a particular sensory neuron, for which we find strong evidence that the spike response variability is caused by both fast channel noise and slow channel noise associated with an adaptation current. This study constitutes a collaborative work with Dr. Karin Fisch and Dr. Jan Benda (LMU Munich), who carried out the experiments and the stochastic simulations of the conductance-based model. The main results are briefly reviewed in this chapter [for more details, see Fisch, 2011]. The theoretical analysis and the simulations of the integrate-and-fire model have been performed by myself and have been published in [Schwalger et al., 2010].

Specifically, we study the source of variability in the spiking response of auditory receptor neurons of *Locusta migratoria* (grasshopper) to acoustic stimuli. These receptor neurons are attached to the tympanum (ear drum), which vibrates in response to incoming sound waves. The mechanical vibrations are further transduced by the receptor cell into electrical currents via stretch-sensitive ion channels, which in turn drive the spike generation. Dynamical stimuli in form of amplitude modulations of sound waves are

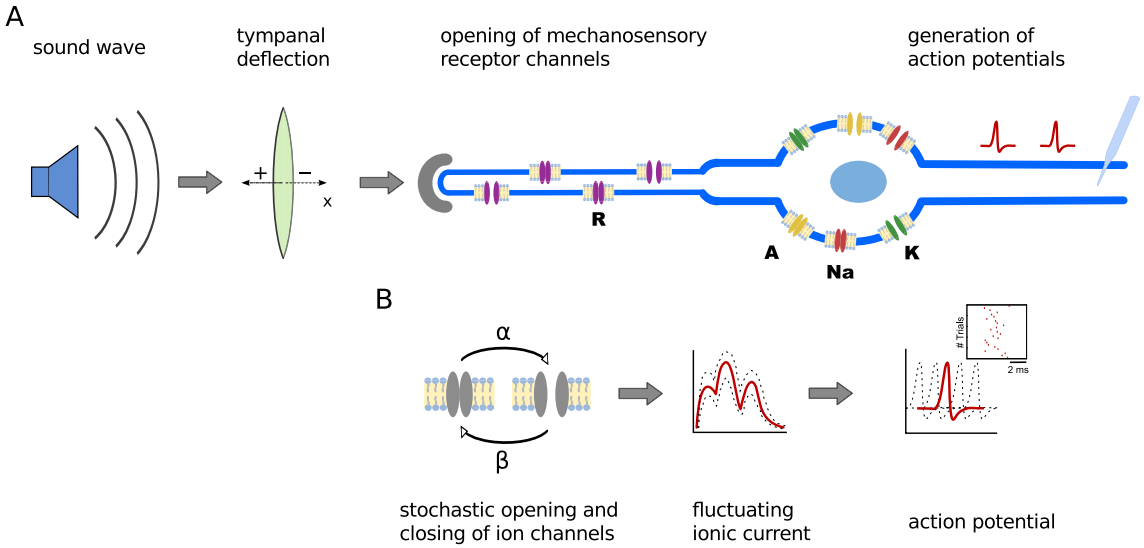

Figure 4.1.: Sketch of auditory signal transduction in locust. **A** Deflections of the tympanal membrane induced by sound stimuli cause stretch-sensitive "receptor channels" (R) in the dendrite of bipolar receptor cells to open and close. This creates a "receptor current", which drives voltage-gated sodium (Na) and potassium (K) channels in the membrane to generate action potentials. These action potentials can be recorded from the axon. An adaptation current mediated by voltage-dependent adaptation channels (Adap) is included to account for the observed spike-frequency adaptation of auditory receptor cells. **B** According to our hypothesis the spike timing variability is caused by channel noise due to the random opening and closings of ion channels. Each population of ion channels can potentially contribute to channel noise. Figure adapted from Fisch [2011].

transmitted remarkably well by these neurons [Machens et al., 2001, 2005] based on precise timings of action potentials [Rokem et al., 2006]. In contrast, the spiking response to pure tone stimuli with constant amplitude are rather variable [Schaette et al., 2005]. In the following, we assume that fluctuations of the mechanical stimulus, including thermal fluctuations of the tympanum, are negligible. This seems a reasonable assumption as simulations of a supra-threshold receptor model with tympanum fluctuations could not explain the high coefficients of variations observed in experiments (data not shown). Because auditory receptor cells do not receive any synaptic input from other neurons, the observed variability is likely caused by intrinsic noise. But what is the exact nature of the noise and what are its statistical properties?

One way to answer this question is to test different hypotheses about the neural noise by using a model of the auditory transduction process (Fig. 4.1). It can be assumed that the major intrinsic source of noise is channel noise [Lecar and Nossal, 1971, Diba et al., 2004, Jacobson et al., 2005, Faisal et al., 2008]. This source of noise can potentially arise for all ionic currents in the cell. Under this assumption, the question becomes, which channel populations contribute most to spike timing variability. This requires to simulate the model of the receptor neuron with different populations of ion channels that mediate (i) the fast receptor current (transduction current) (ii) the fast sodium current and the delayed rectifier potassium current that establish the spike generation and repolarization mechanism and (iii) a slow adaptation current. The latter is needed to account for the observed spike-frequency adaptation of locust auditory receptor cells [Römer, 1976, Benda et al., 2001]. The predictions generated by the model can then be compared to exper-

imental data. Unfortunately, direct somatic recordings of the sub- and suprathreshold membrane potential are infeasible without severely damaging the delicate mechanosensory transduction machinery. It is possible, however, to perform intracellular recordings from the axons of the receptor neurons. This provides the spike times in response to a given acoustic stimulus. Moreover, by repeating the experiment over many trials, one can measure the statistics of the interspike interval (ISI) sequences. Thus, the computational task consists in testing different hypotheses with respect to the reproducibility of the experimental ISI statistics and ruling out those noise sources that are not compatible with these ISI statistics. In this way, the primary source of variability might be identified. This combined experimental and computational approach has been pursued, e.g., by Dr. Karin Fisch in her PhD study [Fisch, 2011].

An essential precondition for this approach to work, is the ability to distinguish different kinds of noise on the basis of the ISI statistics. To this end, it is not only necessary to determine the ISI statistics for certain types of channel noise, but also to identify the aspects of the statistics by means of which different types of channel noise can be discriminated. In previous computational and theoretical studies of adapting neurons, fluctuations were considered to be fast, e.g. Poissonian synaptic spike trains passing through fast synapses [Wang, 1998, Liu and Wang, 2001, Muller et al., 2007] or a white Gaussian input current representing a mixture of intrinsic fluctuations and background synaptic input [Chacron et al., 2003, La Camera et al., 2004, Urdapilleta, 2011]. For auditory receptor cells, however, the intrinsic noise is not only contributed by the fast ionic conductances, but also by the channels that mediate slow adaptation currents. If the number of adaptation channels is not too large, the stochastic opening and closing of single channels will contribute a fluctuating component to the adaptation current. This noise contribution, which was so far ignored in the literature, and its impact on the interspike interval (ISI) statistics is the main subject of this chapter. As a result, analytical tools are put forward to distinguish fast intrinsic noise from slow adaptation noise by means of the stationary ISI statistics. These tools are then applied to the ISI statistics of auditory receptor cells to uncover the primary sources of spiking variability. In conjunction with the computational modeling study of Fisch [2011] we hypothesize that the spiking variability of locust auditory receptor cells is caused by both slow adaptation channel noise and fast (sodium or receptor) channel noise.

The theory is based on a perfect integrate-and-fire (PIF) model with an adaptation current that is mediated by a population of slow voltage-gated adaptation channels. This constitutes a minimal model of tonically firing neurons, where the effect of adaptation channel noise can be analyzed. Thus, the qualitative results of the theory are rather general. In particular, we show that a PIF model with a stochastic adaptation current can be approximated by a PIF neuron driven by a slow external colored noise – a model which has been extensively analyzed in Chap. 2. As a surprising consequence, pure adaptation channel noise induces positive ISI correlations in marked contrast to negative ISI correlations evoked by the combination of fast noise and deterministic adaptation, which has been studied in detail in Chap. 3. Furthermore, the ISI histogram is more peaked and displays a heavier tail than expected for a PIF model with fast current noise. Our results for the PIF (positive ISI correlations, peaked histograms) are qualitatively confirmed by extensive simulations of a conductance-based model with N_a stochastic adaptation channels supporting the generality of our findings.

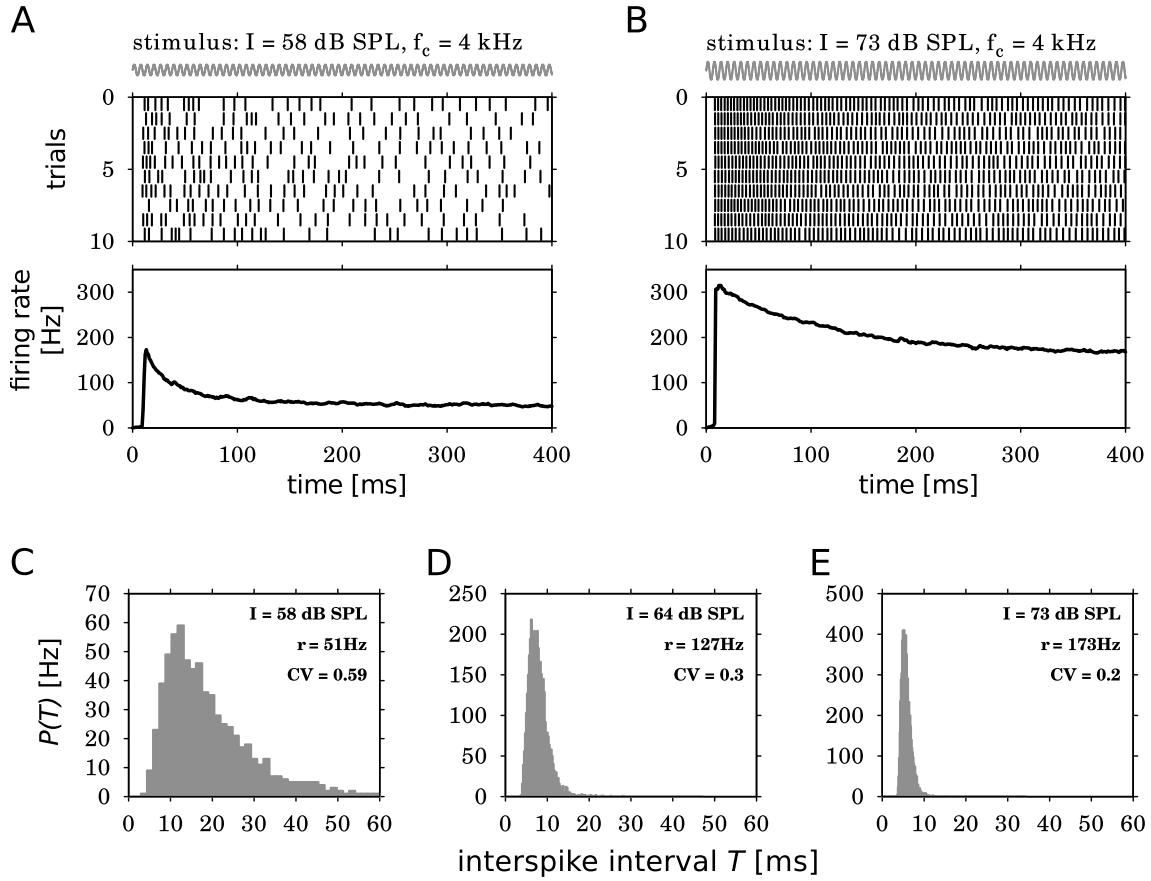

Figure 4.2.: Spiking variability and adaptation of a locust auditory receptor cell. A,B Response of a single cell to a pure tone sound stimulus of $f_c = 4$ kHz (the neuron's preferred frequency) at two different sound intensities. Spike times show variability both within and across trials (top). The trial-averaged firing rate depends on sound intensity and shows the phenomenon of spike-frequency adaptation (bottom). **C – E** ISI densities of the same cell as in **A,B** for increasing sound intensities (and increasing firing rate r) reveal the variability of interspike intervals (ISIs). This variability can be quantified by the coefficient of variation (CV), which decreases with sound intensity. Figure adopted from Fisch [2011].

4.1. The interspike interval statistics of locust auditory receptor cells

The auditory system of locust is a simple-structured and well-established model system, in which the signal processing of well-defined stimuli can be traced in detail. The mechanosensory transduction of acoustic stimuli into electrical currents takes place in 60–80 receptor neurons that are connected via attachment cells to the tympanum, the grasshopper's eardrum. These receptor cells are bipolar neurons each possessing a single dendrite that contains mechanosensory transduction channels. These ion channels are gated by the deflections of the tympanum and will be termed "receptor channels" in the sequel. The transduction current drives voltage-gated ion channels that eventually generate action potentials. These action potentials can be recorded from the auditory nerve, i.e. the receptor cell's axons, far away from the soma and the filigree transduction apparatus. A detailed description of the anatomy of locust auditory receptor cells can be

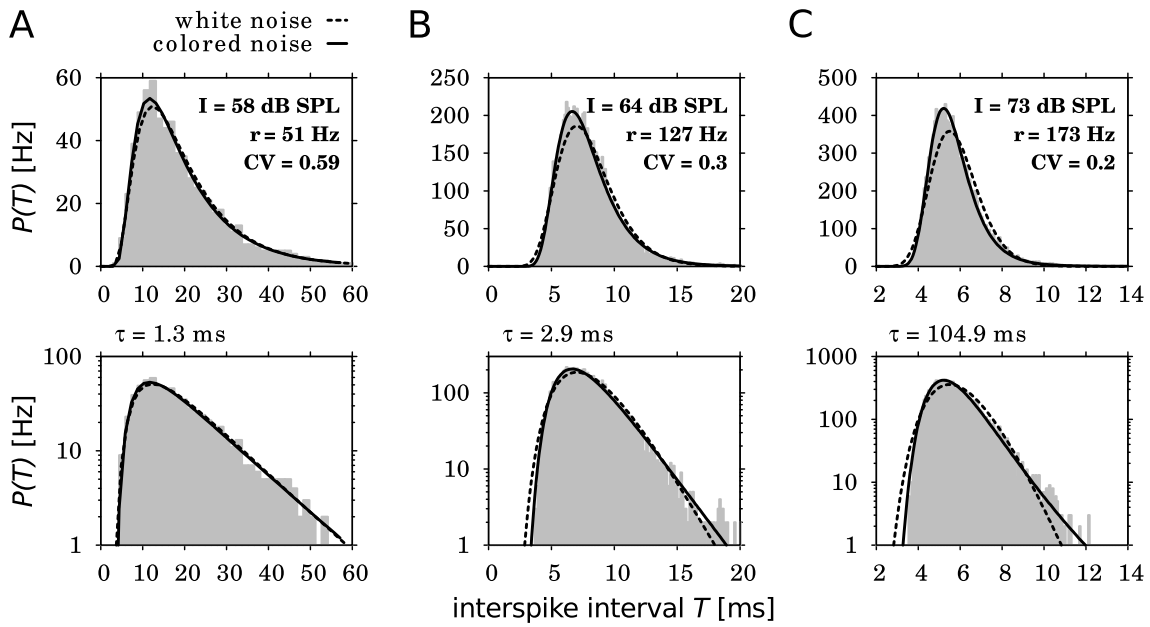

Figure 4.3.: Shape of the ISI densities of a single receptor cell for different sound intensities. The ISI histograms (gray bars) are compared with an inverse Gaussian ISI density $P_{\mathrm{wn}}(t)$, Eq. (2.91) (dashed line), and with the ISI density $P_{\mathrm{cn}}(t)$ of a PIF model driven by colored noise, Eq. (2.90) (solid line). The parameters of $P_{\mathrm{wn}}(t)$ have been chosen such that the distributions yield the same mean and CV as the experimental data. For $P_{\mathrm{cn}}(t)$ the parameter ϵ has been expressed in terms of the CV and the correlation time τ of the colored noise, whereupon τ has been fitted to the data (fit value as indicated). The differences in the tail of the distributions can be seen in the bottom row, where the ISI densities are scaled logarithmically. Figure adopted from Fisch [2011].

found in Gray [1960].

Intracellular recordings. In the following, a short review of the experiments performed by K. Fisch in the lab of J. Benda, LMU Munich, is given. For more details, the reader is referred to Fisch [2011].

Intracellular recordings from the axons of auditory receptor cells have been performed during acoustic stimulation with a pure tone at the characteristic frequency of the neuron. After stimulus onset the auditory neurons exhibited considerable spike-frequency adaptation (Fig. 4.2A). Since we were interested only in the stationary ISI statistics, the initial 200 ms of each trial have been discarded corresponding to the firing rate transient due to spike-frequency adaptation. The stationary firing rate increased in a sigmoidal fashion with sound intensity, and the variability as quantified by the CV decreased with sound intensity [Fisch, 2011]. This is illustrated by the ISI histograms for three different sound intensities (Fig. 4.2C–E). At low firing rates the histograms show a broad distribution of ISIs with CV values that can be as high as 0.9 (not shown). At high firing rates, the ISI histograms showed less variability with CV values that saturate at minimal values of 0.1–0.2.

To assess the origin of the variability, we compared the ISI distributions with canonical noise driven models. For high firing rates the CVs are considerably below 1, where the

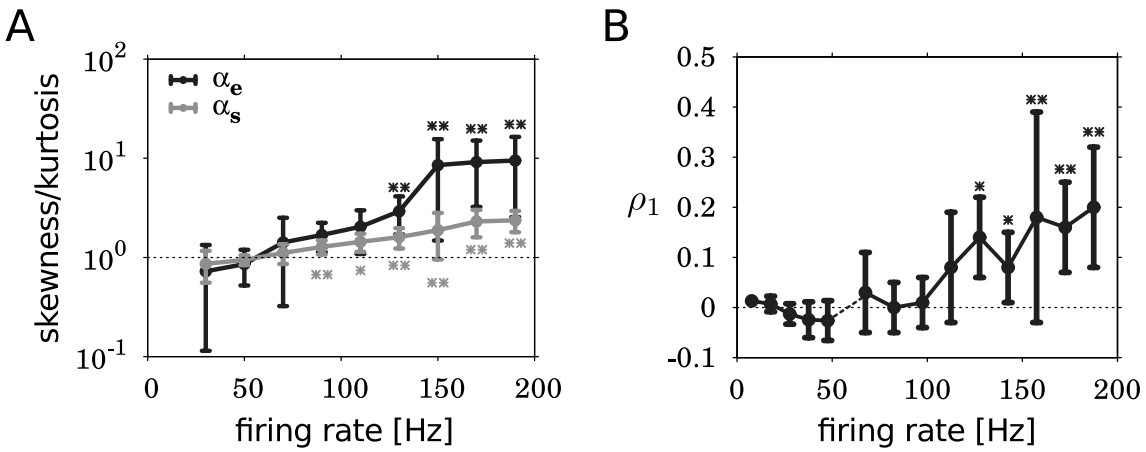

Figure 4.4.: Shape of the ISI histograms and serial correlation coefficient for different firing rates. A Skewness α_s and kurtosis α_e (characterizing the shape of the ISI density) averaged over 12 recorded receptor neurons. The measures α_s and α_e become significantly larger than unity at large firing rates. **B** Serial correlation coefficient at lag 1 shows a transition from slightly negative values (at low firing rates) to positive values (at high firing rates). Figure adopted from Fisch [2011].

receptor cells most likely operate in the supra-threshold regime. The canonical model for such strongly driven neurons is the perfect integrate-and-fire (PIF) model. Driven by white Gaussian noise, this model generates spikes with an inverse Gaussian ISI density, Eq. (1.68). Because the inverse Gaussian density is completely determined by the firing rate and the CV, we can test – by using the measured rate and CV – whether the PIF model driven by white noise is compatible with the ISI distribution data. Indeed, at low firing rates the simple inverse Gaussian density matches the experimental histograms remarkably well (Fig. 4.3A, dashed line). However, at larger firing rates, the inverse Gaussian determined by the measured rate and CV no longer provides a good description of the experimental data (Fig. 4.3B,C, dashed line). The histograms are more peaked and exhibit a longer tail than the inverse Gaussian.

From Chap. 2.2, we know that peaked ISI densities can be generated by a PIF model that is driven by exponentially-correlated colored noise. In this case the ISI density is given by Eq. (2.90) [see also Lindner, 2004a]. Therefore we tested whether this density can account for the observed peaked ISI histograms. The noise parameter ϵ in Eq. (2.90) can be extracted from the measured CV. This leaves one free parameter – the correlation time τ of the colored noise. A fit of the ISI density with respect to τ yields an excellent agreement with the observed ISI histograms in the whole range of firing rates (Fig. 4.3, solid line). Note that in the limit $\tau \to 0$ the ISI density (2.90) converges to the inverse Gaussian density, as shown in Chap. 2.2. This is consistent with the good agreement of an inverse Gaussian at low firing rates, which was mentioned above. In the opposite case of high firing rates, the best fit was obtained for a correlation time τ about 100 ms (Fig. 4.3C). This roughly corresponds to the decay time of spike frequency adaptation.

As suggested in Chap. 2.2, the transition of the ISI density of a PIF model driven by white noise to a PIF model driven by colored noise may be characterized by the skewness α_s and the kurtosis α_e, which are defined in Eq. (2.92) and (2.93). These measures are equal to unity for an inverse Gaussian density. Values larger than unity indicate that the

ISI density is more skewed and more peaked and possesses a longer tail than an inverse Gaussian with the same CV. Figure 4.4A shows that the experimentally measured values for α_s and α_e confirm our previous observations: at low firing rates, these values are close to unity, corresponding to the good match of an inverse Gaussian. In contrast, for high firing rates, the measured values are significantly larger than unity corresponding to the observed peaked ISI densities with long tails. In summary, the shape of the ISI density as quantified by α_s and α_e suggest that the dominant effect of intrinsic noise is that of a white noise source at low firing rates and that of a colored noise at high firing rates.

We further investigated the ISI serial correlations. As known from a number of numerical studies [see e.g. Chacron et al., 2001, Liu and Wang, 2001] and from the analytical theory of Chap. 3, [see Schwalger et al., 2010], the signature of spike-frequency adaptation in the stationary state are negative serial correlations. Since auditory receptor cells exhibit spike-frequency adaptation as apparent from the firing rate transient in Fig. 4.2, negative serial correlations may be expected. Indeed, small, but significantly negative serial correlations were found at low firing rates (Fig. 4.4B). However, at high firing rates the serial correlations were significantly positive.

In conclusion, at low firing rates the ISI statistics (shape of the ISI density and serial correlations) are consistent with an adapting PIF model driven by white noise, whereas at high firing rates the ISI statistics is consistent with a non-adapting PIF model driven by colored noise. In the following analysis, we will show that this phenomenological observation indeed follows from the assumption of two sources of noise: on the one hand, fast channel noise associated with fast ionic currents and, on the other hand, slow channel noise associated with a slow adaptation current.

4.2. How a stochastic adaptation current shapes the statistics of interspike intervals

How can the ISI variability of locust auditory receptor cells in response to pure tone stimuli with constant amplitude be explained? To answer this question, we consider the signal transduction process from an acoustic stimulus to the spike generation of the receptor cell (Fig. 4.1A). A sound wave induces vibrations of the tympanum, which causes mechanosensory ion channels in the dendrite of the receptor cell to open. The resulting receptor current activates voltage-gated sodium and delayed-rectifier potassium channels that eventually trigger action potentials. In the following, we investigate the effect of channel noise arising from slow adaptation currents, i.e. a finite number of adaptation channels (Fig. 1.3), and compare with the effect of channel noise associated with fast ionic currents.

4.2.1. Adapting neuron model driven by two different kinds of noise

To explore the role of channel noise, a minimal point-neuron model of the auditory receptor cell is considered, which comprises a sodium and potassium current for the spike generation, I_{Na} and I_K, a leak current I_L, an M-type adaptation current I_a and a receptor current I_R (Fig. 4.1A). The membrane potential V across the cell membrane must satisfy

the current-balance equation

$$C_{\mathrm{m}}\frac{dV}{dt} = -I_{\mathrm{L}} - I_{\mathrm{Na}} - I_{\mathrm{K}} - I_{\mathrm{a}} - I_{\mathrm{R}}, \tag{4.1}$$

where C_m is the membrane capacity. Assuming that Ohm's law is applicable each of the currents (per unit area) has the form

$$I = g(V - E), \tag{4.2}$$

where g is the conductance per unit membrane area and E is the reversal potential of the respective ionic current. Each of the conductances results from a population of a finite number of ion channels, and may hence be subject to fluctuations.

The time scale of the fluctuations of a conductance must be equal to the relaxation time of the mean conductance with respect to a small perturbation, which is a consequence of the fluctuation-dissipation theorem. The relaxation time of the sodium, delayed-rectifier potassium and receptor currents are much smaller than the mean ISI. Therefore, channel noise associated with these currents can be considered as fast. On the hand, the relaxation time of the adaptation current (or conductance) should be of the same order as the decay time constant of the firing rate adaptation in response to step stimuli. For locust auditory receptor cells the time scale of spike-frequency adaptation is of the order of 100 ms and is thus much larger than the mean ISI (order 10ms). Thus, adaptation is in general not fast and is therefore studied separately.

A detailed simulation study of Eq. (4.1), where each current results from the summed activity of a population of ion channels with realistic kinetics, has been conducted in Fisch [2011]. Complementary to the study by Fisch, the following analysis is based on further simplifying assumptions, which yield rather general insights and predictions for the effect of different types of channel noise. To this end, we rely on a number of theoretical studies that have already dealt with fast channel noise, especially its diffusion approximation [for a review see White et al., 2000]. Applying the diffusion approximation to the population of fast ion channels, the neural dynamics can be in fact stripped down to the model that has already been studied in Chap. 3.

In contrast, the effect of slow conductance fluctuations has, to our knowledge, not yet been addressed analytically. For this reason and to keep the analysis simple, we focus primarily on the effect of slow adaptation channel noise, whereas all fast sources of noise are lumped into a single, unspecific Gaussian white noise source. Specifically, the sum of the fast spike generating currents, the fast receptor current and the leak current are represented as the sum of a deterministic current I_{fast} and Gaussian white noise:

$$-I_{\mathrm{L}} - I_{\mathrm{Na}} - I_{\mathrm{K}} - I_{\mathrm{R}} \approx I_{\mathrm{fast}} + \sqrt{2D}\xi(t)C_m. \tag{4.3}$$

Here, D is the noise intensity and $\xi(t)$ is a delta-correlated Gaussian process, i.e. $\langle \xi(t)\xi(t')\rangle = \delta(t-t')$. Eq. (4.3) corresponds to a diffusion approximation of fast channel noise. Replacing the respective terms in Eq. (4.1) yields

$$C_{\mathrm{m}}\frac{dV}{dt} = I_{\mathrm{fast}} - I_{\mathrm{a}} + \sqrt{2D}\xi(t)C_m. \tag{4.4}$$

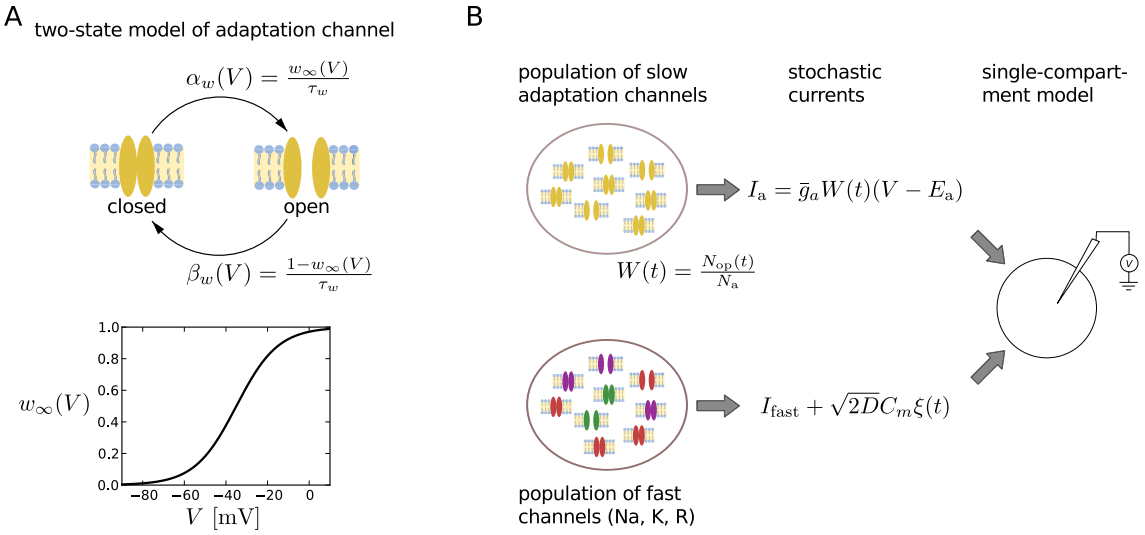

Figure 4.5.: Channel model with voltage-dependent transition rates. A A single channel for an M-type adaptation current is modeled by a two-state process (top): a transition from the closed to the open state occurs with a rate that is proportional to the steady-state open probability $w_\infty(V)$ for a clamped voltage V. The channels are mainly activated during strong depolarizations, i.e. during action potentials (bottom). Closing transitions occur mainly at subthreshold potentials. **B** The macroscopic currents are a result of the total population activity of ion channels. In the model, only the adaptation current is modeled explicitly by individual ion channels. The adaptation current is proportional to the fraction of open adaptation channels $W(t)$, which fluctuates for a finite number of channels. All fast ionic currents (Na - sodium, K - potassium, R - mechanosensory receptor current) are modeled by a deterministic current added by a Gaussian white noise.

This model still contains two different kinds of noise – the slow channel noise inherent to the adaptation current I_a and the white noise term mimicking fast channel noise. Thus, the analysis is reduced to the problem of distinguishing the effect of these two kinds of noise. Note that our method is solely based on the differential effect of slow and fast noise on the ISI statistics of adapting neurons. A distinction between different kinds of fast noise, such as sodium and receptor channel noise, is not feasible with our method.

In general, the currents I_{fast} and I_a on the right-hand side of equation (4.4) depend on the membrane potential through a voltage-dependent conductance dynamics. Such a conductance-based model is, however, still difficult to treat analytically because already the deterministic system constitutes a complex multidimensional, non-linear dynamical system. To still gain analytical insights, we investigate the system in two different variants corresponding to different levels of complexity. In the first variant, which is amenable to an analytical treatment, we approximate I_{fast} by a constant (voltage-independent) current $C_m\mu$. Substituting this approximation in Eq. (4.4) we obtain

$$\dot{V} = \mu - \frac{I_a}{C_m} + \sqrt{2D}\xi(t). \tag{4.5}$$

In addition to that, a fire and reset rule is adopted, according to which the membrane potential V is reset to zero when V crosses a threshold $V_{th} > 0$ from below. The crossing events define the spike times, which are the actual output of the neuron model. This dynamics corresponds exactly to a perfect integrate-and-fire (PIF) model with an adap-

tation current. The PIF model is a minimal model for neurons that are strongly driven by the mean current ("mean-driven" or "supra-threshold" regime). As such, the PIF model seems to be a reasonable model for locust auditory receptor neurons. In fact, given the high firing rates and the non-exponential ISI distributions (Fig. 4.2C–E), these neurons most likely operate in their supra-threshold regime.

In the second variant, numerical simulations of Eq. (4.4) have been conducted by Fisch [2011], where I_{fast} was taken from the conductance-based Traub-Miles model modified by Ermentrout et al. [2001]. In this way, the qualitative predictions of the PIF model could be tested in a biologically more realistic conductance-based model. The specific definition of I_{fast} is given in the appendix C.2.

4.2.2. Model for the stochastic adaptation current

For both the conductance-based model and the PIF model, the adaptation current still needs to be defined. Here, we only consider the simplest adaptation channel model which corresponds to an M-type adaptation current [Brown and Adams, 1980, Madison and Nicoll, 1984] (cf. Sec. 1.3.2). This current is mediated by KCNQ channels, which are slow voltage-dependent potassium channels. Although, M-type channels are partially activated at resting potentials (Fig. 4.5A, [see also Hille, 2001]), the main activation occurs during action potentials. Our results, however, also apply to other sources of noise emerging from a slow adaptation mechanisms as, for instance, slow Ca^{2+} fluctuations in the case of calcium-gated potassium currents (see discussion).

Two-state channel model

We assume a simple setup that allows for a mathematical analysis of slow, voltage-dependent adaptation channels. This setup consists of a population of N_a independent ion channels each of which can reside either in an open or a closed state. A single channel follows the simple kinetics shown in Fig.4.5A. For a population of N_a channels, it is sufficient to follow the number of open channels N_{op} instead of tracing the state of each individual channel. The number of open channels then obeys the reaction kinetics

$$N_{op} \xrightarrow{\alpha_w N_{cl}} N_{op} + 1 \tag{4.6a}$$

$$N_{op} \xrightarrow{\beta_w N_{op}} N_{op} - 1, \tag{4.6b}$$

where $N_{cl}(t) = N_a - N_{op}(t)$ is the number of closed channels.

Transition rates in the conductance-based model. For the conductance-based model, Eq. (C.13), the rates α_w and β_w can be expressed in terms of the steady-state open probability $w_\infty(V)$ of a single channel when the membrane potential is clamped at V and the time scale τ_w of the channel kinetics. In fact, by inverting Eq. (1.7), we find

$$\alpha_w(V) = \frac{w_\infty(V)}{\tau_w} \qquad \beta_w(V) = \frac{1 - w_\infty(V)}{\tau_w}. \tag{4.7}$$

Note that both $w_\infty(V)$ and τ_w can be measured in experiments. The master equation for the open probability $w(t)$ of the two-state model reads

$$\dot{w} = \alpha_w(V)(1-w) - \beta_w(V)w \tag{4.8}$$

or after insertion of Eq. (4.7)

$$\tau_w \dot{w} = -w + w_\infty(V). \tag{4.9}$$

This is in accordance with the typical dynamics of voltage-dependent gating variables in Hodgkin-Huxley type models.

In the conductance-based Traub-Miles model (Sec. C.2), we will use the steady-state open probability given by

$$w_\infty(V) = \left(1 + \exp\left[-\frac{V + 35\text{mV}}{10\text{mV}}\right]\right)^{-1} \tag{4.10}$$

[Ermentrout et al., 2001] (see Fig. 4.5A,bottom). Inserting this relation into Eq. (4.7), both rate functions $\alpha_w(V)$ and $\beta_w(V)$ show a sigmoidal dependence on the voltage. In particular, α_w is appreciably different from zero only during the action potential (i.e. for $V > -50\text{mV}$) whereas β_w only contributes in the opposite range of subthreshold membrane voltages.

Transition rates in the PIF model. In the case of a PIF model, the following problem arises: since the voltage is always subthreshold and action potentials are generated only implicitly, the steady-state open probability $w_\infty(V)$ would not lead to a relevant activation of adaptation channels (cf. Eq. (4.10) and Fig. 4.5A, bottom). How can one still generate an adaptation current that is triggered by spikes? To resolve this problem, we use a simplified variant that distinguishes only between two values of w_∞: one attained when the voltage is subthreshold and another one for the duration of the action potential τ_{AP}. Specifically, at a spike event of the PIF model, w_∞ is explicitly set to one for a duration of $\tau_{\text{AP}} = 1$ ms and otherwise it is set to zero (Fig. 4.6A). Thus, w_∞ becomes an explicit function of time t and the last spike time $t_{i^*} \leq t$:

$$w_\infty(t) = \begin{cases} 1 & \text{if } t_{i^*} \leq t < t_{i^*} + \tau_{\text{AP}} \\ 0 & \text{else.} \end{cases} \tag{4.11}$$

Hence, in the PIF model, the dependence of the rates on the membrane voltage, Eq. (4.7), is replaced by an explicit dependence on time t and the most recent spike time $t_{i^*} \leq t$:

$$\alpha_w(t) = \frac{w_\infty(t)}{\tau_w}, \qquad \beta_w(t) = \frac{1 - w_\infty(t)}{\tau_w}. \tag{4.12}$$

In the same way, the dynamics of the open probability, Eq. (4.9), is replaced by

$$\tau_w \dot{w} = -w + w_\infty(t). \tag{4.13}$$

The assumption that channels can be activated only during spikes ($\alpha_w = 1/\tau_w$) but not in between spikes ($\alpha_w = 0$) is for analytical convenience. However, in Sec. 4.4 we show that our results remain qualitatively the same if a small subthreshold activation ($w_\infty(t) > 0$)

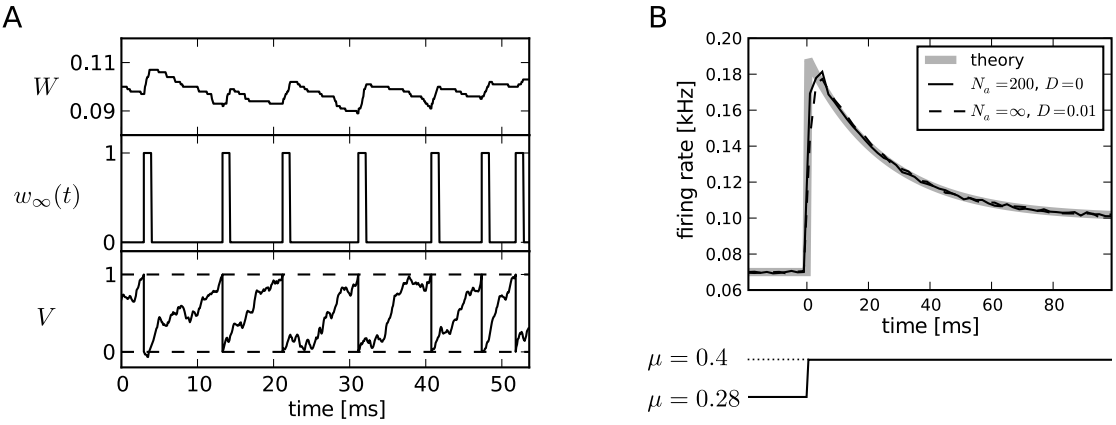

Figure 4.6.: Perfect integrate-and-fire model with stochastic adaptation current, Eq. (4.16)**. A** Membrane potential V (bottom), steady-state open probability w_∞ (middle) and fraction of open adaptation channels W as a function of time (top). Parameter values: $N_\mathrm{a} = 1000$, $D = 0.01 V_\mathrm{th}^2/\mathrm{ms}$, $\tau_w = 100$ ms, $\mu = 0.4 V_\mathrm{th}/\mathrm{ms}$ and $\beta = 3 V_\mathrm{th}/\mathrm{ms}$. **B** The time-dependent firing rate (top) in response to a step stimulus (bottom) shows the same spike-frequency adaptation regardless of the source of noise (stochastic adaptation – solid line, deterministic adaptation plus white noise – dashed line). The gray line shows the theory given by Eq. (3.149).

is allowed, as it is observed for M-type currents.

Adaptation current. In the limit of an infinite population of channels, the fraction of open channels is equal to the open probability. In the Traub-Miles model or the integrate-and-fire model this limit corresponds to an adaptation current of the form [Benda and Herz, 2003]

$$I_\mathrm{a} = \bar{g}_\mathrm{a} w(t)(V - E_\mathrm{a}). \tag{4.14}$$

Here, $\bar{g}_\mathrm{a}$ denotes the maximal conductance (per unit membrane area) and E_a is the reversal potential of the adaptation current.

For a finite population of channels, the fraction of open channels is given by the *stochastic* quantity $W(t) = N_\mathrm{op}(t)/N_\mathrm{a}$, where $N_\mathrm{op}(t)$ is a stochastic process that evolves according to the kinetic scheme Eq. (4.6). In contrast to Eq. (4.14), this yields a stochastic adaptation current

$$I_\mathrm{a} = \bar{g}_\mathrm{a} W(t)(V - E_\mathrm{a}). \tag{4.15}$$

In the following, we want vary the amount of channel noise, without changing the mean current per unit membrane area. To this end, we vary the number of channels in such a way that the maximal conductance per unit membrane area $\bar{g}_\mathrm{a}$ remains constant. This can be realized either by a variation of the total membrane area or by a change of the channel density with a simultaneous scaling of the single channel conductance.

4.2.3. Perfect integrate-and-fire model with a stochastic adaptation current

For the mathematical analysis of the PIF model with adaptation, an effective time scale approximation is applied to the deterministic or stochastic adaptation current, Eq. (4.14) or (4.15), respectively. This approximation amounts to substituting V by the average voltage $E_0 = \langle V \rangle$ to obtain the voltage-independent adaptation current $I_\mathrm{a} = \bar{g}_\mathrm{a} W(t)(E_0 -$

E_a) [Benda and Herz, 2003]. Eq. (4.5) for the PIF model now reads

$$\dot{V} = \mu - \beta W + \sqrt{2D}\xi(t), \tag{4.16}$$

where $\beta = \bar{g}_a(E_0 - E_a)/C_m$ is the maximal value of the adaptation current $\beta W(t)$ and sets the strength of adaptation. In the following, I will make a number of simplifications of the model described by Eq. (4.16). The different ramifications of the model are summarized in Fig. 4.7.

Diffusion approximation

As explained in Sec. 1.1.1, the channel model describing the dynamics of each individual channel can be considerably simplified by a diffusion approximation [Lecar and Nossal, 1971, Fox, 1997, Fox and Lu, 1994]. Following Gillespie [2000], the reaction kinetics Eq. (4.6), can be approximated by a single Langevin equation for $N_{op}(t)$ if the number of transitions in a sufficiently large time interval, which is still smaller than the decay time τ_w, is approximately Gaussian distributed. Under this assumption, we find analogously to the derivation of Eq. (1.6)

$$\dot{N}_{op} = -\beta_w N_{op} + \alpha_w N_{cl} + \sqrt{\beta_w N_{op} + \alpha_w N_{cl}}\xi_a(t) \tag{4.17}$$

with $N_{cl} = N_a - N_{op}$ and Gaussian white noise $\xi_a(t)$, with $\langle \xi_a(t)\xi_a(t')\rangle = \delta(t-t')$. Dividing the last equation by N_a yields

$$\tau_w \dot{W} = -W + w_\infty(t) + \sqrt{\frac{2\tau_w \sigma^2(W, w_\infty(t))}{N_a}}\xi_a(t) \tag{4.18}$$

where $\sigma^2(W, w_\infty(t))$ is given by

$$\sigma^2(W(t), w_\infty(t)) = \frac{1}{2}\left\{[1 - w_\infty(t)]W + w_\infty(t)[1 - W]\right\}. \tag{4.19}$$

Furthermore, the stochastic adaptation variable W can be separated into a deterministic and a stochastic part, $W = w + \eta$. This will be useful for the interpretation of our results. Equation (4.18) can then be rewritten by the two equations

$$\tau_w \dot{w} = -w + w_\infty(t) \tag{4.20}$$

$$\tau_w \dot{\eta} = -\eta + \sqrt{\frac{2\tau_w \sigma^2(w+\eta, w_\infty(t))}{N_a}}\xi_a(t). \tag{4.21}$$

The noise intensity depends on the state variables because the function $\sigma^2(W, w_\infty(t))$ depends explicitly on W and implicitly on V through the $w_\infty(t)$. Therefore, Eq. (4.18) and (4.21) are Langevin equations with multiplicative noise, which are still hard to tackle analytically. For slow adaptation, $\tau_w \gg \langle T\rangle$, however, the variations of $\sigma^2(W, w_\infty(t))$ are averaged out by the slow filter dynamics of adaptation as shown in Sec. C.1. As a result, the function $\sigma^2(W, w_\infty(t))$ can be approximated by its constant mean

$$\langle \sigma^2 \rangle \approx r\tau_{AP} - (r\tau_{AP})^2, \tag{4.22}$$

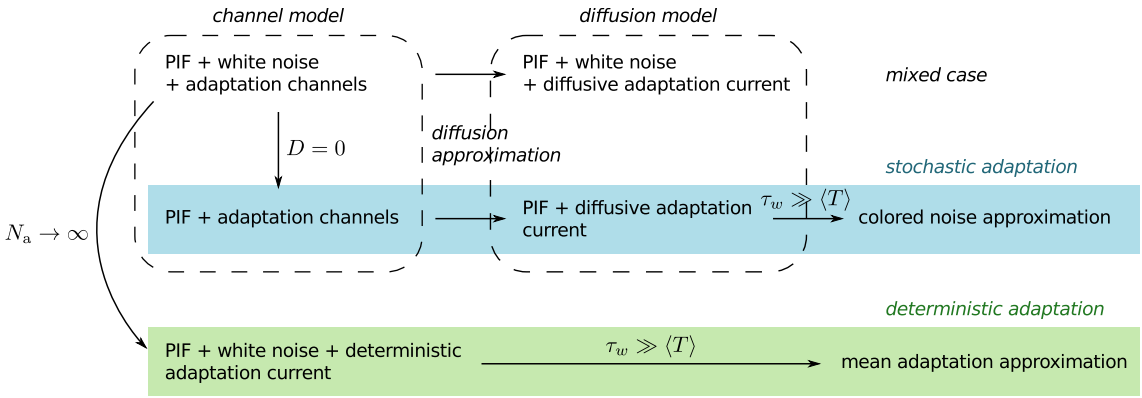

Figure 4.7.: Overview of limit cases and simplifications of the adapting perfect integrate-and-fire (PIF) model. The full model Eq. (4.16) with white Gaussian current noise ("fast noise") and a stochastic adaptation current based on two-state channels (mixed case) is represented in the upper-left corner. It branches into the limit cases $N_a \to \infty$ (Eq. (4.24)) and $D = 0$ corresponding to the cases termed deterministic adaptation (green) and stochastic adaptation (blue), respectively. Furthermore, the discrete stochastic adaptation current based on two-state adaptation channels (channel models) can be coarse-grained by a diffusion approximation yielding the diffusion models for stochastic adaptation (Eq. (4.25)) and the mixed case. For slow adaptation ($\tau_w \gg \langle T \rangle$), the cases of stochastic and deterministic adaptation can be reduced to a colored-noise driven PIF model (colored-noise approximation, Eq. (4.32)) and a white-noise driven PIF model (mean adaptation approximation, Eq. (3.132)), respectively.

where $r = \mu/(V_{\text{th}} + \beta\tau_{\text{AP}})$ is the stationary (adapted) firing rate (see below).

In summary, the adaptation current for a finite population of channels consists of the deterministic adaptation current and an additional Gaussian colored noise with a correlation time τ_w and a variance which is inversely proportional to the number of channels. Overall, we obtain the multi-dimensional Langevin model

$$\dot{V} = \mu - \beta(w + \eta) + \sqrt{2D}\xi(t) \tag{4.23a}$$

$$\tau_w \dot{w} = -w + w_\infty(t) \tag{4.23b}$$

$$\tau_w \dot{\eta} = -\eta + \sqrt{\frac{2\tau_w \langle \sigma^2 \rangle}{N_a}}\xi_a(t). \tag{4.23c}$$

The membrane potential V is thus driven by: (i) the base current μ (mainly representing the mean receptor current), (ii) the white current fluctuations $\xi(t)$ of intensity D (representing channel noise originating from fast sodium, potassium and receptor currents), (iii) the slow colored noise $\eta(t)$ due to the stochasticity of the adaptation dynamics, and (iv) the deterministic feedback of the neuron's spike train $w(t)$ due to the deterministic part of the adaptation (see Fig. 4.8).

4.2.4. Deterministic vs. stochastic adaptation current

To study the individual effects of the two different kinds of noise, we focus on two limit cases: In the limit of infinitely many adaptation channels, the adapting PIF model is only

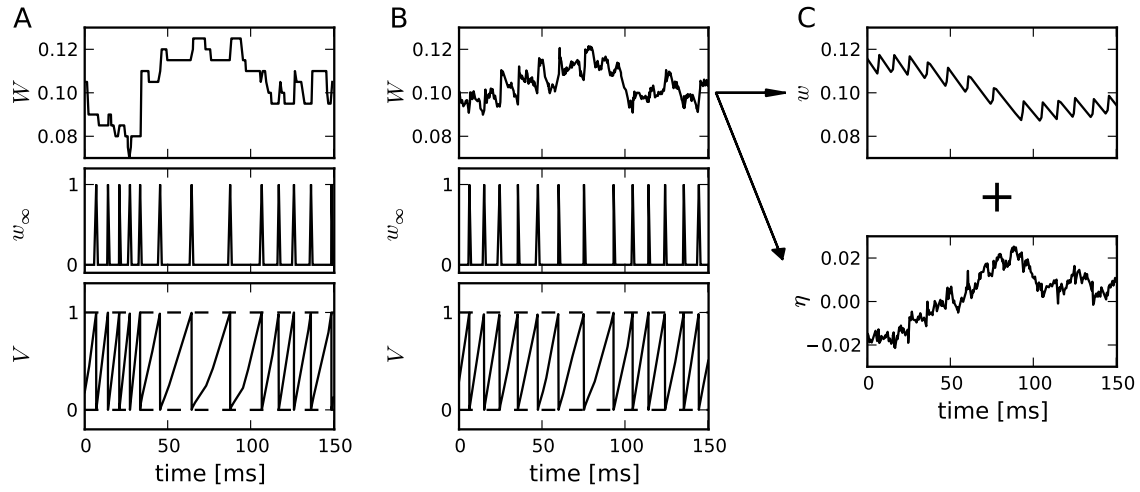

Figure 4.8.: Diffusion approximation of a stochastic adaptation current. **A** Sample traces of the integrate-and-fire dynamics with two-state adaptation channels, Eq. (4.6), (4.16) ($N_\mathrm{a} = 200$ and $D = 0$). The fraction of open channels W (top) exhibits discontinuous jumps with directions that depend on the presence or absence of spikes, which are mimicked by the function $w_\infty(t)$ (middle panel). **B** Sample traces of the coarse-grained diffusion model, Eq. (4.23), with the same 1st and 2nd infinitesimal jump moments of W as in the channel model (**A**). **C** The fraction of open channels W can be split into the deterministic part $w(t)$, Eq. (4.23b), corresponding to $N_\mathrm{a} \to \infty$, and an Ornstein-Uhlenbeck process $\eta(t)$, Eq. (4.23c), with a correlation time equal to the adaptation time constant τ_w (colored noise). Parameter values: $\mu = 0.4\ V_\mathrm{th}/\mathrm{ms}$, $\beta = 3\ V_\mathrm{th}/\mathrm{ms}$, $\tau_w = 100$ ms.

subject to a white noise. In this case, Eq. (4.23) reads

$$\dot{V} = \mu - \beta w + \sqrt{2D}\xi(t), \tag{4.24a}$$

$$\tau_w \dot{w} = -w + w_\infty(t). \tag{4.24b}$$

This case will be called *deterministic adaptation* because the adaptation current βw decays deterministically between subsequent spikes. Note that this model is closely related to the adaptation model investigated in Chap. 3. Below we will use the theoretical results developed in that chapter.

In the opposite limit, we keep only the stochasticity of the adaptation current but omit the white noise. Setting $D = 0$ we obtain

$$\dot{V} = \mu - \beta W \tag{4.25a}$$

$$\tau_w \dot{W} = -W + w_\infty(t) + \sqrt{\frac{2\tau_w \langle \sigma^2 \rangle}{N_\mathrm{a}}}\xi_\mathrm{a}(t) \tag{4.25b}$$

or splitting W into a deterministic part w and a stochastic part η,

$$\dot{V} = \mu - \beta(w + \eta) \tag{4.26a}$$

$$\tau_w \dot{w} = -w + w_\infty(t) \tag{4.26b}$$

$$\tau_w \dot{\eta} = -\eta + \sqrt{\frac{2\tau_w \langle \sigma^2 \rangle}{N_\mathrm{a}}}\xi_\mathrm{a}(t). \tag{4.26c}$$

This model (and the corresponding model based on discrete channel numbers) will be called *stochastic adaptation* because the adaptation current $\beta W = \beta(w + \eta)$ includes the colored noise $\eta(t)$ (Fig. 4.7).

Note that for the model based on individual channels, $W = N_{\mathrm{op}}/N_{\mathrm{a}}$ performs a random walk with discontinuous jumps. The direction of jumps depends on the presence of spikes, the occurrence of which is in turn is affected by W (feedback, Fig. 4.8A). The diffusion approximation of W and the separation of deterministic and stochastic components are illustrated in Fig. 4.8B and 4.8C, respectively. Although the increments of the continuous diffusion process have the same first two moments as the increments of the original jump process, the short-time statistics looks rather different (Fig. 4.8A,B). It is thus *a priori* not clear whether the diffusion approximation yields a reasonable approximation of the ISI statistics, and how the validity of the approximation depends on the channel number N_{a} and the adaptation time constant τ_w. Therefore, we conducted simulations of both the channel model (based on individual channels) and the diffusion model, Eq. (4.23). Remarkably, we find that the diffusion approximation yields a rather accurate approximation for the shape of the ISI density, the coefficient of variation and the serial ISI correlations even for small channel populations. However, significant deviation were found for higher-order statistics like the skewness and kurtosis of the ISI density.

Analytical treatment

The calculation of the ISI statistics (histogram and serial correlations) of the PIF model with noise and spike-frequency adaptation is generally a hard theoretical problem. Here we put forward several novel approximations for the simple limit cases Eq. (4.24) and Eq. (4.26).

Deterministic adaptation. If we introduce the adaptation variable $a = \beta w$ and approximate the train of square pulses $w_\infty(t)$ by a delta-spike train, $w_\infty(t) \approx \tau_{\mathrm{AP}} \sum_i \delta(t - t_i)$, Eq. (4.24) becomes

$$\dot{V} = \mu - a + \sqrt{2D}\xi(t) \tag{4.27a}$$

$$\tau_w \dot{a} = -a + \tilde{\Delta} \sum_i \delta(t - t_i). \tag{4.27b}$$

Here, $\tilde{\Delta} = \beta\tau_{\mathrm{AP}}$ is the strength of adaptation and $\tilde{\Delta}/\tau_w$ is the jump size of the adaptation variable a upon firing. Equation (4.27) has been analyzed in detail in Chap. 3. Hence, in the case of infinitely many adaptation channels, the analytical results for the ISI statistics found in Chap. 3 can be readily used. In particular, the firing rate is given by

$$r = \frac{\lambda\mu}{V_{\mathrm{th}}}, \tag{4.28}$$

where

$$\lambda = \frac{V_{\mathrm{th}}}{V_{\mathrm{th}} + \beta\tau_{\mathrm{AP}}} \tag{4.29}$$

and the serial correlation coefficient is given by the geometric sequence

$$\rho_n = -\frac{\alpha(1-\vartheta)(1-\alpha^2\vartheta)}{1-2\alpha^2\vartheta+\alpha^2}(\alpha\vartheta)^{n-1}, \qquad n \geq 1, \tag{4.30}$$

where

$$\alpha = \exp\left(-\frac{1}{r\tau_w}\right), \qquad \vartheta = \frac{\mu - a^*}{\mu - \alpha a^*}, \qquad a^* = \frac{\tau_{\mathrm{AP}}}{\tau_w(1-\alpha)}. \tag{4.31}$$

(cf. Eq. (3.43)). Furthermore, for typical adaptation time constants that are much larger than the mean ISI, the mean adaptation approximation studied in Sec. 3.4 applies. In this case the adaptation variable is replaced by its mean value [Latham et al., 2000, Fuhrmann et al., 2002, Benda and Herz, 2003, La Camera et al., 2004, Richardson, 2009, van Vreeswijk and Hansel, 2001], which is equivalent to a PIF model without adaptation, but with a reduced base current $\tilde{\mu} = \lambda\mu$ (Eq. (3.132)). Accordingly, the ISI density approximately follows an inverse Gaussian density, Eq. (3.133), and the CV given by Eq. (3.134). Thus, for slow adaptation, $\tau_w \gg \langle T \rangle$, it can be expected that the skewness and kurtosis of the ISI distribution obey $\alpha_{\mathrm{s}} = \alpha_{\mathrm{e}} = 1$.

Stochastic adaptation In the opposite limit of a stochastic adaptation current ($D = 0$, Eq. (4.26)), one can approximate $W = w + \eta$ by a constant part that reduces the base current μ and an effective colored noise. In fact, if the adaptation is slow, i.e. $\tau_w \gg \langle T \rangle$, the spike train looks almost periodic at small time scales with a slowly varying firing rate $\bar{r}(t) = (\mu - \beta W)/V_{\mathrm{th}}$ because fast fluctuations are absent. Because the linear filter in Eq. (4.26b) averages "the spike train" $w_\infty(t)$ on time scales of the order of τ_w, the dynamics of W is not changed noticeably if we replace in Eq. (4.25b) $w_\infty(t)$ by its slowly varying average $\tau_{\mathrm{AP}}\bar{r}(t)$:

$$\tau_w \dot{W} = -W + \frac{\tau_{\mathrm{AP}}}{V_{\mathrm{th}}}(\mu - \beta W) + \sqrt{\frac{2\tau_w\langle\sigma^2\rangle}{N_{\mathrm{a}}}}\xi_{\mathrm{a}}(t).$$

Now, multiplication with $\lambda = V_{\mathrm{th}}/(V_{\mathrm{th}} + \beta\tau_{\mathrm{AP}})$ yields

$$\lambda\tau_w \dot{W} = -\left(W - \frac{\tau_{\mathrm{AP}}\mu}{V_{\mathrm{th}} + \beta\tau_{\mathrm{AP}}}\right) + \sqrt{\frac{2\tau_w\lambda^2\langle\sigma^2\rangle}{N_{\mathrm{a}}}}\xi_{\mathrm{a}}(t).$$

Finally, we introduce the variable $\tilde{\eta} = W - \tau_{\mathrm{AP}}\mu/(V_{\mathrm{th}} + \beta\tau_{\mathrm{AP}})$ and obtain

$$\dot{V} = \tilde{\mu} - \beta\tilde{\eta} \tag{4.32a}$$

$$\tilde{\tau}\dot{\tilde{\eta}} = -\tilde{\eta} + \sqrt{\frac{2\tilde{\tau}\tilde{\sigma}^2}{N_{\mathrm{a}}}}\xi_{\mathrm{a}}(t), \tag{4.32b}$$

where we introduced the effective parameters

$$\tilde{\mu} = \lambda\mu, \qquad \tilde{\tau} = \lambda\tau_w, \qquad \tilde{\sigma}^2 = \lambda\langle\sigma^2\rangle. \tag{4.33}$$

The common scaling factor λ is given by Eq. (4.29). Thus, the case of stochastic adaptation can be mapped to a PIF model without an adaptation variable but a colored noise $\tilde{\eta}(t)$

with renormalized parameters. We call model (4.32) (together with the usual fire-and-reset rule) the *colored noise approximation*.

The PIF model driven by a weak colored noise, i.e. for the model described by Eq. (4.32), has been analyzed in detail in Chap. 2.2. In particular, the ISI density reads [Lindner, 2004a]

$$P(t) = \frac{\langle T\rangle}{2\sqrt{4\pi\epsilon^2\gamma_1^3(t)}} \exp\left[-\frac{(t-\langle T\rangle)^2}{4\epsilon^2\gamma_1(t)}\right] \times \left\{\frac{\left[(\langle T\rangle - t)\gamma_2(t) + 2\gamma_1(t)\right]^2}{2\gamma_1(t)} - \epsilon^2\left[\gamma_2^2(t) - 2\gamma_1(t)e^{-t/\tilde{\tau}}\right]\right\} \quad (4.34)$$

with

$$\langle T\rangle = \frac{V_{\mathrm{th}}}{\lambda\mu}, \qquad \gamma_1(t) = \tilde{\tau}^2\left(\frac{t}{\tilde{\tau}} + e^{-t/\tilde{\tau}} - 1\right), \qquad \gamma_2(t) = \tilde{\tau}\left(1 - e^{-t/\tilde{\tau}}\right). \quad (4.35)$$

Moreover, the coefficient of variation and the serial correlation coefficient are given by the formula (2.97) and (2.100), respectively. In these expressions, $\theta = V_{\mathrm{th}}/(\lambda\mu\tau_w)$ and $\epsilon^2 = \beta^2\tau_{\mathrm{AP}}/(V_{\mathrm{th}}N_{\mathrm{a}}\mu)$. In addition to that, expressions for the skewness and kurtosis are given in Sec. A.3.

Interspike interval density

Figure 4.9A shows ISI densities for the case of deterministic adaptation. As shown in the previous section, the ISI densities can be well described by inverse Gaussian probability densities with mean $V_{\mathrm{th}}/\tilde{\mu}$ (cf. Eq. (1.68). The opposite case of stochastic adaptation is contrasted in Fig. 4.9B. For a small channel population ($N_{\mathrm{a}} = 100$) the discrete nature of the adaptation W still appears in the ISI histogram as single peaks that cannot be averaged out. These peaks are caused by ISIs during which W remains constant. Under this condition, the ISIs attain likewise only discrete values. In contrast, if W changes at least once during a given ISI, the length of the ISI can take a continuous range of values. Such ISIs give rise to the continuous part of the ISI density. In contrast, the diffusion model yields a purely continuous ISI density, which looks like a smoothed version of the ISI histogram of the channel model. As N_{a} increases, the discrete peaks become more and more dense and insignificant, and the ISI density of the channel model is well approximated by the diffusion model. Furthermore, we see that the colored noise approximation, Eq. (4.32), agrees well with the diffusion model, Eq. (4.23). Consequently, the colored noise theory works is a good approximation of the ISI histogram of the channel model if N_{a} is sufficiently large.

One of the main hypotheses of this chapter is that ISI densities of supra-threshold neurons, for which slow channel noise dominates the ISI variability, are not well described by an inverse Gaussian (IG) distribution, whereas the IG density yields a good approximation if fast fluctuations dominate the variability. Strictly speaking, the IG yields the ISI density for a white-noise driven PIF model *without* adaptation, so *a priori* we cannot expect that this density fits any of the cases we consider here. However, as shown in Sec. 4.2.4, the ISI density can be captured by an inverse Gaussian for deterministic

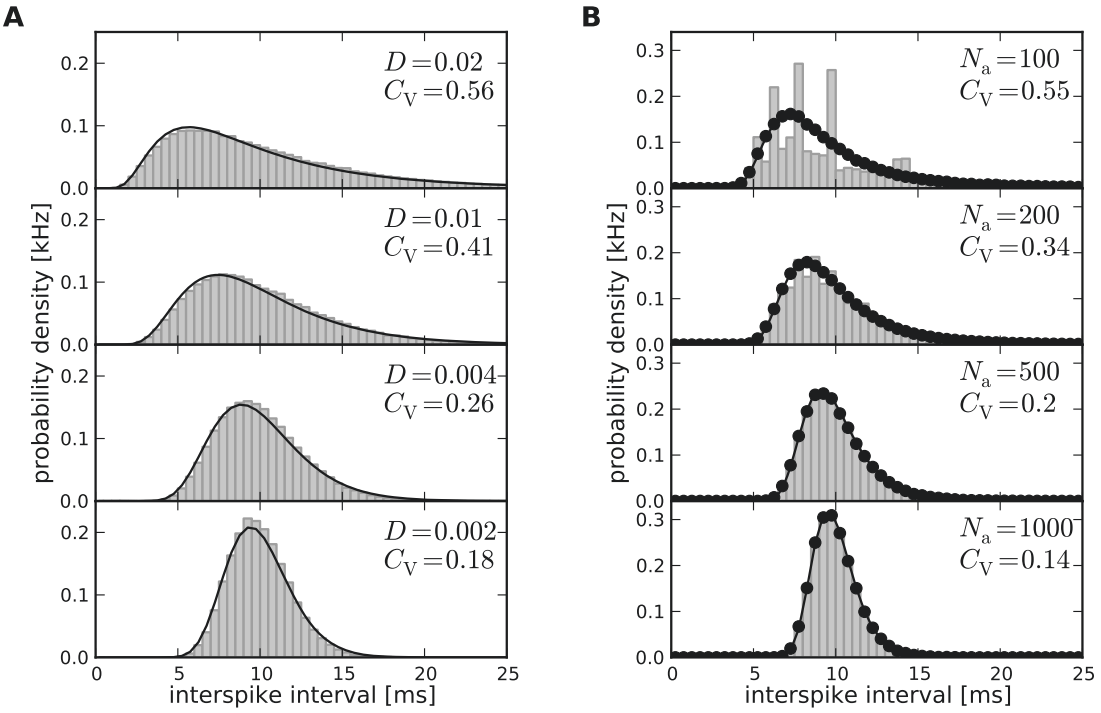

Figure 4.9.: ISI histograms of a PIF neuron with deterministic or stochastic adaptation current. **A** Deterministic adaptation ($N_a \to \infty$) for different intensities D of the white Gaussian noise. Gray bars show the histograms obtained from simulations of Eq. (4.24); solid lines displays the inverse Gaussian density, approximation Eq. (3.133). **B** Stochastic adaptation ($D = 0$) for different N_a as indicated in the panels. The adaptation current was modeled either by the channel model (gray bars), Eq. (4.6), or by the diffusion model (circles), Eq. (4.25). Our colored-noise theory, Eq. (2.90), is displayed by a solid line. Parameter values: $\mu = 0.4\ V_{th}/\text{ms}$, $\beta = 3\ V_{th}/\text{ms}$, $\tau_w = 100$ ms.

adaptation. Figure 4.10A,C shows indeed a good agreement of the IG and the simulated ISI density. The main effect of a slow deterministic adaptation current is to reduce statically the mean input current which is reflected in our approximation by the effective base current $\tilde{\mu}$. Slight deviations of the IG from the simulation result can be seen for large intervals, where the simulated ISI density decays faster than the IG (Fig. 4.10C). This can be understood as follows: in the presence of adaptation, large intervals are suppressed because for large times (after the last spike) the inhibitory effect of the adaptation current subsides – a feature that is not present in the static approximation for the reduced base current. Nevertheless, the deviations are small and will be hardly visible when comparing the inverse Gaussian density to the histogram of limited experimental data sets.

By contrast, the ISI density for stochastic adaptation exhibits a more pronounced peak and a heavier tail than the IG with the same mean ISI and CV (Fig. 4.10B and D). A comparison to an IG density with the same mean and mode or the same mode and CV gave comparably bad fits (data not shown). Instead, the colored noise approximation agrees well with the simulation data.

This suggests that both cases – deterministic and stochastic adaptation – can be distinguished by the shape of the ISI densities even if mean and CV of the ISIs are comparable. To this end, we make use of the skewness α_s and the kurtosis α_e. In fact, figure 4.11

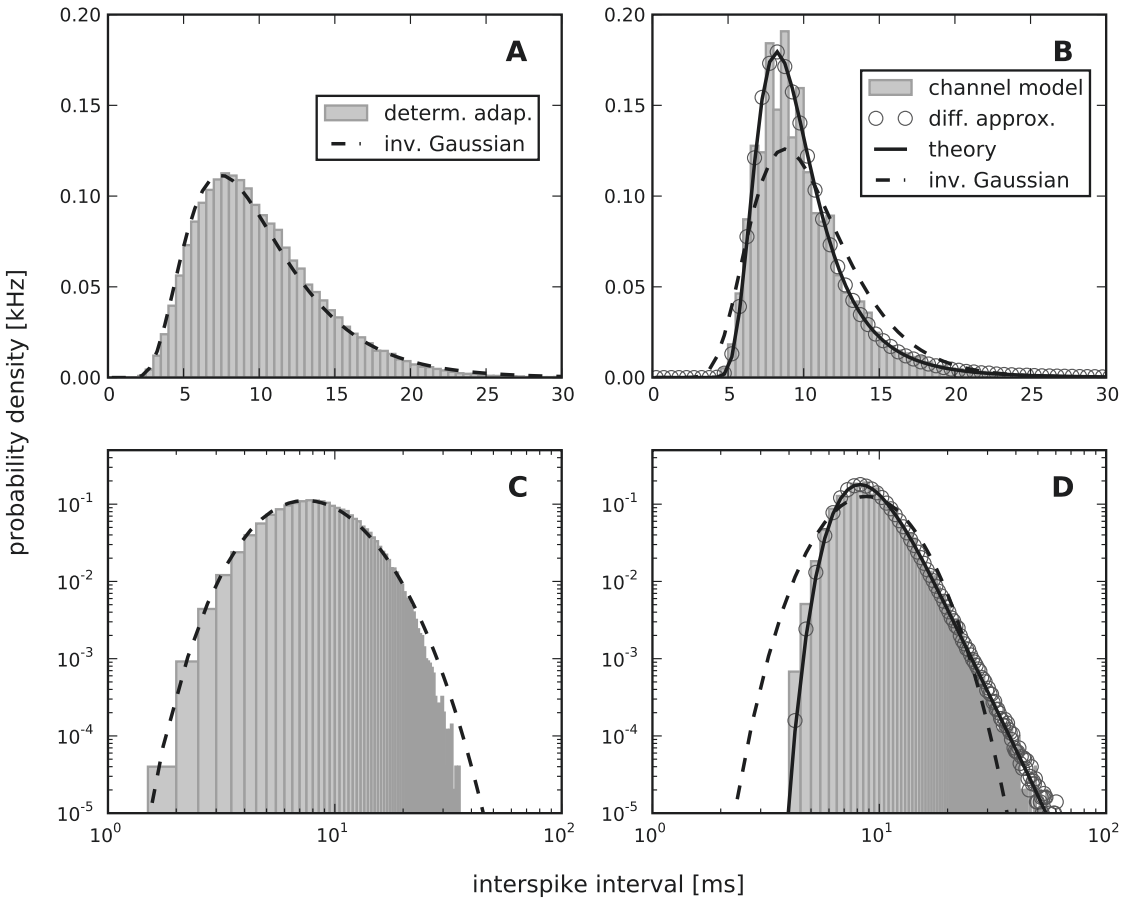

Figure 4.10.: Comparison of ISI densities for deterministic vs. stochastic adaptation. **A** and **C** – The ISI density obtained from a simulation of the model with deterministic adaptation, Eq. (4.24), with noise intensity $D = 0.01\ V_{\mathrm{th}}^2/\mathrm{ms}$ compared to an inverse Gaussian distribution (dashed line), Eq. (1.68). **B** and **D** – ISI density for the stochastic adaptation model with $N_{\mathrm{a}} = 200$ and $D = 0$. The channel model (gray bars) is more peaked than an inverse Gaussian distribution with the same mean and CV (dashed line). The ISI density of the diffusion model, (simulation of Eq. (4.26), circles) is well matched by the colored noise approximation, Eq. (4.32), (solid line). Note the double logarithmic axis in **C** and **D** revealing the tail of the distribution. Other parameter values as in Fig. 4.8.

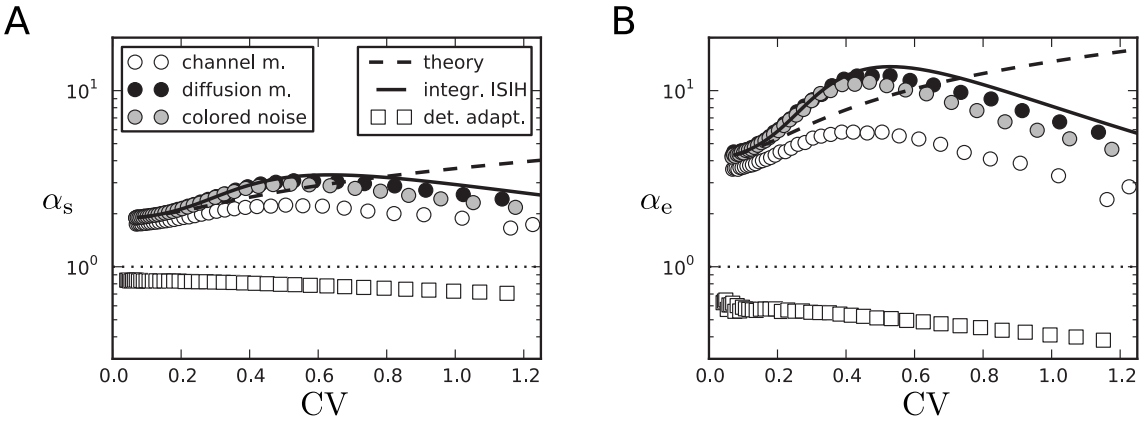

Figure 4.11.: Discrimination between deterministic and stochastic adaptation model by skewness and kurtosis. **A** Skewness α_s and **B** kurtosis α_e for deterministic adaptation (white squares) and for stochastic adaptation (channel model – white circles, diffusion model – black circles, colored noise approximation – gray circles). Different CVs were obtained by varying N_a or D. The dashed line depicts the theoretical curve, Eq. (A.44), and the solid line depicts the semi-analytical result obtained from the moments of the ISI density, Eq. (4.34), using numerical integration.

shows that deterministic and stochastic adaptation can be well discriminated by these measures. In particular, α_s and α_e are clearly larger than unity for stochastic adaptation indicating that the ISI density is more skewed and more peaked compared to an inverse Gaussian. This confirms quantitatively our previous observations. On the other hand, for deterministic adaptation, α_s and α_e are smaller than unity in accordance with our previous observations that the tail of the ISI density decays slightly faster than an inverse Gaussian density.

The kurtosis α_e reveals a strong discrepancy between the channel and the diffusion model with respect to higher-order ISI statistics. The second-order statistics, as expressed by the CV, still matches almost perfectly for both models even at rather small channel numbers (Fig. 4.12A), which is remarkable given the discrete structure of the ISI histogram for small channel numbers (cf. Fig. 4.9 for $N_a = 100$). However, as shown in Fig. 4.12B, the two models clearly differ with respect to the kurtosis α_e when the number of channels becomes small.

The figures 4.11 and 4.12 also support the colored noise approximation, which reproduces the diffusion model (which still includes adaptation) rather accurately. This suggests that the heavy-tail and the peakedness of the ISI density is mainly due to the long-correlations of the colored noise. It has been shown for a related model that such correlations can result in ISI densities with a large kurtosis [Schwalger and Schimansky-Geier, 2008]. To further study this "colored noise effect", we measured the skewness and kurtosis as a function of the time-scale separation between adaptation and spiking dynamics. This can be quantified by the dimensionless parameter $\tau_w/\langle T\rangle = r\tau_w$. In simulations, we varied τ_w and kept the base current at a constant value of $\mu = 0.4$ corresponding to a fixed firing rate of $r = 100$ Hz.

For stochastic adaptation with $N_a = 200$ channels, Fig. 4.13 illustrates that both α_s and α_e are larger than unity and increase strongly with increasing τ_w or increasing firing rate (Fig. 4.13A,B). This increase is more pronounced for the diffusion model than for the

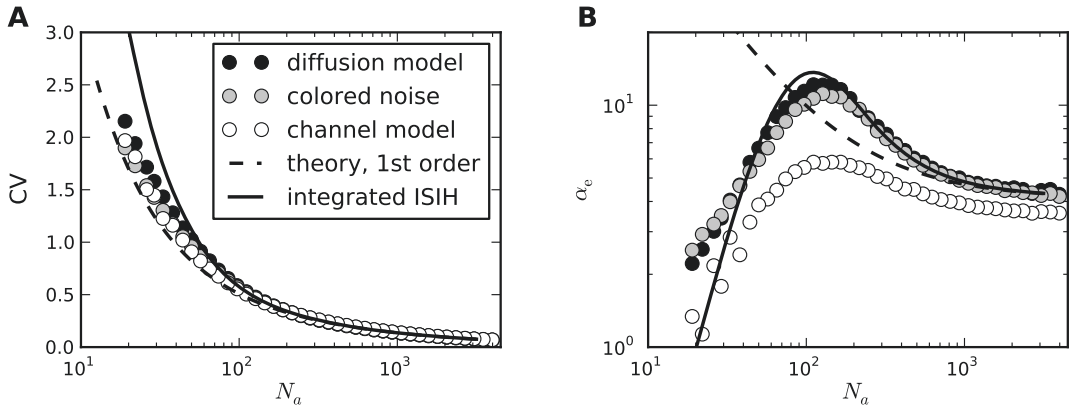

Figure 4.12.: Stochastic adaptation – comparison of diffusion and channel model. A The coefficient of variation as a function of the number of adaptation channels N_a for the diffusion model (black circles, Eq. (4.23)), the channel model (white circles, Eq. (4.6)) and the colored noise approximation (gray circles, Eq. (4.32)). The dashed line depicts the theoretical curve, Eq. (2.97), the solid line depicts the semi-analytical result obtained from the moments of the ISI density, Eq. (2.90), using numerical integration. **B** The corresponding curves for the rescaled kurtosis α_e. The dashed line represents the theory given by Eq. (A.44). The time scale separation was $r\tau_w = \tau_w/\langle T_i\rangle = 10$. Parameter values: $\mu = 0.4\ V_\mathrm{th}/\mathrm{ms}$, $\beta = 3\ V_\mathrm{th}/\mathrm{ms}$, $\tau_w = 100$ ms.

channel model. At large $r\tau_w$ the simulation data deviate from the first-order perturbation theory, Eq. (A.43)) and (A.44), because higher-order terms in the small noise expansion cannot be neglected anymore. The agreement becomes better, when the number of channels becomes larger [Schwalger et al., 2010]. These observations were qualitatively confirmed by corresponding simulations at a smaller base current ($\mu = 0.04$), leading to a lower firing rate of $r = 10$ Hz (data not shown). In particular, quantitatively similar curves were obtained by increasing the number of channels to $N_\mathrm{a} = 2000$ in order to maintain the same effective noise level. It should be noted that in the case of low firing rates the weak-noise expansion might become infeasible if the number of channels is too small. This is, for example, the case for $N_\mathrm{a} = 200$ at a firing rate $r = 10$ Hz, for which the parameter $\epsilon^2 = \beta^2\tau_\mathrm{AP}/(V_\mathrm{th}N_\mathrm{a}\mu)$, which is supposed to be small, becomes larger than unity.

For deterministic adaptation, α_s and α_e approach unity for $r\tau_w \gg 1$ as predicted by the mean-adaptation approximation, which is consistent with an inverse Gaussian ISI density. In the opposite limit of small $r\tau_w$ the parameters α_s and α_e also approach unity. This is intuitively clear, because for $\tau_w \ll \langle T\rangle$ the adaptation variable $w(t)$ decays quickly to zero after each spike. Hence, the base current is almost always equal to μ except for a very short period after a spike where the driving is $\mu - \beta w(t)$. Put differently, the dynamics can be approximated by a PIF model with a constant driving μ and an effective reset value $V_\mathrm{reset} \approx -\beta\tau_\mathrm{AP} < 0$. This yields again an inverse Gaussian ISI distribution (albeit with a larger mean ISI).

In the intermediate range, where the time scale of the adaptation is of the same order as the mean ISI, a pronounced minimum of α_s and α_e is observed in the case of deterministic adaptation. This is due to the decay of adaptation at such a rate that large ISIs are suppressed. As a consequence, the tail of the ISIH decays faster and the ISI density becomes less skewed compared to an inverse Gaussian. The same qualitative behavior

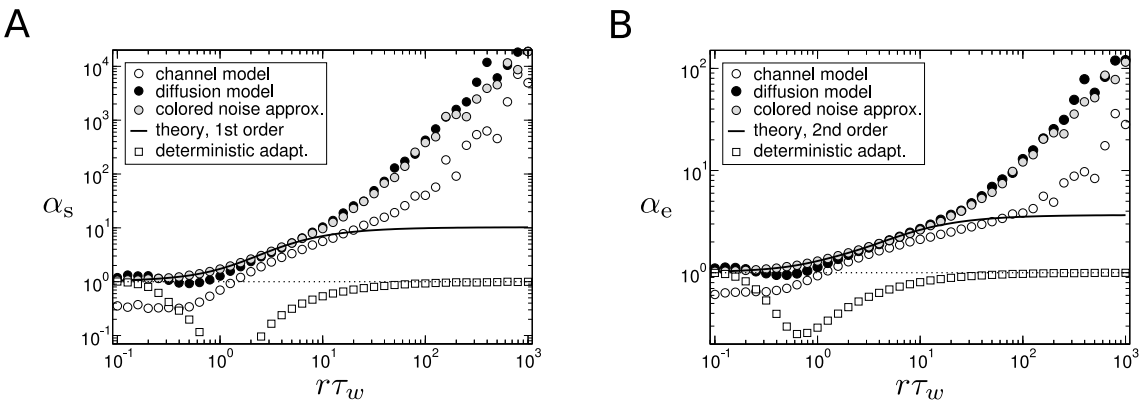

Figure 4.13.: A Skewness α_s and **B** kurtosis α_e as a function of the time scale separation $r\tau_w = \tau_w/\langle T\rangle$ for $N_a = 200$ channels (corresponding $\epsilon = 0.1$) for stochastic adaptation (circles) and $D = 0.01\ V_{th}^2/\text{ms}$ for deterministic adaptation (squares). Theory Eq. (A.43) and (A.44) is displayed by the solid line, the line $\alpha_{s/e} = 1$ is indicated by a dotted line. $r\tau_w$ was varied by changing τ_w at a fixed $\mu = 0.4$t ($\langle T_i\rangle = 10$ ms). Parameter values as in Fig. 4.8.

was verified in simulations at a lower firing rate $r = 10$ Hz (data not shown).

Serial interspike interval correlations

Another clear distinction between stochastic and deterministic adaptation is revealed by the correlations between ISIs. In several numerical studies, it has been found that negative feedback mechanisms like adaptation currents in the presence of white noise give rise to negative correlations between adjacent ISIs [Liu and Wang, 2001, Chacron et al., 2000]. However, a theoretical explanation of this effect has not been provided in these studies. In chapter 3, an analytical expression for the serial correlation coefficient (SCC) in the limit of vanishing noise has been put forward (Eq. (4.30)). According to the theory, the SCC is negative at odd lags, in particular at lag 1. This is indeed observed in our simulations (Fig. 4.14A,C).

In striking contrast, the case of stochastic adaptation yields positive ISI correlations with a slow exponential decay (Fig. 4.14B) as predicted by the theory, Eq. (2.100). In this formula, it becomes evident that the decay constant for the SCC is to first-order given by the ratio $\theta^{-1} = \tilde{\tau}/\langle T_i\rangle$ of effective correlation time $\tilde{\tau} = \lambda\tau$ and mean ISI. The good agreement of the colored noise theory suggests that adaptation noise acts effectively as a colored noise source that slowly modulates the ISIs. It is known that systems with a slow stochastic driving exhibit positive ISI correlations [Middleton et al., 2003, Lindner, 2004a, Schwalger and Schimansky-Geier, 2008]. In fact, in the absence of additional fast fluctuations the ISIs are strongly correlated with the slow noise, which generates positive correlations among ISIs. For instance, if $T_i < \langle T\rangle$ due to a large, positive fluctuation of η, this will on average cause a likewise small $T_{i+1} < \langle T\rangle$ because the slow dynamics of η tends to persist at positive values in the course of several subsequent ISIs.

The magnitude of the serial correlation coefficient strongly depends on the time scale separation as quantified by the dimensionless parameter $r\tau_w = \tau_w/\langle T_i\rangle$ (Fig. 4.14C). For deterministic adaptation the negative correlations become most pronounced at a finite value of $r\tau_w$ and vanish in the limits $r\tau_w \to 0$ and $r\tau_w \to \infty$ as discussed in Chap. 3.2.3. For stochastic adaptation, the positive correlations become strongest for τ_w much larger

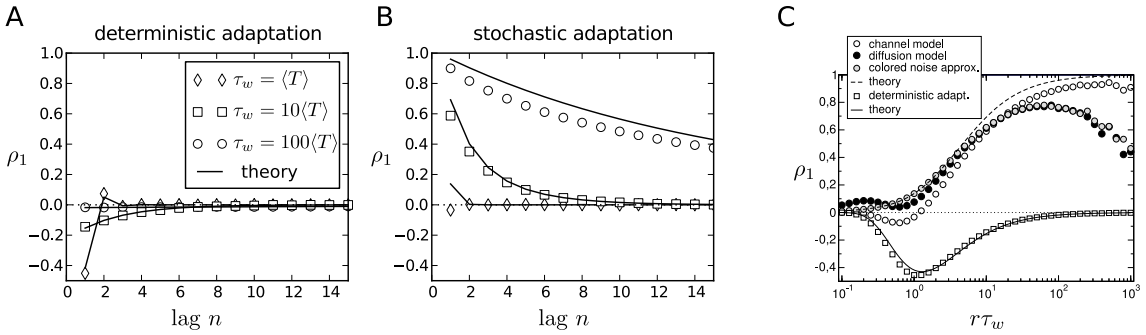

Figure 4.14.: Serial correlation coefficient. **A** The case of deterministic adaptation with $D = 0.01\ V_{\mathrm{th}}^2/\mathrm{ms}$ for different values of the time constant τ_w (as indicated in the legend). The theoretical curves, Eq. (4.30), are depicted by solid lines; the zero baseline is indicated by a dotted line. **B** The case of stochastic adaptation with $N_{\mathrm{a}} = 200$ for different values of the time constant τ_w (as in **A**). The channel model, Eq. (4.6), is represented by white symbols; the theory based on the colored noise approximation, Eq. (4.32), is depicted by a solid line. Other parameters as in Fig. 4.8. **C** Corresponding to Fig. 4.13, the serial correlation coefficient ρ_1 is shown as a function of the time-scale separation (same parameters as in Fig. 4.13).

than the mean ISI (Fig. 4.14C), i.e. $r\tau_w \gg 1$. The channel and diffusion model agree generally quite well, except for very small and very large $r\tau_w$. In the latter case, the Gaussian approximation becomes worse because the opening and closing events of the channels are extremely rare. The expected number of channel transitions in a time window of length t is $N(t) = 2(1 - \langle w \rangle)\langle w \rangle N_{\mathrm{a}} t/\tau_w$ with $\langle w \rangle = \tau_{\mathrm{AP}}/\langle T_i \rangle$. For instance, taking the extreme case $\tau_w = 10^4$ ms at the standard parameters $N_{\mathrm{a}} = 200$, $\langle w \rangle = 0.1$, one would observe only 0.036 transitions on average on the time scale of a single ISI ($t \sim 10$ ms). On this time scale, the fraction of open channels can hardly be approximated by a Gaussian process. A better agreement between channel and diffusion model at large $r\tau_w$ can be obtained by increasing the number of channels [Schwalger et al., 2010].

4.2.5. The mixed case

So far, we found that the two limit cases of the adapting PIF model can be well discriminated by the skewness α_{s} and the kurtosis α_{e} relative to unity and the serial correlation coefficient ρ_1 relative to zero. Can these measures also be utilized to determine the dominating source of noise in the more realistic case where both fast channel noise and slow adaptation channel noise are present? To answer this question, simulations of the adapting PIF model for a fixed intensity of the white noise (mimicking fast channel noise) but variable number of adaptation channels were performed. In this way, the ratio of the two different types of noise can be varied. Note that the mean adaptation current is kept constant in our setting. This can be realized by scaling the single channel conductance or the membrane area with $1/N_{\mathrm{a}}$.

For small numbers of adaptation channels, i.e. large adaptation channel noise, we observed both large values of the kurtosis $\alpha_{\mathrm{e}} > 1$ and a positive serial correlation coefficient of adjacent ISIs (Figs. 4.15A,B, white region). This indicates a strong impact of the colored noise effect. In the opposite case of a large channel population, the expected result for pure deterministic adaptation interacting with a white noise source is recovered. In the intermediate range, there is a critical channel number at which both the kurtosis crosses

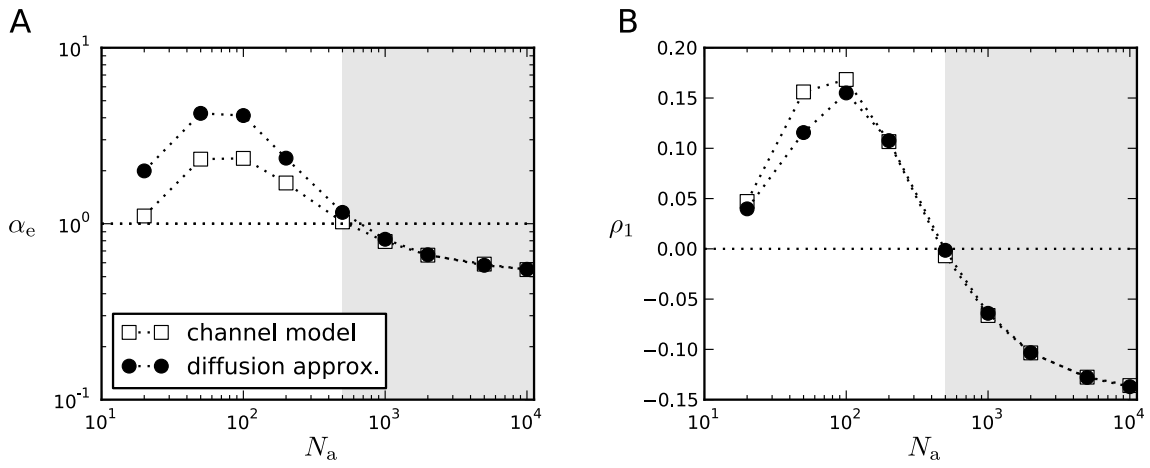

Figure 4.15.: PIF model with a stochastic adaptation current *and* white noise driving – variation of the number of adaptation channels. For a fixed level of white noise ($D = 0.01\ V_{th}^2/\text{ms}$) the number of adaptation channels N_a was varied. For a small channel population slow channel noise dominates, whereas for a large channel population fast fluctuations dominate. **A** Kurtosis α_e for the channel model (white squares) and the diffusion model (black circles). The value corresponding to an inverse Gaussian ISI density is indicated by the horizontal dotted line. **B** Corresponding serial correlation coefficient at lag one. The zero line is indicated by the dotted line. The adaptation time constant was chosen as $\tau_w = 100$ ms, other parameters as in Fig. 4.8.

the line $\alpha_e = 1$ and the serial correlation coefficient changes its sign. This simultaneous change suggests that below the critical channel number, the ISI statistics is dominated by slow adaptation channel noise, whereas above this size it is dominated by the white noise input (gray-shaded region).

A smooth transition from an inverse Gaussian ISI statistics with negative ISI correlations to a peaked ISI density and positive serial correlations has also been observed in the experiment when the firing rate was increased (Fig. 4.4). Can this behavior also be found in our simple model? To answer this question, we conducted simulations, in which both the number of adaptation channels and the intensity of the white noise was fixed and the firing rate was varied by changing the base current μ (Fig. 4.16). We found indeed that for both channel model and diffusion model, the skewness α_s and the kurtosis α_e are smaller than unity at low firing rates and increase to values that are significantly larger than unity when the firing rate is increased. Furthermore, the SCC at lag one changes continuously from negative to positive values with increasing firing rate. These findings agree qualitatively with the experimental data.

In the PIF model, this behavior can be explained by a simple time-scale argument: The effect of the colored noise arising from adaptation channel noise becomes most pronounced at large values of the dimensionless parameter $r\tau_w$ (Fig. 4.13, 4.14C), which quantifies the time-scale separation between adaptation and spiking dynamics. Thus, for large firing rates, the colored noise effect (which is responsible for the skewed and peaked ISI histograms and positive serial correlations) can dominate over negative correlations and inverse Gaussian ISI statistics that are induced by fast fluctuations. In contrast, at low firing rates, the colored noise is not slow on the large time scale of the mean ISI, i.e. the time-scale separation parameter $r\tau_w$ becomes small. Hence, the colored noise effect is weak and the adaptation channel noise effectively adds to the white noise source,

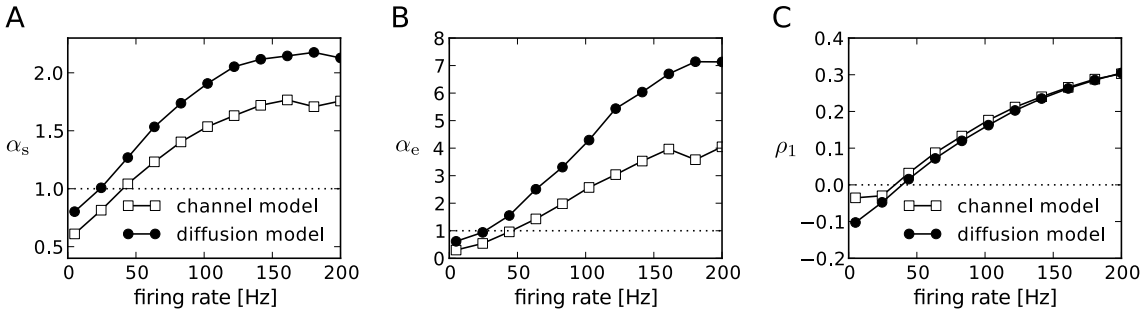

Figure 4.16.: PIF model with a stochastic adaptation current *and* white noise driving – variation of the firing rate (time scale separation). For a fixed white noise ($D = 0.01\ V_{\text{th}}^2/\text{ms}$) and fixed number of adaptation channels N_a the firing rate was varied by a respective variation of the base current μ. This mimics the experimental setup, in which the sound intensity is varied (cf. Fig. 4.4). **A** Skewness α_s, **B** kurtosis α_e for the channel model (white squares) and the diffusion model (black circles). The value corresponding to an inverse Gaussian ISI density is indicated by the dotted line. **C** Corresponding serial correlation coefficient at lag one. The zero line is indicated by the dotted line. Parameter values: $\tau_w = 100$ ms, $\beta = 3\ V_{\text{th}}/\text{ms}$.

resulting in negative serial correlations and an inverse Gaussian statistics.

4.3. Conductance-based model with channel noise

We investigated whether our theoretical predictions based on a PIF model with adaptation are robust with respect to a more detailed model of the ionic currents. To this end, simulations of the conductance-based Traub-Miles model with a M-type adaptation current as defined in Sec. C.2 has been performed by K. Fisch [see also Fisch, 2011]. As in the case of the PIF model, the two cases of white noise input and a slow M-type channel noise are considered separately to assess the individual effects on the ISI statistics. Fig. 4.17 demonstrates that the ISI histograms show essentially the same features as in the PIF model: in the case of white noise input, the shape of the ISI density can be well approximated by an inverse Gaussian distribution which corresponds to the observed firing rate and CV. In the case of a stochastic M-type current, there is a strong disagreement between the ISI density and an inverse Gaussian with the same rate and CV. As in the PIF model, the ISI densities exhibit a sharper peak than the inverse Gaussian.

The different ISI statistics for deterministic vs. stochastic adaptation are compared in more detail in Fig. 4.18. Like in the PIF model (cf. Fig. 4.11), the skewness α_s and kurtosis α_e are significantly smaller for white noise than for adaptation channel noise in a wide range of CVs (Fig. 4.18A,B). This is in accordance with the pronounced peak of the ISI density in the case of a stochastic M current (Fig. 4.17B). However, the values are not strictly separated by $\alpha_{s/e} = 1$ as in the PIF model. This discrepancy might be due to the fact that already the Traub-Miles dynamics with constant input and white noise driving is not exactly given by an inverse Gaussian ISI density. Nevertheless, the kurtosis α_e quickly saturates at a finite value in the large τ_w limit (albeit not at unity, Fig. 4.18C). This is in marked contrast to the case of stochastic adaptation, in which α_e increases strongly. Similarly, the skewness α_s also shows this distinct behavior for stochastic vs. deterministic adaptation, although the increase of α_s is not as strong as for α_e (data not shown).

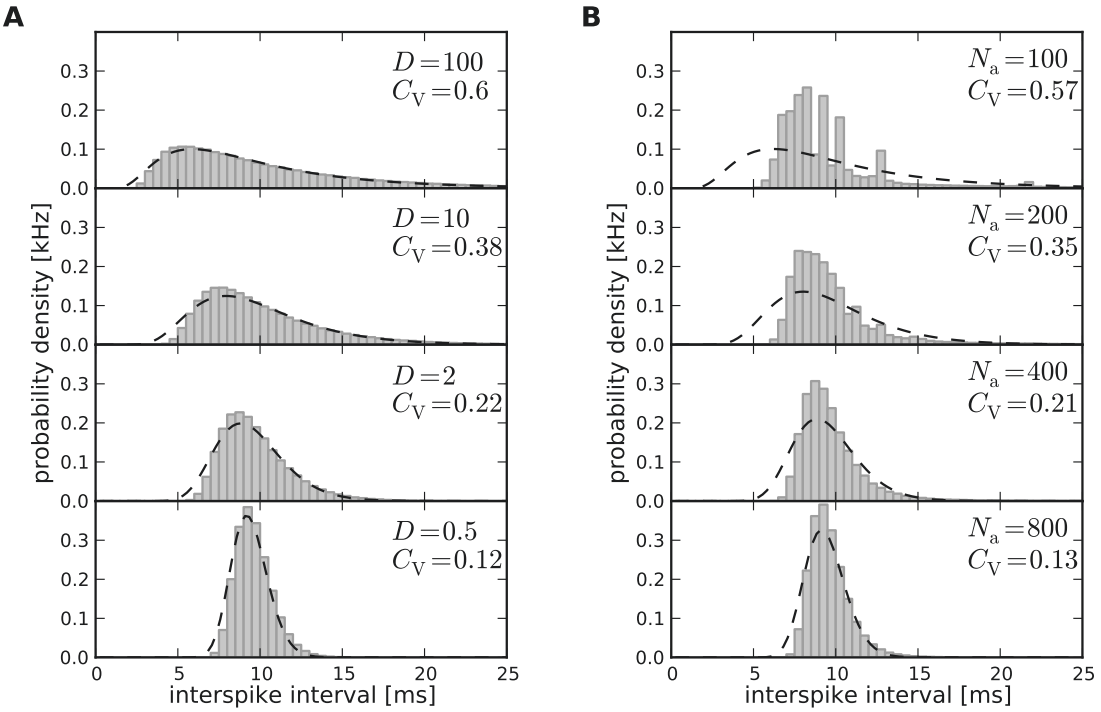

Figure 4.17.: ISI histograms of the conductance-based Traub-Miles model. **A** The ISI densities of the Traub-Miles neuron model with a deterministic M-type adaptation current ($N_a = \infty$) and white noise driving (Eq. (C.13) – gray bars) is shown along with an inverse Gaussian with the same mean and CV (dashed lines). To keep the firing rate at about $r = 100$ Hz, the external driving current was adjusted from top to bottom according to $I = 9$, 16.5, 17.7, 17.9 (in μA/cm^2). The noise intensity D is indicated in units of $(\mu\text{A/cm}^2)^2$/ms. **B** The ISI densities of the Traub-Miles model in the presence of a stochastic M-type adaptation current (gray bars) and an inverse Gaussian with the same mean and CV (dashed line). In all cases, the external driving is $I = 18$ μA/cm^2. Simulation data obtained by K. Fisch [Fisch, 2011].

A clear distinction between both cases appears in the serial correlations of ISIs as shown in Fig. 4.18D. Similar to the PIF model, the case of deterministic adaptation is characterized by negative ISI correlations at lag one, which are strongest at an intermediate time scale τ_w. Furthermore, the case of stochastic adaptation exhibits positive correlation coefficients ρ_1, which show a maximum at an intermediate value of τ_w. This is also in line with the PIF model. The correlations decay rapidly with increasing lag for deterministic adaptation (Fig. 4.18E) and decay exponentially for stochastic adaptation (Fig. 4.18F). As in the PIF model, the exponential decay is slower for large time constants τ_w.

Finally, the case in which both white noise and slow M-type adaptation channel noise is present has been inspected (Fig. 4.18G,H). As in Fig. 4.15, we fixed the noise intensity of the white noise and varied the number of M-type adaptation channels N_a. In the Traub-Miles model one finds a qualitatively similar behavior as in the PIF model: the SCC at lag one shows a transition from positive to negative ISI correlations at a certain number of adaptation channels (Fig. 4.18H). As for the PIF model, this value can be used to define two regimes – one dominated by adaptation noise (white region) and another one dominated by white noise (gray-shaded region). In the adaptation-noise dominated regime the parameter α_e is larger than in the white-noise dominated regime (Fig. 4.18G)

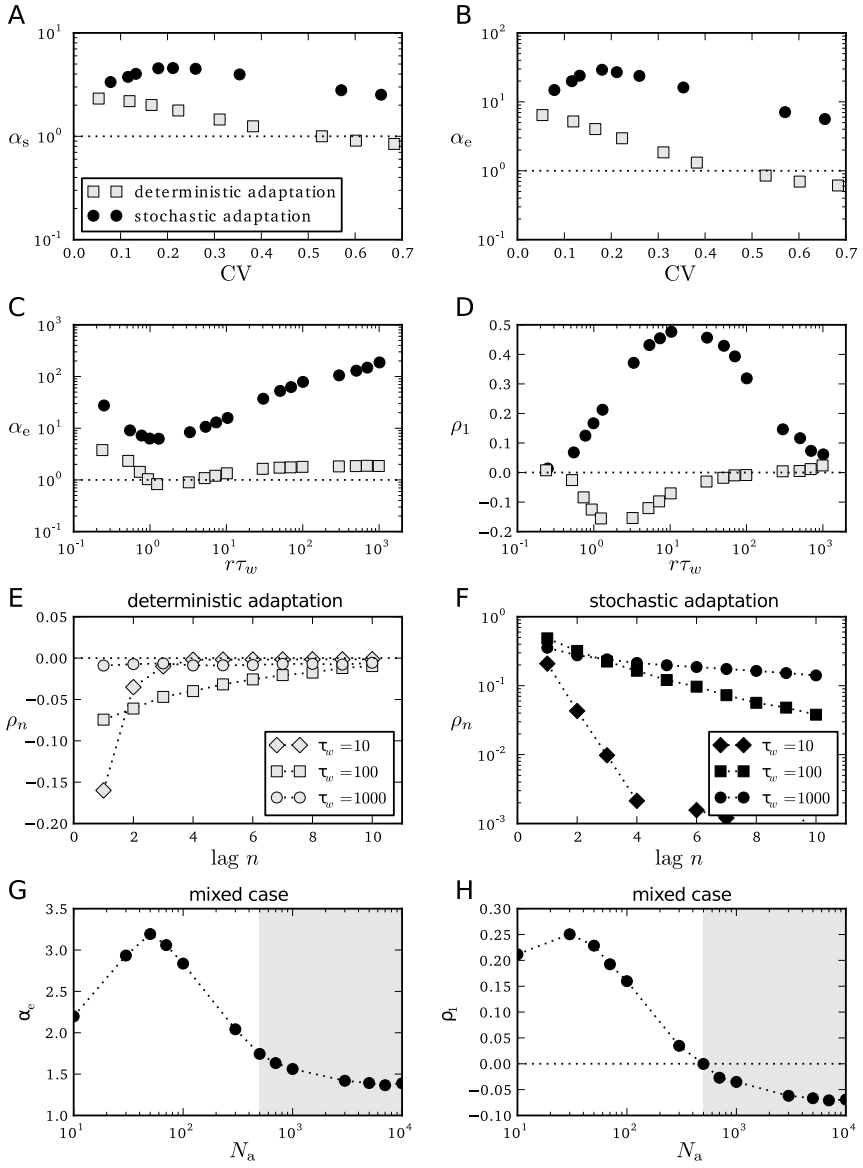

Figure 4.18.: ISI statistics of the Traub-Miles model – deterministic vs. stochastic adaptation. A Skewness α_s and **B** kurtosis α_e as a function of the CV. For stochastic adaptation the number of channels was varied from $N_a = 2000$ to $N_a = 80$; for deterministic adaptation, $N_a = \infty$ – gray squares), the noise intensity was varied from $D = 0.1$ to $D = 200$. The value corresponding to an inverse Gaussian statistics is indicated by the dotted line. **C, D** Kurtosis α_e and the serial correlation coefficient (SCC) at lag 1 as a function of the time scale separation $r\tau_w = \tau_w/\langle T \rangle$. Stochastic adaptation ($N_a = 200$) and deterministic adaptation ($D = 0.01$) are marked as in **A,B**. **E,F** SCC as a function of the lag for different time constants τ_w in ms as indicated (**E** deterministic adaptation, **F** stochastic adaptation; D and N_a as in **C,D**). **G** The rescaled kurtosis α_e in the mixed case at a fixed amount of white noise ($D = 10$) and varying channel numbers N_a. **H** The corresponding values of the SCC at lag one. The intersection of ρ_1 with the zero line defines the adaptation-channel-noise dominated regime (white region) and the white-noise dominated regime (gray-shaded region). The units of the noise intensities are $(\mu\text{A/cm}^2)^2/\text{ms}$. For stochastic adaptation, the base current was $I = 18\ \mu\text{A/cm}^2$. For deterministic adaptation, I was adjusted to result in a firing rate at around $r = 100$ Hz: For $D = 0$, the current I was $18\ \mu\text{A/cm}^2$ and with increasing noise intensity, I decreased to $I = 4\ \mu\text{A/cm}^2$ for $D = 200$. Simulation data obtained by K. Fisch [Fisch, 2011].

(although not smaller than unity as in the PIF model).

The observation that key features of the ISI statistics in the presence of a stochastic adaptation current seem to be conserved across different models suggests a common mechanism underlying these features. As we saw, this mechanism is based upon the fact that a stochastic adaptation current can be effectively described by an independent colored noise. The long-range temporal correlations of this noise naturally yield positive ISI correlations and a slow modulation of the instantaneous firing rate. The latter typically involves a large kurtosis due to the increased accumulation of both short and long ISIs. A significant amount of colored noise can affect the kurtosis and the ISI correlations so strongly that details of the spike generation seem to be of minor importance. Thus, it becomes plausible that the spiking statistics of a rather complex neuron model can be explained by a simple integrate-and-fire model including a stochastic adaptation current.

4.4. Discussion

The theoretical analysis of this chapter was concerned with the effect of a stochastic adaptation current on the ISI statistics. We have contrasted this statistics to the ISI statistics of a neuron with a deterministic adaptation current and an additional white noise current, which is already known from the analysis in Chap. 3. We found that noise arising from slow adaptation channels, yields a more peaked ISI density and positive ISI correlations, in contrast to an inverse Gaussian density and negative ISI correlation in the case of a deterministic adaptation current and white noise. This could be explained by the adaptation channel noise acting like an effective colored noise. We also proposed measures by means of which the influence of adaptation channel noise versus white noise can be distinguished on the bases of the stationary ISI statistics. These measures consist of the skewness α_s, the kurtosis α_e and the serial correlation coefficient at lag 1. These results might be particularly useful in cases, where one noise source dominates over the other.

It is also worth to mention that our results are not specific to channel noise, but can quite generally be used to distinguish between slow and fast noise as the dominating source of noise. For instance, slow noise can also arise from slow synaptic filtering, or slow presynaptic background activity that might be relevant for cortical neurons.

4.4.1. What is the source of spiking variability in locust auditory receptor cells?

These rather general results can be employed as an indirect method to determine the time-scale of the dominating source of spiking variability of locust auditory receptor cells. The data shown in Sec. 4.1, suggest that at least two populations of ion channels contribute to the variability – one with a fast channel kinetics and another one with a slow channel kinetics. If the spiking variability were solely due to fast channel noise the peaked ISI densities and the positive serial correlations would be difficult to explain. On the other hand, if only slow channel noise was present, it would be difficult to explain the small negative serial correlations at low firing rates. However, a mixture of slow and fast channel noises can explain the statistics of the experimentally observed ISI statistics and its dependence on the firing rate. One simple explanation involves a *time-scale argument*:

the effect of the slow noise should be most pronounced at high firing rates because a large skewness, a large kurtosis and positive serial correlations are expected for a strong time scale separation between noise and spiking dynamics. At low rates, the noise correlation time can adopt the order of the mean ISI or become even smaller. In this case, the colored noise effect is not as strong and the "slow" noise can be regarded as fast. An alternative explanation could apply if the *size of fluctuations* of each source of noise depends on the firing rate. For instance, a reduction of fast noise or a magnification of slow noise at large firing rates could also explain the ISI statistics for different firing rates.

What are the origin of the slow and fast noise sources? Slow intrinsic noise is likely to be associated with the slow dynamics of an adaptation mechanism. As one prototypical example of such adaptation noise, we considered channel noise arising from an M current, which is a slow voltage-dependent potassium current of the KCNQ family [Hille, 2001]. However, there are many other adaptation mechanisms, like slow inactivation of the sodium conductance and the AHP current. Which of these mechanisms cause spike-frequency adaptation in locust auditory receptor cells is not known and cannot be deduced by our method. As shown below, the exact implementation of adaptation, however, seems to be of minor importance as long as the fluctuations are associated with the slow part of the adaptation mechanism.

The origin of fast noise is likely due to channel noise associated with fast ionic currents. Potential candidates are sodium, delayed-rectifier potassium and receptor currents. To distinguish between channel noise from different ionic currents, a single-compartment conductance-based model, in which each conductance is modeled by a population of ion channels, has been simulated by Fisch [2011]. In this modeling study, the stochastic dynamics of the sodium and delayed-rectifier potassium channels followed a kinetic Markov scheme of the Hodgkin-Huxley type. The transduction current has been modeled by two-state channels with transition rates that depend on the tympanal deflection. Channel noise stemming from the delayed-rectifier potassium current failed to reproduce the ISI variability as a function of sound intensity [for details, see Fisch, 2011, Fisch et al., 2012]. In contrast, slow adaptation channel noise along with either sodium or receptor channel noise reproduced the ISI statistics.

Whether sodium or receptor channel noise (or both) contribute to ISI variability cannot be concluded from the ISI statistics. Under the assumption that receptor channel noise is the main source of fast fluctuations, the modeling study of Fisch [2011] could reproduce the data using $N_\mathrm{a} = 600$ adaptation channels and $N_R = 20$ receptor channels (Fig. 4.19). These channel numbers might be used as a rough estimate of the number of receptor channels, although care must be taken because a larger number of receptor channels could in part be compensated by a smaller number of adaptation channels [Fisch, 2011].

The modeling study by Fisch [2011] has shown that *different* ISI statistics (CV, skewness, kurtosis and serial correlations) of locust auditory receptor cells *and* their dependence on sound intensity can be reproduced by a minimal conductance-based model including both adaptation channel noise and fast channel noise. In addition to that, these observations can be qualitatively explained by the theoretical results obtained in this chapter, especially the emergence of colored noise from a stochastic adaptation current and its effect on the ISI statistics. This leads us to the strong hypothesis that the observed spike response variability is caused by both adaptation channel noise and fast receptor

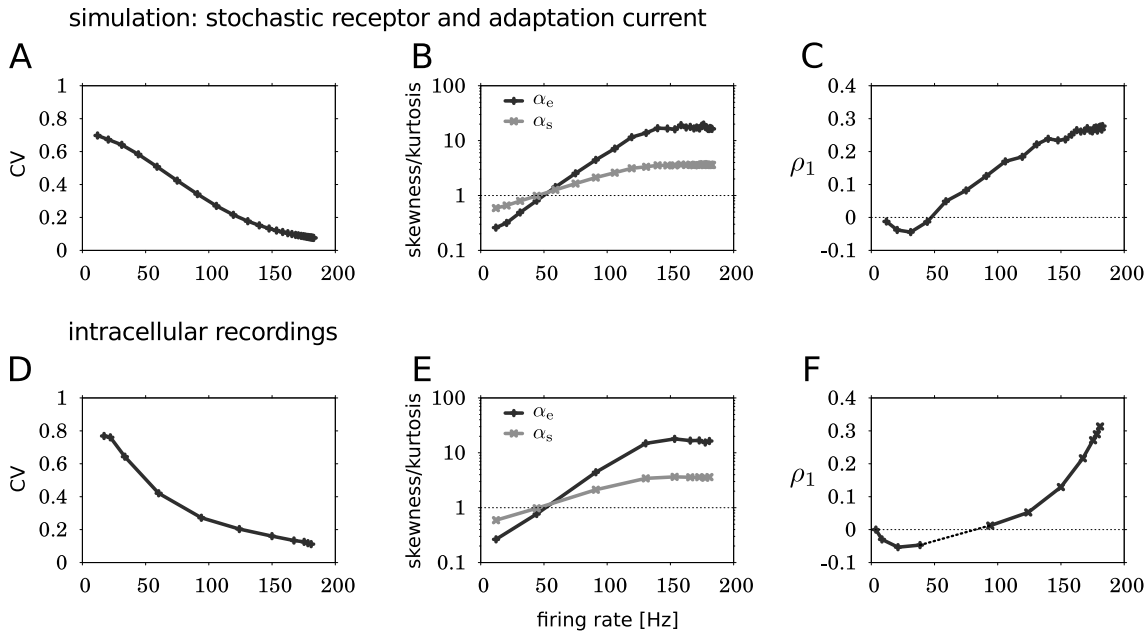

Figure 4.19.: A mixture of a stochastic receptor and a stochastic adaptation current in a channel-based Traub-Miles model can reproduce the ISI statistics of locust auditory receptor cells. **A,D** Coefficient of variation, **B,E** skewness α_s and kurtosis α_e and **C,F** serial correlation coefficient at lag 1 as function of the firing rate (corresponding to different sound intensities). The top row shows the result of a modified Traub-Miles model with a population of $N_a = 600$ M-type adaptation channels and $N_R = 20$ receptor channels. The other currents are deterministic corresponding to populations with a infinite number of ion channels [for details, see Fisch, 2011, Fisch et al., 2012]. The data shown in the bottom row are obtained from intracellular recordings of one cell, except for the negative serial correlation coefficients which were recorded from a different cell at longer (1 min) stimulation to improve the available statistics. Figure adopted from Fisch [2011].

or sodium channel noise. Note that an ultimate "proof" of the contributions of different channel noises to the spike response variability would require direct recordings of the subthreshold voltage fluctuations or the use of pharmacology to block certain channels (e.g. M-type channels). These experiments have yet to be carried out.

4.4.2. General remarks

Stochastic adaptation currents are a source of colored noise

We found that the slow adaptation noise effectively acts as an independent colored noise with a large correlation time. In previous works, slow processes which cause positive ISI correlations were often assumed to be of external origin, e.g. an external stimulus, [Middleton et al., 2003, Moreno-Bote and Parga, 2004, Schwalger and Schimansky-Geier, 2008]. Here, we have shown that an *intrinsic* process, i.e. the fluctuations associated with the stochasticity of adaptation, yields likewise positive ISI correlations. Our finding also provides an alternative explanation of positive ISI correlations in experimental studies [Chacron et al., 2001, Lowen and Teich, 1992]. Moreover, *in vivo* recordings from a looming-sensitive interneuron in the locust optic lobe have revealed both positive correlations at large firing rates and negative correlations at low firing rates [Gabbiani and

Krapp, 2006]. Because this neuron exhibits pronounced spike-frequency adaptation, an intriguingly simple explanation for these observations would be the presence of both fast noise and stochastic adaptation (corresponding to our mixed case). In this case, a large firing rate could indeed lead to a large effective correlation time of the noise associated with the adaptation mechanism and thus to positive ISI correlations.

Other mechanisms leading to spike-frequency adaptation

Spike-frequency adaptation has been ascribed to different mechanisms (see e.g. Benda and Herz [2003]), e.g. calcium-dependent potassium currents (so-called I_{AHP} [Madison and Nicoll, 1984]), slow voltage-dependent M-type currents I_{M} [Brown and Adams, 1980, Madison and Nicoll, 1984] and slow recovery from inactivation of sodium currents [Fleidervish et al., 1996]. In the present study, the M-current has been chosen as an example to illustrate the emergence of slow noise in the adaptation mechanism. In this specific case, it was the finite number of M-type potassium channels that gave rise to slow channel noise. For the other commonly studied adaptation mechanism, the I_{AHP} [Wang, 1998, Liu and Wang, 2001, Ermentrout et al., 2001, Benda and Herz, 2003, Gabbiani and Krapp, 2006, Peron and Gabbiani, 2009a] (cf. Sec. 1.3.2), we face two possible sources of noise: the finite number of potassium channels N_{K} and fluctuations of the local Ca^{2+} concentration c. Proceeding in a similar way as for I_{M}, we would obtain $I_{\mathrm{AHP}} = \bar{g}_{\mathrm{AHP}} K (V - E_{\mathrm{K}})$, with the fraction K of open potassium channels, obeying

$$\tau_k \dot{K} = -K + k_\infty(c) + \sqrt{\frac{2\tau_k \sigma_k^2}{N_{\mathrm{K}}}}\xi_k(t) \tag{4.36}$$

$$\tau_c \dot{c} = -c + \Delta \sum_i \delta(t - t_i) + \sqrt{2D_{\mathrm{Ca}}}\xi_c(t). \tag{4.37}$$

Here, the two Gaussian white noises ξ_k and ξ_c approximately represent the channel noise and the concentration fluctuations due to stochastic removal of calcium, respectively. The calcium gating is characterized by the steady-state activation $k_\infty(c)$. For simplicity, the increase of calcium Δ caused by an action potential is assumed to be deterministic. Importantly, the channel dynamics is fast compared to the slow removal of calcium, i.e. $\tau_k \ll \tau_c$. Following Benda and Herz [2003], the open probability of the potassium channels $k \equiv \langle K \rangle$ adiabatically adjusts to c (i.e. $k \approx k_\infty(c)$) and the relationship is roughly linear (i.e. $k_\infty(c) \propto c$). Thus, we have $I_{\mathrm{AHP}} \propto (c + \eta_k)(V - E_{\mathrm{K}})$, where the "channel noise" η_k possesses a correlation time τ_k. If this correlation time is much smaller than the mean ISI, the channel noise can be approximately treated as white noise. This means, however, that a PIF neuron with a calcium-dependent I_{AHP} instead of I_{M} can likewise be approximated by Eq. (4.23): the fast channel noise can be included into the white noise term $\sqrt{2D}\xi(t)$ and the slow fluctuations of the calcium concentration assume the role of the slow adaptation noise $\eta(t)$. Approximating I_{AHP} again by a voltage-independent current, the PIF model with I_{AHP} would read

$$\dot{V} = \mu - \beta c + \sqrt{2D}\xi(t) \tag{4.38}$$

$$\tau_c \dot{c} = -c + \Delta \sum_i \delta(t - t_i) + \sqrt{2\tilde{D}_{\mathrm{Ca}}}\xi_c(t). \tag{4.39}$$

These equations can indeed be put into the form of Eq. (4.23) by splitting the deterministic and the noise part of c. This illustrates that the main results derived in this chapter are not specific to a certain adaptation current, but apply quite generally to any noise associated with the slow dynamics of adaptation.

The adaptation currents I_{M} and I_{AHP} have been distinguished with respect to their ability to synchronize coupled neurons [Ermentrout et al., 2001] and regarding the influence on neural coding [Prescott and Sejnowski, 2008]. The difference consists in whether the current is activated solely by spikes as in the case of I_{AHP} or whether it is also activated by subthreshold voltages as for I_{M}. For the sake of clarity, we have set the activation function $w_\infty(t)$ of the M-type adaptation current in the PIF model equal to zero at subthreshold voltages, i.e. between spikes (Eq. (4.11)). Thus, the adaptation current in the PIF model, unlike the M-current, was only activated during action potentials. However, the main results of our analysis remain unchanged if a small subthreshold activation is allowed. To illustrate this, let us consider an extended model for which in-between spikes the steady-state activation function w_∞ is not zero but equals the value $\varepsilon < 1$. Instead of Eq. (4.11) we have now

$$w_\infty(t) = \begin{cases} 1 & t_{i^*} \le t < t_{i^*} + \tau_{\mathrm{AP}} \\ \varepsilon & \text{else} \end{cases} \tag{4.40}$$

$$= \varepsilon + (1-\varepsilon) \sum_i \theta(t - t_i)\theta(t_i + \tau_{\mathrm{AP}} - t). \tag{4.41}$$

This only increases the mean adaptation to $\langle w \rangle = \langle w_\infty(t) \rangle = \varepsilon + (1-\varepsilon) r \tau_{\mathrm{AP}}$ (cf. Eq. (C.7)). Similarly, the variance changes according to $\sigma^2 = \langle w \rangle - \langle w \rangle^2$ (cf. Eq. (C.10)). As a result, the effective base current is now given by

$$\tilde{\mu} = \lambda(\mu - \beta\varepsilon) \tag{4.42}$$

with the new scaling factor

$$\lambda = \left[1 + (1-\varepsilon) \frac{\beta \tau_{\mathrm{AP}}}{V_{\mathrm{th}}} \right]^{-1}. \tag{4.43}$$

The colored noise approximation can be carried out in an analogous manner yielding the same result Eq. (4.32) (again with $\tilde{\tau} = \lambda \tau_w$, $\tilde{\sigma}^2 = \lambda \sigma^2$, but the new scaling factor λ, Eq. (4.43)). Thus, it can be expected that in the presence of subthreshold activation of $w(t)$ the colored noise effect (i.e. pronounced peak of ISIH, positive ISI correlations) in the case of stochastic adaptation is preserved. Furthermore, λ still serves as the degree of adaptation, i.e. the ratio of steady-state to initial gain when a step current is applied.

Adaptation channel noise and channel numbers

To study the main effect of adaptation channel noise, we used a minimal two-states model with simple gating kinetics for the single ion channel. There are certainly more realistic channel models. For instance, it is known that the M-channel kinetics is governed by several time scales and more than two internal states [Selyanko and Brown, 1999]. Moreover, the effect of temperature has not been considered here. The temperature is contained only

implicitly in the time-constants of the gating variables. It is not clear, what an increase in temperature would mean for the contribution of adaptation channel noise. Experiments which measures the ISI statistics as a function of temperature and a stochastic model that explicitly accounts for temperature could yield a further test of our hypothesis. Furthermore, channels might not be strictly independent, but channel clusters might exhibit cooperative behavior as reported in Keleshian et al. [2000]. The latter case would actually increase the level of channel noise compared to the case of independent channels, i.e. cooperativity would contribute to stochastic adaptation.

Realistic numbers of M-type channels per neuron are difficult to estimate and the numbers used in this chapter must be seen as a tuning parameter for the channel noise intensity. Channel densities of the M-type have been estimated to be of the order of one functional channel per $4\mu\text{m}^2$ [Villarroel, 1997]. Assuming a spherical cell with a diameter of 10μm, one obtains of the order of 100 channels. Thus, the channel numbers used in this study ($N_\text{a} = 20 - 1000$) seem to be reasonable; and hence the M-current could be a potential source of membrane potential fluctuations.

Validity of the diffusion approximation

The diffusion approximation for the stochastic dynamics of ion channel populations has been studied by several authors [Lecar and Nossal, 1971, Fox and Lu, 1994, Chow and White, 1996, Fox, 1997, Ochab-Marcinek et al., 2009] (cf. Sec. 1.1.1, see also Gillespie [2000] in the context of chemically reacting particles). Here, we have shown how one can map the stochastic dynamics of an population of ion channels with negative feedback to the sum of a deterministic current dynamics and an additive colored noise (see Lecar and Nossal [1971] for a related treatment). In other words, the dynamics could be reduced to an analytically accessible Langevin equation for the membrane potential and the adaptation current. In particular, the effect of the diffusion approximation on the ISI statistics has been investigated and a rather good agreement with the channel model has been observed, despite the small number of channels. This seems surprising, given that for a typical parameter set – $N_\text{a} = 200$, open probability $\langle w \rangle \sim 0.1$ and $\tau_w = 100$ ms – one expects only 1.8 closing transitions (between spikes) and 0.2 open transitions (during action potentials) per millisecond. Apparently, on the time scale of 1 ms the number of transition events is not Gaussian distributed. However, we found that the main effect of the channel noise consists in a slow modulation of the instantaneous firing rate on the large time scale of $\tilde{\tau} = \lambda\tau$, whereas high-frequency components of the noise are of minor importance. Thus, on relevant time scales of the order of 10–100 ms the average number of transitions is much larger and a Gaussian approximation seems to be reasonable.

4.5. Summary

Auditory receptor cells show notable variability in the timings of action potentials in response to acoustic stimuli with constant sound intensity. This variability becomes manifest in the distribution of interspike intervals with CVs ranging from 0.1 to 0.9 depending on sound intensity. Here, we have studied theoretically three hypotheses about the origin of this variability with respect to the ISI statistics:

1. The variability is solely caused by channel noise associated with a slow adaptation current ("stochastic adaptation").
2. The variability is solely caused by channel noise associated with fast ionic currents ("deterministic adaptation").
3. The variability is caused by both slow adaptation channel noise *and* fast channel noise ("mixed case").

The first two cases can be regarded as two opposite limit cases: a small number of adaptation channels and infinitely many fast channels, in the first case; and infinitely many adaptation channels and a small number of fast channels, in the second case. For a real neuron, these limit cases correspond to cases where one source of noise dominates over the other. Using a perfect integrate-and-fire model with adaptation, the ISI statistics could be calculated analytically in both cases.

The analysis revealed large differences between the two limit cases regarding the skewness, the kurtosis and the serial correlations of ISIs. Specifically, the first case could be approximately mapped to a PIF model without adaptation, but with a reduced base current and a colored noise drive with a correlation time that is set by the adaptation time constant. The theoretical analysis of this reduced model has been carried out in Chap. 2. Using the results of that chapter we found that a PIF model with a stochastic adaptation current is characterized by a skewness and a kurtosis which is significantly larger than for an inverse Gaussian ISI density. In addition, the serial correlation coefficient is positive and decays exponentially with the lag. In contrast, the second hypothesis could be reduced to the adapting PIF model driven by white noise, which has been analyzed in Chap. 3. As a result, a deterministic adaptation current and fast fluctuations lead to a skewness and a kurtosis similar to the case of an inverse Gaussian ISI density. In marked contrast to the first case, the second case yields a negative serial correlation coefficient at lag 1.

Finally, the ISI statistics corresponding to the third hypothesis, i.e. to a mixture of slow adaptation channel noise and fast noise, revealed the traits of both limit cases depending on the weight of each noise source as well as the time scale separation between adaptation and spiking dynamics. It is this time-scale separation, that can be altered in the experiment by varying the sound intensity of the stimulus, and thereby changing the firing rate. For an increase of the firing rate, the theory predicts a smooth transition from deterministic to stochastic adaptation (Fig. 4.16). The same qualitative behavior has indeed been observed in the experiment and in a detailed stochastic simulation study (Fig. 4.19). Moreover, a simulation of a conductance-based Traub-Miles model by K. Fisch [Fisch, 2011] supports the robustness of the theoretical results obtained for the adapting PIF model with respect to details of the spike generation. Thus, the distinct effect of colored noise, arising from an adaptation current, on the ISI statistics seems to be rather general for tonically firing neurons that exhibit spike-frequency adaptation. The agreement of general theoretical predictions, detailed stochastic modeling and experimental evidence makes us confident that spike response variability in locust auditory receptor cells is caused by both channel noise from fast ionic currents and a slow adaptation current.

Chapter 5.

Nonrenewal spiking statistics of excitable systems

In the previous chapters, I have mathematically analyzed different variants of the perfect integrate-and-fire (PIF) model that generate spike trains with correlated interspike intervals (ISIs). By deriving analytical expressions for the serial correlation coefficient (SCC), it was shown how external stimuli or colored noise sources are reflected in the correlation structure of the neuronal output and how spike-triggered adaptation currents cause negative serial correlations. The analytical techniques were based on the fact that the PIF model generates spikes already in the absence of noise (supra-threshold regime). This deterministic dynamics has been interpreted as a limit cycle. The effect of noise could then be treated as a perturbation of this limit cycle dynamics. It has been possible to apply the theoretical results to auditory receptor cells, because at high firing rates the coefficients of variations were small, which is an indication for supra-threshold firing. However, as mentioned in section 1.1.2, other neurons, especially cortical neurons, fire at a much lower firing rate and show a high degree of spiking irregularity that resembles a Poisson process [Softky and Koch, 1993, Shadlen and Newsome, 1994, 1998]. These neurons seem to operate in a *subthreshold regime*, also called fluctuation-driven or excitable regime (Sec. 1.1.2). In this regime, fluctuations have a tremendous effect on the spiking dynamics as they cause large deviations from the deterministic dynamics. It is clear that a perturbation theory based on the deterministic dynamics and a weak noise perturbation will fail to describe the dynamics of fluctuation-driven neurons. Thus, for the analysis of an excitable neuron model entirely different techniques must be employed.

To this end, it is important to recognize that spontaneous firing events of an excitable neuron can be regarded as noise-activated escapes from a metastable state, such as the neuron's resting potential. The calculation of escape-time distributions is a prominent problem in the theory of nonlinear stochastic systems. However, the calculation of serial correlations in the sequence of escapes (i.e. sequence of spikes) has received relatively little attention. Here, I show that the escape time statistics can still be used to develop a theory that can capture the correlations in the sequence of ISIs.

To illustrate the basic setting one may think of a leaky integrate-and-fire (LIF) neuron model as a prototypical example of an excitable neuron dynamics (cf. Sec. 1.1.2). Similar to the adapting PIF model of section 3 the LIF model can be augmented with a slow adaptation variable $a(t)$ either in form of an adaptation current [Wang, 1998, Liu and Wang, 2001, Benda and Herz, 2003] or as a dynamic threshold [Chacron et al., 2000, 2001, 2003]. A typical realization of such an *adapting LIF* model is shown in Fig. 5.1A. Between two spikes the adaptation variable decays on a time scale that is large compared to

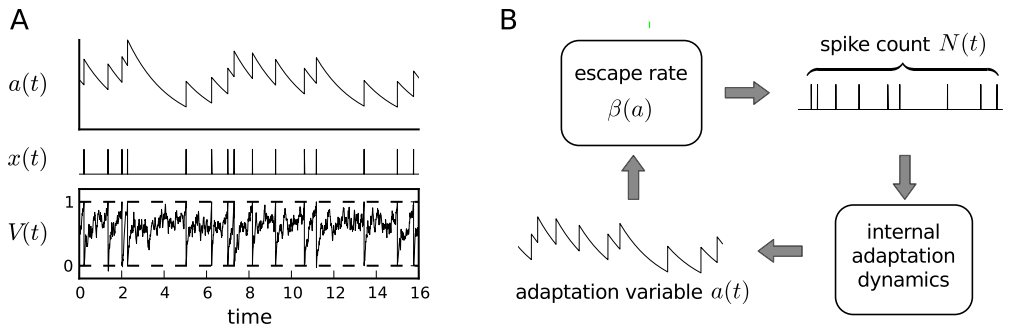

Figure 5.1.: Reduction of an excitable neuron with a slow adaptation variable by an escape rate model. A Realization of the adapting LIF model: The membrane potential V obeys the Langevin equation $\tau_m \dot{V} = -V + \mu - a + \sqrt{2D}\xi(t)$, where $a(t)$ is an adaptation current that evolves according to $\tau_a \dot{a} = -a + \tilde{\Delta} \sum \delta(t - t_i)$. Furthermore, if $V = V_{th}$, a spike is triggered and V is reset to zero. Spiking can be seen as an escape from the (slowly changing) resting potential $E_0 = \mu - a$ to the threshold. Parameter values: $\mu = 0.9$, $D = 0.02$, $\tau_m = 0.1$ $\tau_a = 2$, $\tilde{\Delta} = 0.1\tau_a$. **B** Feedback loop of the escape rate model: Spikes are generated from a Poisson process given by the escape rate $\beta(a)$ that depends on the current value of $a(t)$. This adaptation state is in turn driven by the generated spikes.

the membrane time constant. As a consequence of this time-scale separation, the membrane potential quickly equilibrates to the resting potential, from which it can escape with an escape rate $\beta(a)$ that depends on the slow adaptation variable. Specifically, the decay of $a(t)$ leads to a shrinking of the distance between resting potential and threshold, which entails a slow increase in the escape rate. Furthermore, during each spike the adaptation variable is raised by a fixed amount, which lowers the escape rate and in this way establishes an inhibitory feedback mechanism. This suggests that the spike generation might be approximated by a Poisson process with a state-dependent rate $\beta(a)$ (often called "hazard function"), where the slow dynamics of a is driven by the output spikes (Fig. 5.1B). Note that in this way the dimensionality of the model has been reduced from a two-dimensional fast-slow system to the one-dimensional dynamics of the slow subsystem.

More generally, I assume here that the spiking dynamics of a given excitable neuron model can also be reduced to a hazard function (escape rate) that depends on some slow state variable. Under this assumption, the stochastic evolution of the slow variable as well as the spike count can be described by a master equation, or in other words, the spike count and the slow variable are modeled by a Markov process. A similar approach has been applied to the above problem of adapting neurons by several authors [Muller et al., 2007, Nesse et al., 2010, Farkhooi et al., 2011]. Despite the simplifications (dimensionality reduction), the mathematical treatment of the master equation is still difficult and analytical expressions of higher-order spiking statistics of excitable neurons with adaptation are still lacking[1]. As a first step towards a general analysis of a non-renewal master equation, I consider here a *discrete* state space that comprises a *finite* number of possible states of the slow variable. For the example of an adapting neuron, this corresponds to going from the escape rate $\beta(a)$ defined for continuous a to a finite number of discrete adaptation states a_i with respective escape rates $\beta_i = \beta(a_i)$.

[1] A notable exception is the weak-adaptation theory of Urdapilleta [2011], which is based on a perturbation scheme for the first-passage-time moments developed by Lindner [2004b]

In this chapter, the theory of [Lindner and Schwalger, 2007, Schwalger and Lindner, 2008] for bistable systems is extended to more general systems that also include excitable dynamics. In particular, the kinetic model is generalized from two discrete states to m discrete states and more general transitions between the states are allowed. Moreover, the escape rates β_{ij} may depend on both the initial state j before firing and the final state i after firing. I present a general method for calculating the SCC, which can be applied to a number of simple cases. Specifically, I consider two examples: The first example is a LIF neuron that is driven by dichotomous colored noise. The predictions of the Markovian theory are good if the ISIs associated with each state of the dichotomous noise are as irregular as a Poisson process. For the case that the ISIs are more regular, I develop an alternative non-Markovian theory, which consists of a dichotomous switching between two renewal processes. As a second example, I consider the problem of a spiking neuron with intrinsic feedback resembling an adaptation variable. I derive expressions for the SCC for two different models, which are tested by stochastic simulations of the discrete scheme.

Parts of the results of this chapter have been published in [Schwalger and Lindner, 2010] and [Schwalger et al., 2012].

5.1. General Markov theory for systems with a discrete state space

I consider a system which generates spikes at times t_n and thus increase the spike count $N(t)$ by one as indicated in the coarse-grained view of Fig.5.2A. Interspike intervals are correlated if the spike-generating dynamics is non-Markovian, e.g. if there is memory in the system or in the external driving of the system. In many cases, the non-Markovian dynamics may be approximated by a Markovian dynamics on m discrete states s_i ($i = 1, \ldots, m$) that I will call *internal* (or hidden) states irrespective of the origin of the memory (external driving or intrinsic feedback). These states are shown in Fig.5.2B. There are two different kinds of transitions between these states: those that are associated with a spike (thick arrow in Fig.5.2A) and those that are purely internal. The scheme can be rearranged as shown in Fig.5.2C, which allows to keep track of the number of spikes by a second dimension. Purely internal transitions happen with rates α_{ij} from state s_j to s_i. Transition rates that are associated with a spike are given by β_{ij}. The stochastic evolution of the dynamics is given by the two-dimensional Markovian jump process $(S(t), N(t))$ on the lattice shown in Fig.5.2C. Furthermore, at time $t = 0$ it is assumed that $N(0) = 0$, hence, $N(t)$ yields the number of spikes in the time window $(0, t]$.

5.1.1. Master equation

The two-dimensional Markovian jump process $(S(t), N(t))$ can be described by a Master equation for the probability that $S(t) = s_i$ and $N(t) = n$. Let this probability be denoted

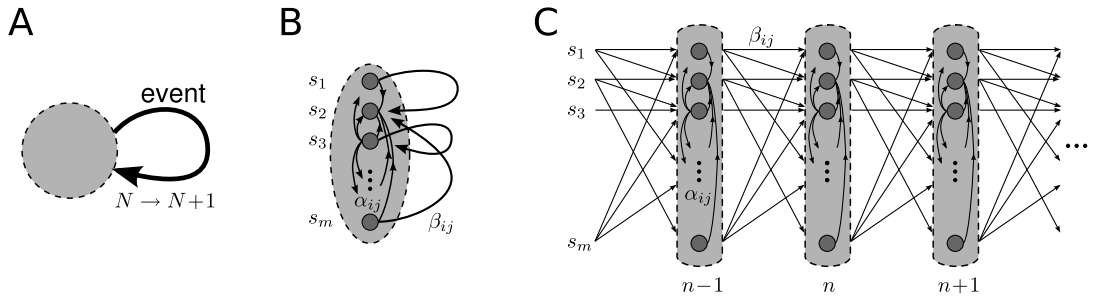

Figure 5.2.: Two-dimensional Markovian jump process. **A** Non-Markovian system that generates spikes. The temporal occurrence of spikes is described by a count variable $N(t)$. **B** Markov approximation of the system by m discrete states s_i. There are internal transitions between states with constant rates α_{ij} and state transitions that are associated with a spike (large arrows with constant rates β_{ij}). **C** Transitions in the two-dimensional state-space (s_i, n): matrix (α_{ij}) (internal transition) and matrix (β_{ij}) (firing events) are the same for every layer n.

by $p_i(n,t)$. Then, the Markov scheme Fig. 5.2C corresponds to the master equation

$$\dot{p}_i(n,t) = -\left(\sum_{\substack{k=1\\k\neq i}}^{m}\alpha_{ki} + \sum_{k=1}^{m}\beta_{ki}\right)p_i(n,t) + \sum_{\substack{k=1\\k\neq i}}^{m}\alpha_{ik}p_k(n,t) + \sum_{k=1}^{m}\beta_{ik}p_k(n-1,t) \tag{5.1}$$

for $i = 1,\ldots,m$. The master equation can be conveniently written in the matrix form

$$\dot{\mathbf{p}}(n,t) = \mathrm{A}\mathbf{p}(n,t) + \mathrm{B}\mathbf{p}(n-1,t), \tag{5.2}$$

where the vector $\mathbf{p}(n,t)$ is made up by the elements $p_i(n,t)$, and A and B are $m \times m$ matrices with elements

$$A_{ij} = \alpha_{ij} - \delta_{i,j}\sum_{k=1}^{m}(\alpha_{ki} + \beta_{ki}), \qquad B_{ij} = \beta_{ij}. \tag{5.3}$$

Next, I consider the marginal probability $p_i(t) = \sum_{n=0}^{\infty} p_i(n,t)$ to find the system in the internal state s_i (irrespective of the number of spikes that have occurred). The initial probabilities are $p_i(n,0) = p_i(0)\delta_{n,0}$ because at time $t = 0$ no spike has occurred yet (that is how I defined $N(t)$ above, namely as the number of spikes in the time interval $(0,t]$). In the following two different ensembles will be considered that correspond to two different initial conditions $p_i(0)$.

In both cases, one can imagine that the process $S(t)$ has been initiated at an arbitrary value at $t = -\infty$, so that at the origin $t = 0$ the process is stationary. In this *stationary* ensemble (cf. Sec. 1.2.1, Fig. 1.8), $p_i(0)$ is taken to be the stationary probability distribution of $S(t)$, which I denote by the vector $\mathbf{p}^{(s)}$.

One can also consider the values of $S(t)$ right after the occurrence of a spike. This yields the sequence $\{S_k\}$ defined by

$$S_k = \lim_{\varepsilon\to 0^+} S(t_k + \varepsilon). \tag{5.4}$$

Here, t_k are the instances of the kth spike. For this second, *conditional* ensemble (cf.

Sec. 1.2.1, Fig. 1.8), the initial distribution is taken as the distribution $\hat{\mathbf{p}}$ of the stationary sequence $\{S_k\}$. In other words, $\hat{\mathbf{p}}$ is the distribution of states upon firing.

The first distribution $\mathbf{p}^{(s)}$ is simply given by the marginal distribution $\mathbf{p}(t) = \sum_n \mathbf{p}(n,t)$ in the stationary state. Summing Eq. (5.2) over n and setting $\dot{\mathbf{p}}(t) = 0$ yields an equation for this density:

$$(\mathrm{A} + \mathrm{B})\mathbf{p}^{(s)} = 0 \tag{5.5}$$

or

$$\mathrm{C}\mathbf{p}^{(s)} = \mathbf{p}^{(s)}, \qquad \mathrm{C} = -\mathrm{A}^{-1}\mathrm{B}. \tag{5.6}$$

Eq. (5.6) states that C has an eigenvalue $\lambda_1 = 1$ with a corresponding eigenvector that is the stationary distribution $\mathbf{p}^{(s)}$.

Similar as in Chap. 2, the distribution upon firing $\hat{\mathbf{p}}$ is proportional to the stationary currents from the state $n-1$ into the states (n, s_i). Hence, the stationary and the conditional distributions are related by

$$\hat{\mathbf{p}} \propto \mathrm{B}\mathbf{p}^{(s)}. \tag{5.7}$$

The factor of proportionality is obtained by normalization. In the following, functions that refer to the conditional ensemble will be marked with a hat.

5.1.2. Serial correlation coefficient

The count statistics of spikes is completely determined by the marginal distribution

$$p(n,t) = \sum_{i=1}^{m} p_i(n,t). \tag{5.8}$$

Furthermore, I define the quantities

$$\tau_i^{(n)} = \int_0^\infty p_i(n,t)\,dt, \qquad \hat{\tau}_i^{(n)} = \int_0^\infty \hat{p}_i(n,t)\,dt \tag{5.9}$$

and

$$\tau^{(n)} = \int_0^\infty p(n,t)\,dt, \qquad \hat{\tau}^{(n)} = \int_0^\infty \hat{p}(n,t)\,dt. \tag{5.10}$$

Here, $\tau_i^{(n)}$ and $\hat{\tau}_i^{(n)}$ yield the average time the system spends in the state (s_i, n) for the two different initial distributions[2]. Likewise, $\tau^{(n)}$ and $\hat{\tau}^{(n)}$ are the respective average residence times in the state n. Because in the conditional ensemble the distribution of states is the same at the beginning of each interval, i.e. immediately after each spike, $\hat{\tau}_i^{(n)}$ does not depend on n. Therefore, one can set

$$\hat{\tau}_i^{(n)} = \hat{\tau}_i, \qquad \hat{\tau}^{(n)} = \hat{\tau}, \tag{5.11}$$

where $\hat{\tau}_i$ is the mean residence time of state s_i and $\hat{\tau}$ is the mean interspike interval.

According to Eq. (1.65), the statistics of interspike intervals of a stationary point process

[2]From a realization of the process $(S(t), N(t))$ I obtain the total time the trajectory spends in state (s_i, n) by integrating $\int_0^\infty \delta_{N(t),n}\delta_{S(t),s_i}\,dt$ where $\delta_{x,y}$ is one if $x = y$ and zero otherwise. The average of the integral (the mean total residence time in (s_i, n)) reduces to the integral over the average $\langle \delta_{N(t),n}\delta_{S(t),s_i}\rangle$. The latter is by definition the probability distribution $p_i(n,t)$.

is linked to the count statistics by [McFadden, 1962]

$$\langle T_k \rangle = \hat{\tau}, \quad \langle T_k^2 \rangle = 2\hat{\tau}\tau^{(0)}, \quad \langle T_k T_{k+n} \rangle = \hat{\tau}\tau^{(n)}. \tag{5.12}$$

Hence, the serial correlation coefficient, Eq. (1.46), can be written as

$$\rho_n = \frac{\tau^{(n)} - \hat{\tau}}{2\tau^{(0)} - \hat{\tau}}, \quad n \geq 1. \tag{5.13}$$

This equation illustrates that the SCC is proportional to the difference of the mean residence times of the two ensembles. Clearly, the difference vanishes as $n \to \infty$ because in this limit the initial distributions are forgotten and both ensembles become equivalent.

In order to compute ρ_n, one has to determine $\tau^{(n)}$. To this end, Eq. (5.2) is integrated over t yielding the system of difference equations

$$\boldsymbol{\tau}^{(n)} = \mathrm{C}\boldsymbol{\tau}^{(n-1)}, \qquad n \geq 1 \tag{5.14}$$

with initial condition

$$\boldsymbol{\tau}^{(0)} = -\mathrm{A}^{-1}\mathbf{p}^{(s)}. \tag{5.15}$$

Here, $\boldsymbol{\tau}^{(n)}$ denotes the vector with elements $\tau_i^{(n)}$. Note that in the conditional ensemble

$$\hat{\boldsymbol{\tau}}^{(0)} = -\mathrm{A}^{-1}\hat{\mathbf{p}}^{(s)} \propto -\mathrm{A}^{-1}\mathrm{B}\mathbf{p}^{(s)} = \mathrm{C}\mathbf{p}^{(s)} = \mathbf{p}^{(s)} \tag{5.16}$$

is an eigenvector of C for the eigenvalue $\lambda_1 = 1$ (Eq. (5.6)). Hence, $\hat{\boldsymbol{\tau}}^{(n)} = \mathrm{C}^n\hat{\boldsymbol{\tau}}^{(0)} = \hat{\boldsymbol{\tau}}^{(0)}$ is independent of n as stated above.

The formal solution of Eq. (5.14)– (5.15) is $\boldsymbol{\tau}^{(n)} = \mathrm{C}^n\boldsymbol{\tau}^{(0)}$. Thus, the computation of the SCC amounts to finding the n-th power of C. This operation is standard and can be achieved, for instance, by transforming C to the Jordan normal form, which requires the determination of (generalized) eigenvectors. If C possesses m linearly independent eigenvectors $\mathbf{v}_1, \ldots, \mathbf{v}_m$, i.e. if C is diagonalizable, the general solution of Eq. (5.14) is given by

$$\boldsymbol{\tau}^{(n)} = c_1\lambda_1^n\mathbf{v}_1 + \cdots + c_m\lambda_m^n\mathbf{v}_m, \tag{5.17}$$

where $c_1, \ldots, c_m$ are constants determined by the initial condition Eq. (5.15) and $\lambda_1, \ldots, \lambda_m$ are the eigenvalues of C. Since $\boldsymbol{\tau}^{(n)}$ tends to $\hat{\boldsymbol{\tau}}$ in the limit $n \to \infty$, the eigenvalues λ_i, $i = 2, \ldots, m$ must satisfy $|\lambda_i| < \lambda_1 = 1$. Thus, we have the general result

$$\rho_n \propto \mathbf{1}(c_2\lambda_2^n\mathbf{v}_2 + \cdots + c_m\lambda_m^n\mathbf{v}_m), \tag{5.18}$$

where the product with the row vector $\mathbf{1} = (1, 1, \ldots, 1)$ yields the summation over all states s_i. Eq. (5.18) shows that the correlations between interspike intervals decay geometrically fast[3].

[3]This observation is also valid in the general case, where C is in general not diagonizable. The reason for this is that the sequence $\{\boldsymbol{\tau}^{(n)}\}$ of processes described by Eq. (5.2) is closely related to the sequence $\{\mathbf{p}^{(n)}\}$ of the distributions of states S_n immediately after the spikes. Because S_n is a realization of a Markov chain, the distribution $\mathbf{p}^{(n)}$ converges geometrically fast to the limit distribution $\hat{\mathbf{p}}$. Indeed, the relationship between $\boldsymbol{\tau}^{(n)}$ and $\mathbf{p}^{(n)}$ is simply a linear map given by $\boldsymbol{\tau}^{(n)} = -\mathrm{A}^{-1}\mathbf{p}^{(n)}$. This follows from the fact that $\boldsymbol{\tau}^{(n)} = \int_0^\infty \mathbf{p}(t)\,dt$, where $\mathbf{p}(t)$ is the solution of $\dot{\mathbf{p}}(t) = \mathrm{A}\mathbf{p}(t)$ with $\mathbf{p}(0) = \mathbf{p}^{(n)}$.

5.2. Excitable systems under dichotomous noise driving

In the next sections, the above described method will be applied to simple neuron models that generate non-renewal spike trains. These examples also serve as a demonstration of the formalism.

As a first example, the problem of a colored noise driven excitable system is addressed. In particular, let us consider a leaky integrate-and-fire model that is driven by both white Gaussian noise and a dichotomous Markov process (Fig. 5.3A). The subthreshold dynamics of the membrane potential V obeys

$$\dot{V} = -V + \mu(t) + \sqrt{2D}\xi(t). \tag{5.19}$$

Here, time is measured in units of the membrane time constant τ_m, which corresponds to setting $\tau_m = 1$. The base current $\mu(t)$ is a dichotomous Markov process (also called "random telegraph process") that switches from the value μ_1 to the value μ_2 with rate α_1 and switches back from μ_2 to μ_1 with rate α_2. Furthermore, $\xi(t)$ is a Gaussian white noise process with noise intensity D. Together, the driving noise $\eta(t) = \mu(t) + \sqrt{2D}\xi(t)$ has mean

$$\langle \eta \rangle = \frac{\alpha_2\mu_1 + \alpha_1\mu_2}{\alpha_1 + \alpha_2} \tag{5.20}$$

and an exponential correlation function

$$\langle \eta(t)\eta(t') \rangle - \langle \eta \rangle^2 = 2D\delta(t-t') + \frac{\alpha_1\alpha_2(\mu_1-\mu_2)^2}{(\alpha_1+\alpha_2)^2} \exp\left[-(\alpha_1+\alpha_2)|t-t'|\right] \tag{5.21}$$

[see e.g. Gardiner, 1985]. The colored noise $\eta(t)$ can be seen as a caricature of an Ornstein-Uhlenbeck process, which is also exponentially correlated but possesses Gaussian statistics (cf. Sec. 2.2). In contrast to an OUP, the process $\eta(t)$ is analytically tractable by the discrete Markovian theory outlined in the previous section.

When the membrane potential V reaches the threshold $V_{th} = 1$, the usual fire and reset rule is invoked, i.e. a spike is emitted and V is reset to zero (Fig. 5.3A). For a slow dichotomous driving, the noiseless dynamics would adiabatically adjust to the quasi equilibrium potentials μ_1 and μ_2 (depending on the state). Thus, if both μ_1 and μ_2 are smaller than one, the dynamics does not reach the threshold in the absence of white noise. In this case, the white noise term representing sources of fast noise (synaptic or intrinsic noise) is necessary to generate spikes (subthreshold or fluctuation-driven regime). In general, $\mu(t)$ is allowed to assume sub- and suprathreshold values. In a biological setting, a slow dichotomous driving can represent slow "oscillations" (< 1 Hz) of the synaptic background activity as observed during slow wave sleep. Such slow population dynamics with so-called "Up" and "Down" states have been frequently reported both in experiments [Steriade et al., 1993, Lampl et al., 1999, Sanchez-Vives and McCormick, 2000] and modeling studies [Compte et al., 2003, Holcman and Tsodyks, 2006, Parga and Abbott, 2007], [for a review, see Wilson, 2008]. Here, I am interested in the effect of such presynaptic input on the ISI statistics and especially on the serial correlations of ISIs.

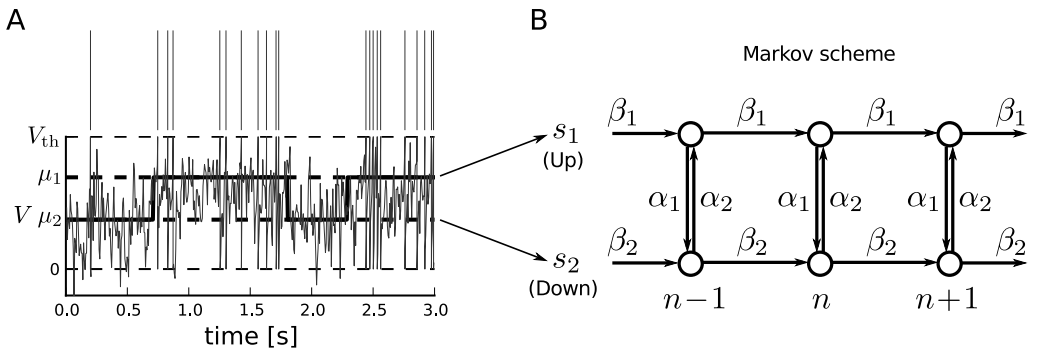

Figure 5.3.: LIF model driven by dichotomous noise and its approximation by a Markovian jump process. A Typical trace of the membrane potential V in the LIF model. $V(t)$ fluctuates about the equilibrium given by the dichotomous process $\mu(t)$ (thick black line), eventually crossing the threshold ($V = V_{\rm th} = 1$), which leads to a spike (top) and a reset of V to zero. The firing rate in state 1 (β_1) is higher than in state 2 (β_2) because μ_1 is closer to the threshold than μ_2. **B** Kinetic Markov scheme describing the dynamics of the tuple $(S(t), N(t))$, where $S(t) = 1$ if $\mu(t) = \mu_1$ and $S(t) = 2$ if $\mu(t) = \mu_2$. Each spike (occurring with rate β_1 or β_2) corresponds to a leftward jump, incrementing the spike count $N(t)$ by one.

5.2.1. Markovian jump process

If the dichotomous driving $\mu(t)$ is well below the threshold the firing events in each state are approximately Poissonian with a coefficient of variation (CV) close to unity [Vilela and Lindner, 2009]. Moreover, if $\mu(t)$ is much slower than the membrane potential (typical time scale $\tau_{\rm m} = 1$), the trajectories quickly equilibrate to the value of $\mu(t)$ after each spike. Thus, the ISIs can be seen as a sequence of escapes from the (time-dependent) equilibrium potential $\mu(t)$ to the threshold. Let β_1 and β_2 denote the firing rates ("escape rates") in state $S = 1$ ($\mu(t) = \mu_1$) and state $S = 2$ ($\mu(t) = \mu_2$), respectively. Then, the LIF model can be approximated by the Markovian jump process shown in Fig. 5.3B. Put differently, the approximation consists of two Poisson processes with rate β_1 and β_2 that alternate with rates α_1 and α_2. Analytical expression for the firing rates β_1 and β_2 of the LIF model with static base current μ and noise intensity D are known. These are given either by exact quadrature formulas or approximate Arrhenius type escape rates [see, e.g. Lindner, 2002]. Here, I assume that these rates are given (either from analytical formulas or from simulations, see Fig. 5.4A,B) because I am mainly interested how serial correlations arise in the driven system and how they can be expressed by the statistics of the static (undriven) system.

I will now derive an expression for the SCC in terms of the parameters $\alpha_{1/2}$ and $\beta_{1/2}$ by using the theory developed in Sec. 5.1. The Markov scheme Fig. 5.3B corresponds to the master equation (5.2) with the 2×2 matrices

$$\mathrm{A} = \begin{pmatrix} -(\beta_1 + \alpha_1) & \alpha_2 \\ \alpha_1 & -(\beta_2 + \alpha_2) \end{pmatrix}, \qquad \mathrm{B} = \begin{pmatrix} \beta_1 & 0 \\ 0 & \beta_2 \end{pmatrix}. \tag{5.22}$$

As explained in Sec. 5.1.1, it is useful to form the matrix $\mathrm{C} = -\mathrm{A}^{-1}\mathrm{B}$:

$$\mathrm{C} = \frac{1}{\beta_1\beta_2 + \beta_1\alpha_2 + \beta_2\alpha_1} \begin{pmatrix} \beta_1(\alpha_2 + \beta_2) & \alpha_2\beta_2 \\ \alpha_1\beta_1 & \beta_2(\alpha_1 + \beta_1) \end{pmatrix}. \tag{5.23}$$

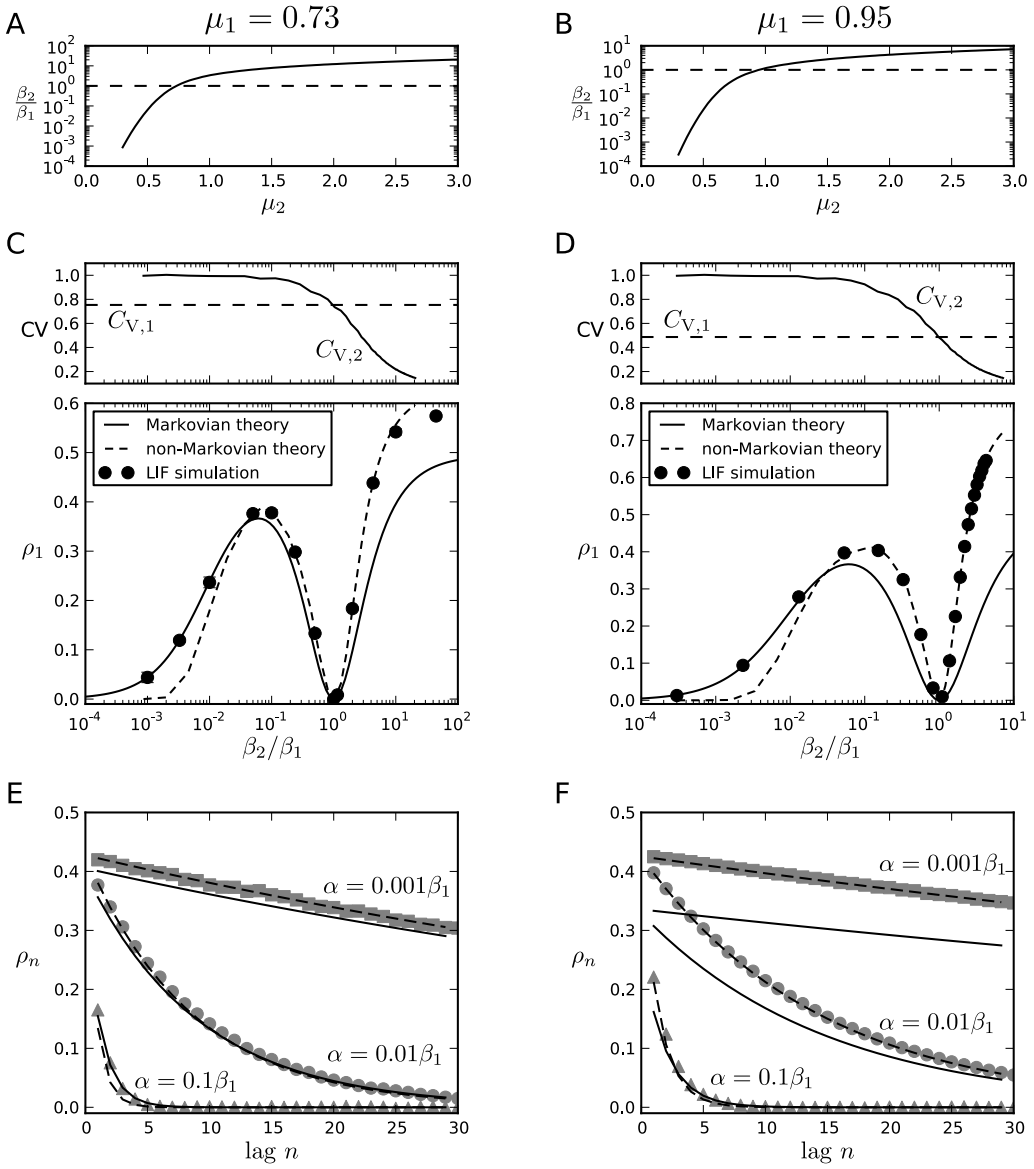

Figure 5.4.: LIF model driven by dichotomous colored noise and Gaussian white noise. The dichotomous driving current switches between the values μ_1 and μ_2 with symmetric rates $\alpha_1 = \alpha_2 \equiv \alpha$. In the left column, μ_1 is fixed to 0.73 well below the threshold, in the right column, μ_1 is fixed to 0.95 close to the threshold. The value of μ_2 is varied in **A–D**. **A,B** Firing rate β_2 corresponding to a static base current μ_2 (solid line) in units of the firing rate β_1 that corresponds to a static base current μ_1 ($\beta_1 = 0.119$ and $\beta_1 = 0.345$ for $\mu_1 = 0.73$ and $\mu_1 = 0.95$, respectively). **C,D** Coefficients of variation corresponding to the static base currents μ_1 (dashed line) and μ_2 (solid line) plotted as a function of the firing rate β_2 (top). Serial correlation coefficient (SCC) at lag 1 for a switching rate $\alpha = 0.01\beta_1$. The static-state rates and CVs in **A–D** have been determined by simulations. **E,F** SCC vs lag for different switching rates (as indicated) for fixed μ_2 (**E** $\mu_2 = 0.524$ corresponding to $\beta_2/\beta_1 = 0.1$, **F** $\mu_2 = 0.65$ corresponding to $\beta_2/\beta_1 = 0.17$). Symbols: simulation, solid line: Markovian theory, Eq. (5.31), dashed line: non-Markovian theory, Eq. (5.37). In all panels, $D = 0.0256$.

According to Eq. (5.6), the stationary probability distribution is given by the eigenvector of C to eigenvalue $\lambda_1 = 1$, which is $\mathbf{v}_1 = (\alpha_2, \alpha_1)^{\mathrm{T}}$. Normalization yields

$$p_1^{(s)} = \frac{\alpha_2}{\alpha_1 + \alpha_2}, \qquad p_2^{(s)} = \frac{\alpha_1}{\alpha_1 + \alpha_2}. \tag{5.24}$$

The second eigenvalue is

$$\lambda_2 = \frac{\beta_1\beta_2}{\beta_1\beta_2 + \alpha_1\beta_2 + \alpha_2\beta_1} < 1 \tag{5.25}$$

and the corresponding eigenvector is $\mathbf{v}_2 = (-\beta_2, \beta_1)^{\mathrm{T}}$. Because the matrix C has two distinct eigenvalues, C is diagonalizable and the solution of Eq. (5.14) has the form $\boldsymbol{\tau}^{(n)} = c_1\lambda_1^n\mathbf{v}_1 + c_2\lambda_2^n\mathbf{v}_2$. On the other hand, from Eq. (5.15) one finds

$$\boldsymbol{\tau}^{(0)} = \frac{1}{(\alpha_1\beta_2 + \alpha_2\beta_1 + \beta_1\beta_2)} \begin{pmatrix} \alpha_2(\alpha_1 + \alpha_2 + \beta_2) \\ \alpha_1(\alpha_1 + \alpha_2 + \beta_1) \end{pmatrix}. \tag{5.26}$$

Matching both expressions at $n = 0$ yields the coefficients

$$c_1 = \frac{1}{\alpha_1\beta_2 + \alpha_2\beta_1}, \qquad c_2 = \frac{\alpha_1\alpha_2(\beta_1 - \beta_2)}{(\alpha_1 + \alpha_2)(\alpha_1\beta_2 + \alpha_2\beta_1)(\alpha_1\beta_2 + \alpha_2\beta_1 + \beta_1\beta_2)}.$$

In the stationary ensemble, the probability distribution of the states 1 and 2 upon firing are found by applying the matrix B to the stationary distribution vector $\mathbf{p}^{(s)}$, yielding $\hat{\mathbf{p}}^{(s)}$:

$$\hat{p}_1^{(s)} = \frac{\alpha_2\beta_1}{\alpha_1\beta_2 + \alpha_2\beta_1}, \qquad \hat{p}_2^{(s)} = \frac{\alpha_1\beta_2}{\alpha_1\beta_2 + \alpha_2\beta_1}. \tag{5.27}$$

This leads to

$$\hat{\boldsymbol{\tau}} = -\mathrm{A}\hat{\mathbf{p}}^{(s)} = \frac{1}{\alpha_1\beta_2 + \alpha_2\beta_1} \begin{pmatrix} \alpha_2 \\ \alpha_1 \end{pmatrix}, \tag{5.28}$$

which by summation of the components yields the mean ISI

$$\langle T \rangle = \hat{\tau} = \frac{\alpha_1 + \alpha_2}{\alpha_1\beta_2 + \alpha_2\beta_1}. \tag{5.29}$$

Using, Eq. (5.12),(5.26) and (5.29) yields the ISI variance

$$\langle \Delta T^2 \rangle = \frac{(\alpha_1 + \alpha_2)^2(\alpha_1\beta_2 + \alpha_2\beta_1 + \beta_1\beta_2) + 2\alpha_1\alpha_2(\beta_1 - \beta_2)^2}{(\alpha_1\beta_2 + \alpha_2\beta_1 + \beta_1\beta_2)(\alpha_1\beta_2 + \alpha_2\beta_1)^2}. \tag{5.30}$$

Finally, the SCC is obtained by invoking Eq. (5.13):

$$\boxed{\rho_n = \lambda_2^n\rho_1, \qquad \rho_1 = \frac{\alpha_1\alpha_2(\beta_1 - \beta_2)^2}{(\alpha_1 + \alpha_2)^2(\alpha_1\beta_2 + \alpha_2\beta_1 + \beta_1\beta_2) + 2\alpha_1\alpha_2(\beta_1 - \beta_2)^2}} \tag{5.31}$$

for $n \geq 1$. As expected from the general theory, the SCC is a geometric series. The SCC cannot become negative because ρ_1 is non-negative and $0 < \lambda_2 < 1$. Hence, the SCC decays from ρ_1 exponentially with the lag and with a typical correlation range of $\ln\left(\frac{1}{\lambda_2}\right)$ ISIs (Fig. 5.4E,F).

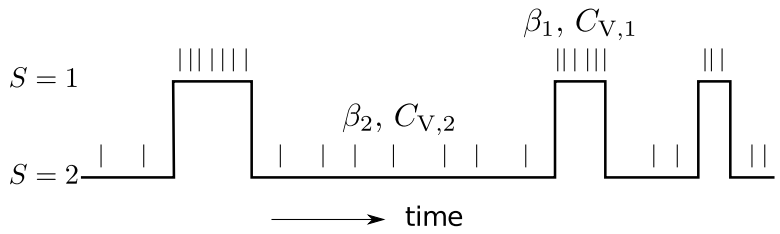

Figure 5.5.: Illustration of the non-Markovian model. The spike train (as indicated by small vertical bars) alternates between two renewal processes with rates α_1 and α_2 depending on the dichotomous Markov process $S(t)$. The firing rate and coefficient of variation of the renewal processes are β_1 and $C_{\mathrm{V},1}$ in state $S = 1$, and β_2 and $C_{\mathrm{V},2}$ in state $S = 2$

Therefore it is sufficient to inspect the behavior of the SCC at lag 1 (Fig. 5.4C,D). For equal firing rates $\beta_1 = \beta_2$ (corresponding to $\mu(t) = \text{const.}$) the serial correlations vanish. This makes sense because the Markovian jump process reduces to a simple Poisson process with rate $\beta_1 = \beta_2$, which is renewal. On the other hand, if one of the firing rates, say β_2, is much smaller than the other rate, the process also becomes renewal (in the limit $\beta_2/\beta_1 \to 0$, $\alpha_{1/2} = \text{const.}$). In fact, in this limit there is no memory of previous ISI because the neuron only fires in state 1, which is consequently also the initial state at the beginning of each ISI irrespective of the ISI history ($\hat{p}_2^{(s)} = 0$). This implies that ρ_1 has a maximum for some finite firing rate β_2 in the range $(-\infty, \beta_1)$. This maximum is indeed observed in simulations and in the theory. The theory, Eq. (5.31), based on the Markovian jump process agrees qualitatively with simulations of the driven LIF model. Furthermore, the exponential decay is well predicted by the Markov theory (Fig. 5.4E). However, deviations appear in cases where the CVs of the single states are considerably smaller than 1 (see Fig. 5.4C,D, top). This is inconsistent with a Markovian jump processes, in which each transition has exponentially distributed waiting times with a CV equal to unity. In particular, it can be expected that the Markov theory fails if $\mu(t)$ is close to the threshold or even suprathreshold. Figure 5.4D,F shows indeed large deviations if the CVs of both states are considerably smaller than one.

5.2.2. Non-Markovian theory

The Markovian approximation of the previous section assumes that the spike train of the LIF model clamped to a particular state, i.e. with a *static* base current $\mu = \mu_1$ or $\mu = \mu_2$, is close to a Poisson process. This means that the single state spike trains are renewal processes with exponential ISI densities. In particular, the single state CVs are assumed to be close to 1 indicating rather irregular spike trains. As shown in Fig. 5.4D,F, this assumption is not met if μ is suprathreshold or slightly below threshold leading to large deviations of the Markovian theory. How can the theory be extended to smaller CVs of the single state, i.e. to spike trains that are more regular than a Poisson process?

One way to achieve this, would be to introduce additional intermediate states into the Markov scheme that have to be passed before the spike count is incremented. For instance, k Poisson steps with rate β_1/k would also yield a total firing rate β_1, but a CV of $1/\sqrt{k}$ (ISI density corresponds to a gamma process of order k in this case). Hence, the irregularity is reduced by a factor $\sqrt{k}$. Although this approach has the advantage that the existing Markovian theory can be readily applied, it is theoretically unpleasing for three

reasons: First, the regularity of the single state is not a free parameter, but is fixed by the topology of the Markov scheme. In particular, the regularity cannot be varied in an easy way: To access how the ISI statistics of the driven system (e.g. the SCC) depends on the single state CVs, one would have to consider a separate topology for each CV and then recompute the ISI statistics of the driven system. Second, it is not obvious how to treat the case in which the CVs of the two states are different. Different numbers of intermediate states could be a solution, but it is not clear how a switching of the dichotomous driving is implemented best, since in this case each state consists of several substates. Third, the complexity of the formulas quickly increases as more and more intermediate states are added (which, however, are necessary for states with a small irregularity).

For these reasons, I pursue an alternative approach that only assumes a sufficiently slow driving. In particular, the LIF model driven by dichotomous noise is regarded as a point process that switches between two renewal processes with given firing rates β_1 and β_2 and coefficients of variation $C_{V,1}$ and $C_{V,2}$. The alternation of the renewal processes is given by the switching rates α_1 and α_2 (Fig. 5.5). This approximation makes sense because for a static base current μ, the purely white noise driven LIF model generates indeed a renewal process. Let $S(t)$ be a dichotomous Markov process (telegraph process) that indicates the state at time t: $S(t) = 1$ if $\mu(t) = \mu_1$ and $S(t) = 2$ if $\mu(t) = \mu_2$. The mean $\bar{\tau}_{1/2}$ and variance $\sigma^2_{1/2}$ of the ISIs in the respective states are thus given by

$$\bar{\tau}_1 = \frac{1}{\beta_1}, \quad \bar{\tau}_2 = \frac{1}{\beta_2}, \quad \sigma_1^2 = \bar{\tau}_1^2 C_{V,1}^2, \quad \sigma_2^2 = \bar{\tau}_2^2 C_{V,2}^2. \tag{5.32}$$

Note that the results do not depend on higher-order ISI moments. The mean residence times in the two states are α_1^{-1} and α_2^{-1}, respectively. Note also that at the transition between two states an ISI can belong to both of them, and its statistics is, in general, different from the ISI statistics of both renewal processes. For a slow driving, however, there are many ISIs in each state distributed according to the respective renewal process. The single overlapping ISI can then be well neglected. Furthermore, note that the process $(N(t), S(t))$ is not Markovian anymore (unless both renewal processes are Poisson processes – the case studied in Sec. 5.2.1). In fact, the probability to spike depends on the time elapsed since the last spike and thus on the history before time t. Therefore, this approach will be called non-Markovian theory, in contrast to the Markovian jump process considered before.

The ISIs within a single state are uncorrelated by assumption. Serial correlations between ISIs only arise due to the temporal correlations in state variable $S(t)$. Although the temporal statistics of $S(t)$ are well known [see, e.g. Gardiner, 1985] (cf. also Eq. (5.21)), the serial statistics of the sequence $\{S_i\}$ (state values immediately after firing) is hard to obtain analytically. However, it is this correlation function with respect to the index i of the ISI sequence $\{T_i\}$ (and not with respect to time t), which is needed for the calculation of the SCC. Here, I use a manipulation which allows us to still use the known temporal statistics of $S(t)$. To this end, I first change the index i in the sequence $\{S_i\}$ to a continuous index x that coincides with i at the end of the i-th ISI. Then, we can consider the state S as a function of the continuous index: S_x also constitutes a realization of a dichotomous Markov process, but with switching rates α_1/β_1 and α_2/β_2, respectively. In fact, the waiting "times" in each state are approximately exponentially distributed with a mean value equal to the mean spike count $\langle n_s \rangle = \beta_s/\alpha_s$ in one epoch of state $s \in \{1, 2\}$ (averaged

over the exponentially distributed durations of epochs in state s).

The expression $\rho_n = (\langle T_i T_{i+n}\rangle - \langle T_i\rangle^2)/\langle \Delta T_i\rangle^2$ for the SCC can be understood as one involving two averages; one with respect to the renewal process for a fixed realization S_x and another one with respect to the ensemble of realizations S_x. For a fixed realization S_x all intervals are only correlated through the dichotomous switching of S_x because of the renewal property of the single states – in particular, $\langle T_i T_{i+n}\rangle = \bar{\tau}_{S_i}\bar{\tau}_{S_{i+n}}$ for $n \geq 1$. The remaining average over S_x yields

$$\langle T\rangle = \sum_{s=1,2} \bar{\tau}_s p_{\mathrm{st}}(s) \tag{5.33}$$

$$\langle T_i T_{i+n}\rangle = \sum_{s,s'=1,2} \bar{\tau}_s \bar{\tau}_{s'} p(s', n; s, 0), \qquad n \geq 1 \tag{5.34}$$

$$\langle T^2\rangle = \sum_{s=1,2} (\sigma_s^2 + \bar{\tau}_s^2) p_{\mathrm{st}}(s). \tag{5.35}$$

Here, $p_{st}(s) = \alpha_{3-s}\beta_s/(\alpha_1\beta_2 + \alpha_2\beta_1)$ are the stationary probabilities of S_x and $p(s, x; s', x')$ is the joint probability distribution of S_x and $S_{x'}$, with $x > x'$ and $s, s' = 1, 2$. The latter is equal to $p(s, x|s', x')p_{\mathrm{st}}(s')$, where the transition probability $p(s, x|s', x')$ is given by [Gardiner, 1985]

$$p(s, x|s', x') = p_{\mathrm{st}}(s) + [\delta_{s,s'} p_{\mathrm{st}}(3-s) - \delta_{s,3-s'} p_{\mathrm{st}}(s)] \exp\left[-\left(\frac{\alpha_1}{\beta_1} + \frac{\alpha_2}{\beta_2}\right)(x - x')\right]. \tag{5.36}$$

As a result, the correlation coefficient for $n \geq 1$ reads [Schwalger et al., 2012]

$$\boxed{\rho_n = \frac{\exp\left[-\left(\hat{\alpha}_1 + \frac{\hat{\alpha}_2}{\gamma}\right) n\right]}{1 + \frac{\gamma\hat{\alpha}_1 + \hat{\alpha}_2}{(1-\gamma)^2\hat{\alpha}_1\hat{\alpha}_2}\left(\gamma\hat{\alpha}_2 C_{V,1}^2 + \hat{\alpha}_1 C_{V,2}^2\right)}} \tag{5.37}$$

with $\gamma = \beta_2/\beta_1$, $\hat{\alpha}_1 = \alpha_1/\beta_1$, $\hat{\alpha}_2 = \alpha_2/\beta_1$. As in the Markovian theory, the SCC decays exponentially with the lag, but with a different correlation lag.

Figure 5.4C–F reveals indeed an excellent agreement of the non-Markovian theory (dashed line) with the LIF simulations. Deviations are only observed at small firing rates: for $\beta_2 \lesssim \alpha_2$ the Markov theory yields a better approximation (Fig. 5.4C,D). The failure at small firing rates can be explained as follows: there is on average less than one interval in the epochs of state 2, and hence the renewal process in state 2 becomes meaningless. Moreover, the duration of epochs of S_i in state 2 are far from being exponentially distributed (for a small number of ISIs this distribution is rather discrete), so S_x cannot be regarded as a dichotomous Markov process. On the other hand, the Markovian theory, which does not require a large number of ISIs per epoch, is justified because of the large CV at low firing rates.

Originally, the expression (5.37) has been derived to explain correlations in a different system [Schwalger et al., 2012]: in a collaborative work with Dr. Jordi Tiana-Alsina, Prof. Dr. M. C. Torrent and Prof. Dr. Jordi Garcia-Ojalvo (Universitat Politècnica de Catalunya, Barcelona), we studied power-dropouts of a semi-conductor laser with optical feedback. The laser intensity exhibits a complex dynamics that can be interpreted as excitable spikes. It has been found that intervals between spontaneous dropouts are cor-

related due to the alternation between two states with different dropout rates and CVs. Using the experimentally measured values of the rates and CVs in the different states, Eq. (5.37) well predicted the spontaneous serial correlations. Furthermore, the formula could be used to predict the correlations in the dropout sequence in the case of an external dichotomous driving.

5.3. Discrete models with self-inhibitory feedback

As a second example, I consider the serial correlation coefficient (SCC) of an excitable neuron with self-inhibitory feedback resembling a spike-triggered adaptation mechanism. A number of simulation studies have demonstrated that such neurons exhibit negative serial correlations. Here, an analytically tractable model with self-inhibitory feedback is presented, for which a formula for the SCC can be derived. This model includes a slow "adaptation" variable that increases upon spiking and decays between firing events. Furthermore, it acts in an inhibitory manner: larger values are associated with a smaller firing probability.

The adaptation variable could represent either an inhibitory current that increases upon spikes [Liu and Wang, 2001, Wang, 1998, Benda and Herz, 2003] or a dynamic threshold [Chacron et al., 2001]. In any case, the adaptation variable can be interpreted as the distance of the resting potential from the excitation threshold. Thus, the "escape" rate depends on the adaptation state. Both features, a state-dependent firing rate and the spike-triggered dynamics of the adaptation variable, can be realized in the framework of a Markovian jump process[4]. Here, I consider the simple case of only *four* discrete adaptation states $s_1, \ldots, s_4$, representing e.g. discrete threshold values or discrete states of an adaptation current. The internal transitions realize the decay of the adaptation variable (cf. Sec. 1.3.2) in the order $s_4 \xrightarrow{3\alpha} s_3 \xrightarrow{2\alpha} s_2 \xrightarrow{\alpha} s_1$ (Fig. 5.6A,D). Note that after each spike the internal state has changed.

Specifically, two models are investigated: In the first model, each spike increases the adaptation variable by two states (Fig. 5.6A). This allows for two possible firing paths, $s_1 \xrightarrow{\beta_1} s_3$ and $s_2 \xrightarrow{\beta_2} s_4$, with the associated firing rates $\beta_1 > \beta_2$. In state s_3 and s_4 firing is not possible. In the second model, the adaptation variable increases by one state upon firing. Spiking is now possible in the states s_1, s_2 and s_3 with rates $\beta_1 > \beta_2 > \beta_3$, respectively (Fig. 5.6D).

[4]Note that the considered Markov model is designed for analyzing a time-homogeneous setting. In particular, it cannot be applied to the phenomenon of adaptation, which refers to the response to a time-dependent stimulus. Nevertheless, I will stick to the notion "adaptation variable" because the present model is intended to approximate the stationary properties of certain adapting neuron models.

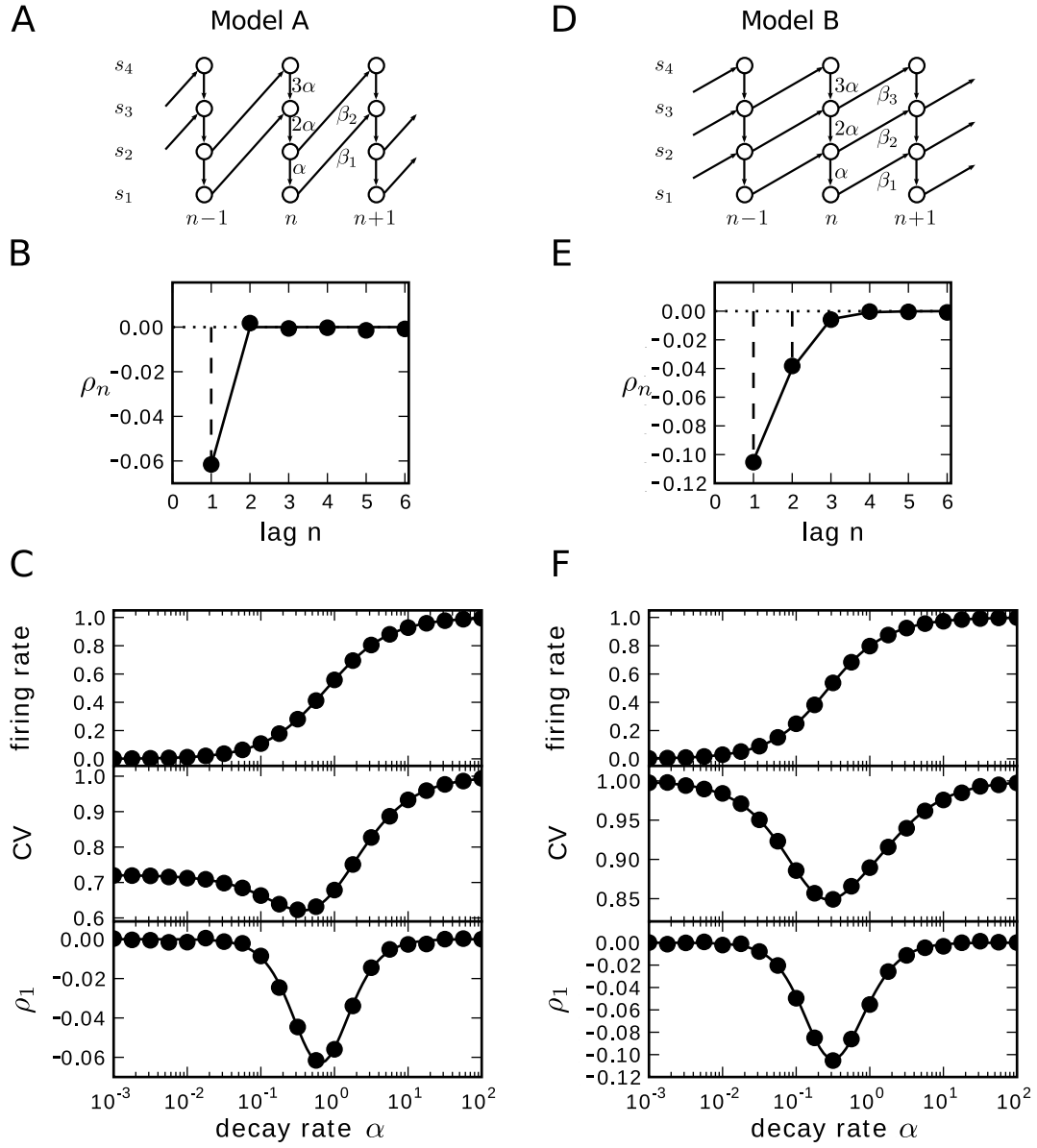

Figure 5.6.: ISI statistics of neuron models with four adaptation states. A Kinetic scheme of neuron model A: The adaptation variable decays with rate α in between spiking events. Spiking is possible in the lower two states with rates $\beta_i = e^{-\gamma(i-1)}$, $i = 1, 2$ and $\gamma = 0.3$. Upon spiking the adaptation variable jumps by two states. **B** Serial correlation coefficient as a function of the lag for $\alpha = 0.56$: simulation (circles) and theory (solid line). **C** Firing rate, coefficient of variation and SCC at lag 1 as a function of the decay rate α of the adaptation variable: simulation (circles) and theory (solid line). **D–F** Neuron model B: Like model A but adaptation variable jumps by one state upon spiking. Spiking is possible in the lower three states with rates $\beta_i = e^{-\gamma(i-1)}$, $i = 1, 2, 3$. In **E** I chose $\alpha = 0.32$.

5.3.1. Neuron model A

The Markov scheme in Fig. 5.6A corresponds to the following matrices

$$\mathrm{A} = \begin{pmatrix} -\beta_1 & \alpha & 0 & 0 \\ 0 & -(\beta_2+\alpha) & 2\alpha & 0 \\ 0 & 0 & -2\alpha & 3\alpha \\ 0 & 0 & 0 & -3\alpha \end{pmatrix}, \quad \mathrm{B} = \begin{pmatrix} 0 & 0 & 0 & 0 \\ 0 & 0 & 0 & 0 \\ \beta_1 & 0 & 0 & 0 \\ 0 & \beta_2 & 0 & 0 \end{pmatrix}, \quad \mathrm{C} = \begin{pmatrix} \frac{\alpha}{\beta_2+\alpha} & \frac{\beta_2\alpha}{\beta_1(\beta_2+\alpha)} & 0 & 0 \\ \frac{\beta_1}{\beta_2+\alpha} & \frac{\beta_2}{\beta_2+\alpha} & 0 & 0 \\ \frac{\beta_1}{2\alpha} & \frac{\beta_2}{2\alpha} & 0 & 0 \\ 0 & \frac{\beta_2}{3\alpha} & 0 & 0 \end{pmatrix}. \tag{5.38}$$

The eigenvalues of C are $\lambda_1 = 1$ and $\lambda_2 = \lambda_3 = \lambda_4 = 0$. The corresponding eigenvectors are

$$\mathbf{v}_1 = \mathbf{p}^{(s)} = \frac{1}{6\alpha^2 + 9\beta_1\alpha + 5\beta_1\beta_2} \left(6\alpha^2, 6\beta_1\alpha, 3\beta_1(\beta_2+\alpha), 2\beta_1\beta_2\right)^T \tag{5.39}$$

and

$$\mathbf{v}_2 = (0,0,1,0)^T, \qquad \mathbf{v}_3 = (0,0,0,1)^T. \tag{5.40}$$

Using Eq. (5.7), the limiting distribution of states immediately after firing is given by

$$\hat{\mathbf{p}} = \left(0, 0, \frac{\alpha}{\beta_2+\alpha}, \frac{\beta_2}{\beta_2+\alpha}\right)^T. \tag{5.41}$$

Clearly, this distribution is non-zero only in the states s_3 and s_4. Equation (5.16) yields the vector of mean residence times in the conditional ensemble $\hat{\boldsymbol{\tau}}$. Summing over all states yields the mean interspike interval (cf. Eq. (5.12))

$$\langle T_k \rangle = \hat{\tau} = \frac{6\alpha^2 + 9\beta_1\alpha + 5\beta_1\beta_2}{6\beta_1(\beta_2+\alpha)\alpha}. \tag{5.42}$$

For the initial condition of the difference equation (5.14) I find from Eq. (5.15) and (5.39)

$$\boldsymbol{\tau}^{(0)} = \frac{1}{\hat{\tau}} \left(\frac{6\alpha^2 + (9\beta_1 + 6\beta_2)\alpha + 5\beta_1\beta_2}{6\beta_1^2(\beta_2+\alpha)^2}, \frac{9\alpha + 5\beta_2}{6\alpha(\beta_2+\alpha)^2}, \frac{3\alpha+5\beta_2}{12\alpha^2(\beta_2+\alpha)}, \frac{\beta_2}{9\alpha^2(\beta_2+\alpha)} \right)^T. \tag{5.43}$$

The matrix power C^n is given through a similarity transformation as

$$\mathrm{C}^n = \mathrm{P}\mathrm{J}^n\mathrm{P}^{-1} \quad \text{where} \quad \mathrm{P} = (\mathbf{v}_1, \mathbf{v}_2, \mathbf{v}_3, \mathbf{v}_4). \tag{5.44}$$

The generalized eigenvector $\mathbf{v}_4$ is the solution of $\mathrm{C}\mathbf{v}_4 - \lambda_3\mathrm{I} = \mathbf{v}_3$ and reads

$$\mathbf{v}_4 = \left(-\frac{3\alpha}{\beta_1}, \frac{3\alpha}{\beta_2}, 0, 0\right)^T. \tag{5.45}$$

The matrix $\mathrm{J} = \mathrm{P}^{-1}\mathrm{C}\mathrm{P}$ is the Jordan normal form of C, the n-th power of which is given by

$$\mathrm{J}^n = \begin{pmatrix} 1 & 0 & 0 & 0 \\ 0 & 0 & 0 & 0 \\ 0 & 0 & 0 & \delta_{n,1} \\ 0 & 0 & 0 & 0 \end{pmatrix}. \tag{5.46}$$

Now we have all the ingredients for calculating the SCC using Eq. (5.12),(5.43) and (5.44). The covariance $\mathrm{cov}(T_k, T_{k+n}) = \langle T_k T_{k+n} \rangle - \langle T_k \rangle^2$ is

$$\mathrm{cov}(T_k, T_{k+n}) = -\frac{\beta_2}{3\beta_1(\beta_2+\alpha)^2}\delta_{n,1} \tag{5.47}$$

and the variance is

$$\mathrm{var}(T_k) = \frac{36\alpha^4 + 72\beta_2\alpha^3 + 45\beta_1^2\alpha^2 + 26\beta_1^2\beta_2\alpha + 13\beta_1^2\beta_2^2}{36\beta_1^2\alpha^2(\beta_2+\alpha)^2}. \tag{5.48}$$

The ratio of the last two expressions yields

$$\rho_n = -\delta_{n,1}\frac{12\beta_1\beta_2\alpha^2}{36\alpha^4 + 72\beta_2\alpha^3 + 45\beta_1^2\alpha^2 + 26\beta_1^2\beta_2\alpha + 13\beta_1^2\beta_2^2}. \tag{5.49}$$

From the theoretical result it becomes clear that in the adaptation model A, adjacent interspike intervals are anti-correlated, whereas the correlations at higher lags vanish (Fig. 5.6B). Furthermore, the correlation coefficient depends only on the ratio of the rates such that we can set one of them to one without loss of generality; in the following $\beta_1 = 1$. In accordance with the inhibitory character of the feedback, I set $\beta_2 = \beta_1 e^{-\gamma}$ with $\gamma > 0$ (the firing rate is reduced for higher adaptation states), optimize with respect to γ and α, and find that $\rho_1 \geq -0.068$. Hence, the adaptation model A reproduces the expected negative interspike interval correlations, however, the absolute correlation strength is rather small[5].

Why do the correlations vanish at higher lags $n \geq 2$? From Fig. 5.6A it becomes clear, that the residence time in $n-1$ cannot influence future residence times, as e.g. that in $n+1$ because all trajectories must pass through the state (s_2, n). This erases any memory of the time spent in $n-1$.

Figure 5.6C shows a comparison of simulations and analytical expressions for the firing rate, the coefficient of variation and the SCC ρ_1 as a function of α for some choice of β_1 and β_2. While the firing rate just increases with the decay rate, the CV and ρ_1 both attain a minimum around $\alpha \approx \beta_1/2$; both minima are largely due to a non-monotonic dependence of the variance on α (mean and covariance increase monotonically with α). It is plausible that for both $\alpha \to 0$ and $\alpha \to \infty$, the spike train becomes a renewal process. In fact, for small rate α, transitions to the next layer always go through β_2; at large rate, the system goes quickly to s_1 and the next spike occurs via the β_1 path. Only for intermediate rates, both paths between layers are used and thus correlations between the residence times in one layer (i.e. between ISIs) become possible.

[5] A closer inspection reveals that the global optimum is at negative γ yielding a slightly increased minimal correlation of $\rho_1 \approx -0.074$. Because $\gamma < 0$ would not correspond to the inhibitory feedback, I do not further consider this parameter choice.

5.3.2. Neuron model B

This model is shown in Fig. 5.6D and corresponds to the matrices:

$$\mathrm{A} = \begin{pmatrix} -\beta_1 & \alpha & 0 & 0 \\ 0 & -(\beta_2+\alpha) & 2\alpha & 0 \\ 0 & 0 & -(\beta_3+2\alpha) & 3\alpha \\ 0 & 0 & 0 & -3\alpha \end{pmatrix}, \qquad \mathrm{B} = \begin{pmatrix} 0 & 0 & 0 & 0 \\ \beta_1 & 0 & 0 & 0 \\ 0 & \beta_2 & 0 & 0 \\ 0 & 0 & \beta_3 & 0 \end{pmatrix}. \tag{5.50}$$

The calculation for this case is analogous to the previous one; the rather tedious expressions of intermediate computational steps are omitted and only the main results are presented: In contrast to model A, the matrix $\mathrm{C} = -\mathrm{A}^{-1}\mathrm{B}$ has one non-vanishing eigenvalue λ_2 smaller than $\lambda_1 = 1$:

$$\lambda_2 = \frac{\beta_3\alpha}{(\alpha+\beta_2)(2\alpha+\beta_3)}. \tag{5.51}$$

The mean interspike interval reads

$$\langle T_k \rangle = \hat{\tau} = \frac{6\alpha^3 + 6\alpha^2\beta_1 + 3\alpha\beta_1\beta_2 + \beta_1\beta_2\beta_3}{6\alpha^3\beta_1 + 6\alpha^2\beta_1\beta_2 + 3\alpha\beta_1\beta_2\beta_3}. \tag{5.52}$$

Furthermore, the serial correlation coefficient is the ratio $\rho_n = \mathrm{cov}(T_k, T_{k+n})/\mathrm{var}(T_k)$ given by

$$\begin{aligned} \mathrm{var}(T_k) = \frac{\lambda_2}{9\alpha^3\beta_1^2\beta_3(2\alpha(\alpha+\beta_2)+\beta_2\beta_3)^2} \big[& 72\alpha^8 + 36\alpha^7(6\beta_2+\beta_3) \\ & + 36\alpha^6\left(2\beta_1^2 + \beta_2(4\beta_2+5\beta_3)\right) + 36\alpha^5\left(\beta_1\beta_2\beta_3 + \beta_1^2(3\beta_2+\beta_3) + \beta_2\beta_3(4\beta_2+\beta_3)\right) \\ & + 2\alpha^4\beta_2\left(12\beta_1\beta_3^2 + 18\beta_2\beta_3^2 + \beta 1^2(27\beta_2+46\beta_3)\right) + \alpha^3\beta_1^2\beta_2\left(18\beta_2^2 + 37\beta_2\beta_3 + 28\beta_3^2\right) \\ & + \alpha^2\beta_1^2\beta_2^2\beta_3(17\beta_2+10\beta_3) + \alpha\beta_1^2\beta_2^2\beta_3^2(6\beta_2+\beta_3) + \beta_1^2\beta_2^3\beta_3^3 \big], \end{aligned} \tag{5.53}$$

and for $n \geq 1$

$$\mathrm{cov}(T_k, T_{k+n}) = \frac{2\lambda_2}{9\alpha^2\beta_1^2\beta_3^2(2\alpha(\alpha+\beta_2)+\beta_2\beta_3)^2}\left(\nu_1\delta_{n1} - \nu_2\lambda_2^n\right), \tag{5.54}$$

where

$$\nu_1 = 3\alpha\beta_1\beta_2\beta_3(\alpha+\beta_2)(2\alpha+\beta_3)(2\alpha(\alpha+\beta_2)+\beta_2\beta_3) \tag{5.55}$$

$$\begin{aligned} \nu_2 = {} & \beta_2\left(12\alpha^2(\alpha+\beta_2) + 3\alpha(4\alpha+\beta_1+4\beta_2)\beta_3 + (3\alpha+2\beta_1+3\beta_2)\beta_3^2\right) \\ & \times \left(\alpha^3(5\beta_1-3\beta_3) + \alpha^2\beta_1(7\beta_2-2\beta_3) + \beta_1\beta_2^2\beta_3 + 2\alpha\beta_1\beta_2(\beta_2+\beta_3)\right). \end{aligned} \tag{5.56}$$

From the theory as well as from Fig. 5.6E it becomes evident that the SCC of model B is nonzero for any finite lag because not all paths go through the same internal state as in model A. Parametrizing the interlayer transition rates as before $\beta_i = e^{-\gamma(i-1)}$, I find that model B can show a modest correlation at lag one of about $\rho_1 \approx -0.12$ that is, however, twice as strong as the strongest negative correlation of model A.

The dependence of firing rate, CV, and correlation coefficient ρ_1 (Fig. 5.6F) is qualitatively similar to the one observed for model A (Fig. 5.6C). CV and ρ_1 attain a minimum at

a rate smaller than $\beta_1 = 1$. Remarkably, the minimum of the CV is still close to a Poisson process ($C_{V,min} \approx 0.85$ compared to $C_{V,min} \approx 0.6$ for model A), whereas (as discussed above) the minimum in the correlation coefficient is deeper than for model A. Model B seems to be a a richer and more realistic representation of an excitable neuron with adaptation. I have also found that by increasing the number of internal states, it is possible to obtain stronger negative correlations than observed here (data not shown).

5.4. Summary

In this chapter, I have developed a Markovian framework for interspike interval correlations, generated by non-Markovian complex systems. I derived the general structure of the serial correlation coefficient and the first two moments of the interspike intervals. Within this approximation, the correlation coefficient decays geometrically with increasing lag; in particular, it is given by a superposition of different exponential functions (possibly with complex arguments). The developed framework is sufficiently general to describe approximately the effect of external drivings, of slow internal variables, and of intrinsic feedback of spike generation on the ISI statistics of various systems.

The theory has been applied to two models of excitable neurons that generate non-renewal spike trains, either because of an external colored noise driving or a self-inhibitory feedback mechanism. In the first case, a leaky integrate-and-fire model driven by Gaussian white noise and dichotomous colored noise has been considered. Such external driving can be regarded as a case study of the effect of colored noise on an excitable neuron. Furthermore, this model has some relevance for neurons participating in a neural network that exhibits slow oscillations ("Up" and "Down" states). For sufficiently slow dichotomous driving the neuron essentially switches between two renewal processes with different rates and CVs. For not too small CVs, the LIF model could be approximated by a Markovian jump process, for which the SCC could be calculated by the general method. The Markovian theory correctly predicted the non-monotonic behavior of the SCC with respect to the ratio of the firing rates. A comparison with simulations of the LIF model also revealed the limitations of the Markovian theory: For CVs considerably smaller than unity, i.e. for renewal processes that are more regular than a Poisson process, the SCC measured from LIF data showed significant deviations from the Markovian theory. For this reason we developed an alternative non-Markovian theory that accounts for the CVs of the two renewal processes as well. For sufficiently slow driving, the non-Markovian theory showed an excellent agreement with the LIF model.

In the second case, we have applied the Markovian theory to models of an excitable neuron with intrinsic feedback of spikes that can mimic an integrate-and-fire neuron with dynamical threshold or with an adaptation current. For these systems, we found a negative correlation of adjacent intervals as it is also observed in experiments on certain neurons [Ratnam and Nelson, 2000, Engel et al., 2008]. However, in these models, we constraint the system to four internal states and achieved only rather modest correlations of $\rho_1 \approx -0.1$. We expect that with the addition of more internal states, stronger negative correlations are feasible. Another interesting task for future research is to compare the results of the presented scheme with simulations of the leaky integrate-and-fire model with dynamical threshold or with an adaptation current.

Chapter 6.

Conclusions

In the last decades a number of studies have provided experimental evidence that the spike trains of many types of neurons are not well described by a renewal point process, i.e. by a process with independent interspike intervals (ISIs). In these studies, significant serial correlations have been observed in the sequence of ISIs. Moreover, the spike count variability often differed strikingly from that of the corresponding renewal spike train that is obtained by shuffling the ISIs. Two important mechanisms that may cause these non-renewal spike trains are temporal correlations in the neuronal input and self-inhibitory feedback realized either by spike-triggered adaptation currents or by dynamic firing thresholds. In both cases, there is memory in the system leading to correlations between ISIs and hence non-renewal spike trains. Here, I addressed the following questions: How do these mechanisms shape the stationary spiking statistics and do they leave a characteristic signature? And vice versa, what does the spiking statistics of a real neuron tells us about the properties of the underlying sources of noise?

To investigate these questions, I studied the ISI statistics of stochastic integrate-and-fire models that are either driven by external *colored noise* or feature a deterministic or stochastic *adaptation current*. These reduced models are simple enough to be analytically tractable but are still capable to capture important neuronal features like sub- and suprathreshold stochastic spike generation, spike-frequency adaptation, channel noise as well as temporal correlations of naturalistic stimuli. By deriving explicit formulas for both the first-order ISI statistics and higher-order ISI statistics, most importantly, the serial correlation coefficient (SCC), it has been possible to analyze the individual effects of colored noise and adaptation currents.

Comparing different situations, I found large differences in the spiking statistics. The most impressive distinction could be made for the suprathreshold regime, especially for the cases of a neuron with a deterministic adaptation current in the presence of fast fluctuations (Chap. 3) versus a neuron with a stochastic adaptation current (Chap. 4). The former case exhibits short-range, *negative* serial correlations and an inverse Gaussian ISI density. On the contrary, in the latter case, intrinsic noise associated to a slow internal adaptation mechanism turned out to be a source of colored noise that remained unnoticed so far. As expected for colored noise, this adaptation noise causes long-range *positive* serial correlations and an ISI density with a more pronounced peak than a corresponding inverse Gaussian density (Chap. 2). Remarkably, in a collaborative work it has been possible to utilize these insights to draw conclusions about the dominating source of noise in a particular sensory neuron solely on the basis of the ISI statistics (Chap. 4). In particular, it has been found that channel noise associated with the adaptation mechanism likely contributes to the response variability of auditory receptor neurons of locusts.

Furthermore, extending a renewal model by colored noise or an adaptation current gives rise to a large variety of ISI statistics. In a supra-threshold neuron with adaptation, the neuron can operate in two different dynamical regimes: depending on the strength and time scale of the adaptation current, the serial correlations may monotonically decay or alternate with the lag (Sec. 3.2.3), the linear response function may be a rather smooth high-pass filter or may show sharp resonance peaks (Sec. 3.4.2) and the spike train power spectrum may be unimodal or may exhibit a multimodal structure (Sec. 3.4.3). In addition to that, a complex temporal structure of the stimulus can lead to a rich serial correlation structure, including oscillating patterns that resemble serial correlations of paddlefish electroreceptors (Sec. 2.4). In the sub-threshold, excitable regime, an optimal amplitude of the colored noise can be achieved that maximizes the SCC (Sec. 5.2). Furthermore, correlations induced by self-inhibitory feedback also show short-range negative serial correlations, although they are generally significantly smaller than in the suprathreshold regime (Sec. 5.3).

Perhaps most importantly, this thesis presents a number of novel analytical techniques to calculate the ISI statistics of non-renewal neuron models. For renewal models, as e.g. white-noise driven integrate-and-fire models, the analysis usually amounts to the solution of a one-dimensional first-passage-time problem, which is theoretically well established and for which standard methods are available [see e.g. Gardiner, 1985, van Kampen, 1992]. It seems that there is no such single concept for non-renewal models. Instead, a diversity of different approaches and approximation techniques had to be used that were tailored to the specific problem. For instance, expressions for the SCC have been obtained by directly calculating the n-th-order variances (Chap. 2), by constructing a stochastic map of the hidden variable (Sec. 3.2), by adiabatic approximation techniques (Chap. 4), by using the count statistics (Chap. 5) and by representing the ISI sequence as a continuous process (Sec. 5.2.2).

From a theoretical point of view, all non-renewal models in this thesis are governed by a hidden variable that forms a Markov chain when sampled at the moments of firing, so-called Markov-renewal processes (Sec. 1.2.6). In principle, the ISI statistics is completely given by the knowledge of the transition probability of the hidden variable from spike to spike (transition probabilities of the Markov chain), the distribution of the hidden variable upon firing (stationary distribution of the Markov chain) and the statistics of the function that generates the ISIs from the Markov chain (conditional ISI statistics). Especially the *upon firing distribution* of the hidden variable is an important concept in the theory of non-renewal neuron models. Preparing the system initially according to this distribution corresponds to the conditional ensemble (realizations that exhibit a spike at time $t = 0$), which is advantageous for a theoretical analysis of the ISI statistics. Therefore, it is not surprising that the analytical calculation of the upon firing distribution has been a recurrent theme in this thesis. In particular, it has served as the initial distribution for the Fokker-Planck equation in Chap. 2 and the master equation in Chap. 5. However, the analytical calculation of the upon firing distribution is often an intricate theoretical problem. In Sec. 3.3.2 I have demonstrated for the case of an adapting neuron how this distribution can be obtained by using the stationary Fokker-Planck equation.

In the supra-threshold regime, weak-noise approximation techniques have proven particularly fruitful. These powerful methods, which have been advanced in Chap. 2 and 3, involve the analysis of the deterministic dynamics of a system and a perturbative treat-

ment of a small amount of additional noise. This allowed us to study the whole range of correlation times, adaptation times and feedback strength on the serial correlation coefficients. The dependence of the SCC on the noise intensity is weak and merely leads to an overall reduction of correlations.

In this thesis, I have carried out detailed analyses of prominent non-renewal neuron models with respect to the higher-order statistics of stationary spike trains. The theoretical insights could be already applied as an indirect method to infer the time scales of the underlying noise sources that cause spike response variability in neurons. However, there are still open problems. For instance, the consequences of adaptation and colored noise on neural coding have not been dealt with in this thesis. These functional aspects are an interesting topic in itself and have been addressed by several studies [for a review see Avila-Akerberg and Chacron, 2011]. However, analytical results in this direction are sparse. Here, the solvable models of this thesis offer a reassessment of the functional implications in the whole parameter range. Furthermore, in the brain neurons are connected in a large network that can show a variety of spatio-temporal activity patterns. Thus, an obvious question is how adaptation currents or colored noise alters the dynamics of neural networks. The role of adaptation and negative serial correlations for the dynamics of neural populations and their information processing capabilities has been investigated only by a few studies [Fuhrmann et al., 2002, Avila-Akerberg and Chacron, 2009, Farkhooi et al., 2011]. It is interesting whether the ideas put forward in this thesis, in particular the limit-cycle representation of adapting neurons in the suprathreshold regime, could yield further insights into the dynamics of coupled neurons with adaptation. For instance, the population study of Avila-Akerberg and Chacron [2009] has assumed a network of particularly simple neurons for which only adjacent interspike intervals are correlated [cf. Lindner et al., 2005a]. How do models with a more complex correlation structure such as found in chapter 3 for the two different regimes (purely negative vs. oscillating correlations) affect the global network dynamics? The solutions to these problems are worth the effort for future studies.

Appendix A.

The perfect integrate-and-fire model driven by colored noise

A.1. Higher-order perturbation theory for the ISI moment generating function

In the following, the derivation of the moment generating function $\bar{P}_n(s)$ and the cumulants of the nth-order intervals $S_n = T_i + \cdots + T_{i+n-1}$ is presented. To this end, the moment generating function is represented as a perturbation series

$$\bar{P}_n(s) = \sum_{m=1}^{\infty} \epsilon^m \bar{P}_n^{(m)}(s), \tag{A.1}$$

where ϵ determines the noise strength and plays the role of a small perturbation parameter. In the perturbation series, Eq. (A.1), the coefficients $\bar{P}_n^{(m)}(s)$ have been already derived for $m = 0, 1, 2$ in the main text, Sec. 2.1.2. Specifically, it was found that $\bar{P}_n^{(0)} = e^{-sn}$, $\bar{P}_n^{(1)} = 0$ and $\bar{P}_n^{(2)} = s^2 e^{-sn} \int_0^n \mathrm{d}\tau_2 \int_0^{\tau_2} \mathrm{d}\tau_1\, C(\tau_1)$. Here, I want to derive the next non-vanishing correction to the moment generating function, which is required to compute the skewness of the ISI density as well as the first noise correction of the coefficient of variation and the serial correlation coefficient. As shown in Sec. 2.1.2, the higher-order terms can be obtained iteratively from

$$\bar{P}_n^{(m)}(s) = -ise^{-sn} \int_0^n \mathrm{d}\tau_m\, \mathbf{b}^{\mathrm{T}} \nabla_{\mathbf{k}} \psi^{(m-1)}(\tau_m, \mathbf{c})\Big|_{\mathbf{c}=0}, \tag{A.2}$$

where

$$\psi^{(1)}(\tau, \mathbf{c}) = i\theta(\tau) s \int_0^{\tau} \mathrm{d}\tau_1\, \mathbf{b}^{\mathrm{T}} \sigma e^{-\tau_1 \mathrm{A}^{\mathrm{T}}} \mathbf{c} \tag{A.3}$$

and

$$\psi^{(m)}(\tau, \mathbf{c}) = \int_{-\infty}^{\tau} \mathrm{d}\tau'\, i\mathbf{b}^{\mathrm{T}} \left[\partial_x \nabla_{\mathbf{k}} \psi^{(m-1)} - \sigma e^{-\tau' \mathrm{A}^{\mathrm{T}}} \mathbf{c} \partial_x \psi^{(m-1)} - s \left(\nabla_{\mathbf{k}} \psi^{(m-1)} - \sigma e^{-\tau' \mathrm{A}^{\mathrm{T}}} \mathbf{c} \psi^{(m-1)} \right) \right] \tag{A.4}$$

for $m \geq 2$.

Thus, in order to calculate higher orders, the derivatives in Eq. (A.4) must be evaluated. This involves the derivative of $\psi^{(m-1)}(\tau, \mathbf{c})$ with respect to x at fixed $\mathbf{k}$ and with respect to $\mathbf{k}$ at fixed x. It is not necessary, however, to compute integrals like in Eq. (A.3) and then re-express $\psi^{(m-1)}$ as a function of x and $\mathbf{k}$. It is instead convenient to apply the chain rule.

Accordingly, the derivatives of a scalar function $f(\tau, \mathbf{c})$ read

$$(\nabla_{\mathbf{k}} f)^{\mathrm{T}} = [\partial_\tau f \nabla_{\mathbf{k}} \tau + (\nabla_{\mathbf{k}} \circ \mathbf{c}) \nabla_{\mathbf{c}} f]^{\mathrm{T}} = (\nabla_{\mathbf{c}} f)^{\mathrm{T}} e^{\tau \mathrm{A}^{\mathrm{T}}} \tag{A.5}$$

and

$$\partial_x f = \partial_\tau f + (\nabla_{\mathbf{c}} f)^{\mathrm{T}} A^{\mathrm{T}} \mathbf{c}. \tag{A.6}$$

In the former equation, we used $\nabla_{\mathbf{k}} \tau = 0$ and $\nabla_{\mathbf{k}} \circ \mathbf{c} = \left(e^{\tau \mathrm{A}^{\mathrm{T}}}\right)^{\mathrm{T}} = e^{\tau A}$ ($\mathbf{a} \circ \mathbf{b}$ denotes the dyadic product, i.e. $(\mathbf{a} \circ \mathbf{b})_{ij} = a_i b_j$). In Eq. (A.6), the relation $\partial_x \mathbf{c} = \partial_x e^{x \mathrm{A}^{\mathrm{T}}} \mathbf{k} = A^{\mathrm{T}} \mathbf{c}$ was used. Using Eq. (A.5), the gradient of $\psi^{(1)}$ with respect to $\mathbf{k}$ takes the form

$$(\nabla_{\mathbf{k}} \psi^{(1)})^{\mathrm{T}} = i\theta(\tau) s \int_0^\tau \mathrm{d}\tau_1 \, \mathbf{b}^{\mathrm{T}} \sigma e^{\tau_1 \mathrm{A}^{\mathrm{T}}}. \tag{A.7}$$

Similarly, one finds

$$\partial_x \psi^{(1)} = i\theta(\tau) s \left(\mathbf{b}^{\mathrm{T}} \sigma e^{-\tau \mathrm{A}^{\mathrm{T}}} \mathbf{c} + \int_0^\tau \mathrm{d}\tau_1 \, \mathbf{b}^{\mathrm{T}} \sigma \underbrace{e^{-\tau_1 \mathrm{A}^{\mathrm{T}}} A^{\mathrm{T}}}_{-\frac{d}{d\tau_1} e^{-\tau_1 \mathrm{A}^{\mathrm{T}}}} \mathbf{c} \right) \tag{A.8}$$

$$= i\theta(\tau) s \mathbf{b}^{\mathrm{T}} \sigma \mathbf{c}. \tag{A.9}$$

Differentiating the last expression with respect to $\mathbf{k}$ by means of Eq. (A.5) yields the mixed derivative

$$(\nabla_{\mathbf{k}} \partial_x \psi^{(1)})^{\mathrm{T}} = i\theta(t) s \mathbf{b}^{\mathrm{T}} \sigma e^{\tau \mathrm{A}^{\mathrm{T}}}. \tag{A.10}$$

Substituting the derivatives into Eq. (A.4) results in the second-order perturbation term

$$\psi^{(2)} = -\theta(\tau) s \int_0^\tau \mathrm{d}\tau_2 \left\{ \mathbf{b}^{\mathrm{T}} \sigma e^{\tau_2 \mathrm{A}^{\mathrm{T}}} \mathbf{b} - \left(\mathbf{b}^{\mathrm{T}} \sigma e^{-\tau_2 \mathrm{A}^{\mathrm{T}}} \mathbf{c} \right) \left(\mathbf{b}^{\mathrm{T}} \sigma \mathbf{c} \right) \right.$$
$$\left. - s \left[\int_0^{\tau_2} \mathrm{d}\tau_1 \, \mathbf{b}^{\mathrm{T}} \sigma e^{\tau_1 \mathrm{A}^{\mathrm{T}}} \mathbf{b} - \left(\mathbf{b}^{\mathrm{T}} \sigma e^{-\tau_2 \mathrm{A}^{\mathrm{T}}} \mathbf{c} \right) \int_0^{\tau_2} \mathrm{d}\tau_1 \, \mathbf{b}^{\mathrm{T}} \sigma e^{-\tau_1 \mathrm{A}^{\mathrm{T}}} \mathbf{c} \right] \right\}. \tag{A.11}$$

This is the first correction to $\psi^{(0)}$ that does not vanish upon setting $\mathbf{c} = 0$.

The calculation of $\psi^{(3)}$ and $\psi^{(4)}$ are rather lengthy. At least not all terms involved in the fourth-order correction must be computed, but only those terms that do not vanish upon setting $\mathbf{c} = 0$. The complete computation of the third order, however, cannot be avoided. To this end, $\psi^{(2)}$ must be differentiated with respect to $\mathbf{k}$ and x. The former derivative reads

$$(\nabla_{\mathbf{k}} \psi^{(2)})^{\mathrm{T}} = -\theta(\tau) s \int_0^\tau \mathrm{d}\tau_2 \left\{ - \left(\mathbf{b}^{\mathrm{T}} \sigma \mathbf{c} \right) \mathbf{b}^{\mathrm{T}} \sigma e^{(\tau - \tau_2) \mathrm{A}^{\mathrm{T}}} - \left(\mathbf{b}^{\mathrm{T}} \sigma e^{-\tau_2 \mathrm{A}^{\mathrm{T}}} \mathbf{c} \right) \mathbf{b}^{\mathrm{T}} \sigma e^{\tau \mathrm{A}^{\mathrm{T}}} \right.$$
$$\left. + s \left(\mathbf{b}^{\mathrm{T}} \sigma e^{-\tau_2 \mathrm{A}^{\mathrm{T}}} \mathbf{c} \right) \int_0^{\tau_2} \mathrm{d}\tau_1 \, \mathbf{b}^{\mathrm{T}} \sigma e^{(\tau - \tau_1) \mathrm{A}^{\mathrm{T}}} + s \left(\int_0^{\tau_2} \mathrm{d}\tau_1 \, \mathbf{b}^{\mathrm{T}} \sigma e^{-\tau_1 \mathrm{A}^{\mathrm{T}}} \mathbf{c} \right) \left(\mathbf{b}^{\mathrm{T}} \sigma e^{(\tau - \tau_2) \mathrm{A}^{\mathrm{T}}} \right) \right\}. \tag{A.12}$$

This derivative vanishes at $\mathbf{c} = 0$, hence, equation (A.2) implies

$$\tilde{P}_n^{(3)}(s) = 0. \tag{A.13}$$

The derivative with respect to x is more involved: using the rule (A.6) leads to

$$\begin{aligned}\partial_x\psi^{(2)} = -\theta(\tau)s\Big\{&C(\tau) - \left(\mathbf{b}^{\mathrm{T}}\sigma e^{-\tau\mathrm{A}^{\mathrm{T}}}\mathbf{c}\right)\left(\mathbf{b}^{\mathrm{T}}\sigma\mathbf{c}\right)\\ &- s\left[\int_0^\tau \mathrm{d}\tau_1\, C(\tau-\tau_1) - \left(\mathbf{b}^{\mathrm{T}}\sigma e^{-\tau\mathrm{A}^{\mathrm{T}}}\mathbf{c}\right)\int_0^\tau \mathrm{d}\tau_1\, \mathbf{b}^{\mathrm{T}}\sigma e^{-\tau_1\mathrm{A}^{\mathrm{T}}}\mathbf{c}\right]\\ &+ \int_0^\tau \mathrm{d}\tau_2\,\Big[-\left(\mathbf{b}^{\mathrm{T}}\sigma\mathbf{c}\right)\mathbf{b}^{\mathrm{T}}\sigma e^{-\tau_2\mathrm{A}^{\mathrm{T}}}A^{\mathrm{T}}\mathbf{c} - \left(\mathbf{b}^{\mathrm{T}}\sigma e^{-\tau_2\mathrm{A}^{\mathrm{T}}}\mathbf{c}\right)\mathbf{b}^{\mathrm{T}}\sigma A^{\mathrm{T}}\mathbf{c}\\ &+ s\left(\mathbf{b}^{\mathrm{T}}\sigma e^{-\tau_2\mathrm{A}^{\mathrm{T}}}\mathbf{c}\right)\int_0^{\tau_2}\mathrm{d}\tau_1\,\mathbf{b}^{\mathrm{T}}\sigma e^{-\tau_1\mathrm{A}^{\mathrm{T}}}A^{\mathrm{T}}\mathbf{c} + s\left(\int_0^{\tau_2}\mathrm{d}\tau_1\,\mathbf{b}^{\mathrm{T}}\sigma e^{-\tau_1\mathrm{A}^{\mathrm{T}}}\mathbf{c}\right)\left(\mathbf{b}^{\mathrm{T}}\sigma e^{-\tau_2\mathrm{A}^{\mathrm{T}}}A^{\mathrm{T}}\mathbf{c}\right)\Big]\Big\}.\end{aligned} \tag{A.14}$$

Taking into account that $e^{-\tau\mathrm{A}^{\mathrm{T}}}A^{\mathrm{T}} = -\frac{d}{d\tau}e^{\tau\mathrm{A}^{\mathrm{T}}}$ and integrating by parts simplifies the expression to

$$\begin{aligned}\partial_x\psi^{(2)} = -\theta(\tau)s\Big\{&\mathbf{b}^{\mathrm{T}}\sigma e^{\tau\mathrm{A}^{\mathrm{T}}}\mathbf{b} - \left(\mathbf{b}^{\mathrm{T}}\sigma\mathbf{c}\right)^2 - \left(\mathbf{b}^{\mathrm{T}}\sigma A^{\mathrm{T}}\mathbf{c}\right)\int_0^\tau \mathrm{d}\tau_1\,\left(\mathbf{b}^{\mathrm{T}}\sigma e^{-\tau_1\mathrm{A}^{\mathrm{T}}}\mathbf{c}\right)\\ &- s\left[\int_0^\tau \mathrm{d}\tau_1\,\mathbf{b}^{\mathrm{T}}\sigma e^{\tau_1\mathrm{A}^{\mathrm{T}}}\mathbf{b} - \left(\mathbf{b}^{\mathrm{T}}\sigma\mathbf{c}\right)\int_0^\tau \mathrm{d}\tau_1\,\mathbf{b}^{\mathrm{T}}\sigma e^{-\tau_1\mathrm{A}^{\mathrm{T}}}\mathbf{c}\right]\Big\}.\end{aligned} \tag{A.15}$$

Differentiating this equation with respect to $\mathbf{k}$ yields the mixed derivative

$$\begin{aligned}(\nabla_{\mathbf{k}}\partial_x\psi^{(2)})^{\mathrm{T}} = -\theta(\tau)s\Big\{&-2\left(\mathbf{b}^{\mathrm{T}}\sigma\mathbf{c}\right)\mathbf{b}^{\mathrm{T}}\sigma e^{\tau\mathrm{A}^{\mathrm{T}}} + \left(\int_0^\tau \mathrm{d}\tau_1\,\mathbf{b}^{\mathrm{T}}\sigma e^{-\tau_1\mathrm{A}^{\mathrm{T}}}\mathbf{c}\right)\mathbf{b}^{\mathrm{T}}\sigma\left(s\mathbb{I}_d - A^{\mathrm{T}}\right)e^{\tau\mathrm{A}^{\mathrm{T}}}\\ &+ \left(\mathbf{b}^{\mathrm{T}}\sigma(s\mathbb{I}_d - A^{\mathrm{T}})\mathbf{c}\right)\int_0^\tau \mathrm{d}\tau_1\,\mathbf{b}^{\mathrm{T}}\sigma e^{\tau_1\mathrm{A}^{\mathrm{T}}}\Big\},\end{aligned} \tag{A.16}$$

where $\mathbb{I}_d$ denotes the $d \times d$ identity matrix. Inserting the derivatives into Eq. (A.4) results in the third-order perturbation term $\psi^{(3)}$:

$$\begin{aligned}\psi^{(3)} = -i\theta(\tau)\frac{s}{\mu^4}\int_0^\tau \mathrm{d}\tau_3\,\Big\{&-2\left(\mathbf{b}^{\mathrm{T}}\sigma\mathbf{c}\right)C(\tau_3) + \left(\int_0^{\tau_3}\mathrm{d}\tau_1\,\mathbf{b}^{\mathrm{T}}\sigma e^{-\tau_1\mathrm{A}^{\mathrm{T}}}\mathbf{c}\right)\left(\mathbf{b}^{\mathrm{T}}\sigma\left(2s\mathbb{I}_d - A^{\mathrm{T}}\right)e^{\tau_3\mathrm{A}^{\mathrm{T}}}\mathbf{b}\right)\\ &+ \left(\mathbf{b}^{\mathrm{T}}\sigma(2s\mathbb{I}_d - A^{\mathrm{T}})\mathbf{c}\right)\left(\int_0^{\tau_3}\mathrm{d}\tau_1\,C(\tau_1)\right)\\ &- \left(\mathbf{b}^{\mathrm{T}}\sigma e^{-\tau_3\mathrm{A}^{\mathrm{T}}}\mathbf{c}\right)\Big[C(\tau_3) - \left(\mathbf{b}^{\mathrm{T}}\sigma\mathbf{c}\right)^2 - \left(\mathbf{b}^{\mathrm{T}}\sigma A^{\mathrm{T}}\mathbf{c}\right)\int_0^{\tau_3}\mathrm{d}\tau_1\,\left(\mathbf{b}^{\mathrm{T}}\sigma e^{-\tau_1\mathrm{A}^{\mathrm{T}}}\mathbf{c}\right)\\ &- s\left(\int_0^{\tau_3}\mathrm{d}\tau_1\,C(\tau_1) - \left(\mathbf{b}^{\mathrm{T}}\sigma\mathbf{c}\right)\int_0^{\tau_3}\mathrm{d}\tau_1\,\mathbf{b}^{\mathrm{T}}\sigma e^{-\tau_1\mathrm{A}^{\mathrm{T}}}\mathbf{c}\right)\Big]\\ &- s^2\int_0^{\tau_3}\mathrm{d}\tau_2\,\Big[\left(\mathbf{b}^{\mathrm{T}}\sigma e^{-\tau_2\mathrm{A}^{\mathrm{T}}}\mathbf{c}\right)\int_0^{\tau_2}\mathrm{d}\tau_1\,C(\tau_3-\tau_1) + \left(\int_0^{\tau_2}\mathrm{d}\tau_1\,\mathbf{b}^{\mathrm{T}}\sigma e^{-\tau_1\mathrm{A}^{\mathrm{T}}}\mathbf{c}\right)C(\tau_3-\tau_2)\Big]\\ &+ s\left(\mathbf{b}^{\mathrm{T}}\sigma e^{-\tau_3\mathrm{A}^{\mathrm{T}}}\mathbf{c}\right)\int_0^{\tau_3}\mathrm{d}\tau_2\,\Big[C(\tau_2) - \left(\mathbf{b}^{\mathrm{T}}\sigma e^{-\tau_2\mathrm{A}^{\mathrm{T}}}\mathbf{c}\right)\left(\mathbf{b}^{\mathrm{T}}\sigma\mathbf{c}\right)\\ &- s\left(\int_0^{\tau_2}\mathrm{d}\tau_1\,C(\tau_1) - \left(\mathbf{b}^{\mathrm{T}}\sigma e^{-\tau_2\mathrm{A}^{\mathrm{T}}}\mathbf{c}\right)\int_0^{\tau_2}\mathrm{d}\tau_1\,\mathbf{b}^{\mathrm{T}}\sigma e^{-\tau_1\mathrm{A}^{\mathrm{T}}}\mathbf{c}\right)\Big]\Big\}.\end{aligned} \tag{A.17}$$

Finally, differentiating this expression with respect to $\mathbf{k}$, setting $\mathbf{c} = 0$, and taking the

scalar product with the vector $\mathbf{b}$ yields

$$\begin{aligned}(\nabla_{\mathbf{k}}\psi^{(3)})^{\mathrm{T}}\mathbf{b}\Big|_{\mathbf{c}=0} = i\theta(\tau)s\int_0^\tau \mathrm{d}\tau_3\ \{&2C(\tau_3)C(\tau)+C(\tau-\tau_3)C(\tau_3)\\ &+\int_0^{\tau_3}\mathrm{d}\tau_1\ \left[C(\tau-\tau_1)C'(\tau_3)+C(\tau_1)C'(\tau)\right]\\ &-2s\int_0^{\tau_3}\mathrm{d}\tau_1\ \left[C(\tau-\tau_1)C(\tau_3)+C(\tau_1)C(\tau)+C(\tau_1)C(\tau-\tau_3)\right]\\ &+s^2\int_0^{\tau_3}\mathrm{d}\tau_2\int_0^{\tau_2}\mathrm{d}\tau_1\ [C(\tau-\tau_2)C(\tau_3-\tau_1)+C(\tau-\tau_1)C(\tau_3-\tau_2)\\ &+C(\tau-\tau_3)C(\tau_2-\tau_1)]\}\end{aligned} \tag{A.18}$$

Using Eq. (A.2), the fourth-order perturbation term of the moment generating function is given by the lengthy formula

$$\begin{aligned}\bar{P}_n^{(4)}(s) = e^{-sn}s^2\int_0^n \mathrm{d}\tau_4\int_0^{\tau_4}\mathrm{d}\tau_3\Big\{&2C(\tau_3)C(\tau_4)+C(\tau_4-\tau_3)C(\tau_3)\\ &+\int_0^{\tau_3}\mathrm{d}\tau_1\ \left[C(\tau_4-\tau_1)C'(\tau_3)+C(\tau_1)C'(\tau_4)\right]\\ &-2s\int_0^{\tau_3}\mathrm{d}\tau_1\ \left[C(\tau_4-\tau_1)C(\tau_3)+C(\tau_1)C(\tau_4)+C(\tau_1)C(\tau_4-\tau_3)\right]\\ &+s^2\int_0^{\tau_3}\mathrm{d}\tau_2\int_0^{\tau_2}\mathrm{d}\tau_1\ [C(\tau_4-\tau_2)C(\tau_3-\tau_1)+C(\tau_4-\tau_1)C(\tau_3-\tau_2)\\ &+C(\tau_4-\tau_3)C(\tau_2-\tau_1)]\Big\}\end{aligned} \tag{A.19}$$

In the formula for the variance of the n-th order interval only the quadratic term in s of last equation enters. Thus, the n-th order variance reads up to fourth order in ϵ

$$\kappa_{2,n} \equiv \mathrm{var}(t_n) = 2(\epsilon^2 K_{2,1} + \epsilon^4 K_{2,2}) + \mathcal{O}(\epsilon^6) \tag{A.20}$$

with

$$K_{2,1} = \int_0^n \mathrm{d}\tau_2\int_0^{\tau_2}\mathrm{d}\tau_1\, C(\tau_1) \tag{A.21a}$$

$$K_{2,2} = \int_0^n \mathrm{d}\tau_4\int_0^{\tau_4}\mathrm{d}\tau_3\left\{2C(\tau_3)C(\tau_4)+C(\tau_4-\tau_3)C(\tau_3)+\int_0^{\tau_3}\mathrm{d}\tau_1\ \left[C(\tau_4-\tau_1)C'(\tau_3)+C(\tau_1)C'(\tau_4)\right]\right\} \tag{A.21b}$$

The third cumulant only involves the cubic term of $\bar{P}_n^{(4)}(s)$, whereas the fourth cumulant involves the quartic term of $\bar{P}_n^{(4)}(s)$ and the quadratic term of $\bar{P}_n^{(2)}(s)$. As a result the leading orders of these cumulants read

$$\kappa_{3,n} = 12\epsilon^4\int_0^n \mathrm{d}\tau_3\int_0^{\tau_3}\mathrm{d}\tau_2\int_0^{\tau_2}\mathrm{d}\tau_1\left[C(\tau_3-\tau_1)C(\tau_2)+C(\tau_1)C(\tau_3)+C(\tau_1)C(\tau_3-\tau_2)\right]+\mathcal{O}(\epsilon^6) \tag{A.22}$$

and

$$\kappa_{4,n} = 24\epsilon^4 \left\{ \int_0^n \mathrm{d}\tau_4 \int_0^{\tau_4} \mathrm{d}\tau_3 \int_0^{\tau_3} \mathrm{d}\tau_2 \int_0^{\tau_2} \mathrm{d}\tau_1 \big[C(\tau_4-\tau_2)C(\tau_3-\tau_1) + C(\tau_4-\tau_1)C(\tau_3-\tau_2) + C(\tau_4-\tau_3)C(\tau_2-\tau_1) \big] - \frac{1}{2}\left[\int_0^n \mathrm{d}\tau_2 \int_0^{\tau_2} C(\tau_1) \right]^2 \right\} + \mathcal{O}(\epsilon^6)$$
$$= \mathcal{O}(\epsilon^6). \tag{A.23}$$

Thus, the fourth cumulant vanishes up to order ϵ^4.

A.2. Density of the nth-order intervals

An approximation for the nth-order interval density including the ISI density can be derived from the characteristic function

$$q(\omega, \mathbf{k}, t) = \int \mathrm{d}x\, e^{i\omega x} \int \mathrm{d}^d y\, e^{i\mathbf{k}\cdot\mathbf{y}} p(x, \mathbf{y}, t), \tag{A.24}$$

where $p(x, \mathbf{y}, t)$ is the joint probability density of the PIF model. This joint p.d.f. satisfies the Fokker-Planck equation (2.13) with the initial condition (2.29). Neglecting again the reflecting boundary, the nth-order interval density is approximately equal to the integrated flux across the threshold defined by $x = n$:

$$P_n(t) = \int \mathrm{d}^d y\, (1 + \epsilon \mathbf{b}^{\mathrm{T}}\mathbf{y}) p(n, \mathbf{y}, t). \tag{A.25}$$

On the other hand, $P_n(t)$ can be represented as the Fourier integral

$$P_n(t) = \frac{1}{2\pi} \int \mathrm{d}\omega\, e^{-i\omega n} \tilde{P}(\omega, t), \tag{A.26}$$

where the Fourier transform of the nth-order interval density is given by

$$\tilde{P}(\omega, t) = \int \mathrm{d}x\, e^{i\omega x} P_x(t) = \int \mathrm{d}x\, e^{i\omega x} \int \mathrm{d}^d y\, (1 + \epsilon \mathbf{b}^{\mathrm{T}}\mathbf{y}) p(x, \mathbf{y}, t). \tag{A.27}$$

Comparing with Eq. (A.24), the function $\tilde{P}(\omega, t)$ can be related to the characteristic function as follows:

$$\tilde{P}(\omega, t) = q(\omega, \mathbf{k}, t) - i\epsilon \left[\nabla_{\mathbf{k}} q(\omega, \mathbf{k}, t)\right]^{\mathrm{T}} \mathbf{b} \Big|_{\mathbf{k}=0}. \tag{A.28}$$

Thus, if the characteristic function $q(\omega, \mathbf{k}, t)$ is known, one can derive the nth-order interval density via Eq. (A.26) and (A.28).

An equation for the characteristic function is obtained by applying the Fourier transform to the Fokker-Planck equation, which yields

$$\partial_t q - \left(\mathbf{k}^{\mathrm{T}} \mathrm{A} + \epsilon\omega \mathbf{b}^{\mathrm{T}}\right) \nabla_{\mathbf{k}} q = \left(-\mathbf{k}^{\mathrm{T}} \beta \mathbf{k} + i\omega\right) q. \tag{A.29}$$

The initial condition for $q(\omega, \mathbf{k}, t)$ at $t = 0$ becomes

$$q(\omega, \mathbf{k}, 0) = \left(1 + i\epsilon \mathbf{b}^{\mathrm{T}} \sigma \mathbf{k}\right) \exp\left(-\mathbf{k}^{\mathrm{T}} \beta \mathbf{k}\right). \tag{A.30}$$

Equation (A.29) with initial condition (A.30) can be again solved by the method of characteristics. The characteristic equations are

$$\dot{\mathbf{k}} = -\mathrm{A}^{\mathrm{T}}\mathbf{k} - \epsilon\omega\mathbf{b} \tag{A.31}$$

$$\dot{q} = \left(-\mathbf{k}^{\mathrm{T}}\beta\mathbf{k} + i\omega\right) q. \tag{A.32}$$

The first equation is solved by

$$\mathbf{k}(t,\mathbf{c}) = e^{-t\mathrm{A}^{\mathrm{T}}}\mathbf{c} - \epsilon\omega\int_0^t \mathrm{d}t'\, e^{-(t-t')\mathrm{A}^{\mathrm{T}}}\mathbf{b}, \tag{A.33}$$

which can be inverted for the "initial" vector $\mathbf{c}$,

$$\mathbf{c}(t,\mathbf{k}) = e^{t\mathrm{A}^{\mathrm{T}}}\mathbf{k} + \epsilon\omega\int_0^t \mathrm{d}t'\, e^{t'\mathrm{A}^{\mathrm{T}}}\mathbf{b}. \tag{A.34}$$

Equation (A.32) is solved by the function

$$q(t,\mathbf{c}) = Q_0(\mathbf{c})\exp\left(-\frac{1}{2}\mathbf{k}^{\mathrm{T}}\sigma\mathbf{k} + i\omega t - \epsilon\omega\mathbf{b}^{\mathrm{T}}\sigma\int_0^t \mathrm{d}t'\,\mathbf{k}(t',\mathbf{c})\right), \tag{A.35}$$

where the relation $\mathrm{A}\sigma + \sigma\mathrm{A}^{\mathrm{T}} = -2\beta$ has been utilized. The prefactor $Q_0(\mathbf{c})$ is determined by the initial condition (A.30):

$$Q_0 = 1 + i\epsilon\mathbf{b}^{\mathrm{T}}\sigma\mathbf{c}. \tag{A.36}$$

Next, the integrand $\mathbf{k}(t',\mathbf{c})$ in Eq. (A.35) has to be replaced by the expression given in Eq. (A.33), followed by a re-substitution of the vector $\mathbf{c} = \mathbf{c}(t,\mathbf{k})$ according to Eq. (A.34). The resulting formula for the characteristic function reads

$$\begin{aligned} q(\omega,\mathbf{k},t) = &\left(1 + i\epsilon\mathbf{b}^{\mathrm{T}}\sigma e^{t\mathrm{A}^{\mathrm{T}}}\mathbf{k} + i\epsilon^2\omega\gamma_2(t)\right) \\ &\times\exp\left(-\frac{1}{2}\mathbf{k}^{\mathrm{T}}\sigma\mathbf{k} + i\omega t - \epsilon\omega\mathbf{b}^{\mathrm{T}}\sigma\int_0^t \mathrm{d}t'\, e^{t'\mathrm{A}^{\mathrm{T}}}\mathbf{k} - \epsilon^2\omega^2\gamma_1(t)\right), \end{aligned} \tag{A.37}$$

where

$$\gamma_1(t) = \int_0^t \mathrm{d}t'' \int_0^{t''} \mathrm{d}t'\, C(t'), \qquad \gamma_2(t) = \int_0^t \mathrm{d}t' C(t'), \qquad C(t) = \mathbf{b}^{\mathrm{T}}\sigma e^{t\mathrm{A}^{\mathrm{T}}}\mathbf{b}. \tag{A.38}$$

Setting $\mathbf{k} = 0$ in the last expression, yields the characteristic function $\Theta(\omega,t) \equiv q(\omega,0,t)$ of the random variable $X(t)$:

$$\Theta(\omega,t) \equiv \int \mathrm{d}x\, e^{i\omega x} p(x,t) = \left[1 + i\epsilon^2\omega\gamma_2(t)\right]\exp\left(i\omega t - \epsilon^2\omega^2\gamma_1(t)\right). \tag{A.39}$$

Taking furthermore the derivative of $q(\omega,\mathbf{k},t)$ with respect to $\mathbf{k}$, setting $\mathbf{k} = 0$ and using Eq. (A.28) yields the Fourier transform of the nth-order interval density,

$$\tilde{P}(\omega,t) = \left[1 + \epsilon^2 C(t) + 2i\epsilon^2\omega\gamma_2(t) - \epsilon^4\omega^2\gamma_2^2(t)\right] e^{i\omega t - \epsilon^2\omega^2\gamma_1(t)}. \tag{A.40}$$

Finally, performing the inverse Fourier transform results in

$$P_n(t) = \frac{1}{2\sqrt{4\pi\epsilon^2\gamma_1^3(t)}} \exp\left[-\frac{(t-n)^2}{4\epsilon^2\gamma_1(t)}\right] \left\{ \frac{\left[(n-t)\gamma_2(t) + 2\gamma_1(t)\right]^2}{2\gamma_1(t)} - \epsilon^2\left[\gamma_2^2(t) - 2\gamma_1(t)C(t)\right] \right\}. \tag{A.41}$$

A.3. Exponentially correlated noise: Skewness and kurtosis of interspike intervals

Higher-order terms of order $\mathcal{O}(\epsilon^6)$ and $\mathcal{O}(\epsilon^8)$ have been computed by using a computer algebra system because they are necessary to calculate the first noise correction to the kurtosis of the n-th order interval. As a result, the cumulants of the non-dimensionalized n-th order intervals read

$$\kappa_1 = n, \tag{A.42a}$$
$$\kappa_2 = 2\hat{\tau}^2(K_{2,1}\epsilon^2 + K_{2,2}\epsilon^4 + K_{2,3}\epsilon^6 + K_{2,4}\epsilon^8), \tag{A.42b}$$
$$\kappa_3 = 6\hat{\tau}^3(K_{3,2}\epsilon^4 + K_{3,3}\epsilon^6 + K_{3,4}\epsilon^8), \tag{A.42c}$$
$$\kappa_4 = 24\hat{\tau}^4(K_{4,3}\epsilon^6 + K_{4,4}\epsilon^8) \tag{A.42d}$$

with $\theta = n/\hat{\tau}$ and

$$K_{2,1} = e^{-\theta} + \theta - 1,$$
$$K_{2,2} = 2e^{-2\theta} + (\theta - 3)e^{-\theta} + 1,$$
$$K_{2,3} = \frac{1}{2}\left[27e^{-3\theta} + (16\theta - 48)e^{-2\theta} + (\theta^2 - 10\theta + 21)e^{-\theta}\right],$$
$$K_{2,4} = \frac{1}{6}\left[1024e^{-4\theta} + 729(\theta - 3)e^{-3\theta} + 48(2\theta^2 - 16\theta + 29)e^{-2\theta} + (\theta^3 - 21\theta^2 + 129\theta - 229)e^{-\theta}\right],$$
$$K_{3,2} = 2\left(1 - e^{-\theta}\right)\left(e^{-\theta} + \theta - 1\right),$$
$$K_{3,3} = 2\left[-9e^{-3\theta} + 4(-2\theta + 5)e^{-2\theta} + (-\theta^2 + 8\theta - 13)e^{-\theta} + 2\right],$$
$$K_{3,4} = -\left[256e^{-4\theta} + 81(3\theta - 8)e^{-3\theta} + 48(\theta^2 - 7\theta + 11)e^{-2\theta} + (\theta^3 - 18\theta^2 + 93\theta - 136)e^{-\theta}\right],$$
$$K_{4,3} = 7e^{-3\theta} + (9\theta - 19)e^{-2\theta} + (2\theta^2 - 14\theta + 17)e^{-\theta} + 5(\theta - 1),$$
$$K_{4,4} = \frac{1}{2}\left[289e^{-4\theta} + 2(179\theta - 429)e^{-3\theta} + 2(51\theta^2 - 320\theta + 439)e^{-2\theta} + 2(2\theta^3 - 32\theta^2 + 141\theta - 169)e^{-\theta} + 29\right].$$

From the cumulants one finds the rescaled skewness and kurtosis as defined in Eq. (2.92) and (2.93):

$$\alpha_\mathrm{s} = \frac{\theta}{\theta - 1 + e^{-\theta}}\left[1 - e^{-\theta} + \epsilon\left(-5e^{-2\theta} + e^{-\theta}(5 - \theta)\right)\right] + \epsilon^2 A_{\mathrm{s},2} \tag{A.43}$$

and

$$\alpha_\mathrm{e} = \frac{\theta^2\left[7e^{-2\theta} + 2(\theta - 6)e^{-\theta} + 5\right]}{5\left(\theta - 1 + e^{-\theta}\right)^2} + \epsilon A_{\mathrm{e},1} \tag{A.44}$$

with

$$A_{\mathrm{s},2} = -\frac{\theta}{2\left(\theta - 1 + e^{-\theta}\right)^3}\Big[154e^{-5\theta} + (337\theta - 528)e^{-4\theta} + (223\theta^2 - 813\theta + 658)e^{-3\theta} + (43\theta^3 - 308\theta^2 + 615\theta - 346)e^{-2\theta} + (\theta^4 - 17\theta^3 + 85\theta^2 - 139\theta + 60)e^{-\theta} + 2\Big]$$

$$A_{\mathrm{e},1} = \frac{\theta^2\left[205e^{-4\theta} + 4(73\theta - 147)e^{-3\theta} + 2(45\theta^2 - 266\theta + 280)e^{-2\theta} + 4(\theta^3 - 16\theta^2 + 60\theta - 44)e^{-\theta} - 1\right]}{10\left(\theta - 1 + e^{-\theta}\right)^3}.$$

A.4. Harmonic noise

In the PIF model driven by harmonic noise and Ornstein-Uhlenbeck (OU) noise, Eq. (2.127), the membrane potential $X(t)$ and the colored noise $\eta(t) = \mathbf{b}^{\mathrm{T}}\mathbf{Y}(t)$ obey the equations

$$\dot{X} = 1 + \epsilon\mathbf{b}\mathbf{Y}, \tag{A.45}$$

$$\dot{\mathbf{Y}} = \mathrm{A}\mathbf{Y} + \mathrm{B}\boldsymbol{\xi}(t), \tag{A.46}$$

where

$$\mathrm{A} = \begin{pmatrix} -\frac{1}{\hat{\tau}} & 0 & 0 \\ 0 & 0 & 1 \\ 0 & -\hat{\omega}_0^2 & -\hat{\gamma} \end{pmatrix}, \qquad \mathrm{B} = \begin{pmatrix} \sqrt{\frac{2}{\hat{\tau}}} & 0 & 0 \\ 0 & 0 & 0 \\ 0 & 0 & \sqrt{2\hat{\gamma}\hat{\omega}_0^2} \end{pmatrix} \tag{A.47}$$

and $\mathbf{b}^{\mathrm{T}} = \left(b, \sqrt{1-b^2}, 0\right)$. The firing threshold is at unity: $X = 1$. According to the general formulas in Sec. A.1, the ISI statistics can be expressed in terms of integrals over the correlation function $C(t)$ of the colored noise. The correlation function of the harmonic noise is known from the classical papers of Chandrasekhar [1943] and Wang and Uhlenbeck [1945]. However, in order to check and demonstrate the proposed method the correlation function will be re-derived in the following section.

Auto-correlation function of the colored noise For the derivation of the auto-correlation function $C(t) = \langle\eta(t')\eta(t'+t)\rangle$, the nth-order variance and the ISI covariance, the additivity property found in Sec. 2.3 can be employed because the Ornstein-Uhlenbeck noise and the harmonic noise are independent. This is also reflected in the block diagonal structure of the matrices A and B. In particular, we have the decompositions

$$C(t) = C_{\mathrm{OU}}(t) + C_{\mathrm{hn}}(t), \tag{A.48a}$$

$$\mathrm{var}(t_n) = \mathrm{var}(t_n)_{\mathrm{OU}} + \mathrm{var}(t_n)_{\mathrm{hn}} + \mathcal{O}(\epsilon^4), \tag{A.48b}$$

$$\mathrm{cov}(T_i, T_{i+n}) = \mathrm{cov}(T_i, T_{i+n})_{\mathrm{OU}} + \mathrm{cov}(T_i, T_{i+n})_{\mathrm{hn}} + \mathcal{O}(\epsilon^4), \tag{A.48c}$$

where the subscripts "OU" and "hn" refer to the models with either Ornstein-Uhlenbeck or harmonic noise driving, i.e. $\dot{X} = 1 + b\mathbf{Y}_1$ and $\dot{X} = 1 + \sqrt{1-b^2}\mathbf{Y}_2$, respectively.

For the first case, i.e. for a PIF model driven by a single OUP, the respective quantities

have been already obtained in Sec. 2.2. They read

$$C_{\mathrm{OU}}(t) = b^2 e^{-\frac{t}{\hat{\tau}}} \tag{A.49}$$

$$\mathrm{var}(t_n)_{\mathrm{OU}} = 2\epsilon^2 b^2 \hat{\tau}^2 \left(e^{-\frac{n}{\hat{\tau}}} + \frac{n}{\hat{\tau}} - 1 \right) + \mathcal{O}(\epsilon^4), \tag{A.50}$$

$$\mathrm{cov}(T_i, T_{i+n})_{\mathrm{OU}} = \epsilon^2 b^2 \hat{\tau}^2 \left(1 - e^{-1/\hat{\tau}}\right)^2 \exp\left(-\frac{n-1}{\hat{\tau}} \right) + \mathcal{O}(\epsilon^4). \tag{A.51}$$

For a PIF model that is driven solely by harmonic noise, the auto-correlation function can be represented as $C_{\mathrm{hn}}(t) = \mathbf{b}_2^{\mathrm{T}} e^{t\mathrm{A}_2} \sigma_2 \mathbf{b}_2$, where $\mathbf{b}_2^{\mathrm{T}} = \left(\sqrt{1-b^2}, 0\right)$, $\sigma_2 = \left(\begin{smallmatrix} 1 & 0 \\ 0 & \hat{\omega}_0^2 \end{smallmatrix}\right)$ and $\mathrm{A}_2 = \left(\begin{smallmatrix} 0 & 1 \\ -\hat{\omega}_0^2 & -\hat{\gamma} \end{smallmatrix}\right)$. The matrix exponential $e^{t\mathrm{A}_2}$ can be obtained from the fundamental solution of the harmonic oscillator. More precisely, let $\mathbf{y}_1(t)$ and $\mathbf{y}_2(t)$ be two linearly independent solutions of the two-dimensional system $\dot{\mathbf{y}} = \mathrm{A}_2 \mathbf{y}$. Then, a fundamental solution is given by the matrix $\mathrm{Y}_h(t) = [\mathbf{y}_1(t), \mathbf{y}_2(t)]$ and the matrix exponential can be computed as $e^{t\mathrm{A}_2} = \mathrm{Y}_h(t)\mathrm{Y}_h^{-1}(0)$. In the underdamped case, $\hat{\omega}_0 > \hat{\gamma}/2$, the independent solutions can be taken as

$$\mathbf{y}_1(t) = \begin{pmatrix} -\frac{\hat{\gamma}}{2}\cos\Omega t + \Omega \sin \Omega t \\ \hat{\omega}_0^2 \cos \Omega t \end{pmatrix} e^{-\frac{\hat{\gamma}}{2}t}, \qquad \mathbf{y}_2(t) = \begin{pmatrix} \Omega \cos \Omega t + \frac{\hat{\gamma}}{2}\sin \Omega t \\ -\hat{\omega}_0^2 \sin \Omega t \end{pmatrix} e^{-\frac{\hat{\gamma}}{2}t}, \tag{A.52}$$

where $\Omega = \sqrt{\hat{\omega}_0^2 - \frac{\hat{\gamma}^2}{4}}$. This results in the following matrix exponential

$$e^{t\mathrm{A}_2} = e^{-\frac{\hat{\gamma}}{2}t} \begin{pmatrix} \cos\Omega t + \frac{\hat{\gamma}}{2\Omega}\sin\Omega t & \frac{1}{\Omega}\sin\Omega t \\ -\frac{\hat{\omega}_0^2}{\Omega}\sin\Omega t & \cos\Omega t - \frac{\hat{\gamma}}{2\Omega}\sin\Omega t \end{pmatrix}, \tag{A.53}$$

from which follows

$$C_{\mathrm{hn}}(t) = (1-b^2) e^{-\frac{\hat{\gamma}}{2}t} \left(\cos\Omega t + \frac{\hat{\gamma}}{2\Omega}\sin\Omega t \right). \tag{A.54}$$

Variance of n-th order intervals, CV Taking the double integral of $C_{\mathrm{hn}}(t)$ in Eq. (A.21) leads to the part of the nth-order variance that is associated with harmonic noise:

$$\mathrm{var}(t_n)_{\mathrm{hn}} = (1-b^2)\frac{2\epsilon^2}{\hat{\omega}_0^2} \left\{ 1 - \frac{\hat{\gamma}^2}{\hat{\omega}_0^2} + \hat{\gamma} n - \frac{a_1 \sin(n\Omega) + a_2 \cos(n\Omega)}{4\Omega\hat{\omega}_0^2} \exp\Big(-\frac{\hat{\gamma}}{2} n\Big) \right\}, \tag{A.55}$$

where

$$a_1 = \frac{\hat{\gamma}}{2}\left(12\Omega^2 - \hat{\gamma}^2\right), \qquad a_2 = \Omega\left(4\Omega^2 - 3\hat{\gamma}^2\right).$$

The coefficient of variation arising from both OU noise and harmonic noise is the determined by the sum of $\mathrm{var}(t_n)_{\mathrm{OU}}$ and $\mathrm{var}(t_n)_{\mathrm{hn}}$ taken at $n = 1$. As a result, the squared CV reads in leading order of ϵ

$$C_{\mathrm{V}}^2 = 2\epsilon^2 \left\{ b^2\hat{\tau}^2 \left(e^{-\frac{1}{\hat{\tau}}} + \frac{1}{\hat{\tau}} - 1 \right) + \frac{1-b^2}{\hat{\omega}_0^2} \left[1 - \frac{\hat{\gamma}^2}{\hat{\omega}_0^2} + \hat{\gamma} - \frac{a_1 \sin(\Omega) + a_2 \cos(\Omega)}{4\Omega\hat{\omega}_0^2} \exp\Big(-\frac{\hat{\gamma}}{2}\Big) \right] \right\}. \tag{A.56}$$

In the case that the OU noise has a small correlation time, $\hat{\tau} \ll 1$, this formula reduces to

$$C_V^2 = 2\hat{D}' + \frac{2\hat{D}}{\hat{\gamma}\hat{\omega}_0^4}\left[1 - \frac{\hat{\gamma}^2}{\hat{\omega}_0^2} + \gamma - \frac{a_1\sin(\Omega) + a_2\cos(\Omega)}{4\Omega\hat{\omega}_0^2}\exp\left(-\frac{\hat{\gamma}}{2}\right)\right]. \tag{A.57}$$

For this formula, it is required that the noise intensity of the OUP is sufficiently small, $\hat{D}' \ll \hat{\tau}$, to ensure that ϵ is still a small parameter.

ISI density The ISI density is given by Eq. (A.41), where the functions $\gamma_1(t)$ and $\gamma_2(t)$ are in this case,

$$\gamma_1(t) = b^2\hat{\tau}^2\left(e^{-\frac{t}{\hat{\tau}}} + \frac{t}{\hat{\tau}} - 1\right) + \frac{1-b^2}{\hat{\omega}_0^2}\left[1 - \frac{\hat{\gamma}^2}{\hat{\omega}_0^2} + \hat{\gamma}t - \frac{a_1\sin(\Omega t) + a_2\cos(\Omega t)}{4\Omega\hat{\omega}_0^2}\exp\left(-\frac{\hat{\gamma}}{2}t\right)\right] \tag{A.58}$$

$$\gamma_2(t) = b^2\hat{\tau}\left(1 - e^{-\frac{t}{\hat{\tau}}}\right) + \frac{1-b^2}{\Omega\hat{\omega}_0^2}\left[\hat{\gamma}\Omega\left(1 - e^{-\frac{\hat{\gamma}}{2}t}\cos\Omega t\right) + \left(\Omega^2 - \frac{\hat{\gamma}^2}{4}\right)e^{-\frac{\hat{\gamma}}{2}t}\sin\Omega t\right]. \tag{A.59}$$

Serial correlation coefficient In the formula for the covariance between ISIs, nominator of Eq. (1.51), the terms of the nth-order variances that are linear in n cancel each other. This leaves for the ISI covariance of a PIF neuron driven by harmonic noise:

$$\mathrm{cov}(T_i, T_{i+n})_{\mathrm{hn}} = \frac{(1-b^2)\epsilon^2}{2\Omega\hat{\omega}_0^4}\exp\left(-\frac{\hat{\gamma}}{2}n\right)\left[\lambda_1\sin(\Omega n) + \lambda_2\cos(\Omega n)\right]. \tag{A.60}$$

with

$$\lambda_1 = a_1\left[1 - \cosh\left(\frac{\hat{\gamma}}{2}\right)\cos\Omega\right] - a_2\sinh\left(\frac{\hat{\gamma}}{2}\right)\sin\Omega \tag{A.61}$$

$$\lambda_2 = a_2\left[1 - \cosh\left(\frac{\hat{\gamma}}{2}\right)\cos\Omega\right] + a_1\sinh\left(\frac{\hat{\gamma}}{2}\right)\sin\Omega \tag{A.62}$$

Summing up the contributions of the OU noise, Eq. (A.51), and the harmonic noise, Eq. (A.60) and dividing by the squared CV, Eq. (A.56) yields the zeroth-order of the serial correlation coefficient:

$$\rho_n = \frac{\epsilon^2}{C_V^2}\left[b^2\hat{\tau}^2\left(1 - e^{-1/\hat{\tau}}\right)^2\exp\left(-\frac{n-1}{\hat{\tau}}\right) + \frac{1-b^2}{2\Omega\hat{\omega}_0^4}\left[\lambda_1\sin(\Omega n) + \lambda_2\cos(\Omega n)\right]\exp\left(-\frac{\hat{\gamma}}{2}n\right)\right]. \tag{A.63}$$

In the case of small correlation times of the OU noise, the first term can be neglected yielding

$$\rho_n = \frac{\hat{D}}{2\hat{\gamma}\Omega\hat{\omega}_0^6 C_V^2}\left[\lambda_1\sin(\Omega n) + \lambda_2\cos(\Omega n)\right]\exp\left(-\frac{\hat{\gamma}}{2}n\right). \tag{A.64}$$

Skewness In the formulas for the third cumulant or for the first correction of the CV, the function $C(t) = C_{\mathrm{OU}}(t) + C_{\mathrm{hn}}(t)$ enters in a non-linear way. Hence, the respective expressions cannot be obtained by simply computing the contributions of the OU noise and the harmonic noise individually and adding them. Instead, the calculation must be

carried out using the full correlation function $C(t)$. Unfortunately, these calculations are rather cumbersome. However, since the focus here is on the effect of harmonic noise, I will consider the case $b = 0$ in the following, which corresponds to the presence of only harmonic noise.

For $b = 0$, Eqs. (A.20)– (A.23) yield the cumulants of the nth-order intervals:

$$\kappa_1 = n, \tag{A.65}$$

$$\kappa_2 = 2\epsilon^2(K_{2,1} + K_{2,2}\epsilon^2) + \mathcal{O}(\epsilon^6), \tag{A.66}$$

$$\kappa_3 = \frac{3\epsilon^4}{\Omega\hat{\omega}_0^2} K_{2,1} \left\{ 4\hat{\gamma}\Omega + e^{-\frac{\hat{\gamma}}{2}} \left[(4\Omega^2 - \hat{\gamma}^2)\sin(\Omega) - 4\hat{\gamma}\Omega\cos(\Omega) \right] \right\} + \mathcal{O}(\epsilon^6), \tag{A.67}$$

$$\kappa_4 = \mathcal{O}(\epsilon^6) \tag{A.68}$$

with

$$K_{2,1} = \frac{1}{\hat{\omega}_0^2} \left[1 - \frac{\hat{\gamma}^2}{\hat{\omega}_0^2} + \hat{\gamma} - \frac{a_1 \sin(\Omega) + a_2 \cos(\Omega)}{4\Omega\hat{\omega}_0^2} \exp\left(-\frac{\hat{\gamma}}{2}\right) \right] \tag{A.69}$$

As in the case of the PIF model driven by a single OUP, we compute the rescaled skewness $\alpha_s = \kappa_3/(3\kappa_2^2)$. In leading order, this quantity does not depend on ϵ, specifically it reads

$$\alpha_s = \frac{1}{\Omega\hat{\omega}_0^2 K_{2,1}} \left[\hat{\gamma}\Omega \left(1 - e^{-\frac{\hat{\gamma}}{2}} \cos\Omega \right) + \left(\Omega^2 - \frac{\hat{\gamma}^2}{4} \right) e^{-\frac{\hat{\gamma}}{2}} \sin\Omega \right] + \mathcal{O}(\epsilon^2). \tag{A.70}$$

Appendix B.

The adapting PIF model driven by white noise

After presenting two supplementary results concerning the conditional statistics of the adapting PIF model in Sec. B.1, I will derive the stationary solution of the Fokker-Planck equation in Sec. B.2, which is the main part of this chapter.

B.1. The conditional ensemble

B.1.1. Weak-noise asymptotics of the conditional ISI density

Here, I want to show that in the weak-noise limit the inverse Gaussian density (3.50) approaches a Gaussian with the same mean and variance as the inverse Gaussian. This property is used in the derivation of the SCC to justify the ansatz Eq. (3.31). From Eq. (3.52) we know that the standard deviation scales with the square root of the noise intensity,

$$\sigma_T(a_i) = \frac{\sqrt{2DT_{\mathrm{det}}(a_i)}}{\mu_{\mathrm{eff}}}, \tag{B.1}$$

hence, the distribution becomes thin and tall. Typical ISIs lie within a few standard deviations around the mean value $T_{\mathrm{det}}(a_i)$ and can be represented as $T_i = T_{\mathrm{det}}(a_i) + \sigma_T T_i'$ for some $T_i' \sim \mathcal{O}(1)$. Thus, to capture the distribution of typical ISIs it is reasonable to ask for the distribution of the rescaled time

$$T_i' = \frac{T_i - T_{\mathrm{det}}(a_i)}{\sigma_T} \sim \mathcal{O}(1). \tag{B.2}$$

This distribution retains a variance of unity in the limit $\sigma_T \to 0$. But what is the shape of this distribution? Substituting $T_i = T_{\mathrm{det}}(a_i) + \sigma_T T_i'$, $D = \sigma_T^2 \mu_{\mathrm{eff}}^2/(2T_{\mathrm{det}})$ in Eq. (3.50) and taking into account that $dT_i' = (\mu_{\mathrm{eff}}/\sqrt{2DT_{\mathrm{det}}})dT_i$ I obtain

$$P(T_i'|a_i) = \frac{1}{\sqrt{2\pi\left(1+\frac{\sigma_T}{T_{\mathrm{det}}}T_i'\right)^3}} \exp\left[-\frac{T_i'^2}{2\left(1+\frac{\sigma_T}{T_{\mathrm{det}}}T_i'\right)}\right] \tag{B.3}$$

$$\sim \frac{1}{\sqrt{2\pi}} \exp\left(-\frac{T_i'^2}{2}\right), \qquad \sigma_T \to 0. \tag{B.4}$$

As a result, the conditional ISI density converges to

$$P(T_i|a_i) \sim \frac{1}{\sqrt{2\pi}\sigma_T} \exp\left[-\frac{(T_i - T_{\mathrm{det}}(a_i))^2}{2\sigma_T^2}\right] \tag{B.5}$$

in the limit $\sigma_T \to 0$, $T_i' = (T_i - T_{\rm det})/\sigma_T = const.$. Hence, the conditional ISI density converges to a Gaussian.

B.1.2. Moments of the transition probability density $p_{\rm tr}(a_{i+1}|a_i)$

An analytical expression for the conditional moments of a_{i+1} given a_i can be derived as follows: Using the transformation (3.5) leads to

$$\langle a_{i+1}^n|a_i\rangle = \int_\Delta^{a_i+\Delta} {\rm d}a_{i+1}\, a_{i+1}^n p(a_{i+1}|a_i) \tag{B.6}$$

$$= \int_0^\infty {\rm d}T_i\, (a_i e^{-T_i/\tau_{\rm a}} + \Delta)^n P(T_i|a_i) \tag{B.7}$$

$$= \sum_{k=0}^n \binom{n}{k} a_i^{n-k}\Delta^k \bar{P}\left(\frac{n-k}{\tau_{\rm a}}\middle| a_i\right), \tag{B.8}$$

where $\bar{P}(s|a_i) = \int_0^\infty {\rm d}T_i\, e^{-sT_i} P(T_i|a_i)$ is the Laplace transform of the conditional ISI density $P(T_i|a_i)$. The Laplace transform of the inverse Gaussian, Eq. (3.50), has the form

$$\bar{P}(s|a_i) = \exp\left[-\left(\sqrt{\tau_{\rm eff}(a_i)s + \frac{1}{4}} - \frac{1}{2}\right)\frac{T_{\rm det}(a_i)}{\tau_{\rm eff}(a_i)}\right], \tag{B.9}$$

where $\tau_{\rm eff}(a_i) = D/\mu_{\rm eff}^2(a_i)$ is an effective time constant. In particular, for $n = 1$ the conditional mean is

$$\langle a_{i+1}|a_i\rangle = a_i\bar{P}\left(\frac{1}{\tau_{\rm a}}\middle| a_i\right) + \Delta. \tag{B.10}$$

Furthermore, from the second moment one obtains a simple expression for the conditional variance

$${\rm Var}(a_{i+1}|a_i) \equiv \langle a_{i+1}^2|a_i\rangle - \langle a_{i+1}|a_i\rangle^2 = a_i^2\left[\bar{P}\left(\frac{2}{\tau_{\rm a}}\middle| a_i\right) - \bar{P}^2\left(\frac{1}{\tau_{\rm a}}\middle| a_i\right)\right]. \tag{B.11}$$

This result will be analyzed in more detail in Sec. 3.3.5, where the variance of the stationary sequence $\{a_i\}$ will be studied.

B.2. Solution of the stationary Fokker-Planck equation

In Sec. 3.3.2, it was shown that the stationary probability density $P_0(V,a)$ is the solution of the following boundary-value problem:

$$-(\mu - a)\partial_V P_0 + \frac{1}{\tau_{\rm a}}\partial_a(aP_0) + \epsilon\hat{D}\partial_V^2 P_0 = 0 \tag{B.12}$$

with the boundary conditions

$$\text{(absorbing threshold)} \qquad P_0(V_{\text{th}}, a) = 0, \tag{B.13}$$

$$\text{(continuity)} \qquad P_0(0^-, a) = P_0(0^+, a), \tag{B.14}$$

$$\text{(reset)} \qquad \partial_V P_0(0^+, a) - \partial_V P_0(0^-, a) = \partial_V P_0(V_{\text{th}}, a - \Delta), \tag{B.15}$$

$$\text{(natural boundaries)} \qquad \lim_{V \to -\infty} P_0(V, a) = 0, \quad \lim_{a \to \infty} P_0(V, a) = 0, \tag{B.16}$$

$$\text{(normalization)} \qquad -\epsilon \hat{D} \int_0^\infty \mathrm{d}a \, \partial_V P_0(V_{\text{th}}, a) = \frac{1}{T^*}. \tag{B.17}$$

Here, a derivation of the stationary solution $P_0(V, a)$ is given.

B.2.1. Region I

As explained in the main text, the solution is sought in different regions as indicated in Fig. 3.13. These partial solutions are then patched together according to the boundary conditions. Let us start with region I, which is defined by $V < 0$ in the case $a^* < \mu$, and by $V > 0$ and $a > \mu$ in the case $a^* > \mu$. The direct limit $\epsilon \to 0$ of Eq. (B.12) yields

$$-(\mu - a)\partial_V P_0 + \frac{1}{\tau_{\text{a}}} \partial_a (a P_0) = 0, \tag{B.18}$$

where it was assumed that the third term $\epsilon \hat{D} \partial_V^2 P_0$ is small compared to the first two terms. The only solution of Eq. (B.18) that satisfies the boundary condition (B.16) is the trivial solution $P_0(V, a) = 0$. This solution, however, does not fulfill the boundary condition (B.14) at $V = 0$ because the left-sided limit $P_0(0^+, a)$ will generally be non-zero. Instead, for $-\epsilon < V \leq 0$ the true solution develops a boundary layer, in which $P(V, a)$ is positive and rises steeply to $P(0^+, a)$ as $V \to 0-$ (Fig. 3.14). This non-vanishing probability corresponds to particles that diffuse into region I after resetting. Due to the rapid change of P_0 within the boundary layer, the diffusion term $\epsilon \hat{D} \partial_V^2 P_0$ is not small compared to the first two terms in Eq. (B.12). Therefore the diffusion term cannot be neglected in the boundary layer. To obtain the leading-order solution close to the reset, the stretched variable $x = V/\epsilon$ is used. Furthermore, I define the function $\hat{P}_0(x, a) = \sqrt{\epsilon} P_0(V, a)$, which satisfies the transformed Fokker-Planck equation

$$-(\mu - a)\partial_x \hat{P}_0 + \frac{\epsilon}{\tau_{\text{a}}} \partial_a (a \hat{P}_0) + \hat{D} \partial_x^2 \hat{P}_0 = 0. \tag{B.19}$$

In leading order, the second term can be neglected yielding the ordinary differential equation

$$-(\mu - a)\partial_x \hat{P}_0 + \hat{D} \partial_x^2 \hat{P}_0 = 0, \tag{B.20}$$

which is subject to the boundary conditions

$$\lim_{x \to -\infty} \hat{P}_0(x, a) = 0 \tag{B.21}$$

$$\hat{P}_0(0^-, a) = \hat{P}_0(0^+, a). \tag{B.22}$$

The solution of Eq. (B.20) that satisfies (B.21) is

$$\hat{P}_0(x,a) = \frac{M(a)}{\lambda(a)} e^{\lambda(a)x}, \tag{B.23}$$

where $\lambda(a) = (\mu - a)/\hat{D}$ and $M(a)$ is a function determined by the continuity condition (B.22). Returning to the variable V, the leading-order solution in region I reads

$$P_0(V,a) = \frac{M(a)}{\sqrt{\epsilon}\lambda(a)} \exp\left(\frac{\lambda(a)V}{\epsilon}\right). \tag{B.24}$$

B.2.2. Region II

In the region that is complement to region I, called region II (see Fig. 3.13), the solution is sought in the neighborhood of the limit curve $\mathcal{C}^*$. Recall that in the deterministic limit, all probability is concentrated on this limit set. Here, we aim at a Gaussian approximation of the probability density around this limit-cycle for weak, but non-vanishing noise. To this end, I use the so-called WKB ansatz [Schuss, 2009]

$$P_0(V,a) = \mathcal{N}(\epsilon)\Psi(V,a) \exp\left(-\frac{\Phi(V,a)}{\epsilon}\right). \tag{B.25}$$

The functions $\Phi(V,a)$ and $\Psi(V,a)$ are independent of ϵ and can be interpreted as a non-equilibrium potential [Graham and Tél, 1984] and a modulation function, respectively. The normalization factor must be proportional to $1/\sqrt{\epsilon}$ (see Sec. B.2.4), specifically it is chosen as

$$\mathcal{N}(\epsilon) = \frac{1}{\sqrt{2\pi\epsilon}}. \tag{B.26}$$

Substituting the ansatz (B.25) into the Fokker-Planck equation (B.12) yields

$$\begin{aligned} 0 = &\left[(\mu - a)\Phi_V - \frac{a}{\tau_\mathrm{a}}\Phi_a + \hat{D}\Phi_V^2\right]\Psi \\ &+ \epsilon\left[-(\mu - a)\Psi_V + \frac{a}{\tau_\mathrm{a}}\Psi_a + \frac{1}{\tau_\mathrm{a}}\Psi - 2\hat{D}\Phi_V\Psi_V - \hat{D}\Phi_{VV}\Psi\right] + \epsilon^2\Psi_{VV}. \end{aligned} \tag{B.27}$$

Here, the indices on Φ and Ψ are shorthand notations for the respective partial derivatives, e.g. $\Phi_V = \partial_V\Phi$, $\Phi_{VV} = \partial_V^2\Phi$. Equating terms with like powers of ϵ to zero results in the system

$$(\mu - a)\Phi_V - \frac{a}{\tau_\mathrm{a}}\Phi_a + \hat{D}\Phi_V^2 = 0 \tag{B.28}$$

$$(\mu - a + 2\hat{D}\Phi_V)\Psi_V - \frac{a}{\tau_\mathrm{a}}\Psi_a = \left(\frac{1}{\tau_\mathrm{a}} - \hat{D}\Phi_{VV}\right)\Psi. \tag{B.29}$$

Equation (B.28) is a first-order, nonlinear partial differential equation for $\Phi(V,a)$, which is independent of $\Psi(V,a)$ and can be solved for $\Phi(V,a)$. The solution can then be inserted into the linear, first-order equation (B.29) for $\Psi(V,a)$. In the context of WKB theory, Eq. (B.28) and (B.29) are called *eikonal* and *transport equation*, respectively.

The solutions Φ and Ψ can in general not satisfy the boundary conditions at both $V = 0$

and $V = V_{\text{th}}$ because they are governed by first-order differential equations. This reflects the boundary layer structure of the solution in region II: The WKB solution (B.25) that satisfies the boundary condition at $V = 0$ is valid in almost the whole region II except for a thin boundary layer of thickness $\mathcal{O}(\epsilon)$ close to the threshold (Fig. 3.14B). In this boundary layer the solution drops rapidly to zero because of the absorbing boundary. In the limit $\epsilon \to 0$, the solution has a discontinuity: it is finite in the whole region II except for the threshold line, where the probability density is zero. Applying boundary layer theory, our strategy will be as follows: first, the WKB solution is calculated, which is valid in the interval $0 \leq V \ll V_{\text{th}} - \epsilon$ ("outer solution"). Second, the leading order inner solution is calculated, which is valid for $0 \ll V \leq V_{\text{th}}$. Finally, inner and outer solutions are asymptotically matched in the overlap region $0 \ll V \ll V_{\text{th}} - \epsilon$.

WKB solution

I want to find the solutions to equation (B.28) and (B.29) that fulfill the following boundary conditions at $V = 0$:

$$\Phi(0, a) = \phi_0(a) \tag{B.30}$$

and

$$\Psi(0, a) = \psi_0(a). \tag{B.31}$$

Here, $\phi_0(a)$ and $\psi_0(t)$ are functions that will be determined later using the reset condition. Furthermore, it must be required that in the deterministic limit $\epsilon \to 0$ all probability is concentrated on the limit curve $\mathcal{C}^*$. This gives rise to further plausible constraints for $\Phi(V, a)$ evaluated on $\mathcal{C}^*$: first, Φ must vanish on $\mathcal{C}^*$, i.e.

$$\Phi(V, a)|_{\mathcal{C}^*} = 0. \tag{B.32}$$

Secondly, to prevent that the probability density diverges in the neighborhood of $\mathcal{C}^*$ as ϵ tends to zero, it must be required that Φ is locally non-negative. This can be ensured by the conditions

$$\Phi_V(V, a)|_{\mathcal{C}^*} = 0, \quad \Phi_a(V, a)|_{\mathcal{C}^*} = 0 \tag{B.33}$$

and

$$\Phi_{VV}(V, a)|_{\mathcal{C}^*} > 0, \quad \Phi_{aa}(V, a)|_{\mathcal{C}^*} > 0. \tag{B.34}$$

Equation (B.28) together with the conditions (B.30) and (B.32)– (B.34) can be solved by the method of characteristics. Accordingly, the solution is sought in a coordinate system, in which the partial differential equation (B.28) becomes an ordinary differential equation. This can be achieved by a variable transformation $(V, a) \to (\tau, s)$, where τ and s are the so-called characteristic coordinates. The transformation law $V = V(\tau, s)$ and $a = a(\tau, s)$ can be found by the characteristic equations that will be derived in the following. Before proceeding, I state the boundary condition on Φ at the reset (Eq. (B.30)) in parametric form. Specifically, $\tau = 0$ is identified with the reset line $\{(V, a)|V = 0\}$ and the reset line is parametrized by the coordinate s as follows:

$$V(0, s) = 0, \quad a(0, s) = s, \qquad s > 0. \tag{B.35}$$

In other words, the coordinate s equals a on the reset line (Fig. 3.15).

In order to apply the method of characteristics, Φ and its partial derivatives Φ_V and Φ_a are regarded as functions of the new variables τ and s. To make this dependence explicit, I introduce the functions

$$\phi(\tau, s) = \Phi(V(\tau, s), a(\tau, s)) \tag{B.36}$$
$$p(\tau, s) = \Phi_V(V(\tau, s), a(\tau, s)) \tag{B.37}$$
$$q(\tau, s) = \Phi_a(V(\tau, s), a(\tau, s)). \tag{B.38}$$

The boundary condition (B.30) at $V = 0$ can now be written as

$$\phi(0, s) = \phi_0(s). \tag{B.39}$$

The constraints (B.32)– (B.34) become at $\tau = 0$ and $s = a^*$

$$\phi(0, a^*) = 0 \tag{B.40}$$
$$p(0, a^*) = 0 \tag{B.41}$$
$$q(0, a^*) = 0 \tag{B.42}$$
$$q_a(0, a^*) > 0, \quad p_V(0, a^*) > 0. \tag{B.43}$$

In terms of p and q, equation (B.28) can be rewritten as

$$F(a, p, q) \equiv (\mu - a)p - \frac{a}{\tau_a}q + \hat{D}p^2 = 0. \tag{B.44}$$

From the theory of first-order partial differential equations, it is known that the partial derivatives p and q satisfy quasilinear first-order partial differential equations. In fact, differentiating F with respect to V and noting that $q_V = \phi_{aV} = p_a$ results in

$$F_p p_V + F_q p_a = 0. \tag{B.45}$$

Analogously, differentiating F with respect to a and using $p_a = \phi_{Va} = q_V$ gives

$$F_p q_V + F_q q_a = -F_a. \tag{B.46}$$

The quasilinear equations (B.45) and (B.46) are solved by the characteristic equations[1]

[1] The general quasilinear equation $a(x, y, u)u_x + b(x, y, u)u_y = c(x, y, u)$ can be solved by the method of characteristics. To this end, we formally regard x and y as a function of a parameter τ. Taking the total derivative of $u(x, y)$ with respect to τ we see that u changes according to $\frac{du}{d\tau} = u_x \frac{dx}{d\tau} + u_y \frac{dy}{d\tau}$. Thus, if we choose $x(\tau)$ and $y(\tau)$ such that

$$\frac{dx}{d\tau} = a(x, y, u), \text{ and } \frac{dy}{d\tau} = b(x, y, u) \tag{B.47}$$

it follows from the quasilinear equation that

$$\frac{du}{d\tau} = c(x, y, u). \tag{B.48}$$

The three last equations are called characteristic equations and form a system of ordinary differential equations. A curve $(x(\tau), y(\tau), u(\tau))$ is called a characteristic. The set of all characteristics that emanate from an initial curve $C_0(s) = (x_0(s), y_0(s), u_0(s))$ (for each s there is one characteristic) form the solution surface $(x(\tau, s), y(\tau, s), u(\tau, s))$ containing the initial curve (boundary condition).

$$\frac{\mathrm{d}V}{\mathrm{d}\tau} = F_p = \mu - a + 2\hat{D}p \tag{B.49}$$

$$\frac{\mathrm{d}a}{\mathrm{d}\tau} = F_q = -\frac{a}{\tau_\mathrm{a}} \tag{B.50}$$

$$\frac{\mathrm{d}p}{\mathrm{d}\tau} = 0 \tag{B.51}$$

$$\frac{\mathrm{d}q}{\mathrm{d}\tau} = -F_a = p + \frac{1}{\tau_\mathrm{a}}q \tag{B.52}$$

with the "initial conditions" (B.35) and

$$p(0,s) = p_0(s), \quad q(0,s) = q_0(s). \tag{B.53}$$

The initial conditions $p_0(s)$ and $q_0(s)$ can be obtained from $\phi_0(s)$. In fact, for q_0 it holds

$$q_0(s) = \Phi_a(0,a) = \partial_s\phi(0,s) = \phi_0'(s). \tag{B.54}$$

Furthermore, equation (B.44) evaluated at $\tau = 0$ yields

$$p_0^2 + \frac{\mu - s}{\hat{D}}p_0 - \frac{s}{\hat{D}\tau_\mathrm{a}}q_0 = 0. \tag{B.55}$$

The quadratic equation has two solutions

$$p_0(s) = -\frac{\mu - s}{2\hat{D}} \pm \sqrt{\frac{(\mu - s)^2}{4\hat{D}^2} + \frac{s}{\hat{D}\tau_\mathrm{a}}q_0} \tag{B.56}$$

$$= -\frac{\mu - s}{2\hat{D}} \pm \sqrt{\frac{(\mu - s)^2}{4\hat{D}^2} + \frac{s}{\hat{D}\tau_\mathrm{a}}\phi_0'(s)}. \tag{B.57}$$

Only one solution satisfies the constraints at $s = a^*$. From Eq. (B.41) and (B.42) it is known that $p_0(a^*) = 0$ and $q_0(a^*) = \phi'(a^*) = 0$. Depending on the sign of $\mu - a^*$ the solution is

$$p_0(s) = -\frac{\mu - s}{2\hat{D}} + \mathrm{sgn}(\mu - a^*)\sqrt{\frac{(\mu - s)^2}{4\hat{D}^2} + \frac{s}{\hat{D}\tau_\mathrm{a}}\phi_0'(s)}. \tag{B.58}$$

Equation (B.51) states that p is conserved along the characteristics, hence

$$p(\tau,s) = p_0(s). \tag{B.59}$$

Using this result, Eqs. (B.49), (B.50) and (B.52) can be easily solved:

$$V(\tau,s) = \left[\mu + 2\hat{D}p_0(s)\right]\tau - \tau_\mathrm{a}s\left(1 - e^{-\tau/\tau_\mathrm{a}}\right), \tag{B.60}$$

$$a(\tau,s) = se^{-\tau/\tau_\mathrm{a}}, \tag{B.61}$$

$$q(\tau,s) = \phi_0'(s)e^{\tau/\tau_\mathrm{a}} - \tau_\mathrm{a}p_0(s)\left(1 - e^{\tau/\tau_\mathrm{a}}\right). \tag{B.62}$$

To obtain an equation for $\phi(\tau,s)$ I take the total derivative of $\Phi(V,a)$ with respect to τ.

Using Eqs. (B.49) and (B.50) this gives

$$\frac{\mathrm{d}\phi}{\mathrm{d}\tau} = \frac{\mathrm{d}\Phi}{\mathrm{d}\tau} = \Phi_V \frac{\mathrm{d}V}{\mathrm{d}\tau} + \Phi_a \frac{\mathrm{d}a}{\mathrm{d}\tau} \tag{B.63}$$

$$= pF_p + qF_q = p(\mu - a) + 2\hat{D}p^2 - \frac{a}{\tau_\mathrm{a}}q = \hat{D}p^2. \tag{B.64}$$

The last equality results from applying the relation (B.44).

As a result, the solution $\Phi(V,a)$ of Eq. (B.28) is given in parametric form as

$$V(\tau,s) = \left[\mu + 2\hat{D}p_0(s)\right]\tau - \tau_\mathrm{a}s\left(1 - e^{-\tau/\tau_\mathrm{a}}\right), \tag{B.65}$$

$$a(\tau,s) = se^{-\tau/\tau_\mathrm{a}}, \tag{B.66}$$

$$\Phi(V,a) \equiv \phi(\tau,s) = \hat{D}p_0^2(s)\tau + \phi_0(s) \tag{B.67}$$

with $t > 0$ and $s > 0$. The function $p_0(s)$ is given by Eq. (B.58). The curves $\mathcal{C}(s) = \{(V,a,\phi)(t)\}$ with the initial conditions $V(0,s) = 0$ $a(0,s) = s$ and $\phi(0,s) = \phi_0(s)$ are called characteristics. Each characteristic is uniquely characterized by the parameter s – the initial condition of a. The union of all characteristics forms a surface in the V,a,Φ-space, which represents the solution $\Phi(V,a)$.

Equation (B.29) for $\Psi(V,a)$ can be solved in a similar manner. As a result, $\Psi(V,a)$ is found in the parametric form as

$$\psi(\tau,s) = \psi_0(s)e^{\tau/\tau_\mathrm{a}}\sqrt{\frac{\mu - s + 2\hat{D}p_0(s)}{2\hat{D}p_0{}'(s)s\tau/\tau_\mathrm{a} + \mu - s + 2\hat{D}p_0(s)}}. \tag{B.68}$$

This solution can be derived as follows: Equation (B.29) is equivalent to the characteristic equations

$$\frac{\mathrm{d}V}{\mathrm{d}\tau} = \mu - a + 2\hat{D}p(s) \tag{B.69}$$

$$\frac{\mathrm{d}a}{\mathrm{d}\tau} = -\frac{a}{\tau_\mathrm{a}} \tag{B.70}$$

$$\frac{\mathrm{d}\psi}{\mathrm{d}\tau} = \left(\frac{1}{\tau_\mathrm{a}} - \hat{D}\phi_{VV}(\tau,s)\right)\psi. \tag{B.71}$$

The solution for V and a is identical to Eqs. (B.65) and (B.66). The equation for ψ can easily be integrated yielding

$$\psi(\tau,s) = \psi_0(s)\exp\left[-\int_0^\tau \mathrm{d}t'\,\left(\hat{D}\phi_{VV}(t',s) - \frac{1}{\tau_\mathrm{a}}\right)\right]. \tag{B.72}$$

At this point, Φ_{VV} is needed, which is in principle available as the solution for $\phi(\tau,s)$ and also its first derivative $p(\tau,s) = \phi_V(\tau,s) = p_0(s)$ are known. An explicit differentiation with respect to V is, however, infeasible because it is impossible to find the inverse transformation law $\tau = \tau(V,a)$ and $s = s(V,a)$ in explicit form. Hence, the solution cannot be expressed as a function of the original variables V and a. However, ϕ_{VV} can be obtained

by implicit differentiation: Using the chain rule yields

$$\phi_{VV}(\tau, s) = \left(\frac{\partial p}{\partial V}\right)_a = \frac{\partial p}{\partial \tau}\left(\frac{\partial \tau}{\partial V}\right)_a + \frac{\partial p}{\partial s}\left(\frac{\partial s}{\partial V}\right)_a = p_0'(s)\left(\frac{\partial s}{\partial V}\right)_a. \tag{B.73}$$

Here, $(\partial f/\partial x)_y$ denotes the partial derivative of f with respect to x with y fixed. At the same time, this notation indicates that f is regarded as a function of x and y. In particular, let us regard V as a function of s and a:

$$V = V(s, a) = \left[\mu + 2\hat{D}p_0(s)\right]\tau_\mathrm{a} \ln\frac{s}{a} - \tau_\mathrm{a} s + \tau_\mathrm{a} a. \tag{B.74}$$

Differentiating this relation with respect to V yields $1 = \left(\frac{\partial V}{\partial s}\right)_a \left(\frac{\partial s}{\partial V}\right)_a$ or

$$\left(\frac{\partial s}{\partial V}\right)_a = \frac{1}{\left(\frac{\partial V}{\partial s}\right)_a} = \frac{1}{2\hat{D}p_0'(s)\tau_\mathrm{a}\ln\left(\frac{s}{a}\right) + \frac{\tau_\mathrm{a}}{s}\left(\mu + 2\hat{D}p_0(s) - s\right)}. \tag{B.75}$$

Inserting into Eq. (B.73) and substituting $a = se^{-\tau/\tau_\mathrm{a}}$ yields

$$\phi_{VV}(\tau, s) = \frac{p_0'(s)}{2\hat{D}p_0'(s)\tau + \frac{\tau_\mathrm{a}}{s}\left(\mu + 2\hat{D}p_0(s) - s\right)}. \tag{B.76}$$

Taking the integral in (B.72) one arrives at (B.68).

Inner solution and asymptotic matching with WKB solution

The rapid change of the solution near the threshold can be treated in essentially the same manner as the solution in region I near the reset potential $V = 0$. In particular, I pass to the stretched variable $x = (V - V_\mathrm{th})/\epsilon$. The function $\hat{P}_0(x, a) = \sqrt{\epsilon}P_0(V, a)$ satisfies again equation (B.19) and the leading order solution that vanishes at the threshold, $x = 0$, is given by

$$\hat{P}_0(x, a) = \frac{N(a)}{\lambda(a)}\left(e^{\lambda(a)x} - 1\right), \tag{B.77}$$

where $\lambda(a) = (\mu - a)/\hat{D}$. The exponential term in (B.77) reveals that the thickness of the boundary layer at the threshold is $d(\epsilon) = \epsilon/\lambda(a) = \mathcal{O}(\epsilon)$ as $\epsilon \to 0$. From this it follows that the WKB solution is a valid asymptotic approximation only for $0 < V < V_\mathrm{th} - \mathcal{O}(\epsilon)$ (Fig. 3.14). On the other hand, I assume that the inner solution is not only valid inside the boundary layer (i.e. $V = V_\mathrm{th} - \mathcal{O}(\epsilon)$), but also at $V = V_\mathrm{th} - \mathcal{O}(\epsilon^{1/2})$. Then, at this position both WKB and inner solution are valid and should match asymptotically. This corresponds to the so-called intermediate limit, where

$$\epsilon \to 0, \quad V \to V_\mathrm{th}, \quad x = \frac{V - V_\mathrm{th}}{\epsilon} \to -\infty. \tag{B.78}$$

In the intermediate limit, the outer solution (B.25) becomes asymptotic to

$$\frac{1}{\sqrt{2\pi\epsilon}}\Psi(V_\mathrm{th}, a)\exp\left(-\frac{\Phi(V_\mathrm{th}, a)}{\epsilon}\right). \tag{B.79}$$

On the other hand, the inner solution (B.77) converges to $-N(a)/[\sqrt{\epsilon}\lambda(a)]$. Equating both limits and solving for $N(a)$ yields

$$N(a) = -\frac{\lambda(a)}{\sqrt{2\pi}}\Psi(V_{\text{th}}, a)\exp\left(-\frac{\Phi(V_{\text{th}}, a)}{\epsilon}\right). \tag{B.80}$$

Patching region I and II

The so far undetermined function $M(a)$ can now be specified by requiring the continuity of the probability density at $V = 0$ (boundary condition (B.22)). Eq. (B.24) and (B.25) results in

$$M(a) = \frac{\mu - a}{\sqrt{2\pi\hat{D}}}\Psi(0, a)\exp\left[-\frac{\Phi(0, a)}{\epsilon}\right]. \tag{B.81}$$

B.2.3. Reset condition

In principle, the reset condition (B.15) and the normalization condition (B.17) can be used to determine the functions $\phi_0(a) = \Phi(0, a)$ and $\psi_0(a) = \Psi(0, a)$. It turns out, however, that this is not feasible in the whole domain $a > 0$. Fortunately, in the case of weak noise, the knowledge of $\phi_0(a)$ and $\psi(a)$ is not necessary for all $a > 1$. Rather, it is sufficient to know the local behavior in the neighborhood of a^* because most probability is located close to the deterministic limit-cycle. This suggests to expand $\phi_0(a)$ and $\psi_0(a)$ about a^* to lowest order in $\delta a = a - a^*$:

$$\phi_0(a) = \frac{\phi_0''(a^*)}{2}\delta a^2 + \mathcal{O}(\delta a^3), \tag{B.82}$$

$$\psi_0(a) = \psi_0(a^*) + \mathcal{O}(\delta a). \tag{B.83}$$

Here, it was taken into account that both $\phi_0(a)$ and $\phi_0'(a)$ vanish on the limit-cycle (cf. equations (B.40) and (B.42)). Hence, $\phi_0(a)$ is locally a parabola. The reset condition can be used to determine $\phi_0''(a^*)$ instead of the whole function $\phi_0(a)$. Afterwards, the normalization condition is used to calculate $\psi_0(a^*)$ (Sec. B.2.4).

Let us rewrite the reset condition for convenience

$$\partial_V P_0(0^+, a) - \partial_V P_0(0^-, a) = \partial_V P_0(V_{\text{th}}, a - \Delta). \tag{B.84}$$

The derivatives can be found from the solutions (B.24), (B.25) and (B.77) in the respective regions. For $a^* < \mu$ they are given by

$$\partial_V P_0(0^+, a) = \frac{1}{\sqrt{2\pi\epsilon^3}}\left(\epsilon\Psi_V(0, a) - \Phi_V(0, a)\psi_0(a)\right)\exp\left(-\frac{\phi_0(a)}{\epsilon}\right) \tag{B.85}$$

$$\partial_V P_0(0^-, a) = \epsilon^{-3/2}M(a) = \frac{\mu - a}{\sqrt{2\pi\epsilon^3\hat{D}}}\psi_0(a)\exp\left(-\frac{\phi_0(a)}{\epsilon}\right) \tag{B.86}$$

$$\partial_V P_0(V_{\text{th}}, a - \Delta) = \epsilon^{-3/2}N(a - \Delta) = -\frac{\mu - a + \Delta}{\sqrt{2\pi\epsilon^3\hat{D}}}\Psi(V_{\text{th}}, a - \Delta)\exp\left(-\frac{\Phi(V_{\text{th}}, a - \Delta)}{\epsilon}\right). \tag{B.87}$$

In the case $a^* > \mu$, the expressions for $\partial_V P_0(0^+, a)$ and $\partial_V P_0(0^-, a)$ have to be inter-

changed. Inserting into (B.84) and neglecting the higher-order term $\epsilon\Psi_V(0,a)$ yields the reset condition in terms of the functions Φ and Ψ:

$$(\mu - a + \Delta)\Psi(V_{\text{th}}, a-\Delta)\exp\left(-\frac{\Phi(V_{\text{th}}, a-\Delta)}{\epsilon}\right) = \\ \text{sgn}(\mu - a)\left(\mu - a + \hat{D}\Phi_V(0,a)\right)\psi_0(a)\exp\left(-\frac{\phi_0(a)}{\epsilon}\right). \quad \text{(B.88)}$$

In this equation, $\Psi(V_{\text{th}}, a-\Delta)$, $\Phi(V_{\text{th}}, a-\Delta)$ and $\Phi_V(0,a)) \equiv p_0(a)$ are functionals of the initial data $\psi_0(a)$ and $\phi_0(a)$. As already mentioned, Eq. (B.88) together with the normalization condition should, in principle, determine $\psi_0(a)$ and $\phi_0(a)$. Unfortunately, there are several obstacles that render Eq. (B.88) intractable and make the determination of $\psi_0(a)$ and $\phi_0(a)$ in the full range $a > 0$ impossible. Firstly, the solution of Ψ and Φ on the threshold line is needed, i.e. for $V = V_{\text{th}}$. Indeed, the full solutions $\psi(\tau, s)$ and $\phi(\tau, s)$ are available by the equations (B.68) and (B.67). However, the characteristic coordinates cannot be explicitly expressed in terms of the coordinates V and a. This problem might be resolved by an approximate inversion of the transformation law (B.65), (B.66) in the interesting region about the limit-cycle, e.g. around the point $V = V_{\text{th}}$, $a = a^* - \Delta$. I will not pursue this approach because an approximate mapping of the threshold line into the t, s-coordinate system resulted in rather complicated formulas, which made a further analytical calculation difficult. Secondly, even if we knew the functions Ψ and Φ on the threshold line, it would be difficult to solve the non-linear equation (B.88), unless $\Phi(V_{\text{th}}, a-\Delta) = \phi_0(a)$, in which case the exponentials would cancel out. And thirdly, $p_0(a)$ and $\psi(\tau, s)$ contain derivatives of $\phi_0(a)$, which would render Eq. (B.88) a nonlinear differential equation. In short, I will not try to satisfy the reset condition for all a.

Local reset condition. The approach pursued here is to demand that the reset condition (B.88) is satisfied only locally around $a = a^*$, i.e. close to the deterministic limit-cycle. This weaker condition will hold strictly only in the asymptotic limit of weak noise. In particular, both sides of Eq. (B.88) are expanded about a^*. In this expansion one can use the properties (B.32) and (B.33) for $\Phi(V,a)$ on the limit-cycle. Specifically it holds $\Phi(V_{\text{th}}, a^* - \Delta) = \phi_0(a^*) = 0$ and $\Phi_a(V_{\text{th}}, a^* - \Delta) = \Phi_a(0, a^*) = 0$. With this, the right hand side of Eq. (B.88) reads up to first order in $\delta a = a - a^*$

$$(\mu - a^* + \Delta)\Psi(V_{\text{th}}, a^* - \Delta) + \left[(\mu - a^* + \Delta)\Psi_a(V_{\text{th}}, a^* - \Delta) - \Psi(V_{\text{th}}, a^* - \Delta)\right]\delta a.$$

The left hand side reads

$$|\mu - a^*|\psi_0(a^*) + \text{sgn}(\mu - a^*)\left[(\mu - a^*)\Psi_a(0, a^*) - (\hat{D}\partial_a\Phi_V(0, a^*) - 1)\psi_0(a^*)\right]\delta a.$$

Equating the zeroth order terms yields the condition

$$(\mu - a^* + \Delta)\Psi(V_{\text{th}}, a^* - \Delta) = |\mu - a^*|\psi_0(a^*) \quad \text{(B.89)}$$

or equivalently

$$\psi(T^*, a^*) = \frac{|\mu - a^*|}{\mu - a^* + \Delta}\psi_0(a^*). \quad \text{(B.90)}$$

In contrast to the full reset condition (B.88), the local conditions only involve the functions $\phi(\tau, s)$, $\psi(\tau, s)$ and its derivatives with respect to V and a on the limit-cycle, i.e. at $s = a^*$. In this way, a cumbersome inversion of the transformation law $(V, a) \to (\tau, s)$ can be avoided. To obtain the leading order of the stationary probability density it is sufficient to compute $\phi_0''(a^*)$ and $\psi(a^*)$. These quantities are completely determined by the zeroth order condition (B.90) and the normalization.

Calculation of $\phi_0''(a^*)$. The solution of $\psi(\tau, s)$, Eq. (B.68), leads to the particular value

$$\psi(T^*, a^*) = \psi_0(a^*) \frac{a^*}{(a^* - \Delta)\sqrt{\nu T^* + 1}} \tag{B.91}$$

with

$$\nu = \frac{2\hat{D} a^{*2} \phi_0''(a^*)}{\tau_a^2 (\mu - a^*)^2}. \tag{B.92}$$

In deriving (B.91), it has been used that $p_0(a^*) = 0$, $e^{T^*/\tau_a} = a^*/(a^* - \Delta)$ and that the derivative of $p_0(s)$ at $s = a^*$ is

$$p_0'(a^*) = \frac{a^* \phi_0''(a^*)}{\tau_a (\mu - a^*)} \tag{B.93}$$

(cf. Eq. (B.58)). Inserting $\psi(T^*, a^*)$ into the zeroth-order reset condition (B.90)the factor $\psi_0(a^*)$ drops out and the resulting equation can be solved for ν:

$$\nu = \frac{1}{T^*} \left[\left(\frac{(\mu - a^* + \Delta) a^*}{(\mu - a^*)(a^* - \Delta)} \right)^2 - 1 \right]. \tag{B.94}$$

Using the definition of ν, Eq. (B.92), the last equation can be solved for $\phi_0''(a^*)$. The final result can be written as

$$\phi_0''(a^*) = \frac{\tau_a^2 \mu \Delta \left[2a^* (\mu - a^* + \Delta) - \mu \Delta \right]}{2\hat{D} a^{*2} T^* (a^* - \Delta)^2}. \tag{B.95}$$

B.2.4. Normalization condition

For the leading approximation of $P_0(V, a)$ it remains to determine the prefactor $\psi_0(a^*)$. This quantity can be obtained from the normalization condition (3.64). We already know the leading order of the firing rate: it is simply given by $1/T^*$ – the inverse of the deterministic period. Thus, the leading order solution of $P_0(V, a)$ must fulfill the equation

$$-\epsilon \hat{D} \int_0^\infty \mathrm{d}a \, \partial_V P(V_{\mathrm{th}}, a) = \frac{1}{T^*}. \tag{B.96}$$

The left hand side of this equation must also be of zeroth order, which can be achieved by properly choosing the factor $\mathcal{N}$ in Eq. (B.25). As it becomes clear below, our choice $\mathcal{N} = 1/\sqrt{2\pi\epsilon}$ was indeed justified because only this scaling of ϵ makes the left hand side of Eq. (B.96) of order zero.

Using Eq. (B.87) yields

$$\frac{1}{T^*} = -\epsilon \hat{D} \int_0^\infty \mathrm{d}a \, \frac{N(a)}{\epsilon^{3/2}} \tag{B.97}$$

$$= \frac{1}{\sqrt{2\pi\epsilon}} \int_0^\infty \mathrm{d}a \, (\mu - a) \Psi(V_{\mathrm{th}}, a) \exp\left(-\frac{\Phi(V_{\mathrm{th}}, a)}{\epsilon} \right). \tag{B.98}$$

For small $\epsilon \ll 1$, the integrand is strongly peaked at $a = a^* - \Delta$. Using Laplace's method [see e.g. Bender and Orszag, 1999], the prefactor of the exponential can be taken at $a = a^* - \Delta$ and can be pulled in front of the integral. Furthermore, $\Phi(V_{\mathrm{th}}, a)$ is expanded to lowest order in $\delta a = a - (a^* - \Delta)$:

$$\Phi(V_{\mathrm{th}}, a) = \frac{1}{2} \Phi_{aa}(V_{\mathrm{th}}, a^* - \Delta)(a - a^* + \Delta)^2. \tag{B.99}$$

Finally, the lower integration bound is extended to $-\infty$ because negative values a do not contribute to the integral for small ϵ. Thus, Eq. (B.98) takes the form

$$\frac{1}{T^*} = \frac{1}{\sqrt{2\pi\epsilon}} (\mu - a^* + \Delta) \Psi(V_{\mathrm{th}}, a^* - \Delta) \int_{-\infty}^\infty \mathrm{d}a \, \exp\left(-\frac{\Phi_{aa}(V_{\mathrm{th}}, a^* - \Delta)}{2\epsilon} (a - a^* + \Delta)^2 \right), \tag{B.100}$$

$$= \frac{\mu - a^* + \Delta}{\sqrt{\Phi_{aa}(V_{\mathrm{th}}, a^* - \Delta)}} \psi(T^*, a^*). \tag{B.101}$$

Here, the Gaussian normalization formula $\int \mathrm{d}a \, \exp(-ba^2/(2\epsilon)) = \sqrt{2\pi\epsilon/b}$ was used. Thus, ϵ cancels out.

The second derivative of Φ with respect to a in Eq. (B.101) is taken on the limit-cycle and the threshold line, which corresponds to $s = a^*$ and $\tau = T^*$. For general τ, Φ_{aa} is given on the limit-cycle by

$$\Phi_{aa}|_{\mathcal{C}}^* = \partial_a q(\tau, a^*) = \frac{\partial q(\tau, a^*)}{\partial \tau} \left(\frac{\partial \tau}{\partial a} \right)_V + \frac{\partial q(\tau, a^*)}{\partial s} \left(\frac{\partial s}{\partial a} \right)_V \Big|_{V = V(\tau, s = a^*)} \tag{B.102}$$

From Eq. (B.52) and (B.62) it follows that $\partial q(\tau, a^*)/\partial \tau = 0$ because $p_0(a^*) = 0$ and $\phi_0(a^*) = 0$; hence the first term in Eq. (B.102) vanishes. For the second term it holds

$$\frac{\partial q(\tau, a^*)}{\partial s} = \phi_0''(a^*) \left[e^{\tau/\tau_{\mathrm{a}}} - \frac{a^*}{\mu - a^*} \left(1 - e^{\tau/\tau_{\mathrm{a}}} \right) \right], \tag{B.103}$$

where (B.62) and (B.93) have been used. In order to compute $(\partial s/\partial a)_V$ I regard V as a function of the variables s and a:

$$V(s, a) = \left[\mu + 2\hat{D} p_0(s) \right] \tau_{\mathrm{a}} \ln \frac{s}{a} - \tau_{\mathrm{a}} s + \tau_{\mathrm{a}} a. \tag{B.104}$$

The partial derivatives of this function at $s = a^*$ are

$$\left(\frac{\partial V}{\partial a}\right)_{s=a^*} = \tau_\mathrm{a}\left(1 - \frac{\mu}{a}\right) \tag{B.105}$$

$$\left(\frac{\partial V}{\partial s}\right)_a\Bigg|_{s=a^*} = \tau_\mathrm{a}\left(\frac{\mu}{a^*} + 2\hat{D}p_0'(a^*)\ln\frac{a^*}{a} - 1\right). \tag{B.106}$$

Using Eqs. (B.93) and (B.92) and substituting $a = a^* e^{\tau/\tau_\mathrm{a}}$ finally results in

$$\left(\frac{\partial s}{\partial a}\right)_{V=V(\tau,s=a^*)} = -\left.\frac{\left(\frac{\partial V}{\partial a}\right)_s}{\left(\frac{\partial V}{\partial s}\right)_a}\right|_{s=a^*,a=a^*e^{-\frac{\tau}{\tau_\mathrm{a}}}} = \frac{\mu e^{\tau/\tau_\mathrm{a}} - a^*}{(\mu - a^*)(\nu\tau + 1)}. \tag{B.107}$$

Thus, it follows

$$\Phi_{aa}|_{\mathcal{C}^*} = \frac{\mu e^{\tau/\tau_\mathrm{a}} - a^*}{(\mu - a^*)(\nu\tau + 1)}\left[e^{\tau/\tau_\mathrm{a}} - \frac{a^*}{\mu - a^*}\left(1 - e^{\tau/\tau_\mathrm{a}}\right)\right]\phi_0''(a^*). \tag{B.108}$$

It can be shown that the prefactor in front of $\phi_0''(a^*)$ becomes unity for $\tau = T^*$. In other words, we have found the remarkable result that Φ exhibits the same shape at the reset and the threshold:

$$\Phi_{aa}(V_\mathrm{th}, a^* - \Delta) = \phi_0''(a^*). \tag{B.109}$$

Substituting $\Phi_{aa}(V_\mathrm{th}, a^* - \Delta) = \phi_0''(a^*)$ into Eq. (B.101) and using (B.91) and (B.94) yields

$$\psi_0(a^*) = \frac{\sqrt{\phi_0''(a^*)}}{|\mu - a^*|T^*}. \tag{B.110}$$

Appendix C.

Neuron models with a stochastic adaptation current

C.1. Perfect integrate-and-fire model

In the main text, we derived a Langevin equation for the perfect integrate-and-fire (PIF) model with an adaptation current mediated by N_a two-state adaptation channels. The subthreshold membrane potential and the fraction of open adaptation channels W obey the dynamical equations

$$\dot{V} = \mu - \beta W + \sqrt{2D}\xi(t), \tag{C.1a}$$

$$\tau_w \dot{W} = -W + w_\infty(t) + \sqrt{\frac{2\tau_w \sigma^2(W, w_\infty(t))}{N_\mathrm{a}}}\xi_\mathrm{a}(t), \tag{C.1b}$$

where $w_\infty(t)$ is unity for a duration of $\tau_\mathrm{AP} = 1$ ms following each threshold crossing ($V = V_\mathrm{th}$) and is zero otherwise. The noise strength $\sigma^2(W, w_\infty(t))$ is given by

$$\sigma^2(W(t), w_\infty(t)) = \frac{1}{2}\left\{[1 - w_\infty(t)]W + w_\infty(t)[1 - W]\right\}. \tag{C.2}$$

Alternatively, the fraction of open channels W may be written as the sum of a deterministic part w and a noise part η:

$$W = w + \eta, \tag{C.3}$$

$$\tau_w \dot{w} = -w + w_\infty(t), \tag{C.4}$$

$$\tau_w \dot{\eta} = -\eta + \sqrt{\frac{2\tau_w \sigma^2(w + \eta, w_\infty(t))}{N_\mathrm{a}}}\xi_\mathrm{a}(t). \tag{C.5}$$

It is a feature of the PIF model that the firing rate is directly proportional to a constant driving current and independent of the noise. However, even for the slowly varying driving current $\mu - \beta W(t)$ in Eq. (C.1a), one can define an instantaneous firing rate

$$\bar{r}(t) = \frac{\mu - \beta W}{V_\mathrm{th}}, \tag{C.6}$$

which can be seen as the slowly varying firing rate that is obtained by averaging the spike train over the time scale τ_w of the adaptation. Averaging over time scales much larger than τ_w yields a constant firing rate r because the process is stationary. Thus, the

(stationary) firing rate can be obtained by averaging Eq. (C.6), which gives $r = (\mu - \beta\langle w\rangle)/V_{\text{th}}$. On the other hand, the firing rate is related to the mean fraction of open channels by averaging Eq. (C.4):

$$\langle w\rangle = \langle w_\infty(t)\rangle = r\tau_{\text{AP}}. \tag{C.7}$$

Solving for r yields

$$r = \frac{\lambda\mu}{V_{\text{th}}}, \tag{C.8}$$

where $\lambda = (1 + \beta\tau_{\text{AP}}/V_{\text{th}})^{-1}$.

Additive-noise approximation The noise term in Eq. (C.1b) or (C.5) is multiplicative because both arguments of the noise strength $\sigma^2(W, w_\infty(t))$ depend on the dynamical variables. For slow adaptation, $r\tau_w \gg 1$, and large N_{a}, however, the relative fluctuations of $\sigma^2(W, w_\infty(t))$ are small and, hence, σ^2 can be treated as constant (additive-noise approximation). This can be seen as follows: The rapid changes of $\sigma^2(W, w_\infty(t))$ due to the switchings of $w_\infty(t)$ between 0 and 1 on the time scale of the mean ISI are averaged out by the linear filter dynamics Eq. (C.5) if $r\tau_w \gg 1$. Thus, in Eq. (C.2) $w_\infty(t)$ can be replaced by its local average $\tau_{\text{AP}}\bar{r}(t)$. Because of Eq. (C.6), σ^2 can therefore be written as a quadratic function of W. As explained in Sec. 4.2.4 (paragraph "Stochastic adaptation"), the variance of W is $\lambda\sigma^2/N_{\text{a}}$. Thus, using $\langle W\rangle = \langle w\rangle$ and $\langle W^2\rangle \approx \lambda\langle\sigma^2\rangle/N_{\text{a}} + \langle w\rangle^2$ the mean of σ^2 can be self-consistently determined. It can be shown that

$$\langle\sigma^2\rangle = \left(\langle w\rangle - \langle w\rangle^2\right) / \left(1 - \frac{\Delta}{(1+\Delta)N_{\text{a}}}\right) \tag{C.9}$$

$$\approx \langle w\rangle - \langle w\rangle^2 \tag{C.10}$$

$$= r\tau_{\text{AP}} - (r\tau_{\text{AP}})^2, \tag{C.11}$$

where $\Delta = \beta\tau_{\text{AP}}/V_{\text{th}}$ and r is given by Eq. (C.8). In the second line we neglected the term that depends on N_{a}^{-1} because for large N_{a} it is much smaller than unity. Similarly, the variance of σ^2 can be calculated neglecting terms that are third and forth order in W. As a result, we obtain $\text{Var}\left[\sigma^2\right] = \frac{(1-\Delta)^2}{4(1+\Delta)N_{\text{a}}}\langle w\rangle + \mathcal{O}\left(\langle w\rangle^2\right)$. The relative fluctuations of the noise intensity are given by $\sqrt{\text{Var}[\sigma^2]}/\langle\sigma^2\rangle$. Inserting the expressions for mean and variance of σ^2 to first order in $\langle w\rangle$, we find that the additive-noise approximation $\sigma(W, w_\infty(t)) \approx \langle\sigma^2\rangle$ is roughly valid if

$$\frac{|1-\Delta|}{2\sqrt{N_{\text{a}}\tau_{\text{AP}}\mu/V_{\text{th}}}} \ll 1. \tag{C.12}$$

For the standard parameter set used in Chap. 4, $\Delta = 3$, $\mu = 0.4$, $\tau_{\text{AP}} = 1$, $V_{\text{th}} = 1$, we find the condition $1/\sqrt{0.4N_{\text{a}}} \ll 1$. For instance, for $N_{\text{a}} = 200$ the relative fluctuations of σ^2 are 11%.

C.2. Modified Traub-Miles model

In Sec. 4.3, the analytical predictions of the PIF model have been tested in the more realistic conductance-based Traub & Miles model modified by Ermentrout et al. [2001]. This model is given by the current-balance equation

$$C_\mathrm{m}\frac{dV}{dt} = -I_\mathrm{Na} - I_\mathrm{K} - I_\mathrm{L} - I_\mathrm{a} + I + \sqrt{2D}\xi(t)\ , \tag{C.13}$$

where $C_\mathrm{m} = 1\ \mu\mathrm{F/cm^2}$ is the membrane capacitance, I is the base current, and D denotes the intensity of Gaussian white noise with correlation function $\langle\xi(t)\xi(t')\rangle = \delta(t-t')$. The deterministic ionic currents are given by the following equations Ermentrout et al. [2001]:

Sodium current: $I_\mathrm{Na} = \bar{g}_\mathrm{Na} m^3 h (V - E_\mathrm{Na})$
$\bar{g}_\mathrm{Na} = 100\ \mathrm{mS/cm^2}$, $E_\mathrm{Na} = +50\ \mathrm{mV}$
$dm/dt = \alpha_\mathrm{m}(V)(1-m) - \beta_\mathrm{m}(V)m$, $dh/dt = \alpha_\mathrm{h}(V)(1-h) - \beta_\mathrm{h}(V)h$
$\alpha_\mathrm{m}(V) = 0.32(V+54)/(1-\exp(-(V+54)/4))$, $\beta_\mathrm{m}(V) = 0.28(V+27)/(\exp((V+27)/5)-1)$
$\alpha_\mathrm{h}(V) = 0.128\exp(-(V+50)/18)$, $\beta_\mathrm{h}(V) = 4/(1+\exp(-(V+27)/5))$.

Potassium current: $I_\mathrm{K} = \bar{g}_\mathrm{K} n^4 (V - E_\mathrm{K})$
$\bar{g}_\mathrm{K} = 80\ \mathrm{mS/cm^2}$, $E_\mathrm{K} = -100\ \mathrm{mV}$, $dn/dt = \alpha_\mathrm{n}(V)(1-n) - \beta_\mathrm{n}(V)n$
$\alpha_\mathrm{n}(V) = 0.032(V+52)/(1-\exp(-(V+52)/5))$, $\beta_\mathrm{n}(V) = 0.5\exp(-(V+57)/40)$.

Leak current: $I_\mathrm{L} = \bar{g}_\mathrm{L}(V - E_\mathrm{L})$
$\bar{g}_\mathrm{L} = 0.2\ \mathrm{mS/cm^2}$, $E_\mathrm{L} = -67\ \mathrm{mV}$.

M-type adaptation current: $I_\mathrm{a} = \bar{g}_\mathrm{a} w (V - E_\mathrm{a})$
$\bar{g}_\mathrm{a} = 1.15\ \mathrm{mS/cm^2}$, $E_\mathrm{a} = -100\ \mathrm{mV}$, $dw/dt = (w_\infty(V) - w)/t_\mathrm{w}(V)$
$t_\mathrm{w}(V) = 11.4\ \tau_\mathrm{w}/(3.3\exp((V+35)/20) + \exp(-(V+35)/20))$, $\tau_\mathrm{w} = 100\ \mathrm{ms}$,
$w_\infty(V) = 1/(1+\exp(-(V+35)/10))$.

In the case of a stochastic adaptation current, the M-type adaptation current is modeled as $I_\mathrm{a} = \bar{g}_\mathrm{a} W (V - E_\mathrm{a})$, where $W = N_\mathrm{op}/N_\mathrm{a}$ denotes the fraction of open channels. As in the PIF model, the adaptation channels were assumed to be binary ion channels with transition rates $\alpha_w(V) = w_\infty(V)/t_\mathrm{w}(V)$ and $\beta_w(V) = (1 - w_\infty(V))/t_\mathrm{w}(V)$. The maximal channel conductance $\bar{g}_\mathrm{a}$ and the constant base current ($I = 18\ \mu\mathrm{A/cm^2}$) were chosen to result in a CV of approximately 0.6 and a firing rate of 100 Hz for a simulation of $N_\mathrm{a} = 100$ ion channels. For the simulation with deterministic adaptation current and additive white noise the base current was adjusted to yield the same rate while keeping the conductance $\bar{g}_\mathrm{a}$ the same. The simulation of this model has been carried out by K. Fisch [Fisch, 2011].

Bibliography

L. F. Abbott and C. van Vreeswijk. Asynchronous states in a network of pulse-coupled oscillators. *Phys. Rev. E*, 48:1483, 1993.

V. S. Anishchenko, A. B. Neiman, F. Moss, and L. Schimansky-Geier. Stochastic resonance: noise-enhanced order. *Physics-Uspekhi*, 42:7, 1999.

O. Avila-Akerberg and M. J. Chacron. Noise shaping in neural populations. *Phys. Rev. E*, 79(1):011914–011914, 2009.

O. Avila-Akerberg and M. J. Chacron. Nonrenewal spike train statistics: causes and functional consequences on neural coding. *Experimental Brain Research*, 2011.

L Badel, S Lefort, R Brette, C C Petersen, W Gerstner, and M J Richardson. Dynamic i-v curves are reliable predictors of naturalistic pyramidal-neuron voltage traces. *J Neurophysiol*, 99(2):656–666, Feb 2008.

S. Bahar, J.W. Kantelhardt, A. Neiman, H.H.A. Rego, D.F. Russell, L. Wilkens, A. Bunde, and F. Moss. Long-range temporal anti-correlations in paddlefish electroreceptors. *Europhys. Lett.*, 56:454, 2001.

C. Bauermeister. The effect of stochastic oscillations on neural firing statistics. Master's thesis, Technische Universität Dresden, 2012.

J M Bekkers, G B Richerson, and C F Stevens. Origin of variability in quantal size in cultured hippocampal neurons and hippocampal slices. *Proc Natl Acad Sci U S A*, 87 (14):5359–5362, 1990.

J. Benda and R. Hennig. Spike-frequency adaptation generates intensity invariance in a primary auditory interneuron. *J Comp Neurosci*, 24(2):113–136, 2008.

J. Benda and A. V. M. Herz. A universal model for spike-frequency adaptation. *Neural Comp.*, 15:2523, 2003.

J. Benda, M. Bethge, M. Hennig, K. Pawelzik, and A.V.M. Herz. Spike-frequency adaptation: Phenomenological model and experimental tests. *Neurocomput*, 38–40:105–110, 2001.

J. Benda, A. Longtin, and L. Maler. Spike-Frequency adaptation separates transient communication signals from background oscillations. *J. Neurosci.*, 25(9):2312–2321, 2005.

J. Benda, L. Maler, and A. Longtin. Linear versus nonlinear signal transmission in neuron models with adaptation currents or dynamic thresholds. *J Neurophysiol*, 104:2806–2820, 2010.

C. M. Bender and S. A. Orszag. *Advanced Mathematical Methods for Scientists and Engineers I: Asymptotic Methods and Perturbation Theory: v. 1*. Springer, 1 edition, 1999.

N. Brenner, O. Agam, W. Bialek, and R. de Ruyter van Steveninck. Statistical properties of spike trains: Universal and stimulus-dependent aspects. *Phys. Rev. E*, 66:031907, 2002.

R. Brette and W. Gerstner. Adaptive exponential integrate-and-fire model as an effective description of neuronal activity. *J Neurophysiol*, 94:3637–3642, 2005.

D A Brown and P R Adams. Muscarinic suppression of a novel voltage-sensitive K+ current in a vertebrate neurone. *Nature*, 283(5748):673–676, 1980.

N. Brunel and V. Hakim. Fast global oscillations in networks of integrate-and-fire neurons with low firing rates. *Neural Computation*, 11:1621, 1999.

N. Brunel and S. Sergi. Firing frequency of leaky integrate-and-fire neurons with synaptic currents dynamics. *J. Theor. Biol.*, 195:87, 1998.

A. Bulsara, S. B. Lowen, and C. D. Rees. Cooperative behavior in the periodically modulated Wiener process: Noise-induced complexity in a model neuron. *Phys. Rev. E*, 49: 4989, 1994.

A. N. Burkitt. Balanced neurons: analysis of leaky integrate-and-fire neurons with reversal potentials. *Biol. Cybern.*, 85(4):247–255, 2001.

A. N. Burkitt. A review of the integrate-and-fire neuron model: I. homogeneous synaptic input. *Biol. Cybern.*, 95:1–19, 2006a.

A. N. Burkitt. A review of the integrate-and-fire neuron model: Ii. inhomogeneous synaptic input and network properties. *Biol. Cybern.*, 95:97–112, 2006b.

R. M. Capocelli and L. M. Ricciardi. Diffusion approximation and first passage time problem for a model neuron. *Kybernetik*, 8:214, 1971.

M. J. Chacron, A. Longtin, M. St-Hilaire, and L. Maler. Suprathreshold stochastic firing dynamics with memory in P-type electroreceptors. *Phys. Rev. Lett.*, 85:1576, 2000.

M. J. Chacron, A. Longtin, and L. Maler. Negative interspike interval correlations increase the neuronal capacity for encoding time-dependent stimuli. *J. Neurosci.*, 21:5328, 2001.

M. J. Chacron, K. Pakdaman, and A. Longtin. Interspike interval correlations, memory, adaptation, and refractoriness in a leaky integrate-and-fire model with threshold fatigue. *Neural Comp.*, 15:253, 2003.

M. J. Chacron, B. Lindner, and A. Longtin. Noise shaping by interval correlations increases neuronal information transfer. *Phys. Rev. Lett.*, 92:080601, 2004a.

M. J. Chacron, B. Lindner, and A. Longtin. Erratum: Noise shaping by interval correlations increases neuronal information transfer. *Phys. Rev. Lett.*, 93:059904, 2004b.

M. J. Chacron, B. Lindner, L. Maler, A. Longtin, and J. Bastian. Experimental and theoretical demonstration of noise shaping by interspike interval correlations. In N.G. Stocks, D. Abbott, and R.P. Morse, editors, *Fluctuations and Noise in Biological, Biophysical and Biomedical Systems III*, volume 5841, page 150. SPIE, 2005a.

M. J. Chacron, A. Longtin, and L. Maler. Delayed excitatory and inhibitory feedback shape neural information transmission. *Phys. Rev. E*, 72:051917, 2005b.

F. S. Chance, L. F. Abbott, and A. D. Reyes. Gain modulation from background synaptic input. *Neuron*, 35(4):773–782, 2002.

S. Chandrasekhar. Stochastic Problems in Physics and Astronomy. *Reviews of Modern Physics*, 15:1–89, 1943.

C. Chow and J. White. Spontaneous action potentials due to channel fluctuations. *Biophys J*, 71(6):3013–3021, 1996.

A Compte, M V Sanchez-Vives, D A McCormick, and X J Wang. Cellular and network mechanisms of slow oscillatory activity (<1 hz) and wave propagations in a cortical network model. *J Neurophysiol*, 89(5):2707–2725, 2003.

D. R. Cox. *Renewal Theory*. Methuen, London, 1962.

D. R. Cox and P. A. W. Lewis. *The Statistical Analysis of Series of Events*. Chapman and Hall, London, 1966.

D. R. Cox and H. D. Miller. *The theory of stochastic processes*. Chapman and Hall, 1965.

D.R. Cox and V. Isham. *Point Processes*. Chapman & Hall, London, 1980.

P. Dayan and L. F. Abbott. *Theoretical Neuroscience: Computational and Mathematical Modeling of Neural Systems*. The MIT Press, 1 edition, 2005.

M Deger, M Helias, C Boucsein, and S Rotter. Statistical properties of superimposed stationary spike trains. *J Comput Neurosci*, 32:443–463, 2012.

A Destexhe and D Paré. Impact of network activity on the integrative properties of neocortical pyramidal neurons in vivo. *J Neurophysiol*, 81(4):1531–1547, 1999.

K. Diba, H. A. Lester, and C. Koch. Intrinsic noise in cultured hippocampal neurons: Experiment and modeling. *J. Neurosci.*, 24(43):9723–9733, 2004.

T. A. Engel, L. Schimansky-Geier, A.V.M. Herz, S. Schreiber, and I. Erchova. Subthreshold Membrane-Potential resonances shape Spike-Train patterns in the entorhinal cortex. *J. Neurophysiol.*, 100(3):1576, 2008.

T. A. Engel, B. Helbig, D. F. Russell, L. Schimansky-Geier, and A.B. Neiman. Coherent stochastic oscillations enhance signal detection in spiking neurons. *Phys. Rev. E*, 80(2): 021919, 2009.

B. Ermentrout, M. Pascal, and B. Gutkin. The effects of spike frequency adaptation and negative feedback on the synchronization of neural oscillators. *Neural Comp*, 13:1285–1310, 2001.

A. A. Faisal, L. P. J. Selen, and D. M. Wolpert. Noise in the nervous system. *Nat Rev Neurosci*, 9:292–303, 2008.

F. Farkhooi, M. F. Strube-Bloss, and M. P. Nawrot. Serial correlation in neural spike trains: Experimental evidence, stochastic modeling, and single neuron variability. *Phys. Rev. E*, 79(2):021905–10, 2009.

F Farkhooi, E Muller, and M P Nawrot. Adaptation reduces variability of the neuronal population code. *Phys. Rev. E*, 83(5 Pt 1):050905–050905, 2011.

K. Fisch. *The contribution of spike-frequency adaptation to the variability of spike responses in a sensory neuron*. PhD thesis, Ludwig-Maximilians-Universität München, 2011.

K. Fisch, T. Schwalger, B. Lindner, A.V.M. Herz, and J. Benda. Channel noise from both slow adaptation currents and fast currents is required to explain spike-response variability in a sensory neuron. *J. Neurosci.*, 32(48):17332–17344, 2012.

R. A. FitzHugh. Impulses and physiological states in theoretical models of nerve membrane. *Biophys. J.*, 1:445, 1961.

I. A. Fleidervish, A. Friedman, and M. J. Gutnick. Slow inactivation of Na+ current and slow cumulative spike adaptation in mouse and guinea-pig neocortical neurones in slices. *J Physiol*, 493(1):83–97, 1996.

N. Fourcaud and N. Brunel. Dynamics of the firing probability of noisy integrate-and-fire neurons. *Neural Comp.*, 14:2057, 2002.

N Fourcaud-Trocmé, D Hansel, C van Vreeswijk, and N Brunel. How spike generation mechanisms determine the neuronal response to fluctuating inputs. *J Neurosci*, 23(37): 11628–11640, 2003.

R. F. Fox. Stochastic versions of the Hodgin-Huxley equations. *Biophys. J.*, 72:2068, 1997.

R. F. Fox and Y. Lu. Emergent collective behavior in large numbers of globally coupled independently stochastic ion channels. *Phys Rev E*, 49(4):3421, 1994.

G. Fuhrmann, H. Markram, and M. Tsodyks. Spike frequency adaptation and neocortical rhythms. *J Neurophysiol*, 88(2):761–770, 2002.

F. Gabbiani and C. Koch. Principles of spike train analysis. In C. Koch and I. Segev, editors, *Methods in Neuronal Modeling:From Ions to Networks*, page 313. MIT Press, Cambridge, Mass., 1989.

F. Gabbiani and H. G. Krapp. Spike-frequency adaptation and intrinsic properties of an identified, looming-sensitive neuron. *J. Neurophysiol.*, 96(6):2951–2962, 2006.

L. Gammaitoni, P. Hänggi, P. Jung, and F. Marchesoni. Stochastic resonance. *Rev. Mod. Phys.*, 70:223, 1998.

C. W. Gardiner. *Handbook of Stochastic Methods*. Springer-Verlag, Berlin, 1985.

C. Geisler and J. M. Goldberg. A stochastic model of the repetitive activity of neurons. *Biophys. J.*, 6(1):53–69, 1966.

G. L. Gerstein and B. Mandelbrot. Random walk models for the spike activity of a single neuron. *Biophys. J.*, 4:41, 1964.

W. Gerstner and W.M. Kistler. *Spiking Neuron Models: Single Neurons, Populations, Plasticity*. Cambridge University Press, Cambridge, 2002.

W Gerstner and R Naud. Neuroscience. how good are neuron models? *Science*, 326(5951): 379–380, Oct 2009.

D. T. Gillespie. The chemical Langevin equation. *J. Chem. Phys.*, 113:297–306, 2000.

R. M. Glantz and J. P. Schroeter. Analysis and simulation of gain control and precision in crayfish visual interneurons. *J Neurophysiol*, 92(5):2747–2761, 2004.

R. Graham and T. Tél. On the weak-noise limit of fokker-planck models. *Journal of Statistical Physics*, 35(5-6):729–748, 1984.

E.G. Gray. The fine structure of the insect ear. *Philosophical Transactions of the Royal Society B*, 243:75–94, 1960.

M. Häusser and B. Mel. Dendrites: bug or feature? *Curr Opin Neurobiol*, 13(3):372–383, 2003.

A. V. Herz, T. Gollisch, C. K. Machens, and D. Jaeger. Modeling single-neuron dynamics and computations: a balance of detail and abstraction. *Science*, 314(5796):80–85, 2006.

B. Hille. *Ion channels of excitable membranes*. Sinauer Associates Inc, 3rd edition, 2001.

A. L. Hodgkin and A. F. Huxley. A quantitative description of membrane current and its application to conduction and excitation in nerve. *J. Physiol. (Lond.)*, 10:500, 1952.

D Holcman and M Tsodyks. The emergence of up and down states in cortical networks. *PLoS Comput Biol*, 2(3):e23, 2006.

A. V. Holden. *Models of the Stochastic Activity of Neurones*. Springer-Verlag, Berlin, 1976.

D. C. Hood and M. A. Finkelstein. Sensitivity to light. In K. R. Boff, L. Kaufmann, and J. P. Thomas, editors, *Handbook of perception and human performance*, volume 1: Sensory processes and perception, chapter 5. Wiley, New York, 1986.

E. M. Izhikevich. *Dynamical Systems in Neuroscience: The Geometry of Excitability and Bursting*. MIT Press, 2005.

G. A. Jacobson, K. Diba, A. Yaron-Jakoubovitch, Y. Oz, C. Koch, I. Segev, and Y. Yarom. Subthreshold voltage noise of rat neocortical pyramidal neurones. *J. Physiol.*, 564(1): 145–160, 2005.

E. R. Kandel, J. H. Schwartz, and T. M. Jessell. *Principles of Neural Science*. Mcgraw-Hill Professional, 4. a. edition, 2000.

J. Keener and J. Sneyd. *Mathematical Physiology: II: Systems Physiology*. Springer, 2nd edition, 2008.

A. M. Keleshian, R. O. Edeson, G. J. Liu, and B. W. Madsen. Evidence for cooperativity between nicotinic acetylcholine receptors in patch clamp records. *Biophys J*, 78(1):1–12, 2000.

B. W. Knight. Dynamics of encoding in a population of neurons. *J. Gen. Physiol.*, 59:734, 1972a.

B. W. Knight. The relationship between the firing rate of a single neuron and the level of activity in a population of neurons. *J. Gen. Physiol.*, 59:767, 1972b.

D. E. Koshland, A. Goldbeter, and J. B. Stock. Amplification and adaptation in regulatory and sensory systems. *Science*, 217(4556):220–225, 1982.

G. Kreiman, R. Krahe, W. Metzner, C. Koch, and F. Gabbiani. Robustness and variability of neuronal coding by amplitude- sensitive afferents in the weakly electric fish eigenmannia. *J Neurophysiol*, 84:189–204, 2000.

G. La Camera, A. Rauch, H. Lüscher, W. Senn, and S. Fusi. Minimal models of adapted neuronal response to in Vivo–Like input currents. *Neural Comp.*, 16(10):2101–2124, 2004.

J. Ladenbauer, M. Augustin, L. Shiau, and K. Obermayer. Impact of adaptation currents on synchronization of coupled exponential integrate-and-fire neurons. *PLoS Comput Biol*, 8(4), 2012.

I Lampl, I Reichova, and D Ferster. Synchronous membrane potential fluctuations in neurons of the cat visual cortex. *Neuron*, 22(2):361–374, 1999.

L. Lapicque. Recherches quantitatives sur l'excitation électrique des nerfs traitéecomme une polarization. *J. Physiol. Pathol. Gen.*, 9:620, 1907.

M. E. Larkum, T. Nevian, M. Sandler, A. Polsky, and J. Schiller. Synaptic integration in tuft dendrites of layer 5 pyramidal neurons: a new unifying principle. *Science*, 325 (5941):756–760, 2009.

P. E. Latham, B. J. Richmond, P. G. Nelson, and S. Nirenberg. Intrinsic dynamics in neuronal networks. I. theory. *J. Neurophysiol.*, 83:808, 2000.

H. Lecar and R. Nossal. Theory of threshold fluctuations in nerves II. Analysis of various sources of membrane noise. *Biophys. J*, 11(12):1068–1084, 1971.

B. Lindner. *Coherence and Stochastic Resonance in Nonlinear Dynamical Systems*. Logos-Verlag, Berlin, 2002.

B. Lindner. Interspike interval statistics of neurons driven by colored noise. *Phys. Rev. E*, 69:022901, 2004a.

B. Lindner. Moments of the first passage time under weak external driving. *J. Stat. Phys.*, 117:703, 2004b.

B. Lindner. Superposition of many independent spike trains is generally not a Poisson process. *Phys. Rev. E*, 73:022901, 2006.

B. Lindner and A. Longtin. Effect of an exponentially decaying threshold on the firing statistics of a stochastic integrate-and-fire neuron. *J. Theo. Biol.*, 232:505, 2005.

B. Lindner and L. Schimansky-Geier. Transmission of noise coded versus additive signals through a neuronal ensemble. *Phys. Rev. Lett.*, 86:2934, 2001.

B. Lindner and T. Schwalger. Correlations in the sequence of residence times. *Phys. Rev. Lett.*, 98(21):210603, 2007.

B. Lindner, L. Schimansky-Geier, and A. Longtin. Maximizing spike train coherence or incoherence in the leaky integrate-and-fire model. *Phys. Rev. E*, 66:031916, 2002.

B. Lindner, J. García-Ojalvo, A. Neiman, and L. Schimansky-Geier. Effects of noise in excitable systems. *Phys. Rep.*, 392:321, 2004.

B. Lindner, M. J. Chacron, and A. Longtin. Integrate-and-fire neurons with threshold noise - a tractable model of how interspike interval correlations affect neuronal signal transmission. *Phys. Rev. E*, 72:021911, 2005a.

B. Lindner, B. Doiron, and A. Longtin. Theory of oscillatory firing induced by spatially correlated noise and delayed inhibitory feedback. *Phys. Rev. E*, 72(6):061919–14, 2005b.

B. Lindner, D. Gangloff, A. Longtin, and J. E. Lewis. Broadband coding with dynamic synapses. *J. Neurosci.*, 29(7):2076–2088, 2009.

Y.-H. Liu and X.-J. Wang. Spike-frequency adaptation of a generalized leaky integrate-and-fire model neuron. *J. Comp. Neurosci.*, 10:25, 2001.

V.N. Livina, S. Havlin, and A. Bunde. Memory in the occurrence of earthquakes. *Phys. Rev. Lett.*, 95:208501, 2005.

S. B. Lowen and M. C. Teich. Auditory-nerve action potentials form a nonrenewal point process over short as well as long time scales. *J. Acoust. Soc. Am.*, 92:803, 1992.

C K Machens, M B Stemmler, P Prinz, R Krahe, B Ronacher, and A V Herz. Representation of acoustic communication signals by insect auditory receptor neurons. *J Neurosci*, 21 (9):3215–3227, 2001.

C K Machens, T Gollisch, O Kolesnikova, and A V Herz. Testing the efficiency of sensory coding with optimal stimulus ensembles. *Neuron*, 47(3):447–456, 2005.

D. V. Madison and R. A. Nicoll. Control of the repetitive discharge of rat CA 1 pyramidal neurones in vitro. *J. Physiol.*, 354(1):319–331, 1984.

Z F Mainen and T J Sejnowski. Reliability of spike timing in neocortical neurons. *Science*, 268(5216):1503–1506, 1995.

J. A. McFadden. On the lengths of intervals in a stationary point process. *J ROY STAT SOC B MET*, 24(2):364–382, 1962.

S. Mensi, R. Naud, C. Pozzorini, M. Avermann, C. C. H. Petersen, and W. Gerstner. Parameter extraction and classification of three cortical neuron types reveals two distinct adaptation mechanisms. *J Neurophysiol*, 2011.

M. Merkel and B. Lindner. Synaptic filtering of rate-coded information. *Phys. Rev. E*, 81 (4 Pt 1):041921–041921, 2010.

J. W. Middleton, M. J. Chacron, B. Lindner, and A. Longtin. Firing statistics of a neuron model driven by long-range correlated noise. *Phys. Rev. E*, 68:021920, 2003.

R. Moreno-Bote and N. Parga. Role of synaptic filtering on the firing response of simple model neurons. *Phys. Rev. Lett.*, 92(2):028102, 2004.

E. Muller, L. Buesing, J. Schemmel, and K. Meier. Spike-frequency adapting neural ensembles: Beyond mean adaptation and renewal theories. *Neural Comp.*, 19(11):2958–3110, 2007.

M. P. Nawrot, C. Boucsein, V. Rodriguez-Molina, A. Aertsen, S. Grun, and S. Rotter. Serial interval statistics of spontaneous activity in cortical neurons in vivo and in vitro. *Neurocomp.*, 70:1717, 2007.

A. Neiman and D. F. Russell. Stochastic biperiodic oscillations in the electroreceptors of paddlefish. *Phys. Rev. Lett.*, 86:3443, 2001.

A. Neiman and D. F. Russell. Two distinct types of noisy oscillators in electroreceptors of paddlefish. *J Neurophysiol*, 92:492–509, 2004.

A. Neiman and D. F. Russell. Models of stochastic biperiodic oscillations and extended serial correlations in electroreceptors of paddlefish. *Phys. Rev. E*, 71(6):061915, 2005.

W. H. Nesse, L. Maler, and A. Longtin. Biophysical information representation in temporally correlated spike trains. *Proc Natl Acad Sci USA*, 107(51):21973–21978, 2010.

A. Ochab-Marcinek, G. Schmid, I. Goychuk, and P. Hänggi. Noise-assisted spike propagation in myelinated neurons. *PhysRev E*, 79(1):011904, 2009.

N Parga and L F Abbott. Network model of spontaneous activity exhibiting synchronous transitions between up and down states. *Front Neurosci*, 1(1):57–66, 2007.

D. H. Perkel, G. L. Gerstein, and G. P. Moore. Neuronal spike trains and stochastic point processes. i. the single spike train. *Biophys. J.*, 7(4):391–418, 1967.

S. P. Peron and F. Gabbiani. Spike frequency adaptation mediates looming stimulus selectivity in a collision-detecting neuron. *Nat Neurosci*, 12(3):318–326, 2009a.

S. P. Peron and F. Gabbiani. Role of spike-frequency adaptation in shaping neuronal response to dynamic stimuli. *Biol. Cybern.*, 100(6):505–520, 2009b.

L. Pontryagin, A. Andronov, and A. Witt. On the statistical investigation of dynamical systems. *Zh. Eksp. Teor. Fiz.*, 3:172, 1933. Reprinted in *Noise in Nonlinear Dynamical Systems*, 1989, ed. by F. Moss and P. V. E. McClintock (Cambridge University Press, Cambridge), Vol. 1, p. 329.

S. A. Prescott and T. J. Sejnowski. Spike-rate coding and spike-time coding are affected oppositely by different adaptation mechanisms. *J Neuroscie*, 28(50):13649–13661, 2008.

R. Ratnam and M. E. Nelson. Nonrenewal statistics of electrosensory afferent spike trains: Implications for the detection of weak sensory signals. *J. Neurosci.*, 20:6672, 2000.

L. M. Ricciardi. *Diffusion Processes and Related Topics on Biology*. Springer-Verlag, Berlin, 1977.

L. M. Ricciardi and L. Sacerdote. The Ornstein-Uhlenbeck process as a model for neuronal activity. *Biol. Cybernetics*, 35:1, 1979.

M. J. E. Richardson. Dynamics of populations and networks of neurons with voltage-activated and calcium-activated currents. *Phys. Rev. E*, 80(2):021928–16, 2009.

M. J. E. Richardson and W. Gerstner. Synaptic shot noise and conductance fluctuations affect the membrane voltage with equal significance. *Neural Comp.*, 17:923, 2005.

H. Risken. *The Fokker-Planck Equation*. Springer, Berlin, 1984.

A Rokem, S Watzl, T Gollisch, M Stemmler, A V Herz, and I Samengo. Spike-timing precision underlies the coding efficiency of auditory receptor neurons. *J Neurophysiol*, 95(4):2541–2552, 2006.

H. Römer. Die informationsverarbeitung tympanaler rezeptorelemente von *locusta migratoria* (acrididae, orthoptera). *J Comp Physiol A*, 109, 1976.

B Ronacher, A Franz, S Wohlgemuth, and R M Hennig. Variability of spike trains and the processing of temporal patterns of acoustic signals-problems, constraints, and solutions. *J Comp Physiol A*, 190(4):257–277, 2004.

R Rosenbaum, J Rubin, and B Doiron. Short term synaptic depression imposes a frequency dependent filter on synaptic information transfer. *PLoS Comput Biol*, 8(6), 2012.

M V Sanchez-Vives and D A McCormick. Cellular and network mechanisms of rhythmic recurrent activity in neocortex. *Nat Neurosci*, 3(10):1027–1034, 2000.

R. Schaette, T. Gollisch, and A.V.M. Herz. Spike-train variability of auditory neurons in vivo: Dynamic responses follow predictions from constant stimuli. *J Neurophysiol*, 93: 3270–3281, 2005.

L. Schimansky-Geier and C. Zülicke. Harmonic noise: Effect on bistable systems. *Z. Phys. B*, 79:451, 1990.

E Schrödinger. Zur theorie der fall- und steigversuche an teilchen mit brownscher bewegung. *Physik. Z.*, 16:289–295, 1915.

Z. Schuss. *Theory and Applications of Stochastic Processes: An Analytical Approach*. Springer, 2009.

T. Schwalger. The influence of temporally correlated noise on sequences of intervals. Diploma thesis, Humboldt-Universität zu Berlin, 2006.

T. Schwalger and B. Lindner. Higher-order statistics of a bistable system driven by dichotomous colored noise. *Phys. Rev. E*, 78:021121–13, 2008.

T. Schwalger and B. Lindner. Theory for serial correlations of interevent intervals. *Eur. Phys. J.-Spec. Top.*, 187(1):211–221, 2010.

T. Schwalger and L. Schimansky-Geier. Interspike interval statistics of a leaky integrate-and-fire neuron driven by gaussian noise with large correlation times. *Phys. Rev. E*, 77: 031914–9, 2008.

T. Schwalger, K. Fisch, J. Benda, and B. Lindner. How noisy adaptation of neurons shapes interspike interval histograms and correlations. *PLoS Comput Biol*, 6(12):e1001026, 2010. doi: 10.1371/journal.pcbi.1001026.

T. Schwalger, J. Tiana-Alsina, M. C. Torrent, J. Garcia-Ojalvo, and B. Lindner. Interspike-interval correlations induced by two-state switching in an excitable system. *EPL*, 99: 10004, 2012.

A. A. Selyanko and D. A. Brown. M-Channel gating and simulation. *Biophys J*, 77(2): 701–713, 1999.

M. Shadlen and W. T. Newsome. The variable discharge of cortical neurons: Implications for connectivity, computation and information coding. *J. Neurosci.*, 18:3870, 1998.

M. N. Shadlen and W. T. Newsome. Noise, neural codes and cortical organization. *Curr. Op. Neurobiol.*, 4:569, 1994.

G. Silberberg, M. Bethge, H. Markram, K. Pawelzik, and M. Tsodyks. Dynamics of population rate codes in ensembles of neocortical neurons. *J Neurophysiol*, 91(2):704–709, 2004.

E. C. Sobel and D. W. Tank. In vivo Ca2+ dynamics in a cricket auditory neuron: An example of chemical computation. *Science*, 263(5148):823–826, 1994.

C. Sobie, A. Babul, and R. de Sousa. Neuron dynamics in the presence of 1/f noise. *Phys. Rev. E*, 83(5):051912, 2011.

W. R. Softky and C. Koch. The highly irregular firing of cortical cells is inconsistent with temporal integration of random EPSPs. *J. Neurosci.*, 13:334, 1993.

R. B. Stein. A theoretical analysis of neuronal variability. *Biophys. J.*, 5:173, 1965.

P N Steinmetz, A Manwani, C Koch, M London, and I Segev. Subthreshold voltage noise due to channel fluctuations in active neuronal membranes. *J Comput Neurosci*, 9(2): 133–148, 2000.

M. Stemmler, M. Usher, and E. Niebur. Lateral interactions in primary visual cortex: a model bridging physiology and psychophysics. *Science*, 269(5232):1877–1880, 1995.

M Steriade, A Nuñez, and F Amzica. Intracellular analysis of relations between the slow (< 1 hz) neocortical oscillation and other sleep rhythms of the electroencephalogram. *J Neurosci*, 13(8):3266–3283, 1993.

R. L. Stratonovich. *Topics in the Theory of Random Noise*, volume 1. Gordon and Breach, New York, 1967.

A. Treves. Mean-field analysis of neuronal spike dynamics. *Network Comput Neural Syst*, 4:259–284, 1993.

H. C. Tuckwell. *Introduction to Theoretical Neurobiology*. Cambridge University Press, Cambridge, 1988.

H. C. Tuckwell. *Stochastic Processes in the Neuroscience*. Society for industrial and applied mathematics, Philadelphia, Pennsylvania, 1989.

E. Urdapilleta. Onset of negative interspike interval correlations in adapting neurons. *Phys Rev E*, 84:041904, 2011.

N. G. van Kampen. *Stochastic Processes in Physics and Chemistry*. North-Holland, Amsterdam, 1992.

R.R. De Ruyter van Steveninck, G. D. Lewen, S. P. Strong, R. Koberle, and W. Bialek. Reproducibility and variability in neural spike trains. *Science*, 275:1805, 1997.

C van Vreeswijk. Stochastic models of spike trains. In S Grün and S Rotter, editors, *Analysis of Parallel Spike Trains*, chapter 1. Springer, 2010.

C. van Vreeswijk and D. Hansel. Patterns of synchrony in neural networks with spike adaptation. *Neural Comp.*, 13(5):959–992, 2001.

T. Verechtchaguina, I.M. Sokolov, and L. Schimansky-Geier. First passage time densities in resonate-and-fire models. *Phys. Rev. E*, 73:031108, 2006.

R D Vilela and B Lindner. Are the input parameters of white noise driven integrate and fire neurons uniquely determined by rate and cv? *J Theor Biol*, 257(1):90–99, 2009.

A. Villarroel. Nonstationary noise analysis of M currents simulated and recorded in PC12 cells. *J Neurophysiol*, 77:2131–2138, 1997.

H S Wang, Z Pan, W Shi, B S Brown, R S Wymore, I S Cohen, J E Dixon, and D McKinnon. Kcnq2 and kcnq3 potassium channel subunits: molecular correlates of the m-channel. *Science*, 282(5395):1890–1893, 1998.

M. C. Wang and G. E. Uhlenbeck. On the theory of Brownian motion II. *Rev. Mod. Phys.*, 17:323, 1945. Reprinted in N. Wax *Selected Papers on Noise and Stochastic Processes* (Dover, New York, 1954).

X. J. Wang. Calcium coding and adaptive temporal computation in cortical pyramidal neurons. *J Neurophysiol*, 79(3):1549–1566, 1998.

B. Wark, B. N. Lundstrom, and A. Fairhall. Sensory adaptation. *Curr Opin Neurobiol*, 17 (4):423–429, 2007.

E. Weisstein. Lambert W function. *From MathWorld – A Wolfram Web Resource*, 2012. `http://mathworld.wolfram.com/LambertW-Function.html`.

J. A. White, J. T. Rubinstein, and A. R. Kay. Channel noise in neurons. *Trends Neuroscie*, 23(3):131–137, 2000.

K. Wiesenfeld, D. Pierson E. Pantazelou, C. Dames, and F. Moss. Stochastic resonance on a circle. *Phys. Rev. Lett.*, 72:2125, 1994.

C Wilson. Up and down states. *Scholarpedia*, 3(6):1410, 2008.

R S Zucker and W G Regehr. Short-term synaptic plasticity. *Annu Rev Physiol*, 64:355–405, 2002.

Danksagung / Acknowledgment

Das Zustandekommen dieser Arbeit ist zu einem beträchtlichen Teil meinem Betreuer und wissenschaftlichem Lehrer Prof. Dr. Benjamin Lindner zu verdanken. Ich danke ihm herzlichst für die inspirierende Betreuung und die volle Unterstützung meiner Doktorarbeit sowie für das große Vertrauen, welches er mir entgegengebracht hat. Seine Begeisterung für die Wissenschaft sowie die freundschaftliche Zusammenarbeit hat die Promotions für mich zu einer großen Freude gemacht.

Einen großen Dank gebührt Prof. Dr. Frank Jülicher vom Max-Planck-Institut für Physik komplexer Systeme in Dresden. Er gab mir die Möglichkeit, dreieinhalb Jahre an diesem wunderbaren Ort meine Dissertation anzufertigen.

I am particularly thankful to Prof. Dr. Jan Benda, Prof. Dr. Jordi Garcia-Ojalvo and Prof. Dr. Alexander Neiman for giving me the opportunity to fit my theoretical formulas to real-world data. I took much pleasure in the experimental collaborations, which were great experiences and from which I learned a lot.

A special thanks goes to Dr. Karin Fisch. She recorded spikes from neurons of the grasshoppers ear. These experiments started an exciting interplay between theory and experiment, a part of which (the theory) has been covered in chapter 4 of this thesis.

I would also like to thank Dr. Jordi Tiana-Alsina and Prof. Dr. Jordi Garcia-Ojalvo for providing me with gigabytes of laser data. The model fitting inspired the non-Markovian theory, which has been presented in chapter 5.

Ein ganz besonderer Dank gilt Dr. Benjamin Friedrich, Dr. Wiebke Potjans, Sergej Voronenko, Dr. Vitaly Belik, Felix Droste und Florian Fruth für das Korrekturlesen von Teilen dieser Arbeit.

Ich danke allen Mitgliedern der Gruppe "Theorie komplexer Systeme und Neurophysik" am Bernstein-Zentrum in Berlin sowie den Mitgliedern der Biophysik am MPI-PKS in Dresden für vier unvergessliche Jahre.

Schließlich möchte ich meiner Familie danken für die große Geduld und Unterstützung.

Selbständigkeitserklärung

Ich erkläre, dass ich die vorliegende Arbeit selbständig und nur unter Verwendung der angegebenen Literatur und Hilfsmittel angefertigt habe sowie aus fremden Quellen übernommene oder modifizierte Stellen als solche gekennzeichnet habe.

Berlin, den 21.08.2012 Tilo Schwalger